

University of Liverpool
Department of Chemistry



UNIVERSITY OF
LIVERPOOL

Transition Metal Terpyridine Complexes for Molecular Electronics

Thesis submitted in accordance with the requirements of the University of
Liverpool for the degree of Doctor of Philosophy.

By

Sarah Chappell

October 2014

Abstract

Currently there is a huge amount of interest in the synthesis and electrical characterisation of single molecules that have the potential for use in electronic devices. In order for this technology to move forward it is necessary to gain insights into structure-property relationships at the nanoscale, as well as a basic understanding of the charge transport through various molecular architectures. It has previously been demonstrated that the electrical properties of redox active single molecules can be investigated as a function of potential. This thesis investigates the single molecule conductance properties of molecules incorporating a transition metal centre.

The research presented in this thesis investigates two major studies. The first is a study into the electrochemical and conductance properties of a variety of transition metal based complexes. Initial electrochemical and conductance investigations of a series of pyterpy transition metal complexes showed a similar conductance for all the series, this was investigated in two different environments. The ligand was then varied and several ruthenium complexes were investigated, to investigate the anchoring group effect and to examine the length and conductance relationship. The data presented here demonstrates a higher conductance for methyl sulphide anchoring group than the pyridyl anchoring group. The data presented showed a low dependence on molecular length, suggesting a hopping transport mechanism. The conductance behaviour of two $[M(\text{pyterpy})_2](\text{PF}_6)_2$ complexes were investigated as a function of potential in an ionic liquid medium. The data presented exhibited an increase in conductance as the redox potential was reached.

The second study investigated the conductance behaviour of two 6-porphyrin nanorings. This is the first conductance study on these porphyrin based complexes. The study investigated a 'complete' and 'broken' nanoring and showed a smaller than expected difference in conductance between them. This preliminary study has allowed for the development of the structure to investigate possible quantum interference effects.

Acknowledgements

I firstly would like to thank my supervisor Prof. Simon Higgins for his help and support over the past four years and the opportunity to work in his research group. I would also like to extend my appreciation to my secondary supervisor, Prof. Richard Nichols and Prof. Don Bethell for all the advice and support.

I also would like to thank the Higgins-Nichols research group for their support and help. I would like to thank all the friends I have made throughout my time at Liverpool, in particular the lasting friendships built with Dr Carly Brooke and Dr Alex Lawrenson. Special mention must go to Dr Sam Catarelli for being a great friend and a massive support throughout both our PhD projects.

On a personal note, I would like to thank all my friends for supporting me throughout my PhD, in particular Leah, Pete and Dave. Special mention must go to Shaun Walker who has always been enthusiastic and supportive towards my studies. I'd also like to thank Rebekah and Michelle for their fantastic ability to take my mind off my work and Steve's parents for welcoming me into their family. A debt of gratitude is owed to my sister Jenny, her husband Peter, Henry and Abigail for their support and constant supply of Sunday roast dinners!

I'd like to thank and Steve for always being there for me as without him none of this would have been possible.

Contents

Abstract.....	i
Acknowledgements.....	ii
Abbreviations.....	vii
List of Figures.....	viii
List of Schemes.....	xvii
List of Tables.....	xviii
Chapter 1.....	1
1.1 Introduction.....	2
1.1.1 Introduction to Molecular Electronics:.....	2
1.2 Conductance measurements:.....	6
1.3 Scanning tunneling microscope:.....	7
1.3.1 Quantum Tunneling:.....	8
1.3.2 Calculating the conductance:.....	9
1.3.4 <i>Scanning Tunneling Microscope Instrumentation</i>	9
1.4 Self-Assembled Monolayers:.....	10
1.5 Electrochemistry.....	11
1.5.1 Electrode Reactions.....	11
1.5.2 Voltammetry.....	12
1.5.3 Cyclic Voltammetry.....	12
1.5.4 Monolayer Voltammetry.....	18
1.5.5 Laviron Analysis.....	19
1.5.6 Electrode Analysis.....	19
1.5.7 Solvent.....	20
1.6 Techniques for measuring the conductance:.....	21
1.6.1 $I(s)$ Method.....	21
1.6.2 $I(t)$ Method.....	23
1.6.3 Break junctions:.....	24
1.6.4 Electrochemically Controlled STM (EC-STM) technique:.....	25
1.7 Charge Transport.....	26
1.7.1 Coherent Charge Transport.....	26
1.7.2 Superexchange.....	28
1.7.3 Simmons Model.....	28

1.7.4 Resonant Tunneling	29
1.7.5 Non-Coherent Charge Transport: Hopping Regime.....	30
1.7.6 Transfer between Charge Transport Mechanisms.....	31
1.8 Modifying the Conductance:.....	32
1.8.1 Anchoring Group	32
1.8.2 Transmission Coefficients.....	35
1.8.3 Conductance Groups:.....	36
1.8.4 Medium Effects.....	37
1.8.5 Redox Gating:	40
1.9 Research Study Aim and Summary	43
1.10 References	46
Chapter 2	51
2.1 General Introduction.....	52
2.1.1 Transition Metal Complexes	52
2.1.2 Medium effects	56
2.1.3 Cyclic Voltammetry.....	56
2.2 Aim	59
2.3 Synthesis	59
2.3.1 Synthesis of 4'-(pyridin-4-yl)-2,2':6',2''-terpyridine (3)	59
2.3.2 Synthesis of [Ru(4'-(pyridin-4-yl)-2,2':6',2''-terpyridine) ₂](PF ₆) ₂ (4).....	60
2.3.3 Synthesis of [Fe(4'-(pyridin-4-yl)-2,2':6',2''-terpyridine) ₂](PF ₆) ₂ (5)	61
2.3.4 Synthesis of [Co(4'-(pyridin-4-yl)-2,2':6',2''-terpyridine) ₂](PF ₆) ₂ (6)	62
2.3.5 Synthesis of [Cr(4'-(pyridin-4-yl)-2,2':6',2''-terpyridine) ₂](PF ₆) ₃ (8).....	63
2.4 Methods.....	64
2.4.1 Single Molecule Conductance Measurements:.....	65
2.4.2 Cyclic Voltammetry Measurements:	65
2.5 Results	66
2.5.1 Conductance Results:.....	66
2.5.2 Cyclic Voltammetry.....	76
2.6: Discussion	86
2.7 Conclusions and Future Work.....	91
2.8 References.....	92
Chapter 3	95

3.1 General Introduction.....	96
3.1.1 Anchoring group.....	96
3.1.2 Molecular Length.....	100
3.1.3 Aim.....	102
3.2 Synthesis.....	102
3.3.1 Synthesis of 4'-[4-(pyridin-4-yl)phenyl]-2,2':6',2''-terpyridine (12).....	102
3.3.2 Synthesis of 4'-(methylthio)-2,2':6',2''-terpyridine (16).....	103
3.3.3 Synthesis of 4'-(4-(methylthio)phenyl)-2,2':6',2''-terpyridine (18).....	104
3.3.4 Synthesis of 4'-(4'-(methylthio)-[1,1'-biphenyl]-4-yl)-2,2':6',2''-terpyridine (20).....	105
3.3.5 Synthesis of Ruthenium Complexes.....	106
3.3.6 Synthesis of [Ru(2,6-di(pyridin-2-yl)pyrazine) ₂](PF ₆) ₂ (22).....	106
3.3.7 Synthesis of [Ru(4'-[4-(pyridin-4-yl)phenyl]-2,2':6',2''-terpyridine) ₂](PF ₆) ₂ (23).....	107
3.3.8 Synthesis of [Ru(4'-(methylthio)-2,2':6',2''-terpyridine) ₂](PF ₆) ₂ (24).....	107
3.3.9 Synthesis of [Ru(4'-(4-(methylthio)phenyl)-2,2':6',2''-terpyridine) ₂](PF ₆) ₂ (25).....	108
3.3.10 Synthesis of [Ru(4'-(4'-(methylthio)-[1,1'-biphenyl]-4-yl)-2,2':6',2''-terpyridine) ₂](PF ₆) ₂ (26).....	109
3.3 Experimental Methods.....	110
3.3.1 Sample Preparation.....	110
3.4 Results.....	111
3.4.1 Conductance Results.....	111
3.4.1.1 Pyridyl anchoring group analogues.....	111
3.4.1.2 Methyl Sulphide Anchoring Group Analogues.....	117
3.5 Discussion.....	121
3.6 Conclusion and Future Work.....	123
3.7 References.....	124
Chapter 4.....	128
4.1 General Introduction.....	129
4.1.1 Introduction.....	129
4.2 Aim.....	134
4.3 Methods.....	134
4.3.1 Synthesis.....	134

4.3.2 Conductance Measurements.....	134
4.3.3 Cyclic Voltammetry.....	135
4.4 Results	135
4.4.1 Cyclic Voltammetry.....	135
4.4.2: Conductance Measurements.....	138
4.4.3: Conductance Studies of [Fe(pyterpy) ₂](PF ₆) ₂ under electrochemical control	138
4.4.4: Conductance Studies of Co(pyterpy) ₂ (PF ₆) ₂ under electrochemical control	144
4.5: Discussion	148
4.6 Conclusions and Future work.....	150
4.7 References.....	151
Chapter 5	153
5.1 General Introduction.....	154
5.1.1 Introduction.....	154
5.2 Aim	160
5.3 Methods.....	160
5.4 Results	161
5.4.1 Conductance Measurements	161
5.5: Discussion	173
5.6 Conclusions and Future Work.....	176
5.7 References.....	177
Chapter 6	179
6.1 References.....	183
Chapter 7	184
7.1 General Experimental Procedures.....	185
7.1.1 Purification	185
7.1.2 Chromatography.....	185
7.1.3 Analytical Data.....	185
7.4 Syntheses.....	186
7.5 Scanning Tunneling Microscopy Measurements	198
7.6 Cyclic Voltammetry	199
7.7 All References	202

Abbreviations

AFM	Atomic Force Microscope
BDA	1,4-Benzenediamine
1,4-BDT	1,4-Benzenedithiol
BJ	Break Junction
CE	Counter Electrode
CH ₃ CN	Acetonitrile
CH ₃ OH	Methanol
CV	Cyclic Voltammetry
DFT	Density Functional Theory
EC	Electrochemical
EC-STM	Electrochemical Scanning Tunneling Microscope
ESA	Electrochemical Surface Area
HOMO	Highest Occupied Molecular Orbital
I-V	Current-Voltage
LUMO	Lowest Unoccupied Molecular Orbital
MCBJ	Mechanically Controlled Break Junction
OPE	Oligo(1,4-phenylene ethynylene)
OPERu	Ruthenium(II) bis(-arylacetylide)-complex
OPI	Oligophenyleneimines
Ph	Phenyl
PPT	4'-[4-(Pyridin-4-yl)phenyl]-2,2':6',2''-terpyridine
pTTF	pyrrolo-tetrathiafulvalene
pyterpy	4'-(Pyridin-4-yl)-2,2':6',2''-terpyridine
RE	Reference Electrode
RTIL	Room Temperature Ionic Liquid
SAM	Self-Assembled Monolayer
SCE	Saturated Calomel Electrode
SHE	Standard Hydrogen Electrode
STM	Scanning Tunneling Microscope
TBATFB	Tetrabutylammonium Tetrafluoroborate
TCNQ	Tetracyanoquinodimethane
TT	4'-(Methylthio)-2,2':6',2''-terpyridine

TTF	Tetrathiafulvalene
TPT	4'-(4-(Methylthio)phenyl)-2,2':6',2''-terpyridine
TPPT	4'-(4'-(Methylthio)-[1,1'-biphenyl]-4-yl)-2,2':6',2''-terpyridine
UHV	Ultra High Vacuum
UV	Ultraviolet
V	Viologen
WE	Working Electrode

List of Figures

Figure 1.1: The proposed structure of Aviram and Ratners rectifying molecule. ⁷	3
Figure 1.2: Energy diagrams of the Aviram-Ratner theory of molecular rectification. (a) Donor-(σ -bridge)-acceptor molecule between two electrodes with no applied voltage. (b) Forward bias applied causing realignment of molecular orbitals to allow tunneling within the junction to occur. (c) Energetically unfavoured tunneling when a reverse bias is applied. E_f – Fermi level of electrodes, ϕ – work function of electrode, V – potential applied to the electrode. Figure adapted from reference 7.	4
Figure 1.3: The chemical structure of the molecule investigated by Aviram <i>et al.</i> ⁸	5
Figure 1.4: (a) Chemical structure of 1,4-benzenedithiol (1,4-BDT) and (b) Schematic of 1,4-BDT trapped between two electrodes as investigated by Tour <i>et al.</i> ⁹	6
Figure 1.5: An example of a metal-molecule-metal junction.....	6
Figure 1.6: Schematic of the Scanning Tunneling Microscope (STM).....	7
Figure 1.7: Quantum tunneling through a potential barrier. At the tip and surface the energy of the electron (E) is greater than the potential (V), in the barrier the potential is larger than the energy of the electron. So in classical mechanics the electron is forbidden to be located in the barrier. Quantum mechanics allows the electron to “tunnel” through the gap. E_f is the Fermi Level of the electrodes, ϕ is the workfunction of the electrode and V_{bias} is the applied bias.....	8
Figure 1.8: Schematic of the self-assembly process to form monolayers on the required substrate.	11
Figure 1.9: A single electron transfer reaction for the reduction of Fe^{3+} to Fe^{2+}	12
Figure 1.10: The potential waveform of a cyclic voltammogram applied to the working electrode. The potential will be swept linearly from E_1 to E_2	13
Figure 1.11: An example cyclic voltammogram, showing the cathodic peak current i_{pc} , cathodic peak potential E_{pc} , anodic peak current i_{pa} , anodic peak potential E_{pa} and the half peak potential, $E_p/2$	14
Figure 1.12: A typical 3-electrode cyclic voltammetry experimental set up. Showing the working, counter, and reference electrode.	15

Figure 1.13: A cyclic voltammogram for a gold polycrystalline electrode in a phosphate buffer. Gold oxide reduction peak highlighted in orange is the peak required for further analysis.....	17
Figure 1.14: Experimentally obtained cyclic voltammograms exhibiting decreasing rate constants.....	18
Figure 1.15: A example symmetrical voltammogram for a fully reversible species adsorbed onto an electrode surface.....	19
Figure 1.16: Au(111) “butterfly” peak observed in H ₂ SO ₄ . The butterfly peak is located within the blue lines. Figure taken from reference 30.....	20
Figure 1.17: The I(s) method as developed by Haiss <i>et al.</i> ^{10c} (a) A conducting tip is moved in close to the substrate and can bind to a molecule. (b) The tip withdraws and the molecule bridges the gap, causing a plateau in the current distance curve. (c) As the tip is withdrawn further the contact breaks. When no molecule is present the black curve is observed, when a molecule is present a plateau appears, as shown in the red curve.....	22
Figure 1.18: Example plateau showing the analysis and location of S _{break off}	23
Figure 1.19: Schematic of the I(t) technique and the resultant current jumps. The current jumps were taken from Dr. Leary’s thesis. ³⁶ The tip remains in a constant height above the substrate. Molecules can then bridge the gap as shown in (b).	23
Figure 1.20: Schematic of the Mechanical Break Junction technique (MCBJ).....	24
Figure 1.21: Schematic of Tao’s <i>in-situ</i> break junction technique. ^{10a} (a) The tip is moved down towards the substrate surface and crashes into the substrate (b). The tip is then withdrawn from the surface (c) allowing a molecule to have the possibility of bridging the gap. As the tip is withdrawn further the molecule falls off (d)	25
Figure 1.22: Schematic of electrochemically controlled STM. A STM controller interfaced with a biopotentiostat is used and a four electrode set up, comprising of a working electrode (W.E), Counter Electrode (C.E), Reference Electrode (R.E) and the tip is the fourth electrode.	26
Figure 1.23: A plot of conductance vs. sample potential, exhibiting an off-on-off profile as the redox potential is swept.....	30
Figure 1.24: The hopping transport mechanism.....	30
Figure 1.25: Example OPI molecular structure studied by Choi <i>et al.</i> ⁴⁵	31
Figure 1.26: The change in transport mechanism as recorded by Choi <i>et al.</i> ⁴⁵ for a series of oligophenyleneimine (OPI) wires. Figure taken from reference 45.....	31
Figure 1.27: Conductance results reported by Park <i>et al.</i> (A) Structure of molecule trapped between two gold electrodes. (B) Example plateaux obtained for each anchoring group. (C) 1D histogram of the single molecule conductance for each anchoring group. (D) Length dependence of the recorded conductance for each anchoring group. Results taken from reference 46C.....	34
Figure 1.28: Structure of the porphyrin molecule investigated by Li <i>et al.</i> Taken from reference 69.....	35
Figure 1.29: The low (a), medium (b) and high (c) conductance referred to as A, B and C respectively.....	36

Figure 1.30: Chemical structure of 1,4-benzenediamine (BDA).	37
Figure 1.31: The chemical structure of the oligothiophenes ($6Th_n6$) studied by Leary <i>et al.</i> ¹⁶	38
Figure 1.32: Conductance histograms for $6Th_36$ under air (left), $V_{bias} = 0.4$ V and $I_0 = 7$ nA and argon (right), $V_{bias} = 1.0$ V and $I_0 = 7$ nA. Histograms taken from Dr. Leary's thesis. ³⁶	39
Figure 1.33: Chemical structure of the room temperature ionic liquid 1-butyl-3-methylimidazolium trifluoromethanesulfonate, (BMIM-OTf)	39
Figure 1.34: The length dependent conductance of α,ω -alkanedithiols in ambient and ionic liquid environments. Image taken from reference 34a.	40
Figure 1.35: Chemical Structure of 6PTTF6, 6V6 and 6Ph6	40
Figure 1.36: The conductance data for (a) 6V6 (b) 6PTTF6 and (c) 6Ph6. Taken from reference 61.	41
Figure 1.37: Plot of sample potential vs. conductance for 6pTTF6 overlaid with the cyclic voltammogram for 6pTTF6 (blue line). Taken from reference 34b.	42
Figure 1.38: The transition metal molecular wires investigated by Albrecht <i>et al.</i> ⁶² bound to the required substrate. The arcs present in (1) and (2) correspond to 2,2-bipyridine.	42
Figure 1.39: Shows the tunneling current enhancement as the redox potential for the osmium complex is swept. Figure taken from reference 33b.	43
Figure 2.1: Chemical structure of the organometallic complex investigated by Liu <i>et al.</i> ⁴	53
Figure 2.2: Chemical structure of terpyridine	53
Figure 2.3: Chemical structure of the organometallic complex to be investigated.	54
Figure 2.4: Schematic of the stepwise formation of terpyridine based molecular wires. a) Assembly of the terpyridine ligand on to the gold surface. b) Coordination of the metal centre (Co or Fe) to the ligand. c) Coordination of the terpyridine linker ligand. d) The processes b and c are repeated as required. Figure taken from reference 6.	55
Figure 2.5: Chemical structure of the systems studied by Zhou <i>et al.</i> ⁸ Figure taken from reference 8.	56
Figure 2.6: Molecular structure of the Os(II) complex studied by Albrecht <i>et al.</i> ¹⁴	58
Figure 2.7: CV data of Ossac on Au(111) in aqueous 0.1 M HClO ₄ (black) and ionic liquid, BMIM-PF ₆ (red); scan rate - 0.1 V/s. Figure taken from reference 14.	58
Figure 2.8: ¹ H NMR spectra recorded in CD ₃ OD, a) Cr(pyterpy) ₂ (PF ₆) ₃ . b) Cr(pyterpy) ₂ (PF ₆) ₃ and NaOH.	64
Figure 2.9: Data for 4,4'-bipyridine in ambient conditions $V_{bias} = 0.6$ and $I_0 = 40$ nA (a) Histogram of 505 $I(s)$ scans (b) 2D histogram showing conductance relative to total break-off distance (c) Histogram of the experimental break-off distances (d) example $I(s)$ traces (distance is relative and does not represent actually break-off distance)	67
Figure 2.10: Data for [Ru(pyterpy) ₂](PF ₆) ₂ in ambient conditions $V_{bias} = 0.6$ and $I_0 = 40$ nA (a) Histogram of 520 $I(s)$ scans (b) 2D histogram showing conductance relative to total break-off distance (c) Histogram of the experimental break-off distances (d)	

example $I(s)$ traces (distance is relative and does not represent actually break-off distance).....	68
Figure 2.11: Data for $[\text{Fe}(\text{pyterpy})_2](\text{PF}_6)_2$ in ambient conditions $V_{\text{bias}} = 0.6$ and $I_0 = 40$ nA (a) Histogram of 413 $I(s)$ scans (b) 2D histogram showing conductance relative to total break-off distance (c) Histogram of the experimental break-off distances (d) example $I(s)$ traces (distance is relative and does not represent actually break-off distance).....	69
Figure 2.12: Data for $[\text{Co}(\text{pyterpy})_2](\text{PF}_6)_2$ in ambient conditions $V_{\text{bias}} = 0.6$ and $I_0 = 40$ nA (a) Histogram of 508 $I(s)$ scans (b) 2D histogram showing conductance relative to total break-off distance (c) Histogram of the experimental break-off distances (d) example $I(s)$ traces (distance is relative and does not represent actually break-off distance).....	70
Figure 2.13: Data for $[\text{Cr}(\text{pyterpy})_2](\text{PF}_6)_3$ in ambient conditions $V_{\text{bias}} = 0.6$ and $I_0 = 40$ nA (a) Histogram of 511 $I(s)$ scans (b) 2D histogram showing conductance relative to total break-off distance (c) Histogram of the experimental break-off distances (d) example $I(s)$ traces (distance is relative and does not represent actually break-off distance).....	71
Figure 2.14: Data for 4,4'-bipyridine in ionic liquid $V_{\text{bias}} = 0.6$ and $I_0 = 40$ nA (a) Histogram of 440 $I(s)$ scans (b) 2D histogram showing conductance relative to total break-off distance (c) Histogram of the experimental break-off distances (d) example $I(s)$ traces (distance is relative and does not represent actually break-off distance)	72
Figure 2.15: Data for $[\text{Ru}(\text{pyterpy})_2](\text{PF}_6)_2$ in ionic liquid $V_{\text{bias}} = 0.6$ and $I_0 = 40$ nA (a) Histogram of 538 $I(s)$ scans (b) 2D histogram showing conductance relative to total break-off distance (c) Histogram of the experimental break-off distances (d) example $I(s)$ traces (distance is relative and does not represent actually break-off distance)	73
Figure 2.16: Data for $[\text{Fe}(\text{pyterpy})_2](\text{PF}_6)_2$ in ionic liquid $V_{\text{bias}} = 0.6$ and $I_0 = 40$ nA (a) Histogram of 401 $I(s)$ scans (b) 2D histogram showing conductance relative to total break-off distance (c) Histogram of the experimental break-off distances (d) example $I(s)$ traces (distance is relative and does not represent actually break-off distance)	74
Figure 2.17: Data for $[\text{Co}(\text{pyterpy})_2](\text{PF}_6)_2$ in ionic liquid $V_{\text{bias}} = 0.6$ and $I_0 = 40$ nA (a) Histogram of 508 $I(s)$ scans (b) 2D histogram showing conductance relative to total break-off distance (c) Histogram of the experimental break-off distances (d) example $I(s)$ traces (distance is relative and does not represent actually break-off distance)	75
Figure 2.18: Data for $[\text{Cr}(\text{pyterpy})_2](\text{PF}_6)_3$ in ionic liquid $V_{\text{bias}} = 0.6$ and $I_0 = 40$ nA (a) Histogram of 510 $I(s)$ scans (b) 2D histogram showing conductance relative to total break-off distance (c) Histogram of the experimental break-off distances (d) example $I(s)$ traces (distance is relative and does not represent actually break-off distance)	76
Figure 2.19: Cyclic Voltammogram of 7 mM $[\text{Ru}(\text{pyterpy})_2](\text{PF}_6)_2$ in 0.1 M TBATFB MeCN electrolyte. The potential scale has been calibrated to the Fc/Fc^+ couple. Scan rates 0.05 Vs^{-1} to 1 Vs^{-1}	77
Figure 2.20: Cyclic Voltammogram of 7 mM $[\text{Fe}(\text{pyterpy})_2](\text{PF}_6)_2$ in 0.1 M TBATFB MeCN electrolyte. The potential scale has been calibrated to the Fc/Fc^+ couple. Scan rates 0.02 Vs^{-1} to 1 Vs^{-1}	78

Figure 2.21: Cyclic Voltammogram of 7 mM [Co(pyterpy) ₂](PF ₆) ₂ in 0.1 M TBATFB MeCN electrolyte. The potential scale has been calibrated to the Fc/Fc ⁺ couple. Scan rates 0.02 Vs ⁻¹ to 1 Vs ⁻¹ .	79
Figure 2.22: Cyclic Voltammogram of 7 mM [Cr(pyterpy) ₂](PF ₆) ₃ in 0.1 M TBATFB MeCN electrolyte. The potential scale has been calibrated to the Fc/Fc ⁺ couple. Scan rates 0.02 Vs ⁻¹ to 1 Vs ⁻¹ .	80
Figure 2.23: Cyclic Voltammogram of 7 mM [Ru(pyterpy) ₂](PF ₆) ₂ in BMIM-TFSA electrolyte. The potential scale has been calibrated to the Fc/Fc ⁺ couple. Scan rates 0.02 Vs ⁻¹ to 1 Vs ⁻¹ .	81
Figure 2.24: Cyclic Voltammogram of 7 mM [Fe(pyterpy) ₂](PF ₆) ₂ in BMIM-TFSA electrolyte. The potential scale has been calibrated to the Fc/Fc ⁺ couple. Scan rates 0.02 Vs ⁻¹ to 1 Vs ⁻¹ .	82
Figure 2.25: Cyclic Voltammogram of 7 mM [Co(pyterpy) ₂](PF ₆) ₂ in BMIM-TFSA electrolyte. The potential scale has been calibrated to the Fc/Fc ⁺ couple. Scan rates 0.02 Vs ⁻¹ to 1 Vs ⁻¹ .	83
Figure 2.26: Cyclic Voltammogram of 7 mM [Cr(pyterpy) ₂](PF ₆) ₃ in BMIM-TFSA electrolyte. The potential scale has been calibrated to the Fc/Fc ⁺ couple. Scan rates 0.02 Vs ⁻¹ to 1 Vs ⁻¹ .	84
Figure 2.27: Cyclic Voltammogram of 7 mM Ferrocene in BMIM-TFSA electrolyte. Scan rates 0.02 Vs ⁻¹ to 1 Vs ⁻¹ .	85
Figure 2.28: Chemical structure of the pyridyl capped oligo-porphyrins studied by Sedghi <i>et al.</i> ²⁸	88
Figure 2.29: Histogram of Ionic Liquid, BMIM-TFSA showing no conductance peaks	90
Figure 3.1: The chemical structure of the transition metal complexes to be investigated to see the variation of anchoring group vs. conductance	97
Figure 3.2: Molecular structure of the porphyrin studied by Li <i>et al.</i> ⁵³ Figure adapted from reference ⁵³	97
Figure 3.3: a) shows the compounds investigated in the study b) and c) show the clear presence of two conductances, high and low for each of the four compounds. Figure taken from reference 48.	99
Figure 3.4: Logarithm of the low (blue), medium and high conductance group for alkanedithiols as a function of number of CH ₂ groups (N) in ambient conditions and a bias of +0.6 V. Taken from reference 88.	101
Figure 3.5: The ruthenium complexes investigated by Kim <i>et al.</i> Figure taken from reference 90.	101
Figure 3.6: The chemical structure of the ligands investigated in this study	102
Figure 3.7: Data for [Ru(2,6-di(pyridin-2-yl)pyrazine) ₂](PF ₆) ₂ in ambient conditions $V_{bias} = 0.6$ V and $I_0 = 40$ nA (a) Histogram of 506 $I(s)$ scans (b) 2D histogram showing conductance relative to total break-off distance (c) Histogram of the experimental break-off distances (d) example $I(s)$ traces (distance is relative and does not represent actually break-off distance).	112
Figure 3.8: Data for [Ru(pyterpy) ₂](PF ₆) ₂ in ambient conditions $V_{bias} = 0.6$ V and $I_0 = 40$ nA (a) Histogram of 520 $I(s)$ scans (b) 2D histogram showing conductance relative to	

total break-off distance (c) Histogram of the experimental break-off distances (d) example $I(s)$ traces (distance is relative and does not represent actually break-off distance).....	113
Figure 3.9: Data for $[\text{Ru}(\text{PPT})_2](\text{PF}_6)_2$ in ambient conditions $V_{bias} = 0.6 \text{ V}$ and $I_0 = 20 \text{ nA}$ (a) Histogram of 468 $I(s)$ scans (b) 2D histogram showing conductance relative to total break-off distance (c) Histogram of the experimental break-off distances (d) example $I(s)$ traces (distance is relative and does not represent actually break-off distance)	114
Figure 3.10: (a) Plot of the conductance vs. distance (Au-Molecule-Au) of the ruthenium pyridyl series. (b) Plot of the $\ln(\sigma)$ vs. distance (Au-Molecule-Au) of the ruthenium pyridyl series. Where blue triangle is $[\text{Ru}(\text{pyrazine})_2](\text{PF}_6)_2$, red circle is $[\text{Ru}(\text{pyterpy})_2](\text{PF}_6)_2$ and black square is $[\text{Ru}(\text{PPT})_2](\text{PF}_6)_2$.	114
Figure 3.11: Data for $[\text{Co}(2,6\text{-di}(\text{pyridin-2-yl})\text{pyrazine})_2](\text{BF}_4)_2$ in ambient conditions $V_{bias} = 0.6 \text{ V}$ and $I_0 = 40 \text{ nA}$ (a) Histogram of 502 $I(s)$ scans (b) 2D histogram showing conductance relative to total break-off distance (c) Histogram of the experimental break-off distances (d) example $I(s)$ traces (distance is relative and does not represent actually break-off distance).....	116
Figure 3.12: Data for $[\text{Co}(\text{pyterpy})_2](\text{PF}_6)_2$ in ambient conditions $V_{bias} = 0.6 \text{ V}$ and $I_0 = 40 \text{ nA}$ (a) Histogram of 508 $I(s)$ scans (b) 2D histogram showing conductance relative to total break-off distance (c) Histogram of the experimental break-off distances (d) example $I(s)$ traces (distance is relative and does not represent actually break-off distance).....	117
Figure 3.13: (a) Plot showing conductance vs. distance for the cobalt series. (b) plot of $\ln(\text{conductance})$ vs. distance for both the cobalt and ruthenium series.....	117
Figure 3.14: Data for $[\text{Ru}(\text{TT})_2](\text{PF}_6)_2$ in ambient conditions $V_{bias} = 0.6 \text{ V}$ and $I_0 = 40 \text{ nA}$ (a) Histogram of 542 $I(s)$ scans (b) 2D histogram showing conductance relative to total break-off distance (c) Histogram of the experimental break-off distances (d) example $I(s)$ traces (distance is relative and does not represent actually break-off distance)	118
Figure 3.15: Data for $[\text{Ru}(\text{TPT})_2](\text{PF}_6)_2$ in ambient conditions $V_{bias} = 0.6$ and $I_0 = 40 \text{ nA}$ (a) Histogram of 528 $I(s)$ scans (b) 2D histogram showing conductance relative to total break-off distance (c) Histogram of the experimental break-off distances (d) example $I(s)$ traces (distance is relative and does not represent actually break-off distance)	119
Figure 3.16: Data for $[\text{Ru}(\text{TPPT})_2](\text{PF}_6)_2$ in ambient conditions $V_{bias} = 0.6 \text{ V}$ and $I_0 = 20 \text{ nA}$ (a) Histogram of 550 $I(s)$ scans (b) 2D histogram showing conductance relative to total break-off distance (c) Histogram of the experimental break-off distances (d) example $I(s)$ traces (distance is relative and does not represent actually break-off distance)	120
Figure 3.17: (a) plot of conductance vs. distance for the methyl sulphide series. (b) plot of $\ln(\sigma)$ vs. distance for the methyl sulphide series.....	120
Figure 3.18: (a) Plot of conductance vs. distance for both ruthenium pyridyl and methyl sulphide series. (b) plot of $\ln(\sigma)$ vs. distance for the two series.....	121
Figure 4.1 Schematic of the conductance behaviours exhibited when redox active molecules are measured as a function of potential (a) on-off type behaviour. (b) off-on-off type behaviour.	130

Figure 4.2: (a) Schematic of the Mn ²⁺ complex attached to gold electrodes. (b) Fabricated three-terminal device. (c) Molecular structure of the Mn ²⁺ complex. Figure adapted from reference ¹⁰¹	131
Figure 4.3: (a) Cyclic voltammetry results for the Osmium Bisterpyridine complex in BMIM-PF ₆ (red line) and aqueous HClO ₄ (black line). Scan Rate 0.1 V/s (b) Tunneling current enhancement in ionic liquid measured using an EC-STM (c) Schematic of the Os complex between the tip and substrate. Figure adapted from reference 33b.	132
Figure 4.4: (a) Molecular system investigated. (b) Conductance (blue dots) and cyclic voltammetry (black line) for [Os(pyterpy) ₂ (PF ₆) ₂] as recorded by Zhou <i>et al.</i> ⁶⁸ Figure adapted from reference 68.	133
Figure 4.5: Schematic of the investigated complexes between two electrodes.	134
Figure 4.6: Cyclic voltammogram of [Fe(pyterpy) ₂](PF ₆) ₂ monolayer in BMIM-TFSA electrolyte. The potential scale has been calibrated to the Fc/Fc ⁺ couple. Scan rates 0.1 Vs ⁻¹ to 50 Vs ⁻¹	136
Figure 4.7: (A) Plot of E _p (V) vs. ln(v) for [Fe(pyterpy) ₂](PF ₆) ₂ (B) The section utilised to calculate v. Black is E _p ^c and Red is E _p ^a	137
Figure 4.8: Cyclic Voltammogram of [Co(pyterpy) ₂](PF ₆) ₂ monolayer in BMIM-TFSA electrolyte. The potential scale has been calibrated to the Fc/Fc ⁺ couple.....	137
Figure 4.9: Plot of E _p (V) vs. ln(v) for [Co(pyterpy) ₂](PF ₆) ₂ (B) The section utilised to calculate v. Black is E _p ^c and Red is E _p ^a	138
Figure 4.10: Conductance histograms of [Fe(pyterpy) ₂](PF ₆) ₂ using sample potentials of (a) 1.05 V, (b) 1 V, (c) 0.95 V, (d) 0.9 V, (e) 0.85 V and (f) 0.8 V, obtained using the <i>I(s)</i> method; V _{BIAS} = +0.6 V ; I ₀ = 40 nA ; 257, 516, 533, 502, 535 and 501 scans were analysed respectively. Sample potentials are with respect to the Pt quasi reference.....	139
Figure 4.11: Conductance histograms of [Fe(pyterpy) ₂](PF ₆) ₂ using sample potentials of (g) 0.75 V, (h) 0.7 V, (i) 0.65 V, (j) 0.6 V, (k) 0.55 V and (l) 0.45 V, obtained using the <i>I(s)</i> method; V _{BIAS} = +0.6 V ; I ₀ = 40 nA ; 507, 501, 512, 303, 253 and 255 scans were analysed respectively. Sample potentials are with respect to the Pt quasi reference....	140
Figure 4.12: 2D Conductance histograms of [Fe (pyterpy) ₂](PF ₆) ₂ relative to break off distance using sample potentials of (a) 1.05 V, (b) 1 V, (c) 0.95 V, (d) 0.9 V, (e) 0.85 V and (f) 0.8 V. Sample potentials are with respect to the Pt quasi reference.	142
Figure 4.13: 2D Conductance histograms of [Fe (pyterpy) ₂](PF ₆) ₂ relative to break off distance using sample potentials of (g) 0.75 V, (h) 0.7 V, (i) 0.65 V, (j) 0.6 V, (k) 0.55 V and (l) 0.45 V. Sample potentials are with respect to the Pt quasi reference.....	143
Figure 4.14: Conductance of [Fe(pyterpy) ₂](PF ₆) ₂ vs. Sample potential, V vs. Fc/Fc ⁺ . Redox potential given by red line.	143
Figure 4.15: Conductance histograms of [Co(pyterpy) ₂](PF ₆) ₂ using sample potentials of (a) -0.8 V, (b) -0.6 V, (c) -0.4 V, (d) -0.35 V, (e) -0.25 V and (f) -0.15 V, obtained using the <i>I(s)</i> method; V _{BIAS} = +0.6 V ; I ₀ = 40 nA ; 258, 309, 265, 510, 508 and 562 scans were analysed respectively. Sample potentials are with respect to the Pt quasi reference....	144
Figure 4.16: Conductance histograms of [Co(pyterpy) ₂](PF ₆) ₂ using sample potentials of (g) -0.05 V, (h) 0 V, (i) 0.05 V, (j) 0.15 V, (k) 0.25 V, (l) 0.4 V, (m) 0.6 V and (n) 0.8 V, obtained using the <i>I(s)</i> method; V _{BIAS} = +0.6 V ; I ₀ = 40 nA ; 491, 540, 502, 425, 421, 365,	

323 and 329 scans were analysed respectively. Sample potentials are with respect to the Pt quasi reference.....	145
Figure 4.17: 2D Conductance histograms of [Co(pyterpy)₂](PF₆)₂ relative to break off distance using sample potentials of (a) -0.8 V, (b) -0.6 V, (c) -0.4 V, (d) -0.35 V, (e) -0.25 V, (f) -0.15 V, (g) -0.05 V, (h) 0 V, (i) 0.05 V, (j) 0.15 V and (k) 0.25 V. Sample potentials are with respect to the Pt quasi reference.....	147
Figure 4.18: 2D Conductance histograms of [Co(pyterpy) ₂](PF ₆) ₂ relative to break off distance using sample potentials of (l) 0.4 V, (m) 0.6 V and (n) 0.8 V. Sample potentials are with respect to the Pt quasi reference.....	148
Figure 4.19: Conductance of [Co(pyterpy) ₂](PF ₆) ₂ vs. Sample potential, V vs. Fc/Fc ⁺ . Redox potential position given by the red line.	148
Figure 5.1: Molecular structure of the simplest porphyrin, porphine.....	154
Figure 5.2: (a) Chemical structure of the oligo-porphyrin (1-3) and reference (5) molecules to be investigated. (b) ln(conductance) vs. calculated sulfur-sulfur distance of the molecule. Figure adapted from reference 79a.....	155
Figure 5.3: Scheme of 14 nm long porphyrin based molecular wire. Figure adapted from reference 103d.	156
Figure 5.4: Chemical structure of six-porphyrin nanoring bound to gold electrode.	157
Figure 5.5: Schematic of quantum interference.	158
Figure 5.6: Schematic of the para-stilbene and meta-counterpart as reported by Aradhya <i>et al.</i> ¹⁰⁵	159
Figure 5.7: Chemical structure of the porphyrin based nanorings to be studied. (A) The complete nanoring (B) The broken nanoring, with the two breaks being signalled by the red arrows.....	160
Figure 5.8: Data for Complete Nanoring in ambient conditions $V_{bias} = 0.6$ and $I_0 = 8$ nA (a) Histogram of 513 $I(s)$ scans (b) 2D histogram showing conductance relative to total break-off distance (c) Histogram of the experimental break-off distances (d) example $I(s)$ traces (distance is relative and does not represent actually break-off distance)	162
Figure 5.9: Data for Complete Nanoring in ambient conditions $V_{bias} = 0.6$ and $I_0 = 20$ nA (a) Histogram of 520 $I(s)$ scans (b) 2D histogram showing conductance relative to total break-off distance (c) Histogram of the experimental break-off distances (d) example $I(s)$ traces (distance is relative and does not represent actually break-off distance)	163
Figure 5.10: Data for Complete Nanoring in ambient conditions $V_{bias} = 0.6$ and $I_0 = 60$ nA (a) Histogram of 526 $I(s)$ scans (b) 2D histogram showing conductance relative to total break-off distance (c) Histogram of the experimental break-off distances (d) example $I(s)$ traces (distance is relative and does not represent actually break-off distance)	164
Figure 5.11: Data for Complete Nanoring in mesitylene conditions $V_{bias} = 0.6$ and $I_0 = 8$ nA (a) Histogram of 502 $I(s)$ scans (b) 2D histogram showing conductance relative to total break-off distance (c) Histogram of the experimental break-off distances (d) example $I(s)$ traces (distance is relative and does not represent actually break-off distance).....	165
Figure 5.12: Data for Complete Nanoring in mesitylene conditions $V_{bias} = 0.6$ and $I_0 = 20$ nA (a) Histogram of 467 $I(s)$ scans (b) 2D histogram showing conductance relative to	

total break-off distance (c) Histogram of the experimental break-off distances (d) example $I(s)$ traces (distance is relative and does not represent actually break-off distance).....	166
Figure 5.13: Data for Complete Nanoring in mesitylene conditions $V_{bias} = 0.6$ and $I_0 = 60$ nA (a) Histogram of 455 $I(s)$ scans (b) 2D histogram showing conductance relative to total break-off distance (c) Histogram of the experimental break-off distances (d) example $I(s)$ traces (distance is relative and does not represent actually break-off distance).....	167
Figure 5.14: Data for Broken Nanoring in ambient conditions $V_{bias} = 0.6$ and $I_0 = 8$ nA (a) Histogram of 571 $I(s)$ scans (b) 2D histogram showing conductance relative to total break-off distance (c) Histogram of the experimental break-off distances (d) example $I(s)$ traces (distance is relative and does not represent actually break-off distance)	168
Figure 5.15: Data for Broken Nanoring in ambient conditions $V_{bias} = 0.6$ and $I_0 = 20$ nA (a) Histogram of 502 $I(s)$ scans (b) 2D histogram showing conductance relative to total break-off distance (c) Histogram of the experimental break-off distances (d) example $I(s)$ traces (distance is relative and does not represent actually break-off distance)	169
Figure 5.16: Data for broken Nanoring in ambient conditions $V_{bias} = 0.6$ and $I_0 = 60$ nA (a) Histogram of 582 $I(s)$ scans (b) 2D histogram showing conductance relative to total break-off distance (c) Histogram of the experimental break-off distances (d) example $I(s)$ traces (distance is relative and does not represent actually break-off distance)	170
Figure 5.17: Data for Broken Nanoring in mesitylene conditions $V_{bias} = 0.6$ and $I_0 = 8$ nA (a) Histogram of 399 $I(s)$ scans (b) 2D histogram showing conductance relative to total break-off distance (c) Histogram of the experimental break-off distances (d) example $I(s)$ traces (distance is relative and does not represent actually break-off distance)	171
Figure 5.18: Data for broken Nanoring in mesitylene conditions $V_{bias} = 0.6$ and $I_0 = 20$ nA (a) Histogram of 452 $I(s)$ scans (b) 2D histogram showing conductance relative to total break-off distance (c) Histogram of the experimental break-off distances (d) example $I(s)$ traces (distance is relative and does not represent actually break-off distance)	172
Figure 5.19: Data for broken Nanoring in mesitylene conditions $V_{bias} = 0.6$ and $I_0 = 60$ nA (a) Histogram of 486 $I(s)$ scans (b) 2D histogram showing conductance relative to total break-off distance (c) Histogram of the experimental break-off distances (d) example $I(s)$ traces (distance is relative and does not represent actually break-off distance)	173
Figure 7.1: Cyclic Voltammogram of Au(111) surface in a 0.1 M H_2SO_4 electrolyte referenced to SCE. Scan Rate 0.1 V/s.....	200
Figure 7.2: Cyclic voltammogram of Au polycrystalline electrode in 0.1 M phosphate buffer referenced to SCE. Scan rate 0.05 V/s.....	200

List of Schemes

Scheme 2.1: Synthetic Pathway to 4'-(pyridin-4-yl)-2,2':6',2''-terpyridine.....	60
---	----

Scheme 2.2: Synthesis of $[\text{Ru}(4'-(\text{pyridin-4-yl})-2,2':6',2''\text{-terpyridine})_2](\text{PF}_6)_2$	61
Scheme 2.3: Synthesis of $[\text{Fe}(4'-(\text{pyridin-4-yl})-2,2':6',2''\text{-terpyridine})_2](\text{PF}_6)_2$	61
Scheme 2.4: Synthesis of $[\text{Co}(4'-(\text{pyridin-4-yl})-2,2':6',2''\text{-terpyridine})_2](\text{PF}_6)_2$	62
Scheme 2.5: Synthesis of $[\text{Co}(4'-(\text{pyridin-4-yl})-2,2':6',2''\text{-terpyridine})_2](\text{PF}_6)_3$	63
Scheme 2.6: Synthesis of $\text{Cr}(4'-(\text{pyridin-4-yl})-2,2':6',2''\text{-terpyridine})_2(\text{PF}_6)_3$	63
Scheme 3.1: Synthesis of 4'-[4-(pyridin-4-yl)phenyl]-2,2':6',2''-terpyridine.....	103
Scheme 3.2: Synthetic pathway to 4'-(methylthio)-2,2':6',2''-terpyridine	104
Scheme 3.3: Synthetic pathway to 4'-(4-(methylthio)phenyl)-2,2':6',2''-terpyridine ...	105
Scheme 3.4: Synthetic pathway to 4'-(4'-(methylthio)-[1,1'-biphenyl]-4-yl)-2,2':6',2''-terpyridine	106
Scheme 3.5: Synthesis of $[\text{Ru}(2,6\text{-di}(\text{pyridin-2-yl})\text{pyrazine})_2](\text{PF}_6)_2$	107
Scheme 3.6: Synthesis of $[\text{Ru}(4'-[4-(\text{pyridin-4-yl})\text{phenyl}]-2,2':6',2''\text{-terpyridine})_2](\text{PF}_6)_2$	107
Scheme 3.7: Synthesis of $[\text{Ru}(4'-(\text{methylthio})-2,2':6',2''\text{-terpyridine})_2](\text{PF}_6)_2$	108
Scheme 3.8: $[\text{Ru}(4'-(4-(\text{methylthio})\text{phenyl})-2,2':6',2''\text{-terpyridine})_2](\text{PF}_6)_2$	109
Scheme 3.9: $[\text{Ru}(4'-(4'-(\text{methylthio})-[1,1'-\text{biphenyl}]-4\text{-yl})-2,2':6',2''\text{-terpyridine})_2](\text{PF}_6)_2$	110

List of Tables

Table 1.1 Possible conduction mechanisms for the Coherent charge transport regime adapted from reference ⁴⁰⁻⁴¹	27
Table 1.2: Values for the transmission coefficients and binding energies for various anchoring groups. Data adapted from reference 41a.....	35
Table 2.1: Redox potentials of iron(II), ruthenium(II) and osmium(II) complexes of 2,2':6',2''-terpyridine and 4'-(4-pyridin-4-yl)-2,2':6',2''-terpyridine (V, vs. internal ferrocene-ferrocenium; MeCN solution, $[\text{Bu}^n_4][\text{BF}_4]$ supporting electrolyte). Data taken from reference 11.....	57
Table 2.2: The recorded redox potentials $E_{1/2}$ and the difference between the anodic and cathodic peak potentials ΔE_p for 7 mM $[\text{Ru}(\text{pyterpy})_2](\text{PF}_6)_2$ in a 0.1 M TBATFB solution of MeCN. The average redox potential for ferrocene is used to calibrate the potential scale.	77
Table 2.3: The recorded redox potentials $E_{1/2}$ and the difference between the anodic and cathodic peak potentials ΔE_p for 7 mM $[\text{Fe}(\text{pyterpy})_2](\text{PF}_6)_2$ in a 0.1 M TBATFB solution of MeCN. The average redox potential for ferrocene is used to calibrate the potential scale.	78
Table 2.4: The recorded redox potentials $E_{1/2}$ and the difference between the anodic and cathodic peak potentials ΔE_p for 7 mM $[\text{Co}(\text{pyterpy})_2](\text{PF}_6)_2$ in a 0.1 M TBATFB solution of MeCN. The average redox potential for ferrocene is used to calibrate the potential scale.	79

Table 2.5: The recorded redox potentials $E_{1/2}$ and the difference between the anodic and cathodic peak potentials ΔE_p for 7 mM $[\text{Cr}(\text{pyterpy})_2](\text{PF}_6)_3$ in a 0.1 M TBATFB solution of MeCN. The average redox potential for ferrocene is used to calibrate the potential scale.	80
Table 2.6: The recorded redox potentials $E_{1/2}$ and the difference between the anodic and cathodic peak potentials ΔE_p for 7 mM $[\text{Ru}(\text{pyterpy})_2](\text{PF}_6)_2$ in BMIM-TFSA. The average redox potential for ferrocene is used to calibrate the potential scale.	82
Table 2.7: The recorded redox potentials $E_{1/2}$ and the difference between the anodic and cathodic peak potentials ΔE_p for 7 mM $[\text{Fe}(\text{pyterpy})_2](\text{PF}_6)_2$ in BMIM-TFSA. The average redox potential for ferrocene is used to calibrate the potential scale.	83
Table 2.8: The recorded redox potentials $E_{1/2}$ and the difference between the anodic and cathodic peak potentials ΔE_p for 7 mM $[\text{Co}(\text{pyterpy})_2](\text{PF}_6)_2$ in BMIM-TFSA. The average redox potential for ferrocene is used to calibrate the potential scale.	84
Table 2.9: The recorded redox potentials $E_{1/2}$ and the difference between the anodic and cathodic peak potentials ΔE_p for 7 mM $[\text{Cr}(\text{pyterpy})_2](\text{PF}_6)_3$ in BMIM-TFSA. The average redox potential for ferrocene is used to calibrate the potential scale.	85
Table 2.10: The recorded redox potentials $E_{1/2}$ and the difference between the anodic and cathodic peak potentials ΔE_p for 7 mM Ferrocene in BMIM-TFSA.....	86
Table 2.11: Summary of the conductance data.....	86
Table 2.12: Summary of the break off data for the conductance measurements.....	89
Table 2.13: Summary of the cyclic voltammetry results.....	90
Table 3.1: Summary of Single Molecule Conductance results of Porphyrins measured using the STM Break Junction method and DFT calculation results. Taken from reference 53.	98
Table 3.2: Estimate of the total break-of distance for all the measured complexes compared to the length of the molecule sandwiched between two gold electrodes.	121
Table 4.1: Summary of the conductance data	140
Table 4.2: Summary of break off distance	141
Table 4.3: Summary of the conductance data	146
Table 4.4: Summary of the break off distance data calculated.	146
Table 4.5: The recorded redox potentials $E_{1/2}$ for $M(\text{pyterpy})_2(\text{PF}_6)_2$ complexes in BMIM-TFSA for solution and monolayer voltammetry results calibrated to ferrocene reference.....	149
Table 5.1: Conductance results and calculated length for the oligo-porphyrin and reference molecules investigated by Sedghi <i>et al.</i> Data taken from reference 79b.....	155
Table 5.2: Summary of the complete nanoring in ambient environment conductance data and estimated break off distance.	164
Table 5.3: Summary of the complete nanoring data, including conductance and estimated break off distance.....	167
Table 5.4: Summary of the broken nanoring in ambient environment conductance data and estimated break off distance.	170
Table 5.5: Summary of the broken nanoring data, including conductance and estimated break off distance.	173

Table 5.6: Summary of the conductance data for porphyrin based Nanoring complexes.	174
Table 5.7: Summary of the estimated total break off distances for both nanorings.	175

Chapter 1

Introduction

1.1 Introduction

In 1965, the co-founder of Intel, Gordon Moore, predicted that the number of components that could be fitted on to a single silicon chip would double every year.¹ In 1975 he altered his prediction to doubling every two years.² This prediction is known as Moore's Law. Having stayed true for at least forty years, Moore's Law has been evidenced by the great increase in computer processing power over that time. These developments have been driven by progression in photolithography techniques for use on silicon to form the ever shrinking silicon chips. Yet, the production of these devices is becoming increasingly elaborate and expensive.³ Moore himself has pointed out that although the number of transistors that can fit onto a silicon chip has increased exponentially, the cost to produce these new chips has also increased greatly.⁴ Current methods used to create such small devices are referred to as the 'top-down' approach, which involves the scaling down of bulk systems.

'Top-down' solid-state electronics is expected to reach its fundamental physical limit within the next ten years. At such a small scale, problems have arisen from the miniaturisation of top-down electronics including charge leakage from the insulating silicon dioxide layer⁵ as well as the need for improved fabrication techniques to accommodate such small systems. Eventually it will no longer be feasible to continue reducing these silicon-based electronic devices, thus generating an essential drive in the exploration of alternative fabrication methods. It is theorised that the 'bottom-up' approach where systems are built from atoms or molecules – a field known as molecular electronics, will soon rise to prominence.

1.1.1 Introduction to Molecular Electronics:

Richard Feynman gave a lecture in 1959 entitled "There's plenty of room at the bottom".⁶ In this legendary lecture, Feynmann discusses the possibility of manipulating matter at the atomic scale. Although it was considered practically impossible at the time, this lecture is considered to be the inspiration for the field of nanotechnology which developed decades later.

In 1974, Aviram and Ratner first proposed the use of organic compounds for a pathway through which electrons could travel, for use in rectifying molecular

electronic components.⁷ They proposed a rectifying organic molecule with properties similar to a p-n junction. This was achieved by using substituents to affect the π -electron density on the organic molecule to achieve rectifying effects. The molecule studied consisted of an electron accepting group and an electron donating group separated by an insulating σ -bridge as shown in Figure 1.1. The σ -bridge ensures that the donor, tetrathiafulvalene (TTF) and accepting, tetracyanoquinodimethane (TCNQ) moieties are connected but do not electronically interact and also helps to keep molecular rigidity.

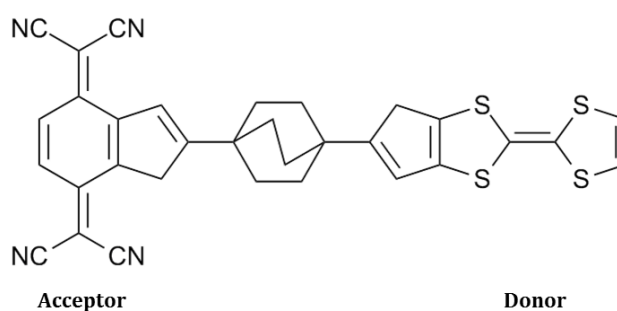


Figure 1.1: The proposed structure of Aviram and Ratners rectifying molecule.⁷

When applying a forward voltage to the system, the electrons tunnel from the cathode to the lowest unoccupied molecular orbital (LUMO) of the acceptor and simultaneously from the highest occupied molecular orbital (HOMO) of the donor to the anode. An electron can then tunnel from the occupied LUMO of the acceptor to the empty HOMO of the donor when the orbitals are energetically close enough, resulting in the ground state being restored. The energetically favourable energy diagram (Figure 1.2(b)), proposed by Aviram and Ratner, shows that electron transfer in the system will occur when there is a forward voltage.

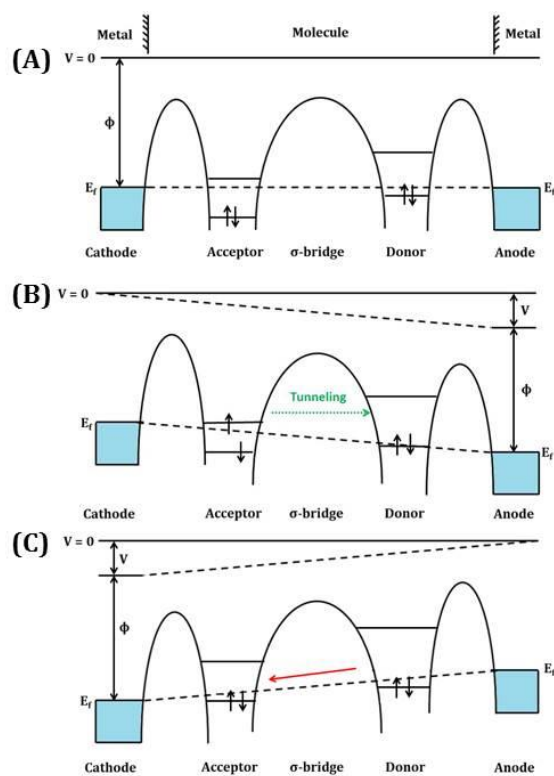


Figure 1.2: Energy diagrams of the Aviram-Ratner theory of molecular rectification. (a) Donor-(σ -bridge)-acceptor molecule between two electrodes with no applied voltage. (b) Forward bias applied causing realignment of molecular orbitals to allow tunneling within the junction to occur. (c) Energetically unfavoured tunneling when a reverse bias is applied. E_f - Fermi level of electrodes, ϕ - work function of electrode, V - potential applied to the electrode. Figure adapted from reference 7.

When a reverse voltage is applied the mechanism is energetically unfavourable as the LUMO of the donor is higher in energy than the HOMO of the acceptor, Figure 1.2(c). This results in rectification within the system and the molecule behaving like a p-n junction. Although this theoretical work showed the possibilities of using single molecules in electronic devices, their idea was considered impossible to be tested experimentally. It is possible for tunneling to occur under a reverse bias if the voltage applied to the junction is high enough. For this to occur, the LUMO of the donor would need to be lowered to the Fermi level of the anode and the Fermi level of the second electrode would have to be below the HOMO of the acceptor to make tunneling from the donor to an acceptor possible.

It was in 1988 that Aviram *et al.* measured the current-voltage (I-V) characteristics of a hemiquinone based molecule using a scanning tunneling microscope as shown in Figure 1.3.⁸

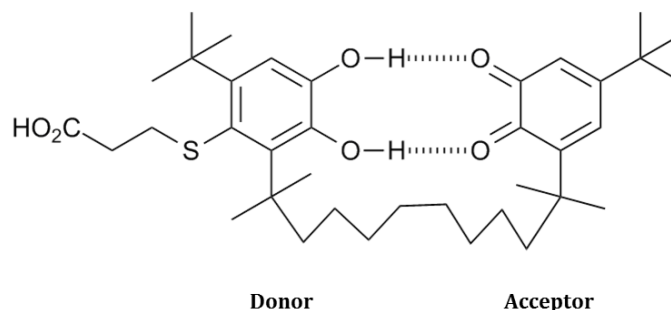


Figure 1.3: The chemical structure of the molecule investigated by Aviram *et al.*⁸

This was completed by forming a monolayer of the hemiquinone on an Au(111) surface. Current-voltage data was measured at various areas of the gold surface, using a Pt tip. When the measurements were made on a flat surface, the I-V result resembled that for bare Au. When a hemiquinone molecule was present in the junction, however, the current peaked at -200 mV when the potential was swept in a negative direction. This result was not observed when sweeping in the positive direction. Although this result could be due to different metals being used as contacts, the result is a landmark in the field, being the first measurement of its kind to be reported.

In 1997, Tour *et al.* completed what is believed to be the first transport measurements on a single molecule junction.⁹ They reported the single molecule conductance of 1,4-benzenedithiol (1,4-BDT), as shown below in Figure 1.4. They used a mechanically controlled break junction (MCBJ) in ambient condition to complete the measurements.

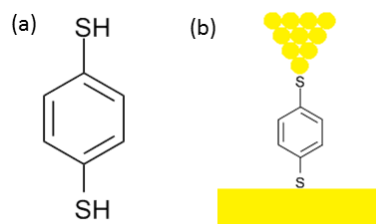


Figure 1.4: (a) Chemical structure of 1,4-benzenedithiol (1,4-BDT) and (b) Schematic of 1,4-BDT trapped between two electrodes as investigated by Tour *et al.*⁹

This pioneering result was a breakthrough in the field of single molecule electronics and resulted in an increase of interest in the field. 1,4-BDT has been extensively studied using a variety of methods. Since this pioneering work by Tour *et al.*, a variety of experimental techniques have been developed to probe the conductance of single molecules. However for the field to progress forward an understanding of electron transport mechanisms are required.

1.2 Conductance measurements:

To measure the conductance, a molecule is trapped between two electrodes (Figure 1.5). This results in a metal-molecule-metal junction, the electrical properties of which can then be investigated. The conductance measurements are completed using most commonly a scanning tunneling microscope (STM),¹⁰ atomic force microscope (AFM)¹¹ or mechanically controlled break junctions (MCBJ).^{9,12}

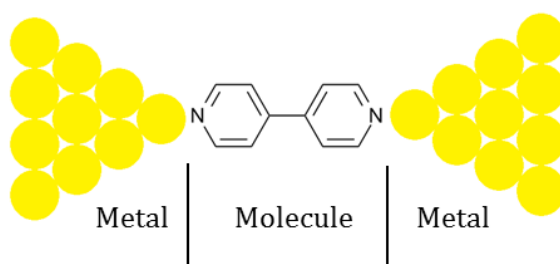


Figure 1.5: An example of a metal-molecule-metal junction

For all the single molecule conductance measurements in this report a STM is utilised.

1.3 Scanning tunneling microscope:

The scanning tunneling microscope was developed in 1981 by Gerd Binnig and Heinrich Rohrer whilst working at the IBM Zurich research laboratories in Switzerland.¹³ The development of the STM would earn them the Nobel Prize in Physics in 1986.¹⁴

As well as imaging, the STM can manipulate single atoms on the substrate. These investigations can be completed using a variety of substrates as well as different environmental conditions, such as UHV,¹⁵ ambient, argon,¹⁶ in liquid¹⁷ and at varying temperatures.¹⁸ This ability to investigate various properties has allowed the STM to become a key surface characterisation technique.

The STM is based upon the principles of quantum tunnelling. A schematic of the STM set up can be seen in Figure 1.6.

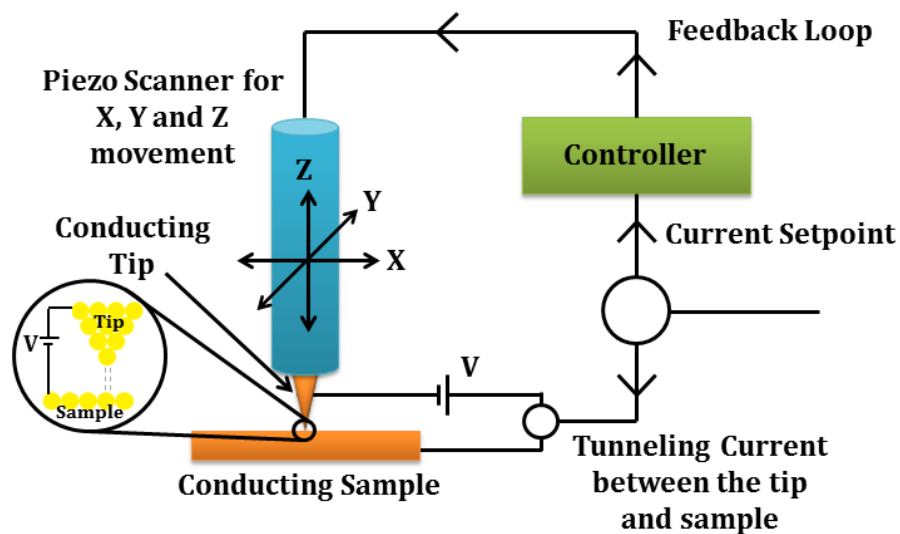


Figure 1.6: Schematic of the Scanning Tunneling Microscope (STM)

Typically the STM is operated by bringing the conducting tip close to the substrate with the required sample on it. A tunneling current can then be obtained by applying a bias voltage between the tip and sample. The conducting tip is then kept in constant height or constant current mode. In constant height mode the tip remains in a constant height above the substrate and the tunneling current varies depending on the surface properties. In constant current mode a

feedback loop is used to adjust the height of the tip to keep the tunneling current constant.

1.3.1 Quantum Tunneling:

Classical mechanics predicts the electron will not pass the barrier when the energy of an electron is below the barrier height upon which it is incident. Quantum mechanics contradicts this and predicts that the electron will not necessarily reflect, but may penetrate the barrier; this is shown in Figure 1.7.

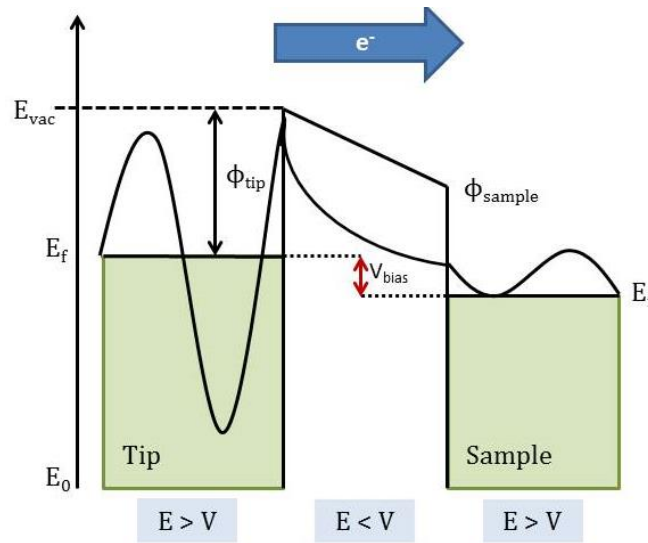


Figure 1.7: Quantum tunneling through a potential barrier. At the tip and surface the energy of the electron (E) is greater than the potential (V), in the barrier the potential is larger than the energy of the electron. So in classical mechanics the electron is forbidden to be located in the barrier. Quantum mechanics allows the electron to “tunnel” through the gap. E_f is the Fermi Level of the electrodes, ϕ is the workfunction of the electrode and V_{bias} is the applied bias

In the STM, $E > V$ regions are the tip and substrate and the electronic wavefunction oscillates. Within the barrier $E < V$, which is the gap between the tip and substrate, electrons are classically forbidden to exist. When this barrier is thin enough, electrons tunnel between the STM tip and substrate and a current will flow.

The tunneling current between the tip and substrate is given by Equation 1.1.¹⁹

$$I(d) \propto \exp(-2\kappa d) \quad \text{where} \quad \kappa = \sqrt{2m\phi/\hbar} \quad \text{Equation 1.1}$$

Where $I(d)$ is tunneling current, m is mass of electron, \hbar is Planck's constant/ 2π , d is the distance between the substrate and the tip and, ϕ is the work function. The tunneling current depends exponentially on the distance (d) between the substrate and the tip. This results in the tunneling current being lower the further away the tip is from the substrate. This dependency allows for precise control of the tip-sample separation which results in high vertical resolution.

1.3.2 Calculating the conductance:

The conductance of the single molecule junction is calculated using the Landauer formula, shown below in Equation 1.2.²⁰

$$G = \frac{I}{V} = \frac{2e^2}{h} T_L T_R T_{mol} \quad \text{Equation 1.2}$$

Where G is the conductance, I is the current through the junction, V is the applied bias, e is the elementary charge, h is Planck's constant, and T_L , T_R and T_{mol} are the transmission coefficients of the left contact, right contact and the molecule, respectively. It can be seen below in Equation 1.3, that the maximum conductance per conductance channel is the situation where $T = T_L T_R T_{mol} = 1$ with T being a measure of the efficiency of the electron transmission across the junction. This is called the quantum of conductance, G_0 .

$$G_0 = 2e^2/h = 77500 \text{ nS} \quad \text{Equation 1.3}$$

1.3.4 Scanning Tunneling Microscope Instrumentation:

The STM is made up of various parts which allow the instrument to work effectively; a few of these are listed below.

Scanner: The scanner allows the tip to move in 3 perpendicular directions: X, Y and Z. The stepper motor will bring the tip within close proximity of the substrate and the piezo crystals move the tip to the set point current required. When a voltage is applied, the piezo crystals contract and expand with nanoscale precision.

Feedback Loop: The feedback loop ensures that constant current is maintained. When the tunneling current deviates from the current set by the user an error signal is produced and the feedback loop adjusts the position of

the tip until the correct tunneling current is achieved. The gain setting determines the sensitivity to error and must be selected carefully.

Tip: The tip is one of the most important parts of the STM set up. The quality of the tip can have a great effect on the operation of the STM. It is essential that the tip is a sharp conducting material. Optimum performance is achieved when the tunneling current flows through a single atom at the end of the tip as when tunneling occurs through multiple atoms on the tip, anomalous imaging artefacts can appear. It is therefore essential to control the shape of the tips. This can be achieved by cutting the tip which often results in a single atom protruding at the end of the tip. The tips can also be etched electrochemically which allows a level of control over the geometry of the tip.

1.4 Self-Assembled Monolayers:

Self-assembled monolayers allow the formation of the required monolayer on the substrate.²¹ This involves depositing the required molecules onto the substrate from solution or gas. The molecule has to have two main parts, the anchoring group and the back bone. The anchoring group connects the back bone to the required substrate. The effect of the choice of anchoring group will be discussed further in Section 1.8.1. A large range of concentrations can be used as well as a variety of solvents. The formation of the monolayer involves immersing the substrate in a solution of the molecule allowing the molecules to chemisorb, and physisorb to the substrate. During this time the molecules organise themselves on the substrate surface. After the immersion time the substrate is rinsed with the solvent to remove any physisorbed molecules. The substrate can then be dried with nitrogen gas, this process is shown in Figure 1.8.

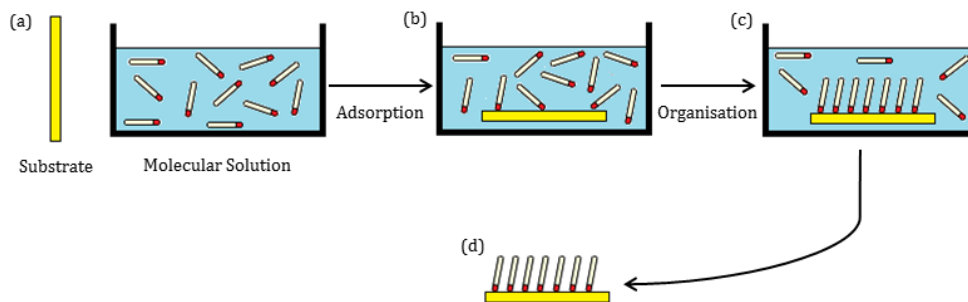


Figure 1.8: Schematic of the self-assembly process to form monolayers on the required substrate.

To form reproducible SAMs the parameters, such as, concentration and temperature have to be well controlled. For all the single molecule conductance measurements completed in this project a low coverage self-assembled monolayer was formed.

1.5 Electrochemistry

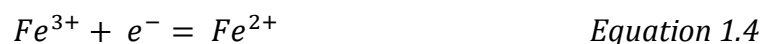
Electrochemistry is the study of the reactions that occur at the electrode-electrolyte interface and the transfer of electrons between the two. As the interest in redox gated single molecule junctions increases it is important to fully understand the electrochemical properties of the molecule of interest.

1.5.1 Electrode Reactions

A typical electrode reaction involves the transfer of charge between a species in solution and an electrode. This reaction will ideally involve a series of steps:

1. The reactant moves to the electrode-electrolyte interface – this is called mass transport.
2. Electron transfer then occurs via quantum mechanical tunneling between the reactant close to the electrode and the electrode.
3. The product will then move away from the electrode allowing fresh reactant to reach the electrode.

A simple example of an electrode reaction is a single electron transfer reaction such as the reduction of Fe^{3+} to Fe^{2+} as seen in Equation 1.4.²²



In this case the Fe^{3+} will move towards the electrode interface, where it will gain an electron resulting in the reduction to Fe^{2+} . The formed Fe^{2+} will then move away from the electrode, allowing further Fe^{3+} to reach the interface, this process can be seen below in Figure 1.9.

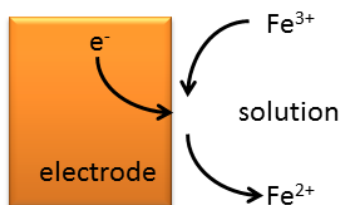


Figure 1.9: A single electron transfer reaction for the reduction of Fe^{3+} to Fe^{2+}

1.5.2 Voltammetry

Voltammetry is a method used to investigate the electrochemical properties of a molecule of interest. There are several forms of voltammetry:

- Potential Step
- Linear Sweep
- Cyclic Voltammetry

For each of these voltammetry experiments, a voltage or series of voltages are applied and the resulting current is measured.²³ In potential step voltammetry the applied voltage is immediately jumped from one voltage to another. The resulting current is measured as a function of time. In linear sweep voltammetry, a fixed potential range is used. The voltage is scanned from a lower limit to an upper limit. The resulting current is plotted as a function of voltage rather than time as in potential step measurements. The results allow either the oxidation or reduction potential to be calculated.

1.5.3 Cyclic Voltammetry

Cyclic voltammetry is a technique which is frequently used to investigate the electrochemistry of the molecules of interest. The results reported in this thesis have been completed using the cyclic voltammetry technique.

A cyclic voltammetry experiment involves applying a potential to the working electrode which changes with time, as seen in Figure 1.10.

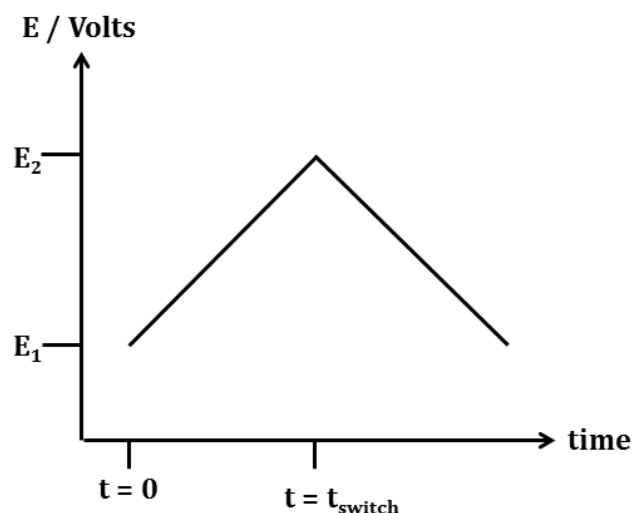


Figure 1.10: The potential waveform of a cyclic voltammogram applied to the working electrode. The potential will be swept linearly from E_1 to E_2 .

The current flowing through the working electrode is recorded as a function of the applied potential, resulting in a voltammogram of current vs. potential, as shown in Figure 1.11. The starting potential E_1 is usually selected so that the chemical species being investigated is not initially oxidised or reduced. The potential is then swept to the second selected potential E_2 , at which point the direction of the scan is changed and the potential then sweeps back to the starting potential. The potentials are chosen so that the oxidation or reduction processes are within the potential range.

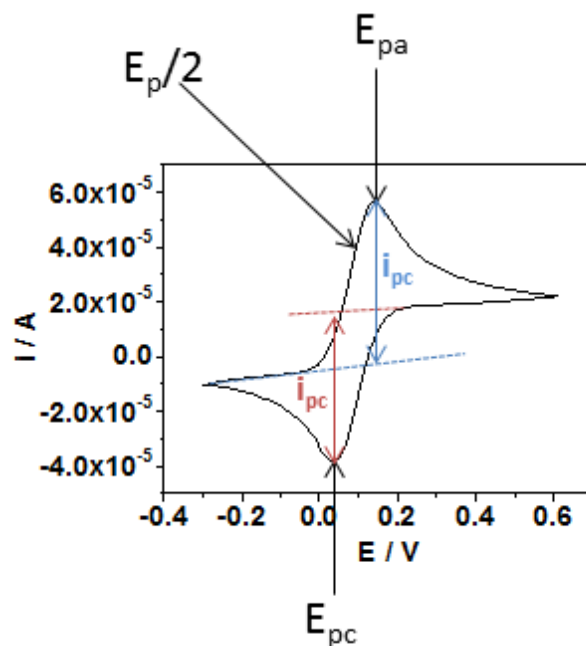


Figure 1.11: An example cyclic voltammogram, showing the cathodic peak current i_{pc} , cathodic peak potential E_{pc} , anodic peak current i_{pa} , anodic peak potential E_{pa} and the half peak potential, $E_p/2$.

A typical cyclic voltammetry experiment consists of three electrodes, a working electrode, a reference electrode and a counter electrode. An electrolyte is used in the solvent to ensure conductivity. The solution remains unstirred. The combination of electrode, electrolyte and solvent determines the possible potential range. The working electrode is where the reaction takes place; a controlled surface area is important for interpretation of the cyclic voltammetry results. The working electrode is commonly made of inert metals such as gold or inert carbon such as glassy carbon. Depending on the reaction being studied (oxidation or reduction), the working electrode can be called the anode or cathode. The counter electrode allows the transfer of current and has a surface area comparable or greater than that of the working electrode. If an oxidation is taking place at the working electrode, a reduction will occur at the counter electrode. So if the working electrode is behaving as an anode, the counter electrode will behave as a cathode and vice versa. The counter electrode is also formed from inert materials such as gold, platinum or carbon. The reference electrode has a stable known potential and is used to measure the potential of the system without passing a current through it. There are many reference

electrodes available with various potentials that can be referenced back to the standard reference electrode, the hydrogen electrode. The half-cell reaction for the standard hydrogen electrode is seen below in Equation 1.5.



The standard hydrogen electrode absolute potential is estimated to be about 4.44 V at 25 °C, but to allow comparison with all other electrode reactions, the SHE potential is declared to be 0 V. A standard experimental set up can be seen below in Figure 1.12.

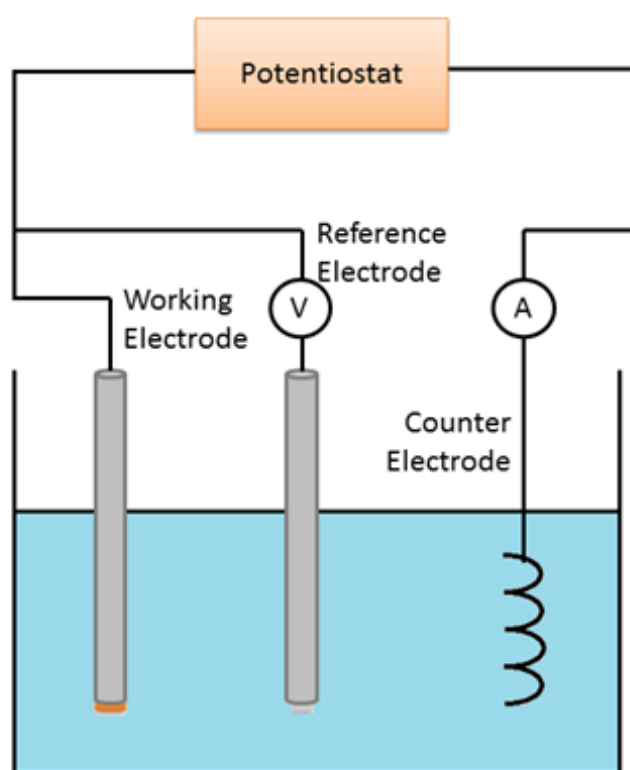


Figure 1.12: A typical 3-electrode cyclic voltammetry experimental set up. Showing the working, counter, and reference electrode.

Under conditions of equilibrium at an electrode surface, the Nernst equation defines the electrode potential for each electrochemical reaction with the activities of oxidised, O and reduced, R species given by Equation 1.6:²³

$$E = E^o + \frac{RT}{nF} \ln \left(\frac{C_O}{C_R} \right) \quad \text{Equation 1.6}$$

Where E is the potential and E^0 is the standard redox potential for the couple involving O and R, C_o is the concentration of the oxidised part of the couple and C_r is the concentration of the reduced part. R is the gas constant, T is the temperature, F is Faraday's constant and n is the amount of electrons transferred.

The shape of the voltammogram is determined by the electron transfer kinetics of the reaction. Voltammograms can be predicted, their peak current is given by the Randles-Ševčík equation, as shown in Equation 1.7.²⁴

$$I_p = 0.4463 nFAc \sqrt{\frac{nFDv}{RT}} \quad \text{Equation 1.7}$$

Where I_p is the peak height, A is the area of the working electrode, c is the concentration, D is the diffusion coefficient, v is the scan rate, R is the molar gas constant, T is the temperature in K, F is Faraday's constant and n is the number of electrons. If the Randles-Ševčík equation is used to calculate the diffusion coefficient, the rate constant can then be calculated according to Nicholson, Equation 1.8.²⁵

$$\varphi = \frac{\gamma^\alpha k_s}{\sqrt{\pi a v D_a}} \quad \text{Equation 1.8}$$

Where φ is the charge transfer parameter, α is the charge transfer coefficient, k_s is the standard rate constant for electron transfer, v is the scan rate, γ is $\sqrt{\frac{D_a}{D_c}}$, D_a is the diffusion coefficient for the reduced species, D_c is the diffusion coefficient for the oxidised species, a is nF/RT , n is the number of electrons, F is Faraday's constant, R is the molar gas constant and T is the temperature in K.

The electrochemical surface area (ESA) of a gold polycrystalline electrode can be calculated following standard literature procedures.²⁶

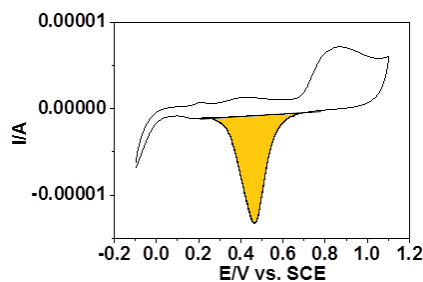


Figure 1.13: A cyclic voltammogram for a gold polycrystalline electrode in a phosphate buffer. Gold oxide reduction peak highlighted in orange is the peak required for further analysis.

The determination of the area was done by integration of the gold oxide reduction peak (Figure 1.13). Then the ESA is the ratio between the charge of the gold oxide reduction on the studied electrode surface and the standard reference charge for polycrystalline gold, $(390 \pm 10) \mu\text{C cm}^{-2}$.

For a reversible electrochemical reaction the recorded voltammogram has to show the following characteristics.²³

1. The positions of the peak voltage do not change as a function of scan rate.
2. Peak currents are proportional to the square root of the scan rate.
3. The voltage separation between the peaks is

$$\Delta E = E_p^a - E_p^c = \frac{59}{n} \text{ mV}$$

4. Ratio of peak currents is 1

$$\left| \frac{i_p^a}{i_p^c} \right| = 1$$

Electrochemically irreversible reactions occur when the surface equilibrium is not maintained due to the slow electron transfer rate. Quasi-reversible reactions are an intermediate between the two. The effect of decreasing electron transfer rate can be seen in Figure 1.14.

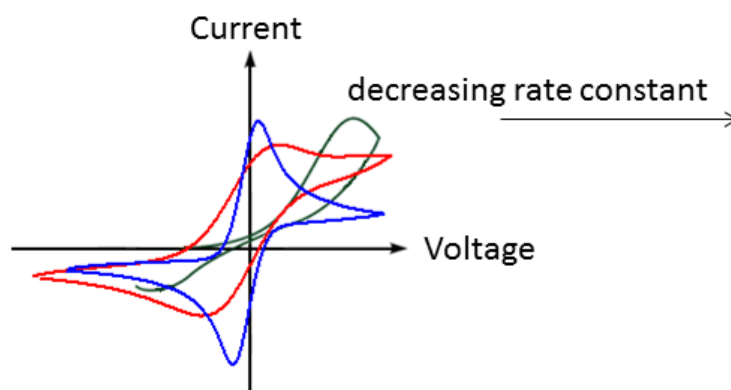


Figure 1.14: Experimentally obtained cyclic voltammograms exhibiting decreasing rate constants.

The blue voltammogram in Figure 1.14 shows a faster rate constant and is reversible. The red and green voltammograms show the effects of a decreasing rate constant with the peaks eventually becoming asymmetrical. For the green curve the voltage range examined would need to be widened for complete investigation to occur.

1.5.4 Monolayer Voltammetry

As well as being a useful characterisation tool for solutions, cyclic voltammetry can be used to investigate the electrochemical properties of monolayers of the molecule of interest formed on the surface of the working electrode.²⁷ A symmetrical voltammogram would be produced for a fully reversible species adsorbed onto an electrode surface, Figure 1.15.

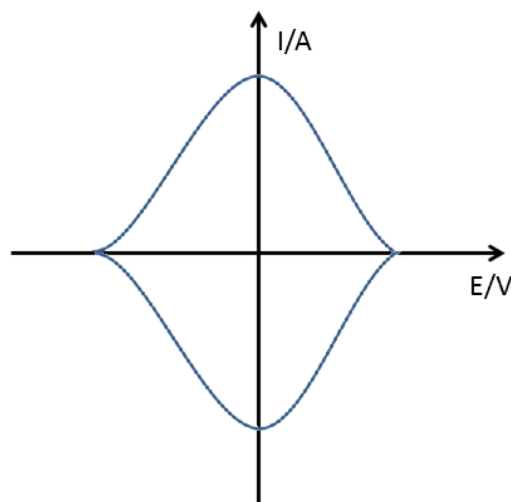


Figure 1.15: A example symmetrical voltammogram for a fully reversible species adsorbed onto an electrode surface.

The symmetrical nature of the voltammogram is due to the reaction not being subject to diffusion like solution voltammetry and there being a set amount of reactant available. When the reaction is quasi-reversible, asymmetrical peaks will be observed.

1.5.5 Laviron Analysis

In 1979, Laviron reported the determination of the electron transfer rate constant, k_{ET} of species adsorbed to an electrode.²⁸ The rate constant can be established by applying the constraint of $\eta = 0$ to Equation 1.9, which can be reduced to Equation 1.10.²⁹

$$\log k_{APP} = \alpha \log(1 - \alpha) + (1 - \alpha) \log \alpha - \log \left(\frac{RT}{nFv} \right) - \frac{\alpha(1-\alpha)nF\eta}{2.3RT} \quad \text{Equation 1.9}$$

$$k_{ET} = \frac{\alpha nFv_c}{RT} = (1 - \alpha) \frac{nFv_a}{RT} \quad \text{Equation 1.10}$$

Where k_{APP} is the apparent rate constant, α is the transfer coefficient, R is the gas constant, T is temperature, n is, F is Faraday's constant, v is scan rate, η is the overpotential and the x-intercept of the graph E_p vs. $\ln(v)$ provides v_c and v_a .

1.5.6 Electrode Analysis

Using cyclic voltammetry, it is possible to investigate the quality of the working electrode. Hamelin have shown that it is possible to monitor the quality of Au(111) single crystals, as seen in Figure 1.16.³⁰

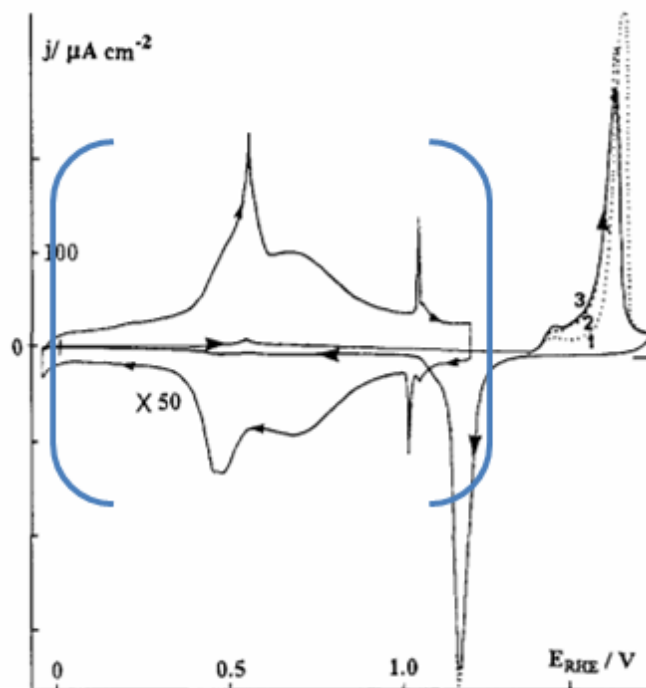


Figure 1.16: Au(111) “butterfly” peak observed in H₂SO₄. The butterfly peak is located within the blue lines. Figure taken from reference 30.

The voltammetry is completed in H₂SO₄. The adsorption of sulphate ions results in a defined “butterfly” peak occurring in the double layer region of the voltammogram. The Au(111) crystal can be checked by looking at the quality of the recorded butterfly peak.

1.5.7 Solvent

The chosen solvent to be used for the cyclic voltammetry experiments is of great importance due to the molecules of interest having different properties. It is essential to choose a solvent with a suitable potential range for the molecule.

Aqueous

In aqueous cyclic voltammetry, a saturated calomel reference electrode (SCE) is commonly used due to its stability and ease of use. The half-cell equation for the SCE can be seen below in Equation 1.11.



The SCE has a potential of 0.244 V vs. SHE at room temperature. Aqueous solvents have been thoroughly investigated, although often most cost effective

aqueous electrolytes do not exhibit a large potential range window like organic solvents.

Organic

The use of organic solvents for cyclic voltammetry is of great interest due to the wider accessible potential range than aqueous solvents; however an electrolyte is still required.³¹ Generally, the experimental set up involves the working, counter and reference electrodes, electrolyte and then referenced to an internal standard, typically ferrocene. Anhydrous conditions can be used for sensitive molecules. Acetonitrile has been shown to be effective for investigating the electrochemistry of transition metal complexes.³²

Room Temperature Ionic Liquid (RTIL)

Room temperature ionic liquids have been shown to be successful solvents for use in electrochemistry.³³ RTILs have a wider potential range and, unlike organic solvents, have no need for an additional electrolyte due to their high conductivity. Ionic liquids are typically used in a dry environment. Their low volatility and ability to be used in single molecule electronics measurements make ionic liquids an attractive solvent to be used consistently throughout both cyclic voltammetry and conductance measurements.^{33b, 34}

1.6 Techniques for measuring the conductance:

1.6.1 $I(s)$ Method

The $I(s)$ method which was developed by Haiss *et al.*^{10c} A low coverage self-assembled monolayer (SAM) is fashioned on an Au(111) substrate. The Au STM tip is then brought close to small distance above the substrate using the current setpoint (I_0). The Au tip is then gradually lifted away from the surface (increasing z-position) whilst remaining in a constant (x,y) position, as the tip is pulled away from the surface, the current drops exponentially. When a molecule bridges this gap between the gold substrate and tip, a plateau is then observed in the current-distance curve, as shown in Figure 1.17.

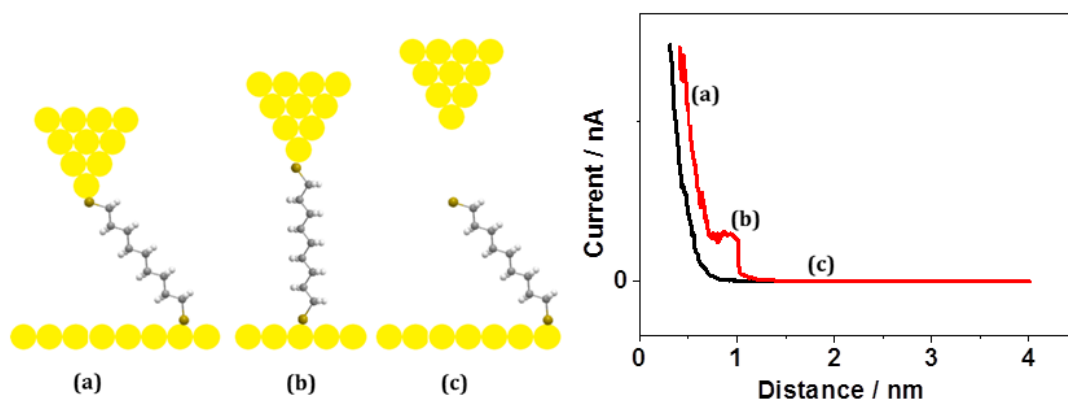


Figure 1.17: The $I(s)$ method as developed by Haiss *et al.*^{10c} (a) A conducting tip is moved in close to the substrate and can bind to a molecule. (b) The tip withdraws and the molecule bridges the gap, causing a plateau in the current distance curve. (c) As the tip is withdrawn further the contact breaks. When no molecule is present the black curve is observed, when a molecule is present a plateau appears, as shown in the red curve.

The conductance of the molecule can be determined using a statistical analysis once data from at least 500 plateaus are plotted into a histogram.

To further confirm the formation of molecular junctions, an estimated break off distance (S_{total}) can be calculated and compared to the length of the molecule when trapped between two gold atoms (calculated using Spartan[®]), which should be similar. The total break off distance is a sum of two components, Equation 1.12.

$$S_{total} = s_0 + \Delta S \quad \text{Equation 1.12}$$

The term s_0 is the distance between the tip and substrate at a predetermined set point (I_0). To calibrate this, several $I(s)$ scans are collected that show no plateaus. These scans are then plotted as $\ln(I)$ versus s ($\ln(\text{current})$ vs. distance displacement) in the distance range relevant to the experiment. Linear regression is then used to determine $d(\ln I)/d(s)$, i.e. the slope of the plot. The distance between the tip and substrate can then be calculated at a given set point value (I_0) using Equation 1.13:

$$s_0 = \frac{\ln(G_0 \cdot \frac{V_{bias}}{I_0})}{d(\ln I)/d(s)} \quad \text{Equation 1.13}$$

Where G_0 is the point contact conductance of gold (77500 nS) and V_{bias} is the bias applied. The term ΔS is the measure of the distance travelled by the tip from the set point current to $S_{break-off}$ which is the point at which the plateau returns to exponential decay. ΔS is calculated for every plateau included in the conductance histogram and often shows some variation due to the random nature of the junction breaking process, Figure 1.18. Due to this, an average of the experimental break off distances is used in Equation 1.12.

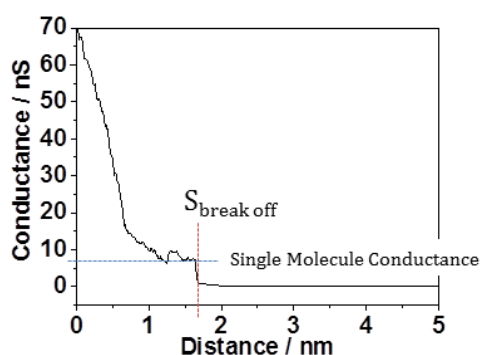


Figure 1.18: Example plateau showing the analysis and location of $S_{break-off}$.

1.6.2 $I(t)$ Method

Haiss *et al.* has also developed another STM technique known as the $I(t)$ technique.³⁵ This technique also involves the molecule bridging the gap between the substrate and the tip. The tip however is kept at a constant height, Figure 1.19. A jump in the current can be observed in a current-time plot when a molecule bridges the gap and current flows through the molecule.

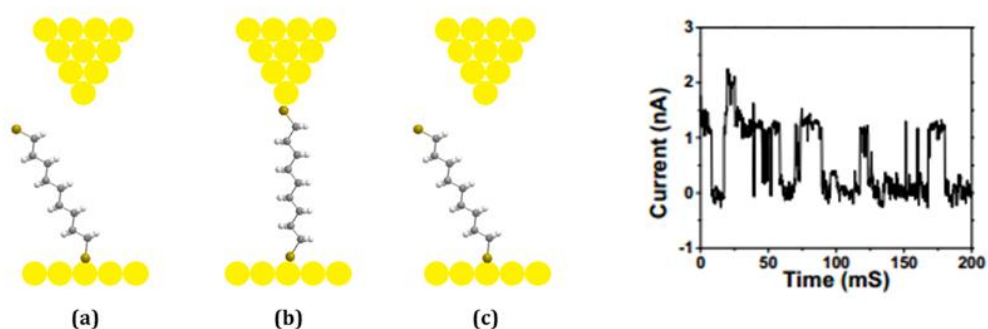


Figure 1.19: Schematic of the $I(t)$ technique and the resultant current jumps. The current jumps were taken from Dr. Leary's thesis.³⁶ The tip remains in a constant height above the substrate. Molecules can then bridge the gap as shown in (b).

The data are then plotted into a histogram and from this the conductance of the molecule can be established.

1.6.3 Break junctions:

1.6.3.1 Mechanically controlled break junction technique:

The MCBJ was introduced by Moreland and Ekin in 1985.³⁷ They measured the electron tunneling configurations of superconductors using a thin wire of a Nb-Sn filament mounted onto a flexible glass beam. This was further developed by Muller *et al.* in 1992.³⁸ The basic principle consists of stretching a thin metal wire by bending the substrate with a mechanical actuator until the metal wire snaps providing two separate electrodes. Relaxing the force upon the substrate allows the junction to close again (Figure 1.20).

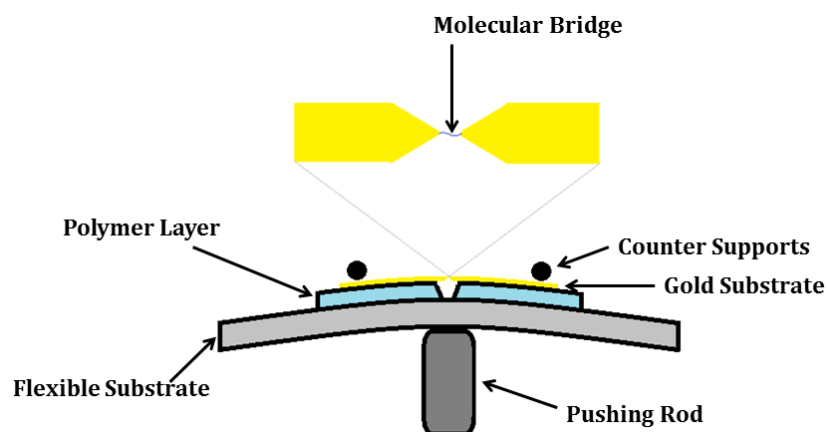


Figure 1.20: Schematic of the Mechanical Break Junction technique (MCBJ).

It is possible for molecules to bridge this gap, resulting in the production of conductance plateaus. This allows the conductance of single molecules to be calculated.

1.6.3.2 In-situ Break Junction technique:

In 2003, Tao *et al.* proposed an *in-situ* break junction technique.^{10a} This technique has become a widely used method for measuring single molecule conductance.³⁹ The technique involves crashing the gold tip into the gold substrate to establish contact; the tip is then withdrawn, until there is no metal-metal contact. As the tip withdraws, molecules can spontaneously form bridges

in the gap. As the tip is withdrawn further, the molecular junction breaks; this can be seen in the schematic shown in Figure 1.21.

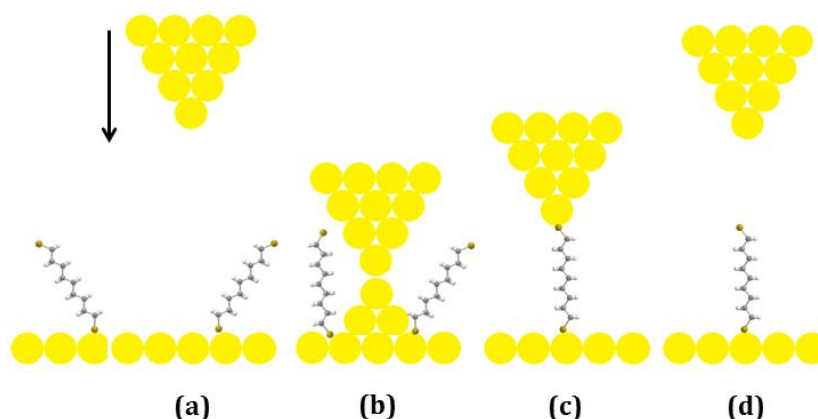


Figure 1.21: Schematic of Tao's *in-situ* break junction technique.^{10a} (a) The tip is moved down towards the substrate surface and crashes into the substrate (b). The tip is then withdrawn from the surface (c) allowing a molecule to have the possibility of bridging the gap. As the tip is withdrawn further the molecule falls off (d)

This produces current jumps similar to the ones seen for the $I(s)$ technique (Figure 11) which are then analysed in histograms once multiple cycles are completed

1.6.4 Electrochemically Controlled STM (EC-STM) technique:

As the interest in redox active molecular junctions increases, it is essential to be able to alter the redox state *in-situ* whilst conductance measurements are taking place.^{10c} This can be achieved by using an STM interfaced with a bipotentiostat. This allows the bias to remain constant whilst changing the sample or tip potential, or the sample bias to be changed whilst the potential of the tip can be maintained at a constant value with respect to the reference electrode. A four electrode set up is used, as shown in Figure 1.22.

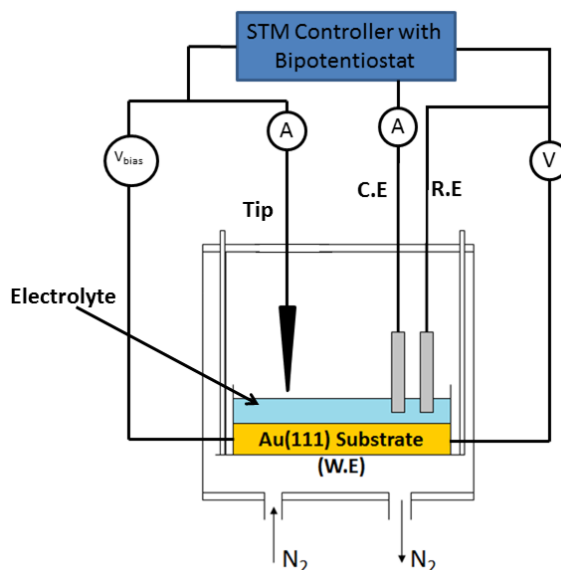


Figure 1.22: Schematic of electrochemically controlled STM. A STM controller interfaced with a bipotentiostat is used and a four electrode set up, comprising of a working electrode (W.E), Counter Electrode (C.E), Reference Electrode (R.E) and the tip is the fourth electrode.

Metal wires (typically Pt or Au) act as the counter and reference electrode, the Au(111) substrate acts as the working electrode and the tip is the fourth electrode. The tip needs to be coated (e.g. Apiezon[®] wax) to prevent any faradaic current flowing between the tip and substrate. An electrolyte is present to aid charge transport.

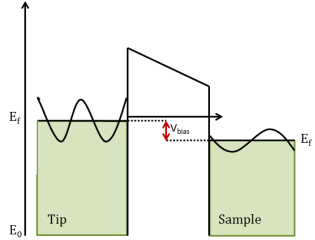
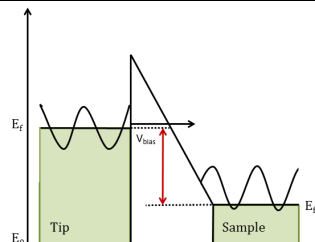
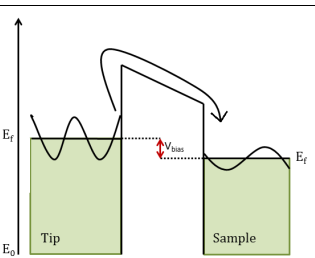
1.7 Charge Transport

1.7.1 Coherent Charge Transport

In the coherent charge transport regime, electrons flow elastically through the molecules without exchanging energy. Coherent charge transport is predominantly associated with shorter molecules due to the electron not residing on the molecule long enough for an inelastic scattering event to occur.⁴⁰

Possible conduction mechanisms for the coherent charge transport regime can be seen below in Table 1.1. Generally coherent charge transports are temperature independent apart from thermionic emission which exhibits exponential temperature dependence.

Table 1.1 Possible conduction mechanisms for the Coherent charge transport regime adapted from reference 40-41

Conduction Mechanism	Schematic	Characteristic Behaviour	Temp Dependence	Voltage Dependence
Direct Tunneling		$J \sim V \exp\left(-\frac{2d}{h} \sqrt{2m\phi_B}\right)$	None	$J \sim V$
Fowler-Nordheim Tunneling		$J \sim V^2 \exp\left(-\frac{4d\sqrt{2m}\phi_B^{3/2}}{3q\hbar V}\right)$	None	$\ln\left(\frac{J}{V^2}\right) \sim \frac{1}{V}$
Thermionic emission		$J \sim T^2 \exp\left(-\frac{\phi_B - \sqrt{qV/4\pi\epsilon d}}{K_B T}\right)$	$\ln\left(\frac{J}{T^2}\right) \sim \frac{1}{T}$	$\ln(J) \sim V^{1/2}$

Where J is the current density, V is the applied bias, d is the barrier length, h is Planck's constant, m is the electron mass, ϕ_B is the barrier height, q is the electronic charge, T is the temperature, ϵ is permittivity of the insulating film and K_B is the Boltzmann constant.

Direct tunneling and Fowler-Nordheim conductance mechanisms are two manifestations of coherent tunneling through a barrier. Direct tunneling refers to the situation at low bias, when the voltage is lower than the barrier height. Fowler-Nordheim is similar to field emission where the voltage is larger than the barrier height, which has the effect of making the barrier triangular and hence effectively shorter. Thermionic emission conduction mechanism occurs when the electrons are excited over the barrier; this conduction mechanism is highly temperature dependent.

1.7.2 Superexchange

Superexchange is a coherent charge transport mechanism introduced by McConnell in 1961.⁴² In the electron superexchange model, electron transfer is aided by the presence of a high-lying empty bridge orbital as it is transferred between the degenerate donor and acceptor orbitals. The electron does not occupy any of the bridge orbitals during the transfer event, unlike in the hopping regime as described in Section 1.7.5.

1.7.3 Simmons Model

The Simmons model describes the current tunneling density of a molecular junction as an arbitrary barrier, as shown below in Equation 1.14.^{41b, 43}

$$J = J_0 \{ \varphi_B \exp(-A\sqrt{\varphi_B}) - (\varphi_B + eV) \exp(-A\sqrt{\varphi_B + eV}) \} \quad \text{Equation 1.14}$$

$$\text{Where } A = 2\alpha d / h \sqrt{2m} \text{ and } J_0 = e / 2\pi h \alpha^2 d^2$$

where e is the charge of electron and α is a unitless adjustable parameter that is introduced to modify the simple rectangular barrier model or account for an effective mass, $\alpha = 1$ for a rectangular barrier.

For low bias range, the Simmons model is simplified to Equation 1.15. The average barrier height is independent of the applied voltage and there is no molecular energy level, direct tunneling is the mechanism.^{41a}

$$J \approx \left(\frac{e^2 V \sqrt{2m\varphi_B}}{h^2 d} \right) \exp \left(- \frac{4\pi d \sqrt{2m\varphi_B}}{h} \right) \quad \text{Equation 1.15}$$

This can be rewritten into a form for comparison to experiment using the decay constant, β as presented in Equation 1.16.^{41a}

$$J \propto V \exp(-\beta d) \quad \text{with } \beta = \frac{4\pi \sqrt{2m\varphi_B}}{h} \quad \text{Equation 1.16}$$

For a high bias range, the Simmons model can be simplified to Equation 1.17. The average barrier height is reduced and eventually the voltage is high enough so that the Fermi level of electrode 2 is lower than the conduction band of electrode 1. The electron transport mechanism for this is Fowler-Nordheim.

$$J \approx \left(\frac{2\pi e^3 V^2}{hd^2 \varphi_B} \right) \exp\left(-\frac{8\pi d \sqrt{2m} \varphi_B^{3/2}}{3heV} \right) \quad \text{Equation 1.17}$$

which can be rewritten as expressed in Equation 1.18:

$$J \propto V^2 \exp(-\beta_{FN} d) \quad \text{with} \quad \beta_{FN} = \frac{8\pi \sqrt{2m}}{3heV} \varphi_B^{3/2} \quad \text{Equation 1.18}$$

Thermionic Emission can be described using the Schottky-Richardson relation as seen in Equation 1.19:

$$I = AT^2 \exp\left(-\frac{e\varphi_{TE} - e \sqrt{\frac{qV}{4\pi\epsilon_0\epsilon_r d}}}{kT} \right) \quad \text{Equation 1.19}$$

where A is the effective Richardson constant, φ_{TE} is the thermal emission barrier height, ϵ_0 is the permittivity of vacuum and ϵ_r is the dielectric constant of the molecular layer.

1.7.4 Resonant Tunneling

One of the dominant electron transfer regimes through a redox-active molecule is resonant tunneling.⁴⁴ It is a two-step electron transfer mechanism which involves the molecular orbitals present on the molecular bridge. By changing the sample potential, the redox state of the molecular wire can be changed. It is more favourable for electrons to traverse the molecule at the redox potential which results in an increase in conductance. An off-on-off profile is predicted for resonant tunneling, with the on state being at the redox potential as shown in Figure 1.23.

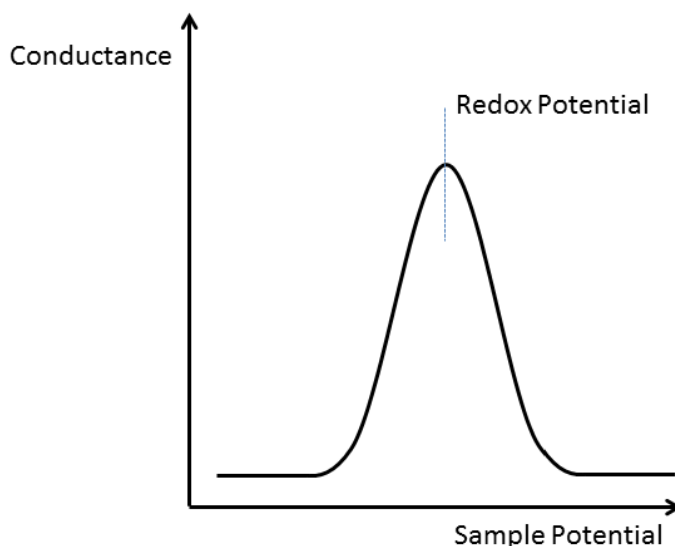


Figure 1.23: A plot of conductance vs. sample potential, exhibiting an off-on-off profile as the redox potential is swept.

1.7.5 Non-Coherent Charge Transport: Hopping Regime

The incoherent charge transport regime is more dominant in molecules of longer length. This is due to the time the electron takes to traverse the bridge being longer than the time it would take for inelastic events to occur.⁴⁰ In extreme cases when the tunneling time is much longer than the inelastic scattering time, the current is transport by electrons that hop from one section of the molecule to another, Figure 1.24.

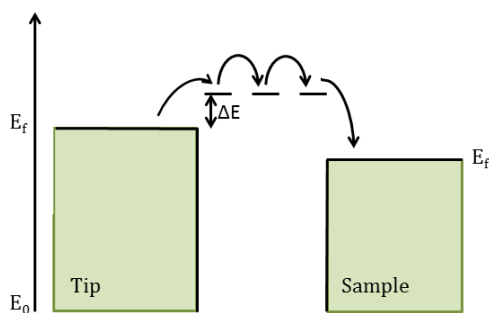


Figure 1.24: The hopping transport mechanism.

The hopping regime can be identified by the following characteristics, the conductance decays linearly with molecular wire length and the conductance depends exponentially on the temperature. The hopping mechanism follows a classical Arrhenius relation, as seen below in Equation 1.20.

$$J \sim \frac{V}{d} \exp\left(-\frac{E_a}{k_B T}\right) \quad \text{Equation 1.20}$$

Where E_a is the activation energy.

1.7.6 Transfer between Charge Transport Mechanisms

Choi *et al.* have demonstrated the molecule's ability to transfer between different electron transport mechanisms, as shown in Figure 1.26.⁴⁵ They investigated the conductance of a series of conjugated oligophenyleneimines (OPI) molecules (Figure 1.25) using an atomic force microscope (AFM).

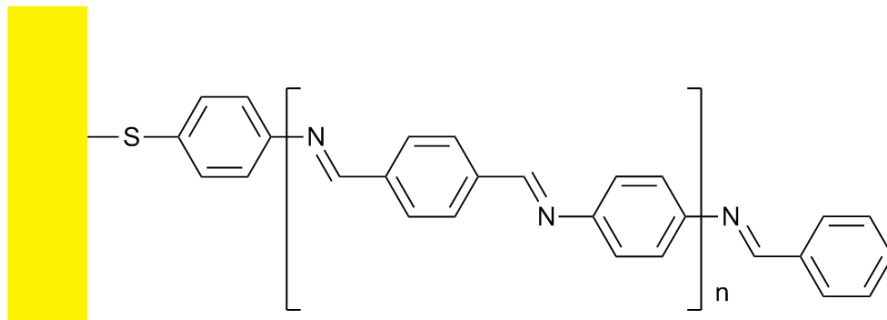


Figure 1.25: Example OPI molecular structure studied by Choi *et al.*⁴⁵

The results achieved showed two clear regions of length dependence, which indicates a change in transport mechanism. They observed the transition from direct tunneling to hopping as the length of conjugated oligophenyleneimine (OPI) wires was varied from 1.5 to 7.3 nm.

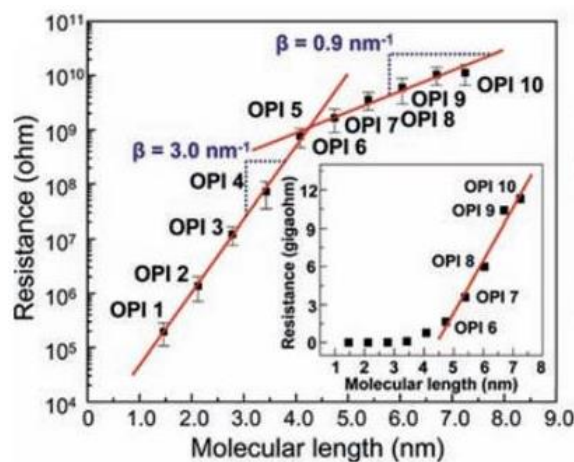


Figure 1.26: The change in transport mechanism as recorded by Choi *et al.*⁴⁵ for a series of oligophenyleneimine (OPI) wires. Figure taken from reference 45.

It was shown that near 4 nm in length, the mechanism of transport in the wires changes abruptly. This was evidenced by striking changes in the length, temperature and electric field dependence of the current voltage characteristics. A linear fit to the data found the shorter molecules exhibited an attenuation factor of 3 nm^{-1} , which corresponds to the non-resonant tunneling transport mechanism. The longer molecules attenuation factor was found to be around 0.9 nm^{-1} , which corresponds to the hopping transport mechanism.

1.8 Modifying the Conductance:

1.8.1 Anchoring Group

An important factor that affects charge transport through molecular junctions is the strength of the molecule-metal coupling. This can be tuned chemically with the selection of the anchoring group used on the molecule to be studied.

For use in single molecule electronics, thiolates have been the most extensively studied contact group, due to their high affinity for, and strong covalent bond formation with, Au substrates. Due to the variable geometries possible in the bonding between Au and thiols, the reliability of conductance measurements on single molecules could be affected. The ideal anchoring group would provide reproducible, well-defined binding, strong anchoring and a small contact resistance. Various other contacts have been investigated including amine,⁴⁶ nitrile,⁴⁷ pyridyl,^{48 49 46b, 50} thioether,^{46c, 51} carboxylic acid^{46d, 52} and nitro.^{47b} Different anchoring groups, however, have different (and sometimes multiple) contact geometries, different coupling strengths and different electron transport mechanisms (LUMO- or HOMO- controlled) which will result in varied conductance results.

Chen *et al.* compared the conductances of thiol-, amine- and carboxylic acid-terminated alkanes.^{46d} They reported the conductance to decrease in the following order: thiol > amine > carboxylic acid. This result is expected due to the Au-S forming a strong covalent bond, the Au-NH₂ forming a weaker covalent bond and the Au-COO⁻ binding through ionic and coordination interactions. They found that all the anchoring groups exhibited exponential decay with molecular length. The conductance values of all the molecules were found to be

temperature-independent, which indicates a coherent tunneling mechanism. The amine and carboxylic acid anchoring groups were found to be pH sensitive, due to the anchoring groups being protonated or deprotonated depending on the pH of the solution, this is shown to have an effect on the reported conductance. At lower pH the anchoring groups are -NH_3^+ and -COOH while at higher pH the anchoring groups are -NH_2 and -COO^- . It was reported at low pH the amine anchoring group failed to produce any molecular junctions, this is due to protonation of the amine. The carboxylic anchoring group successfully forms junctions at a low pH but found the conductance is greatly enhanced at a higher pH due to the deprotonation which enhances the binding ability of the anchoring group to the gold substrate. No pH dependency was found for the thiol anchoring group.

Park *et al.* have shown using the break junction technique that dimethyl phosphine (-PMe_2), diphenyl phosphine (-PPh_2) and methyl sulphides (-SMe) are successful anchoring groups for use in single molecule electronics.^{46c} The molecules investigated were n-butyl terminated with the required anchoring group, as seen in Figure 1.27. They reported the conductance decreasing in the following sequence $\text{-PMe}_2 > \text{-SMe} > \text{-PPh}_2$.

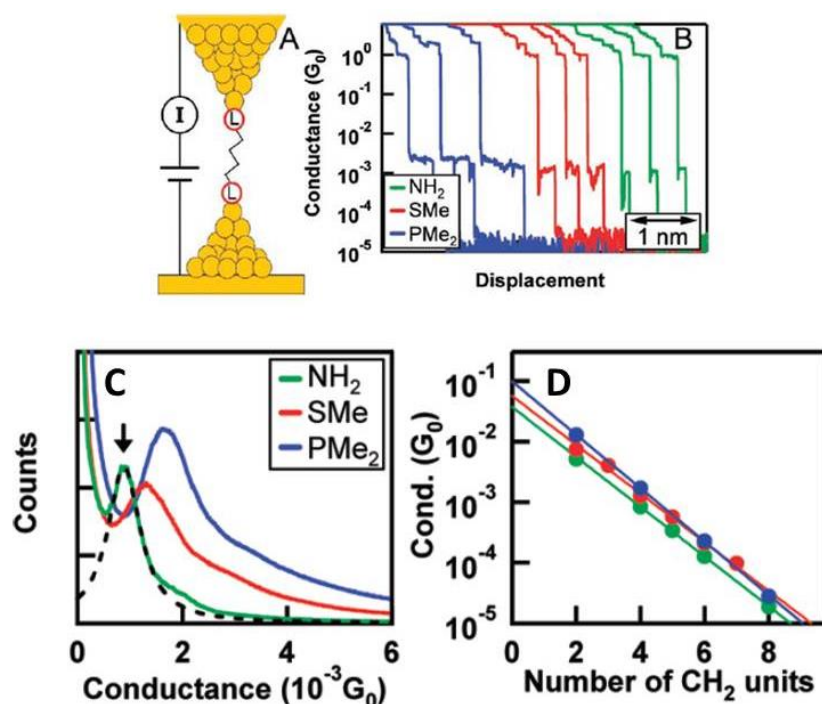


Figure 1.27: Conductance results reported by Park *et al.* (A) Structure of molecule trapped between two gold electrodes. (B) Example plateaux obtained for each anchoring group. (C) 1D histogram of the single molecule conductance for each anchoring group. (D) Length dependence of the recorded conductance for each anchoring group. Results taken from reference 46C.

The results show well defined peaks for all three anchoring groups. A clear logarithmic length dependence is also reported. The σ -donation from the lone pair to the metal substrate is known to decrease in strength as follows, phosphines > amines > sulphides. π -back donation is more predominant in phosphines > sulphides > amines. The high conductance of $-\text{PMe}_2$ can be attributed to the π -back donation.

Li *et al.* have investigated the effect of anchoring group on porphyrin molecular junctions,⁵³ using a wide variety of anchoring groups with the break junction technique, including two novel groups, sulphonate (SO_3^-) and hydroxyl (OH). The structure and variety of anchoring groups can be seen below in Figure 19.

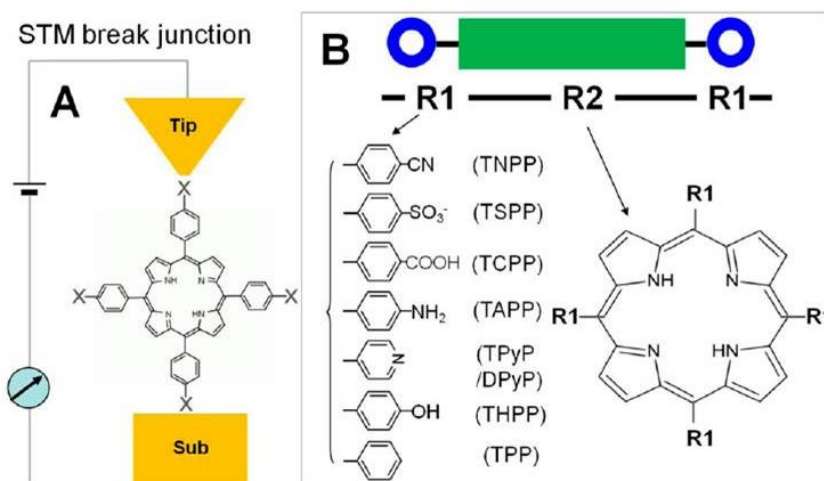


Figure 1.28: Structure of the porphyrin molecule investigated by Li *et al.* Taken from reference 69.

The reported single molecule conductance values for the anchoring groups followed this sequence: pyridyl > amine > sulfonate > nitrile > carboxylic acid. The high recorded conductance value for the pyridyl anchoring group could be due to the anchoring atom (N) already being directly part of the π -system which could result in better binding to the gold substrate.

1.8.2 Transmission Coefficients

The transmission coefficients of the interfacial contacts, T_L and T_R (Equation 1.21) are relevant to the contact conductance, G_{con} which is calculated by combining the transmission coefficients of the contacts and G_0 resulting in Equation 1.21.^{41a}

$$G_{con} = G_0 T_L T_R \quad \text{Equation 1.21}$$

T_L and T_R are dependent upon the nature of the contact between the anchoring group and the substrate. Values for the transmission coefficient and binding energy for a number of anchoring groups can be seen below in Table 1.2.

Table 1.2: Values for the transmission coefficients and binding energies for various anchoring groups. Data adapted from reference 41a.

System	$T_{L,R}$	Bond	Binding Energy (eV)
Au-S-	0.81	Au-S	1.73

Au-N-	0.19	Au-N	0.35
Au-carboxylate	0.08	Au-O	0.09
Au-fullerene	0.1	Au-C ₆ H ₆	0.09

A stronger binding energy gives a lower contact resistance, and results in a higher conductance. The Au-S shows the highest transmission coefficient and the highest binding energy whilst the Au-carboxylate shows a transmission coefficient which is a factor of 10 smaller. These results show that the Au-N bond seems to be a good alternative to Au-S.

As the HOMO is the closest to the gold Fermi level, thiols show hole transport through the HOMO.⁵⁴ Anchoring groups expected to use the LUMO transport channel are pyridines,⁵⁵ amines⁵⁵⁻⁵⁶ and nitriles.^{47a, 57}

1.8.3 Conductance Groups:

Haiss *et al.* suggested three conductance groups can be observed for a molecular wire.⁵⁸ These different conductance groups are observed depending on the adsorption of the anchoring group to the substrate and tip, as seen in Figure 1.29. The conductance groups exhibit low, medium and high conductance referred to as A, B and C respectively.

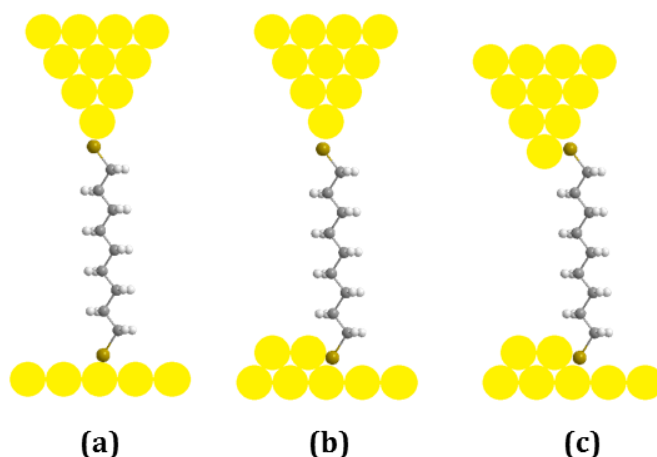


Figure 1.29: The low (a), medium (b) and high (c) conductance referred to as A, B and C respectively.

The low (A) conductance group is considered to be when the anchoring groups bind to a flat surface at both ends. The medium (B) and high (C) conductance

groups are understood to occur when either one or both anchoring groups adsorb at a step edge on the substrate.

1.8.4 Medium Effects

Conductance measurements are often taken in different environments. Measurements can be taken in ambient and inert conditions as well as in a variety of solvents. Although completing conductance measurements in solvent reduces contaminations from the ambient environment, it has been shown in some cases that varying the environment can have an effect on the recorded conductance result. A range of environments have been investigated including, air, inert gas atmosphere (Ar, N₂),¹⁶ UHV,¹⁵ organic solvents (mesitylene),¹⁷ aqueous solutions^{10c} and ionic liquids.^{34a} This larger range of environments allows the medium to be examined to see how it affects the single molecule conductance results.

Li *et al.* in 2006 reported the conductance of octanedithiol in various environments using the break junction technique.¹⁷ They reported the single molecule conductance remains constant for both the high and low conductance groups in toluene, dodecane, water and 0.1 M NaClO₄. This result implies that the solvent does not have an effect on the conductance of alkanedithiols.

In 2011, Fatemi *et al.* investigated the single molecule conductance properties of 1,4-benzenediamine (BDA) in different solvents using the break junction technique (Figure 1.30).⁵⁹ The results reported showed that the single molecule conductance can be changed dependent on the solvent environment.

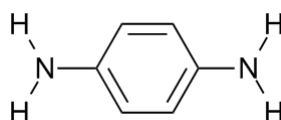


Figure 1.30: Chemical structure of 1,4-benzenediamine (BDA).

They measured the single molecule conductance in 13 different solvents and found that the solvent can increase the conductance by as much as 50 %. This was found to be due to the contact metal work function being altered when the solvent binds to uncoordinated Au atoms. The variation in the conductance can then be attributed to the difference in the binding energy of the solvent.

Nakashima *et al.* also investigated the single molecule conductance properties of BDA in various environments; tetraglyme, mesitylene, water and N₂.⁶⁰ The conductance of BDA was found to decrease, when the environment was changed from tetraglyme to mesitylene, to water and finally to N₂. This decrease is due to the interaction between the solvent and the Au electrodes. The conductance decreases as the probability of the solvent replacing a BDA on an uncoordinated Au site also decreases. This is due to increased solvent interactions causing a reduction in the separation between the gold Fermi level and the HOMO of the BDA in the junction.

Leary *et al.* have investigated a series of oligothiophene containing molecular wires (Figure 1.31) with varying number of thiophene (Th) units ($n = 1, 2, 3$ and 5) sandwiched between two thiol terminated alkyl chains.¹⁶ It was reported that the recorded conductance measurements completed using the $I(s)$ technique were found to vary greatly in the presence of a water solvation shell. This effect was found to be prominent for longer molecular wires.

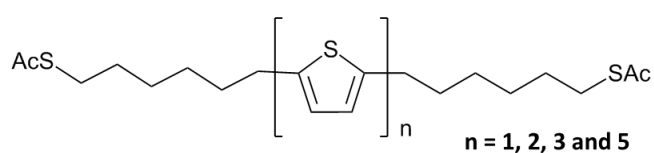


Figure 1.31: The chemical structure of the oligothiophenes (6Th_n6) studied by Leary *et al.*¹⁶

The results recorded for 6Th₃6 exhibit a large change in the conductance when the measurements were taken in an argon environment after a 24 hr purge, (0.012 ± 0.006) nS to the results recorded in ambient conditions, (1 ± 0.2) nS. The conductance in argon is almost 100 times smaller than in air, the conductance histograms can be seen below (Figure 1.32). When the results were recorded in UHV, the conductance was recorded to be 0.04 nS.

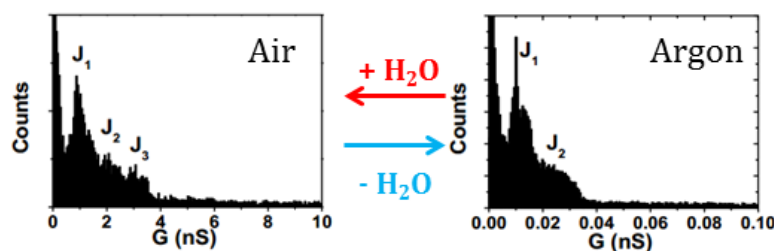


Figure 1.32: Conductance histograms for 6Th₃6 under air (left), $V_{bias} = 0.4$ V and $I_0 = 7$ nA and argon (right), $V_{bias} = 1.0$ V and $I_0 = 7$ nA. Histograms taken from Dr. Leary's thesis.³⁶

The conductance for the monothiophene molecule was found to remain constant in ambient and argon conditions. The fact that the conductance of alkanedithiols remains constant in different environments suggests that the interaction is through the thiophene units; more water molecules are involved for longer oligothiophene units.

1.8.4.1 Room Temperature Ionic Liquid:

It has recently been shown by Kay *et al.* that single molecule conductance measurements can be completed in a room temperature ionic liquid (RTIL). A RTIL consists of an organic cation and an inorganic or organic anion, as shown below in Figure 1.33.

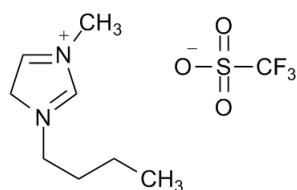


Figure 1.33: Chemical structure of the room temperature ionic liquid 1-butyl-3-methylimidazolium trifluoromethanesulfonate, (BMIM-OTf)

They are molten at room temperature and have several advantages over aqueous solvents due to their wider potential window, high conductivity, wider thermal range and low volatility.

Kay *et al.* reported that a series of α,ω -alkanedithiols could form successful single molecule junctions using the $I(s)$ technique in a RTIL, 1-butyl-3-methylimidazolium trifluoromethanesulfonate (BMIM-OTf).^{34a} The low and

medium conductance groups are in good correlation with measurements previously recorded in air for the series, as shown below in Figure 1.34.

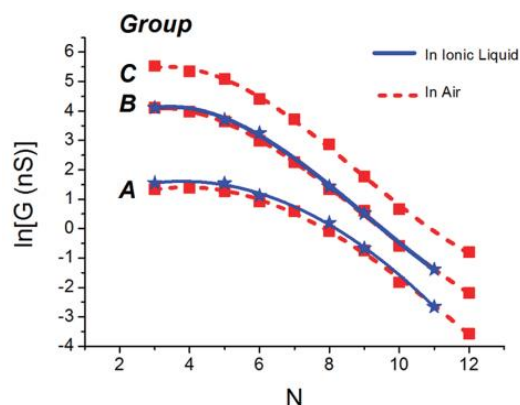


Figure 1.34: The length dependent conductance of α,ω -alkanedithiols in ambient and ionic liquid environments. Image taken from reference 34a.

These recorded results demonstrate that single molecule conductance measurements can be taken in a RTIL reliably.

1.8.5 Redox Gating:

When the molecule is in different redox states, it will often exhibit a change in conductance. An early example of a redox gating was reported by Haiss *et al.* in 2003.^{10c} The conductance of 6-[1'-(6-mercapto-hexyl)-[4,4']bipyridinium]-hexane-1-thiol iodide (6V6), Figure 1.35 was investigated using the $I(s)$ technique. They reported a reversible change in the conductance as the molecule was switched from the oxidized to reduced state with the conductance changing from 0.5 to 2.6 nS.

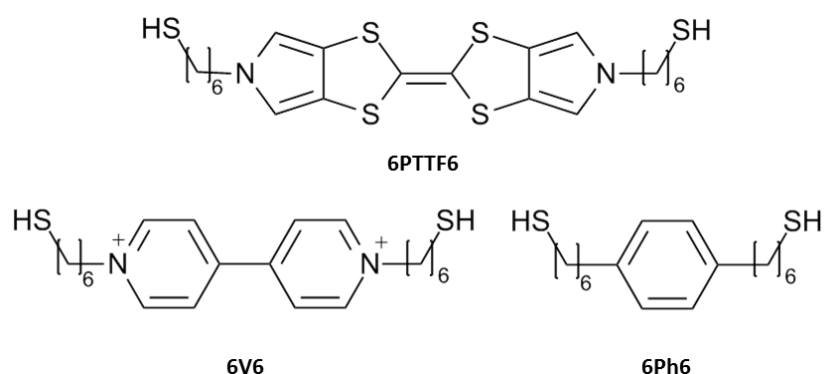


Figure 1.35: Chemical Structure of 6PTTF6, 6V6 and 6Ph6

In a later study by Haiss *et al.*, the conductance-overpotential of redox active pyrrolo-tetrathiafulvalene (pTTF) and viologen (V) was studied and the conductance-electrode potential behaviour of the redox inactive phenyl (Ph) group.⁶¹

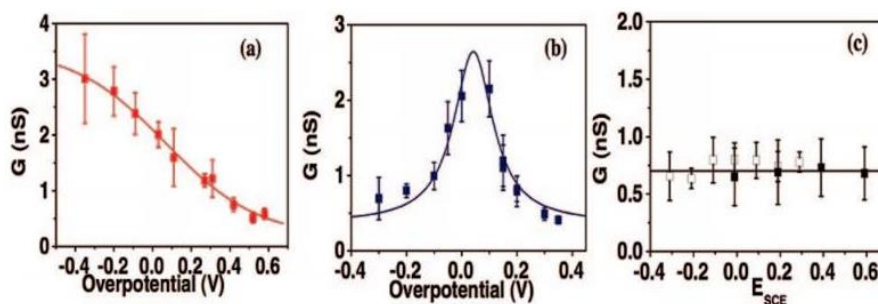


Figure 1.36: The conductance data for (a) 6V6 (b) 6pTTF6 and (c) 6Ph6. Taken from reference 61.

The conductance results for 6V6 (Figure 1.36(a)) show a clear on-off transition as the redox potential is swept, yet the 6pTTF6 conductance results (Figure 1.36(b)) show a clear off-on-off transition as the molecules redox potential is swept. The redox inactive 6Ph6 exhibits an off like conductance (Figure 1.36(a)). As the spacer $-(CH_2)_6-SH$ chains remain constant throughout the study, the changes in conductance must be originating from the redox active/inactive moieties at the centre of the molecular wires.

Recently Kay *et al.* have shown the potential for using room temperature ionic liquids as a medium for single molecule conductance measurements under electrochemical control.^{34b} The molecule to be studied was once again 6pTTF6. Due to the wider potential window available in a RTIL both redox transitions of 6pTTF6 were accessible for investigation.

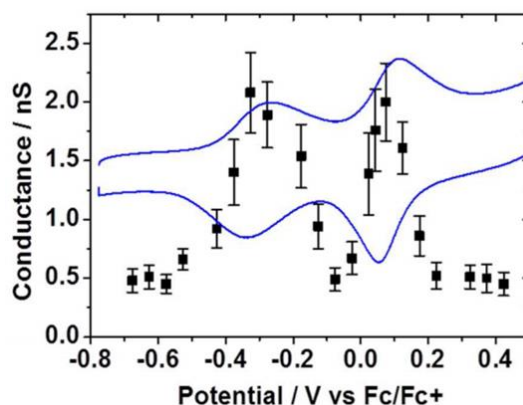


Figure 1.37: Plot of sample potential vs. conductance for 6pTTF6 overlaid with the cyclic voltammogram for 6pTTF6 (blue line). Taken from reference 34b.

The conductance was found to increase at the redox potential from ~ 0.5 to ~ 2 nS for both redox transitions, Figure 1.37. In aqueous electrolyte, only the first redox transition is observed, this result confirms the advantage of using ionic liquids for studying electrochemical conductance gating across multiple redox states of the target molecule.

Albrecht *et al.* have successfully conducted a series of electrochemical *in situ* STM measurements using scanning tunneling spectroscopy on several transition metal complexes,⁶² which are shown in Figure 1.38 below.

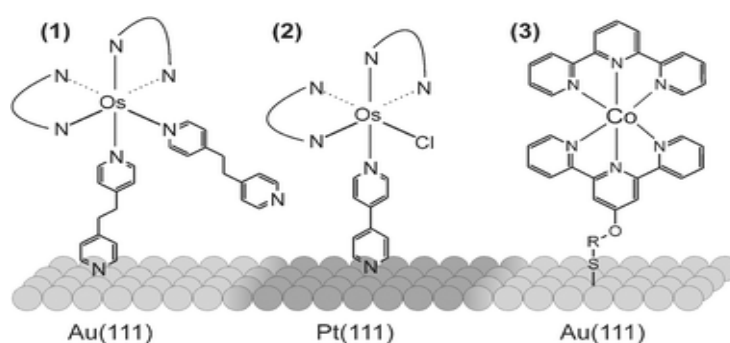


Figure 1.38: The transition metal molecular wires investigated by Albrecht *et al.*⁶² bound to the required substrate. The arcs present in (1) and (2) correspond to 2,2-bipyridine.

The molecules proposed by Albrecht *et al.* have two fully accessible redox states with potentials which are within a suitable range for electrochemical analysis using Au(111), and have shown that both the Os and Co complexes are ideal for use within transition metal molecular wires. By varying the ligand surrounding the metal centre, the redox potentials can be varied over a wider range. The

reported results show a clear tunneling current maximum near the redox potentials for the osmium complexes. The cobalt complex shows a weaker tunneling feature than the one reported for the osmium complexes. They suggest this difference is due to the larger intramolecular nuclear reorganisation and weaker electronic coupling to the electrodes, and therefore the smaller interfacial electron transfer rate constants.

Albrecht *et al.* have shown the ability to use ionic liquid, 1-butyl-3-methylimidazoliumhexafluorophosphate (BMIM-PF₆) in scanning tunneling spectroscopy to investigate the Os(II)/Os(III) transition for a monolayer of an osmium bisterpyridine complex, Figure 1.39.^{33b}

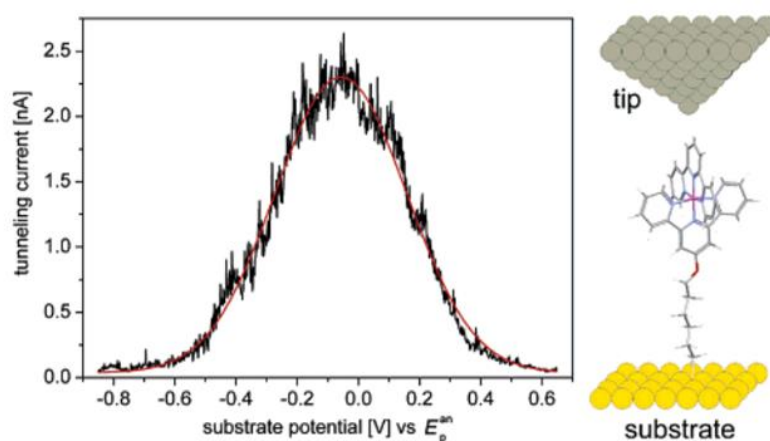


Figure 1.39: Shows the tunneling current enhancement as the redox potential for the osmium complex is swept. Figure taken from reference 33b.

The result exhibits an off-on-off transition as the redox potential is swept, and once again highlights the ability to gate the redox active transition metal centre and the advantages of using an ionic liquid as the results were able to be recorded over a wider potential range.

1.9 Research Study Aim and Summary

The research in this project focuses on terpyridine based transition metal complexes and porphyrin based molecular wires.

The first research study was aimed at investigating the viability of terpyridine based transition metal complexes for the use in single molecule electronics with

the view of investigating the conductance as a function of electrochemical control.

As described previously, various redox active molecules have been investigated and shown to exhibit interesting conductance effects, including a study in ionic liquid. The transition metal complexes have redox states, which can be easily accessed, with the ability to functionalise the ligand makes them ideal candidates to investigate the effect of electrochemical gating. The conductance measurements as a function of electrochemical control were completed in ionic liquid.

Prior to the measurements under electrochemical control, preliminary single molecule conductance investigations into various transition metal complexes were performed to ensure the successful formation of molecular junctions in both ambient and ionic liquid environment. This was followed by electrochemical investigations by completing solution cyclic voltammetry in organic and ionic liquid electrolyte, to establish the most suitable transition metal centre. This was followed by monolayer cyclic voltammetry investigations in ionic liquid electrolyte.

The variation of the single molecule conductance of the terpyridine based transition metal complexes with anchoring group was investigated. This was completed by varying the ligand with a pyridyl- and a thioether- anchoring group. The anchoring group has been shown to exhibit great effects on the single molecule conductance, so it will be of interest to study the effect on transition metal complexes.

The length dependence of the conductance has been shown to be an important effect in molecular electronics. In this study, the length of the ligand coupled to a transition metal centre is varied to see how the conductance is affected. Previously, transition metal complexes with multiple transition metal centres have been investigated and their attenuation factor calculated. The calculated attenuation factor for the single transition metal centred complexes will allow comparison to other molecular systems and allow the deduction of the charge transport mechanism.

The second research study was a preliminary investigation into the single molecule conductance of porphyrin based nanorings using the I(s) technique. A 'complete' 6-porphyrin nanoring and a 'broken' 6-porphyrin nanoring were investigated in two different environments and the conductance compared. Porphyrins have been shown to be effective molecular wires and comparison of the nanoring and linear porphyrin chains will be of great interest.

A study for the molecules used the Spartan® implementation of density functional theory (DFT) which was used to calculate the molecular orbitals of the molecules, with one gold atom attached to each head-group. A B3LYP hybrid exchange correlation function in conjunction with 6-31G* basis set was used, and the core gold orbitals were represented by pseudopotentials.

1.10 References

1. Moore, G. E., Cramming more components onto integrated circuits. McGraw-Hill New York, NY, USA: 1965.
2. Moore, G. E., Progress in digital integrated electronics. *IEDM Tech. Digest* **1975**, 11.
3. Balzani, V.; Credi, A.; Venturi, M., Molecular devices and machines. *Nano Today* **2007**, 2 (2), 18-25.
4. Moore, G. E. In *Lithography and the future of Moore's law*, SPIE's 1995 Symposium on Microlithography, International Society for Optics and Photonics: 1995; pp 2-17.
5. Tour, J. M., Molecular electronics. Synthesis and testing of components. *Accounts of Chemical Research* **2000**, 33 (11), 791-804.
6. Feynman, R. P., There's plenty of room at the bottom. *Engineering and Science* **1960**, 23 (5), 22-36.
7. Aviram, A.; Ratner, M. A., Molecular rectifiers. *Chemical Physics Letters* **1974**, 29 (2), 277-283.
8. Aviram, A.; Joachim, C.; Pomerantz, M., Evidence of switching and rectification by a single molecule effected with a scanning tunneling microscope. *Chemical Physics Letters* **1988**, 146 (6), 490-495.
9. Reed, M. A.; Zhou, C.; Muller, C.; Burgin, T.; Tour, J., Conductance of a molecular junction. *Science* **1997**, 278 (5336), 252-254.
10. Xu, B.; Tao, N. J., Measurement of single-molecule resistance by repeated formation of molecular junctions. *Science* **2003**, 301 (5637), 1221-1223.
11. Haiss, W.; Nichols, R. J.; Higgins, S. J.; Bethell, D.; Höbenreich, H.; Schiffrin, D. J., Wiring nanoparticles with redox molecules. *Faraday Discussions* **2004**, 125, 179-194.
12. Haiss, W.; van Zalinge, H.; Higgins, S. J.; Bethell, D.; Höbenreich, H.; Schiffrin, D. J.; Nichols, R. J., Redox state dependence of single molecule conductivity. *Journal of the American Chemical Society* **2003**, 125 (50), 15294-15295.
13. Cui, X.; Primak, A.; Zarate, X.; Tomfohr, J.; Sankey, O.; Moore, A.; Moore, T.; Gust, D.; Harris, G.; Lindsay, S., Reproducible measurement of single-molecule conductivity. *Science* **2001**, 294 (5542), 571-574.
14. Weber, H.; Reichert, J.; Weigend, F.; Ochs, R.; Beckmann, D.; Mayor, M.; Ahlrichs, R.; Löhneysen, H., Electronic transport through single conjugated molecules. *Chemical Physics* **2002**, 281 (2), 113-125.
15. Binnig, G.; Rohrer, H.; Gerber, C.; Weibel, E., Surface studies by scanning tunneling microscopy. *Physical Review Letters* **1982**, 49 (1), 57.
16. Binnig, G.; Rohrer, H., Scanning tunneling microscopy—from birth to adolescence (Nobel Lecture). *Angewandte Chemie International Edition in English* **1987**, 26 (7), 606-614.
17. Fujihira, M.; Suzuki, M.; Fujii, S.; Nishikawa, A., Currents through single molecular junction of Au/hexanedithiolate/Au measured by repeated formation of break junction in STM under UHV: Effects of conformational change in an alkylene chain from gauche to trans and binding sites of thiolates on gold. *Physical Chemistry Chemical Physics* **2006**, 8 (33), 3876-3884.
18. Leary, E.; Höbenreich, H.; Higgins, S. J.; Van Zalinge, H.; Haiss, W.; Nichols, R. J.; Finch, C.; Grace, I.; Lambert, C.; McGrath, R., Single-molecule solvation-shell sensing. *Physical Review Letters* **2009**, 102 (8), 086801.

19. Li, X.; He, J.; Hihath, J.; Xu, B.; Lindsay, S. M.; Tao, N., Conductance of single alkanedithiols: Conduction mechanism and effect of molecule-electrode contacts. *Journal of the American Chemical Society* **2006**, *128* (6), 2135-2141.
20. Haiss, W.; van Zalinge, H.; Bethell, D.; Ulstrup, J.; Schiffrin, D. J.; Nichols, R. J., Thermal gating of the single molecule conductance of alkanedithiols. *Faraday Discussions* **2006**, *131*, 253-264.
21. Halbritter, J., Tunnel channels, spectroscopy and imaging in STM. *Applied Physics A* **1998**, *66* (1), S181-S186.
22. Landauer, R., Spatial variation of currents and fields due to localized scatterers in metallic conduction. *IBM Journal of Research and Development* **1957**, *1* (3), 223-231.
23. Ulman, A., Formation and structure of self-assembled monolayers. *Chemical Reviews* **1996**, *96* (4), 1533-1554; Vericat, C.; Vela, M.; Benitez, G.; Carro, P.; Salvarezza, R., Self-assembled monolayers of thiols and dithiols on gold: new challenges for a well-known system. *Chemical Society Reviews* **2010**, *39* (5), 1805-1834; Nuzzo, R. G.; Allara, D. L., Adsorption of bifunctional organic disulfides on gold surfaces. *Journal of the American Chemical Society* **1983**, *105* (13), 4481-4483.
24. Compton, R. G.; Sanders, G. H., *Electrode potentials*. Oxford Univ. Press: 1996.
25. Compton, R. G.; Banks, C. E., *Understanding voltammetry*. World Scientific: 2007.
26. Oldham, K. B., Analytical expressions for the reversible Randles-Sevcik function. *Journal of Electroanalytical Chemistry and Interfacial Electrochemistry* **1979**, *105* (2), 373-375.
27. Nicholson, R. S., Theory and Application of Cyclic Voltammetry for Measurement of Electrode Reaction Kinetics. *Analytical Chemistry* **1965**, *37* (11), 1351-1355.
28. Carvalhal, R. F.; Sanches Freire, R.; Kubota, L. T., Polycrystalline Gold Electrodes: A Comparative Study of Pretreatment Procedures Used for Cleaning and Thiol Self-Assembly Monolayer Formation. *Electroanalysis* **2005**, *17* (14), 1251-1259.
29. Finklea, H. O.; Snider, D. A.; Fedyk, J.; Sabatani, E.; Gafni, Y.; Rubinstein, I., Characterization of octadecanethiol-coated gold electrodes as microarray electrodes by cyclic voltammetry and ac impedance spectroscopy. *Langmuir* **1993**, *9* (12), 3660-3667.
30. Laviron, E., General expression of the linear potential sweep voltammogram in the case of diffusionless electrochemical systems. *Journal of Electroanalytical Chemistry and Interfacial Electrochemistry* **1979**, *101* (1), 19-28.
31. Eckermann, A. L.; Feld, D. J.; Shaw, J. A.; Meade, T. J., Electrochemistry of redox-active self-assembled monolayers. *Coordination Chemistry Reviews* **2010**, *254* (15), 1769-1802.
32. Hamelin, A., Cyclic voltammetry at gold single-crystal surfaces. Part 1. Behaviour at low-index faces. *Journal of Electroanalytical Chemistry* **1996**, *407* (1-2), 1-11; Hamelin, A.; Martins, A., Cyclic voltammetry at gold single-crystal surfaces. Part 2. Behaviour of high-index faces. *Journal of Electroanalytical Chemistry* **1996**, *407* (1), 13-21.

33. Kolthoff, I., A review of electrochemistry in non-aqueous solvents. *Pure and Applied Chemistry* **1971**, *25* (2), 305-326.
34. Balula, Maria S.; Gamelas, José A.; Carapuça, Helena M.; Cavaleiro, Ana M. V.; Schlindwein, W., Electrochemical Behaviour of First Row Transition Metal Substituted Polyoxotungstates: A Comparative Study in Acetonitrile. *European Journal of Inorganic Chemistry* **2004**, *2004* (3), 619-628.
35. Buzzeo, M. C.; Evans, R. G.; Compton, R. G., Non-haloaluminate room-temperature ionic liquids in electrochemistry—A review. *ChemPhysChem* **2004**, *5* (8), 1106-1120.
36. Albrecht, T.; Moth-Poulsen, K.; Christensen, J. B.; Hjelm, J.; Bjørnholm, T.; Ulstrup, J., Scanning tunneling spectroscopy in an ionic liquid. *Journal of the American Chemical Society* **2006**, *128* (20), 6574-6575.
37. Kay, N. J.; Nichols, R. J.; Higgins, S. J.; Haiss, W.; Sedghi, G.; Schwarzacher, W.; Mao, B.-W., Ionic Liquids As a Medium for STM-Based Single Molecule Conductance Determination: An Exploration Employing Alkanedithiols. *The Journal of Physical Chemistry C* **2011**, *115* (43), 21402-21408.
38. Kay, N. J.; Higgins, S. J.; Jeppesen, J. O.; Leary, E.; Lycoops, J.; Ulstrup, J.; Nichols, R. J., Single-molecule electrochemical gating in ionic liquids. *Journal of the American Chemical Society* **2012**, *134* (40), 16817-16826.
39. Zalinge, H., Measurement of single molecule conductivity using the spontaneous formation of molecular wires. *Physical Chemistry Chemical Physics* **2004**, *6* (17), 4330-4337.
40. Leary, E. Single Molecule Conductance of Dithiahexyl-Aryl Compounds. University of Liverpool, 2008.
41. Moreland, J.; Ekin, J., Electron tunneling experiments using Nb-Sn “break”junctions. *Journal of Applied Physics* **1985**, *58* (10), 3888-3895.
42. Muller, C.; Van Ruitenbeek, J.; De Jongh, L., Experimental observation of the transition from weak link to tunnel junction. *Physica C: Superconductivity* **1992**, *191* (3), 485-504.
43. Kaliginedi, V.; Moreno-García, P.; Valkenier, H.; Hong, W.; García-Suárez, V. M.; Buitter, P.; Otten, J. L.; Hummelen, J. C.; Lambert, C. J.; Wandlowski, T., Correlations between molecular structure and single-junction conductance: A case study with oligo (phenylene-ethynylene)-type wires. *Journal of the American Chemical Society* **2012**, *134* (11), 5262-5275; Hong, W.; Manrique, D. Z.; Moreno-Garcia, P.; Gulcur, M.; Mishchenko, A.; Lambert, C. J.; Bryce, M. R.; Wandlowski, T., Single molecular conductance of tolans: experimental and theoretical study on the junction evolution dependent on the anchoring group. *Journal of the American Chemical Society* **2012**, *134* (4), 2292-2304.
44. Scheer, E., *Molecular electronics: an introduction to theory and experiment*. World Scientific: 2010; Vol. 1.
45. Karthäuser, S., Control of molecule-based transport for future molecular devices. *Journal of Physics: Condensed Matter* **2011**, *23* (1), 013001.
46. Wang, W.; Lee, T.; Reed, M. A., Mechanism of electron conduction in self-assembled alkanethiol monolayer devices. *Physical Review B* **2003**, *68* (3), 035416.
47. McConnell, H. M., Intramolecular charge transfer in aromatic free radicals. *The Journal of Chemical Physics* **1961**, *35* (2), 508-515.

48. Simmons, J. G., Generalized formula for the electric tunnel effect between similar electrodes separated by a thin insulating film. *Journal of Applied Physics* **1963**, *34* (6), 1793-1803.
49. Zhang, J.; Kuznetsov, A. M.; Medvedev, I. G.; Chi, Q.; Albrecht, T.; Jensen, P. S.; Ulstrup, J., Single-molecule electron transfer in electrochemical environments. *Chemical Reviews* **2008**, *108* (7), 2737-2791; Schmickler, W.; Widrig, C., The investigation of redox reactions with a scanning tunneling microscope: experimental and theoretical aspects. *Journal of Electroanalytical Chemistry* **1992**, *336* (1), 213-221.
50. Choi, S. H.; Kim, B.; Frisbie, C. D., Electrical resistance of long conjugated molecular wires. *Science* **2008**, *320* (5882), 1482-1486.
51. Arroyo, C. R.; Leary, E.; Castellanos-Gómez, A.; Rubio-Bollinger, G.; González, M. T.; Agraït, N., Influence of Binding Groups on Molecular Junction Formation. *Journal of the American Chemical Society* **2011**, *133* (36), 14313-14319; Venkataraman, L.; Klare, J. E.; Nuckolls, C.; Hybertsen, M. S.; Steigerwald, M. L., Dependence of single-molecule junction conductance on molecular conformation. *Nature* **2006**, *442* (7105), 904-907.
52. Hong, W.; Manrique, D. Z.; Moreno-García, P.; Gulcur, M.; Mishchenko, A.; Lambert, C. J.; Bryce, M. R.; Wandlowski, T., Single Molecular Conductance of Tolanes: Experimental and Theoretical Study on the Junction Evolution Dependent on the Anchoring Group. *Journal of the American Chemical Society* **2011**, *134* (4), 2292-2304.
53. Park, Y. S.; Whalley, A. C.; Kamenetska, M.; Steigerwald, M. L.; Hybertsen, M. S.; Nuckolls, C.; Venkataraman, L., Contact Chemistry and Single-Molecule Conductance: A Comparison of Phosphines, Methyl Sulfides, and Amines. *Journal of the American Chemical Society* **2007**, *129* (51), 15768-15769.
54. Chen, F.; Li, X.; Hihath, J.; Huang, Z.; Tao, N., Effect of Anchoring Groups on Single-Molecule Conductance: Comparative Study of Thiol-, Amine-, and Carboxylic-Acid-Terminated Molecules. *Journal of the American Chemical Society* **2006**, *128* (49), 15874-15881.
55. Mishchenko, A.; Zotti, L. A.; Vonlanthen, D.; Bürkle, M.; Pauly, F.; Cuevas, J. C.; Mayor, M.; Wandlowski, T., Single-Molecule Junctions Based on Nitrile-Terminated Biphenyls: A Promising New Anchoring Group. *Journal of the American Chemical Society* **2010**, *133* (2), 184-187.
56. Zotti, L. A.; Kirchner, T.; Cuevas, J. C.; Pauly, F.; Huhn, T.; Scheer, E.; Erbe, A., Revealing the Role of Anchoring Groups in the Electrical Conduction Through Single-Molecule Junctions. *Small* **2010**, *6* (14), 1529-1535.
57. Kamenetska, M.; Quek, S. Y.; Whalley, A. C.; Steigerwald, M. L.; Choi, H. J.; Louie, S. G.; Nuckolls, C.; Hybertsen, M. S.; Neaton, J. B.; Venkataraman, L., Conductance and Geometry of Pyridine-Linked Single-Molecule Junctions. *Journal of the American Chemical Society* **2010**, *132* (19), 6817-6821.
58. Tam, E. S.; Parks, J. J.; Shum, W. W.; Zhong, Y.-W.; Santiago-Berríos, M. E. B.; Zheng, X.; Yang, W.; Chan, G. K. L.; Abruña, H. D.; Ralph, D. C., Single-Molecule Conductance of Pyridine-Terminated Dithienylethene Switch Molecules. *ACS Nano* **2011**, *5* (6), 5115-5123.
59. Xu, B.; Xiao, X.; Tao, N. J., Measurements of Single-Molecule Electromechanical Properties. *Journal of the American Chemical Society* **2003**, *125* (52), 16164-16165.

60. Capozzi, B.; Dell, E. J.; Berkelbach, T. C.; Reichman, D. R.; Venkataraman, L.; Campos, L. M., Length-Dependent Conductance of Oligothiophenes. *Journal of the American Chemical Society* **2014**, *136* (29), 10486-10492; Dell, E. J.; Capozzi, B.; DuBay, K. H.; Berkelbach, T. C.; Moreno, J. R.; Reichman, D. R.; Venkataraman, L.; Campos, L. M., Impact of Molecular Symmetry on Single-Molecule Conductance. *Journal of the American Chemical Society* **2013**, *135* (32), 11724-11727.
61. Martín, S.; Haiss, W.; Higgins, S.; Cea, P.; López, M. C.; Nichols, R. J., A Comprehensive Study of the Single Molecule Conductance of α,ω -Dicarboxylic Acid-Terminated Alkanes. *The Journal of Physical Chemistry C* **2008**, *112* (10), 3941-3948.
62. Li, Z.; Smeu, M.; Ratner, M. A.; Borguet, E., Effect of Anchoring Groups on Single Molecule Charge Transport through Porphyrins. *The Journal of Physical Chemistry C* **2013**, *117* (29), 14890-14898.
63. Pauly, F.; Viljas, J. K.; Cuevas, J. C.; Schön, G., Density-functional study of tilt-angle and temperature-dependent conductance in biphenyl dithiol single-molecule junctions. *Physical Review B* **2008**, *77* (15), 155312; Jones, D. R.; Troisi, A., Single Molecule Conductance of Linear Dithioalkanes in the Liquid Phase: Apparently Activated Transport Due to Conformational Flexibility. *The Journal of Physical Chemistry C* **2007**, *111* (39), 14567-14573.
64. Bagrets, A.; Arnold, A.; Evers, F., Conduction Properties of Bipyridinium-Functionalized Molecular Wires. *Journal of the American Chemical Society* **2008**, *130* (28), 9013-9018.
65. Quek, S. Y.; Kamenetska, M.; Steigerwald, M. L.; Choi, H. J.; Louie, S. G.; Hybertsen, M. S.; Neaton, J. B.; Venkataraman, L., Mechanically controlled binary conductance switching of a single-molecule junction. *Nat Nano* **2009**, *4* (4), 230-234.
66. Sun, L.; Diaz-Fernandez, Y. A.; Gschneidner, T. A.; Westerlund, F.; Lara-Avila, S.; Moth-Poulsen, K., Single-molecule electronics: from chemical design to functional devices. *Chemical Society Reviews* **2014**, *43* (21), 7378-7411.
67. Haiss, W.; Martín, S.; Leary, E.; Zalinge, H. v.; Higgins, S. J.; Bouffier, L.; Nichols, R. J., Impact of junction formation method and surface roughness on single molecule conductance. *The Journal of Physical Chemistry C* **2009**, *113* (14), 5823-5833.
68. Fatemi, V.; Kamenetska, M.; Neaton, J.; Venkataraman, L., Environmental control of single-molecule junction transport. *Nano letters* **2011**, *11* (5), 1988-1992.
69. Nakashima, S.; Takahashi, Y.; Kiguchi, M., Effect of the environment on the electrical conductance of the single benzene-1, 4-diamine molecule junction. *Beilstein Journal of Nanotechnology* **2011**, *2* (1), 755-759.
70. Leary, E.; Higgins, S. J.; van Zalinge, H.; Haiss, W.; Nichols, R. J.; Nygaard, S.; Jeppesen, J. O.; Ulstrup, J., Structure– Property Relationships in Redox-Gated Single Molecule Junctions– A Comparison of Pyrrolo-Tetrathiafulvalene and Viologen Redox Groups. *Journal of the American Chemical Society* **2008**, *130* (37), 12204-12205.
71. Albrecht, T.; Moth-Poulsen, K.; Christensen, J. B.; Guckian, A.; Bjørnholm, T.; Vos, J. G.; Ulstrup, J., In situ scanning tunnelling spectroscopy of inorganic transition metal complexes. *Faraday Discussions* **2006**, *131*, 265-279.

Chapter 2

Conductance of

Transition Metal Based

Molecular Wires

2.1 General Introduction

The conductance of various systems have been extensively studied since the first reported single molecule conductance results in 1997.¹ While a vast selection of organic molecular wire systems have previously been investigated, incorporating a transition metal has only recently started to be of interest.² Several transition metal complexes will be studied using cyclic voltammetry and scanning tunneling microscopy to assess their suitability for further investigation of conductance under electrochemical control.

2.1.1 Transition Metal Complexes

Several organic molecular wire systems and their functionalities have been investigated. Highly functional redox active molecule wires have been prepared and shown both experimentally and theoretically to exhibit interesting conductance results. The ability to control the access to different molecular charge states via a gate electrode is of great interest and opens up a larger range of opportunities for the development of single molecule devices. Incorporating a metal centre has only recently started to become of interest due to the ability to conduct complex experiments.²⁻⁴ Transition metal complexes are particularly interesting for use in molecular electronics due to the ability to control the redox chemistry and access multiple redox states along with the flexibility in structure, owing to the ability to vary the ligand structure, anchoring group and metal centre to suit the required needs.

Liu *et al.* have compared the conductance results of an oligo(1,4-phenylene ethynylene) (OPE) to a ruthenium(II) bis(-arylacetylide)-complex (OPERu) functionalised with thioacetate anchoring groups at both ends, as seen below in Figure 2.1.⁴ The conductance measurements were completed using the break junction technique using a decanethiol monolayer matrix which would allow the OPE systems to protrude above the decanethiol molecules.

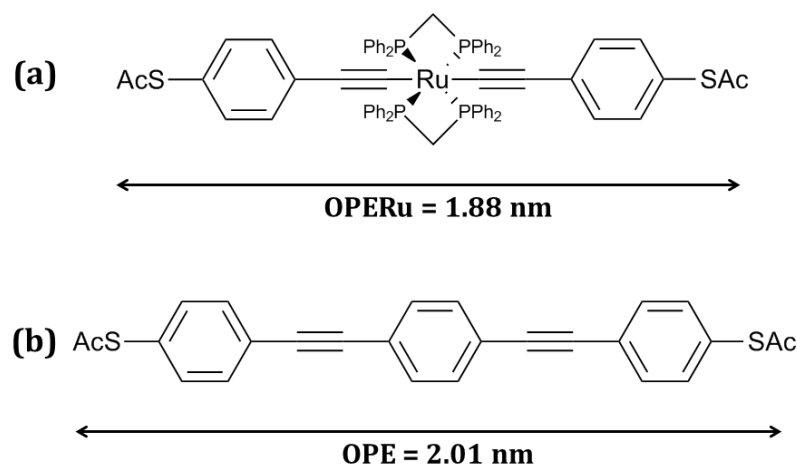


Figure 2.1: Chemical structure of the organometallic complex investigated by Liu *et al.*⁴

The single molecule conductance for the OPERu complex was measured to be (19 ± 7) nS which is larger than the measured conductance for the OPE which was (3.6 ± 2) nS. This high conductance result from OPERu resulted from the smaller separation between its HOMO and the gold Fermi level, although the shorter length of the OPERu (Figure 2.1) will have contributed slightly to the higher conductance result. This result confirms the potential of measuring the conductance of organometallic complexes.

Functionalised terpyridine units are of interest for use in molecular electronics but have not been extensively studied. As a terpyridine unit has three nitrogen atoms it is able to act as a tridentate ligand, Figure 2.2. Functionalisation of the terpyridine ligand can also be easily achieved making them an ideal ligand to use in transition metal complex single molecule conductance measurements. There have been extensive successful studies into terpyridine as a complexing ligand for various transition metal ions. The common geometry of the bisterpyridine complexes is a distorted octahedral geometry, because the most common connectivity for the transition metal ion is hexacoordinate.

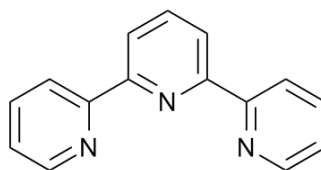


Figure 2.2: Chemical structure of terpyridine

Metal-terpyridine complexes of the standard type $[M(\text{tpy})_2]X_2$ where for example M is Ru, Co, Fe and X is Cl^- , PF_6^- , ClO_4^- have been studied.⁵ An important characteristic is the strength of the metal-ligand coordinative bond within these complexes. Stability is explained by strong metal-ligand ($d-\pi^*$) back donation as well as a strong chelate effect being present.

The complexes to be investigated are $[\text{Cr}(4'-(\text{pyridin-4-yl})-2,2':6',2''\text{-terpyridine})_2](\text{PF}_6)_3$ and $[\text{M}(4'-(\text{pyridin-4-yl})-2,2':6',2''\text{-terpyridine})_2](\text{PF}_6)_2$ with M being Ru, Fe and Co as shown in Figure 2.3.

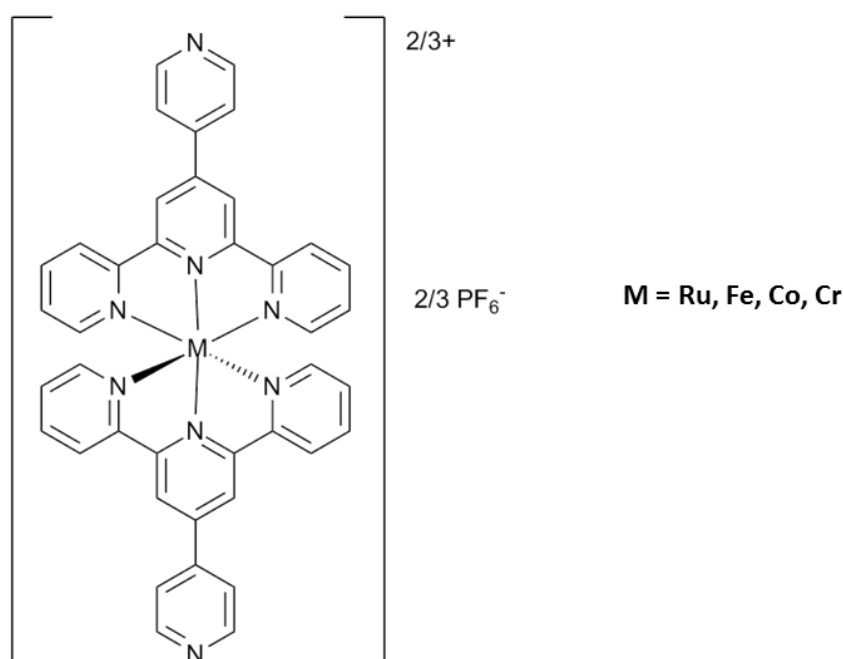


Figure 2.3: Chemical structure of the organometallic complex to be investigated.

By varying the metal centre and keeping the ligand constant, the effect of the metal centre on the conductance can be investigated. The $[\text{Ru}(4'-(\text{pyridin-4-yl})-2,2':6',2''\text{-terpyridine})_2](\text{PF}_6)_2$ is a stable low spin diamagnetic complex with the following electron configuration $[\text{Kr}]4d^6$. The $[\text{Fe}(4'-(\text{pyridin-4-yl})-2,2':6',2''\text{-terpyridine})_2](\text{PF}_6)_2$ complex is also low spin diamagnetic but with an electron configuration of $[\text{Ar}]3d^6$. The $[\text{Co}(4'-(\text{pyridin-4-yl})-2,2':6',2''\text{-terpyridine})_2](\text{PF}_6)_2$ is high spin paramagnetic with an electron configuration of $[\text{Ar}]3d^7$ and the $[\text{Cr}(4'-(\text{pyridin-4-yl})-2,2':6',2''\text{-terpyridine})_2](\text{PF}_6)_3$ is also paramagnetic with an electron configuration of $[\text{Ar}]3d^3$. Investigating these four different metal centres will allow it to be seen if there is any difference in the

single molecule conductance and assess their suitability for single molecule conductance under potential control.

Rampi *et al.* have shown the stability of terpyridine based molecular junctions by obtaining conductive molecular wires up to 40 nm long. This was achieved *in situ* by assembling the metal centred molecular wire on metal substrates using a stepwise coordination of the metal ion to the terpyridine based ligands, as shown below in Figure 2.4.⁶ The metal centres investigated were cobalt and iron and were found to have a attenuation factors of $\beta = 0.001$ and 0.028 \AA^{-1} respectively. These β -values are extremely low in comparison to other organic wires.⁷ This could be due to labile transition metals such as Co^{2+} undergoing ligand exchange as well as ligand coordination which may suggest there will be ligand scrambling resulting in the chain lengths not all being equal. The conductance could be dominated by the shorter wires, making the attenuation factor low.

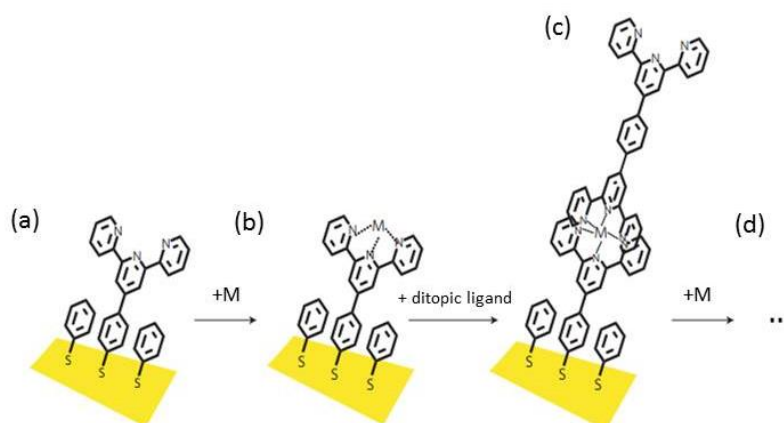


Figure 2.4: Schematic of the stepwise formation of terpyridine based molecular wires. a) Assembly of the terpyridine ligand on to the gold surface. b) Coordination of the metal centre (Co or Fe) to the ligand. c) Coordination of the terpyridine linker ligand. d) The processes b and c are repeated as required. Figure taken from reference 6.

Zhou *et al.* have measured the conductance of three different redox active systems with two incorporating a transition metal, Figure 2.5.⁸ The systems were investigated using the *in-situ* break junction technique in aqueous 1 M NaClO_4 under potential control.

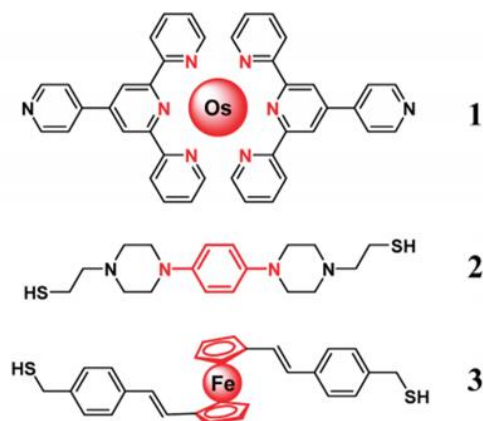


Figure 2.5: Chemical structure of the systems studied by Zhou *et al.*⁸ Figure taken from reference 8.

The group establish that the systems can form successful molecular junctions and exhibit redox state dependence; this will be discussed further in Chapter 4. Complex 1 is of particular interest as it has an identical ligand structure to the complexes investigated in this chapter and shows the successful ability of the ligand to bind to the substrate to form the molecular junctions. The off-state conductance of the osmium complex was found to be 2.1 nS and the on-state conductance was 17.8 nS.

2.1.2 Medium effects

As discussed in Chapter 1 it is essential to choose the correct medium and it has previously shown that the ionic liquids are useful media for single molecule conductance studies under potential control.^{9, 10} It was therefore essential to investigate the use of the ionic liquid, BMIM-TFSI as a medium for studying the conductances of $[M(\text{pyterpy})_2](\text{PF}_6)_{2/3}$ systems as well as measuring the conductance in ambient without potential control to ensure the successful formation of molecular junctions. It was essential to investigate the voltammetry of the $[M(\text{pyterpy})_2](\text{PF}_6)_{2/3}$ systems in both organic solvent (MeCN) and in ionic liquid to establish suitability for conductance measurements under electrochemical control.

2.1.3 Cyclic Voltammetry

Cyclic voltammetry on various terpyridine based transition metal complexes has been extensively studied in organic solvent.¹¹⁻¹³ Constable *et al.* have studied the electrochemistry of three 4'-(pyridin-4-yl)-2,2':6',2''-terpyridine

(pyterpy) transition metal complexes, Os, Fe and Ru.¹¹ The group also studied the terpyridine equivalents allowing comparisons between the electrochemistry to be made. All the complexes were found to be electrochemically active and exhibit a fully reversible M(II)-M(III) redox process, as seen in Table 2.1.

Table 2.1: Redox potentials of iron(II), ruthenium(II) and osmium(II) complexes of 2,2':6',2''-terpyridine and 4'-(4-pyridin-4-yl)-2,2':6',2''-terpyridine (V, vs. internal ferrocene-ferrocenium; MeCN solution, [Buⁿ][BF₄] supporting electrolyte). Data taken from reference 11.

Complex	M ^(II) -M ^(III) / V
[Fe(pyterpy) ₂](BF ₄) ₂	0.80
[Fe(terpy) ₂](BF ₄) ₂	0.74
[Ru(pyterpy) ₂](PF ₆) ₂	0.95
[Ru(terpy) ₂](PF ₆) ₂	0.92
[Os(pyterpy) ₂](PF ₆) ₂	0.62
[Os(terpy) ₂](PF ₆) ₂	0.58

The exhibited [M(pyterpy)₂] M(II)-M(III) redox processes occurred at a slightly more positive potential than the potential observed for the [M(terpy)₂] for each transition metal centre. This suggests that the 4-pyridyl substituent is weakly electron withdrawing when placed on the 4' position of the terpyridine ligand. These results will act as a comparison for the cyclic voltammetry results in ionic liquid.

The use of ionic liquids as an electrolyte for electrochemistry of terpyridine organometallic complexes has not been as extensively studied. Albrecht *et al.* have however shown the suitability for these complexes by studying an asymmetrical osmium bis-terpyridine complex monolayer, [Os(4'-(6-acetylthiohexyloxy)-2,2';6',2''-terpyridine)(2,2';6',2''-terpyridine)](PF₆)₂, whose molecular structure is shown in Figure 2.6.¹⁴

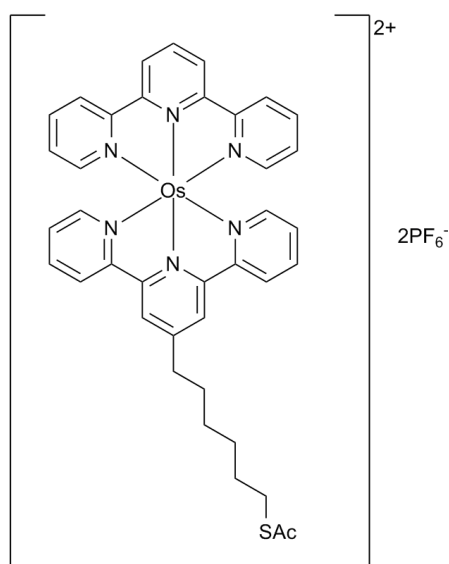


Figure 2.6: Molecular structure of the Os(II) complex studied by Albrecht *et al.*¹⁴

The cyclic voltammetry was performed in aqueous and ionic liquid, 1-butyl-3-methylimidazoliumhexafluorophosphate (BMIM-PF₆) electrolyte, Figure 2.7.

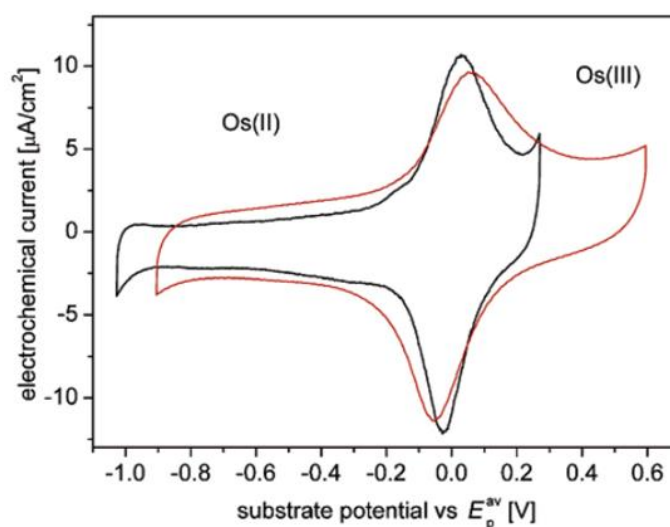


Figure 2.7: CV data of Ossac on Au(111) in aqueous 0.1 M HClO₄ (black) and ionic liquid, BMIM-PF₆ (red); scan rate - 0.1 V/s. Figure taken from reference 14.

These results confirm the great potential for the investigation of the electrochemical properties of molecules using ionic liquid. The surface redox potential was determined to be $E_{1/2} = +0.58$ V vs. SCE. This redox potential was in good agreement with values previously reported confirming the suitability of ionic liquid for investigation.¹⁵

2.2 Aim

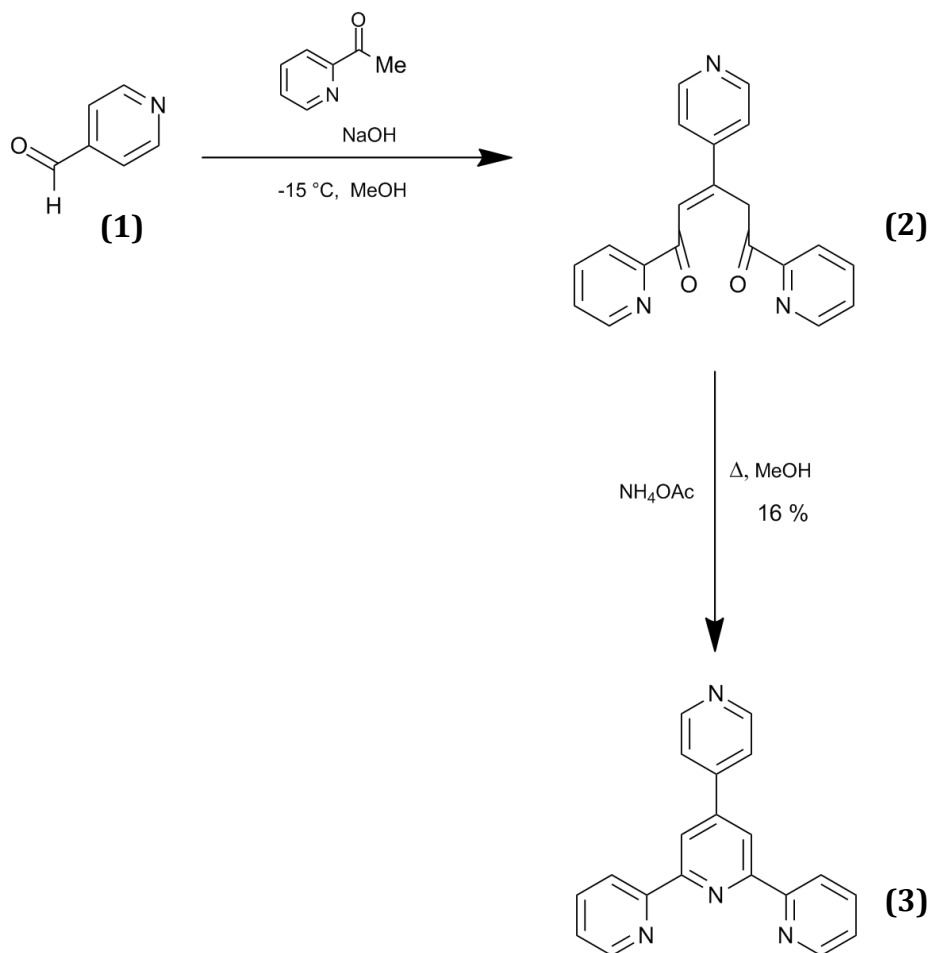
The main aim of this study was to investigate the conductance of several terpyridine based transition metal complexes, to elucidate the effect of varying the transition metal ion on the conductance. In addition, it was of interest to investigate whether the medium (i.e. ambient, or ionic liquid) has any effect on the conductance at open circuit, before any study of redox state dependence of conductance was undertaken (see Chapter 4). The electrochemistry of the complexes in organic solvent and then ionic liquid to assess their suitability for electrochemically controlled STM was also important for the latter.

2.3 Synthesis

All transition metal complexes were synthesised and characterised prior to cyclic voltammetry and conductance investigations. Bipyridine and all starting materials were obtained from Sigma Aldrich and used as received unless otherwise stated.

2.3.1 Synthesis of 4'-(pyridin-4-yl)-2,2':6',2''-terpyridine (3)

The synthesis of 4'-(pyridin-4-yl)-2,2':6',2''-terpyridine was completed following a standard literature procedures shown in Scheme 2.1.¹⁶ This was the reaction of 4-pyridinecarboxaldehyde with two equivalents of 2-acetyl pyridine yielding an enedione intermediate which, after an *in situ* ring closure with ammonium acetate, afforded the product, 4'-(pyridin-4-yl)-2,2':6',2''-terpyridine.

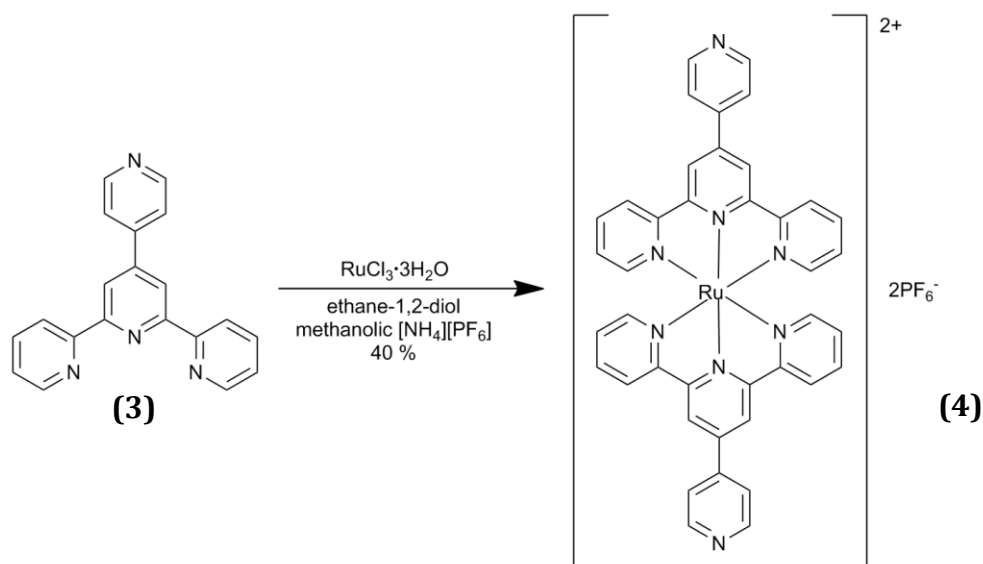


Scheme 2.1: Synthetic Pathway to 4'-(pyridin-4-yl)-2,2':6',2''-terpyridine

The yield achieved is much lower than the recorded literature value of 69 % by Persaud *et al.*¹⁶ this lower value could be due to product being lost during the reaction not going to completion and product being lost during the purification procedure but enough product was isolated to continue the synthesis of the transition metal complexes.

2.3.2 Synthesis of [Ru(4'-(pyridin-4-yl)-2,2':6',2''-terpyridine)₂](PF₆)₂ (4)

The synthesis of [Ru(4'-(pyridin-4-yl)-2,2':6',2''-terpyridine)₂](PF₆)₂ was completed following literature procedures as shown in Scheme 2.2.¹⁷ This involved heating a solution of RuCl₃·3H₂O and 4'-(pyridin-4-yl)-2,2':6',2''-terpyridine in ethane-1,2-diol to reflux. The complex was then purified by exchange of the counter ions, followed by column chromatography. This yielded the title complex as a red solid.

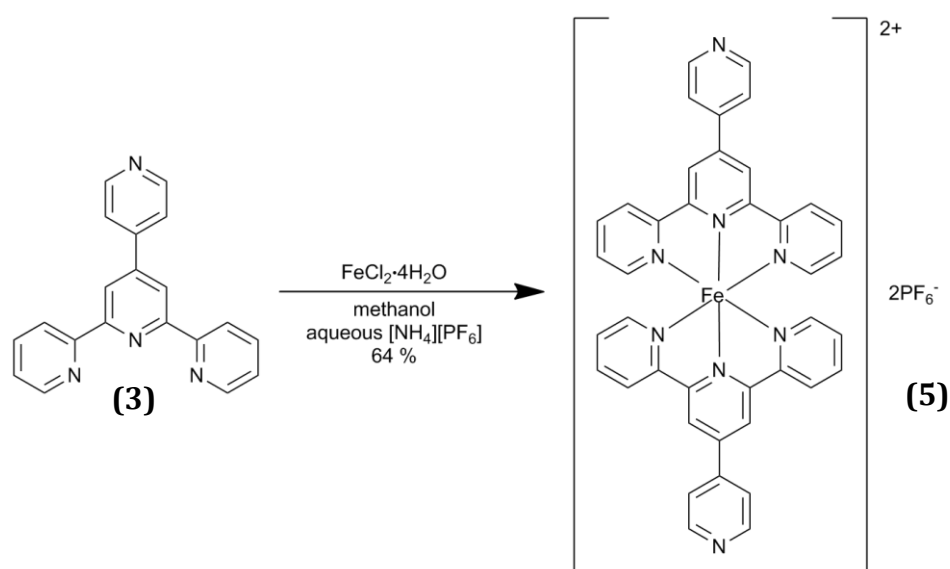


Scheme 2.2: Synthesis of $[\text{Ru}(4'-(\text{pyridin-4-yl})-2,2':6',2''\text{-terpyridine})_2](\text{PF}_6)_2$

This yield was once again lower than the recorded literature yield of 60 %.¹¹

2.3.3 Synthesis of $[\text{Fe}(4'-(\text{pyridin-4-yl})-2,2':6',2''\text{-terpyridine})_2](\text{PF}_6)_2$ (5)

The synthesis of $[\text{Fe}(4'-(\text{pyridin-4-yl})-2,2':6',2''\text{-terpyridine})_2](\text{PF}_6)_2$ was completed following literature procedures,¹² namely, by stirring a solution of $\text{FeCl}_2 \cdot 4\text{H}_2\text{O}$ and 4'-(pyridin-4-yl)-2,2':6',2''-terpyridine in methanol. The complex was purified by precipitation following exchange of the counter ions, as shown in Scheme 2.3. This yielded the title complex as a purple solid.

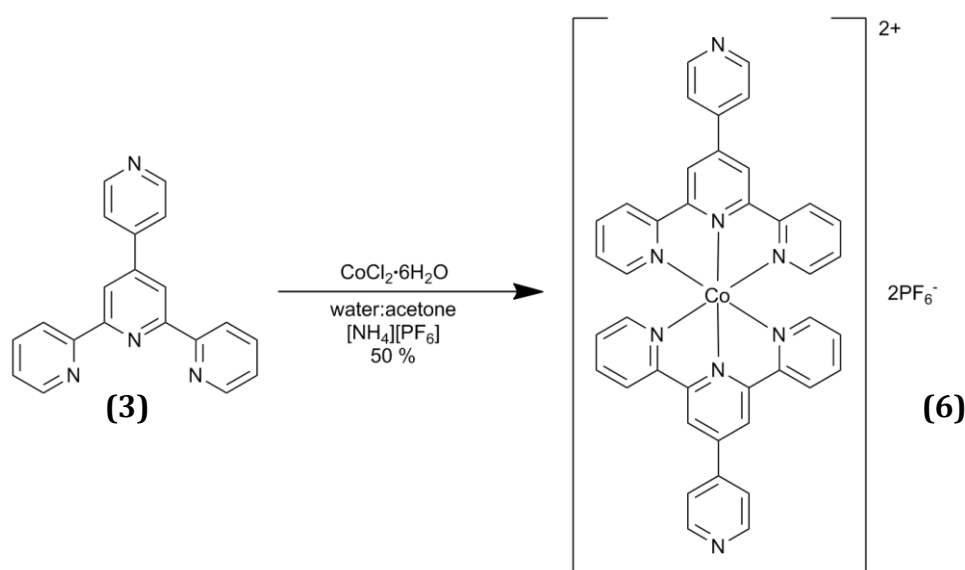


Scheme 2.3: Synthesis of $[\text{Fe}(4'-(\text{pyridin-4-yl})-2,2':6',2''\text{-terpyridine})_2](\text{PF}_6)_2$

The recorded yield of 64 % was once again lower than the literature yield of 80 %.

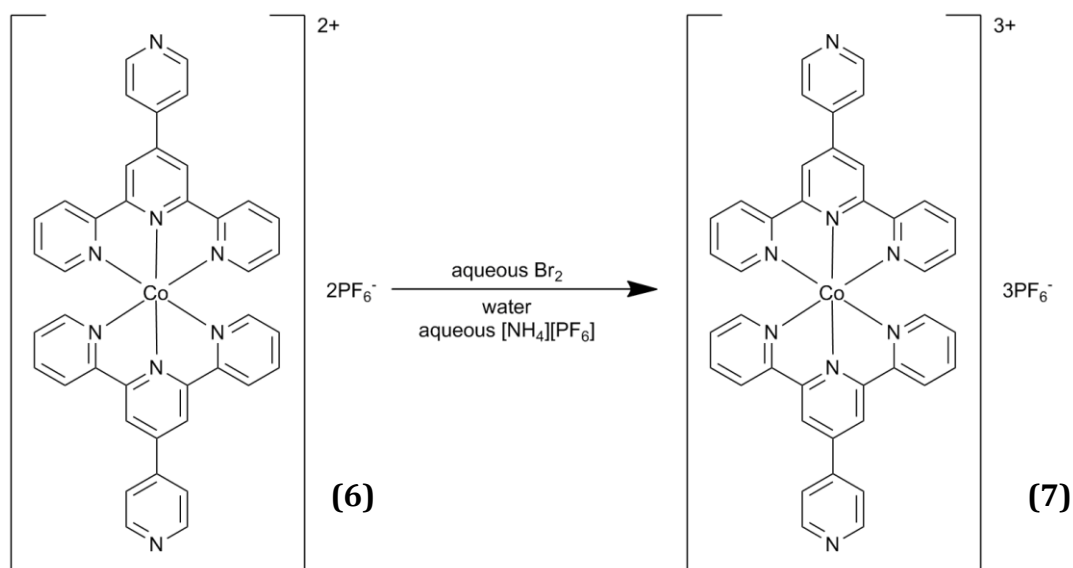
2.3.4 Synthesis of [Co(4'-(pyridin-4-yl)-2,2':6',2''-terpyridine)₂](PF₆)₂ (6)

The synthesis of [Co(4'-(pyridin-4-yl)-2,2':6',2''-terpyridine)₂](PF₆)₂ was completed by adapting a literature procedure as shown in Scheme 2.4.¹⁸ An acetone solution of 4'-(pyridin-4-yl)-2,2':6',2''-terpyridine was treated with an aqueous solution of CoCl₂·6H₂O the reaction was stirred at room temperature and then purification was completed via counter ion exchange. The title compound was precipitated as a red solid.



Scheme 2.4: Synthesis of [Co(4'-(pyridin-4-yl)-2,2':6',2''-terpyridine)₂](PF₆)₂

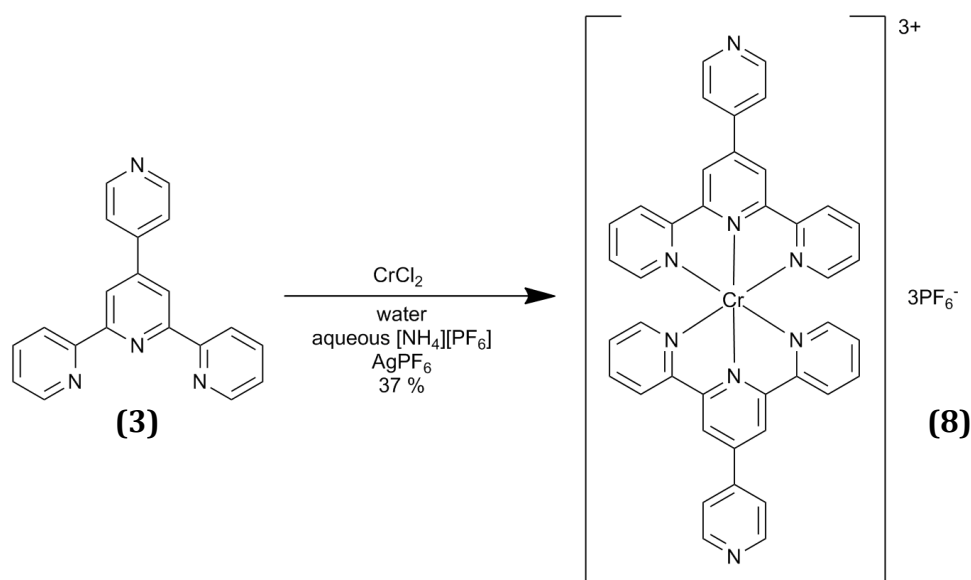
The recorded yield for [Co(pyterpy)₂](PF₆)₂ was only slightly less than the reported literature yield of 60 %, ¹⁸ the procedure was slightly adapted so this proved a successful result. Due to the paramagnetic nature of the Co²⁺ complex, a small portion was further oxidised to the diamagnetic Co³⁺ complex to allow standard NMR analysis to be completed. This was achieved by oxidation with a saturated solution of aqueous Br₂ which after further purification by recrystallization, the Co(III) complex was obtained as an orange solid, as shown below in Scheme 2.5.



Scheme 2.5: Synthesis of $[\text{Co}(4'-(\text{pyridin-4-yl})-2,2':6',2''\text{-terpyridine})_2](\text{PF}_6)_3$

2.3.5 Synthesis of $[\text{Cr}(4'-(\text{pyridin-4-yl})-2,2':6',2''\text{-terpyridine})_2](\text{PF}_6)_3$ (8)

The synthesis of $[\text{Cr}(4'-(\text{pyridin-4-yl})-2,2':6',2''\text{-terpyridine})_2](\text{PF}_6)_3$ was completed by adapting a literature procedure.^{19, 20} Using standard Schlenk techniques, a solution of $4'-(\text{pyridin-4-yl})-2,2':6',2''\text{-terpyridine}$ and CrCl_2 was stirred at room temperature. Subsequent reaction with AgPF_6 followed by purification and counter ion exchange resulted with the title compound being recovered as an orange solid, the synthetic pathway is shown in Scheme 2.6.



Scheme 2.6: Synthesis of $[\text{Cr}(4'-(\text{pyridin-4-yl})-2,2':6',2''\text{-terpyridine})_2](\text{PF}_6)_3$

Due to the paramagnetic nature of the Cr³⁺ complex standard NMR analysis was not suitable. Attempts to determine the molecular ion using electrospray ionisation mass spectrometry failed. It has been previously found in the literature that analysis of chromium terpyridine complexes is challenging.²⁰ Constable *et al.* have investigated the lability of bisterpyridine chromium(III) complexes. They investigate the ¹H NMR of [Cr(terpy)₂](PF₆)₃ in CD₃OD and as expected no signals are recorded in the aromatic region of the spectra. However, after addition of solid NaOH to the sample, signals corresponding to the free ligand were observed. This experiment was completed for the synthesised [Cr(pyterpy)₂](PF₆)₃ complex and similar results were obtained, Figure .

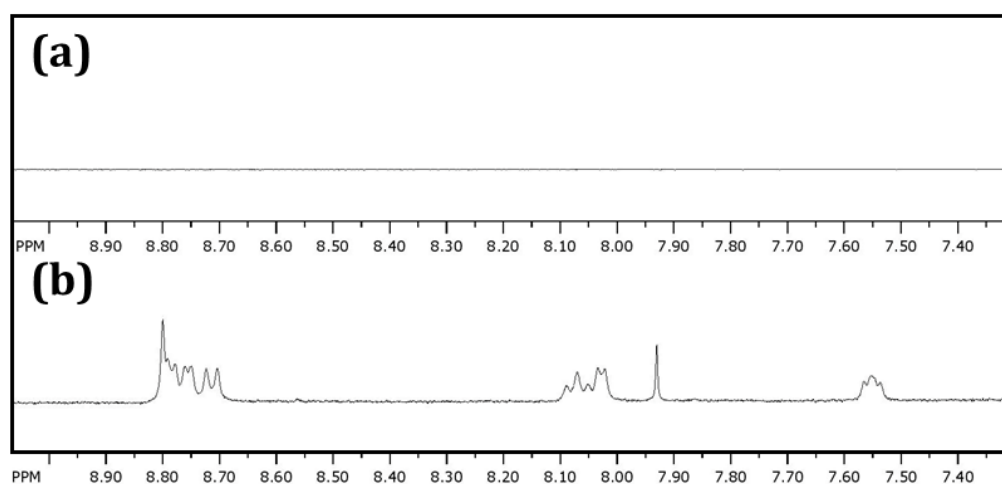


Figure 2.8: ¹H NMR spectra recorded in CD₃OD, a) Cr(pyterpy)₂(PF₆)₃. b) Cr(pyterpy)₂(PF₆)₃ and NaOH.

As reported by Constable *et al.* for the [Cr(terpy)₂](PF₆)₃ the [Cr(pyterpy)₂](PF₆)₃ shows no peaks in CD₃OD which was expected, Figure 2.8(a). It can be seen that upon addition of NaOH signals are observed in the aromatic region of the NMR spectrum which correspond to the free pyterpy ligand, Figure 2.8(b). This result suggests the successful synthesis of the [Cr(pyterpy)₂](PF₆)₃ complex has been completed. The yield was significantly lower than the literature yield of 72 %.¹⁹ The procedure however was adapted for the pyterpy ligand so would require optimising.

2.4 Methods

The transition metal complexes were synthesised as described in Section 2.3.

2.4.1 Single Molecule Conductance Measurements:

The samples were prepared using commercial thin film gold on glass slides (Arrandee®) which was flame annealed using a Bunsen burner immediately prior to use. The freshly annealed slide was immersed into a warmed 5×10^{-5} M dichloromethane solution of the required complex for 1 min to allow the molecules to adsorb to the surface. The slide was then rinsed with EtOH and dried with a blast of N_2 to remove any physisorbed material. Au STM tips were prepared by cutting 0.25 mm Au wire (99.99 %, Goodfellow).

Conductance measurements were completed using an Agilent 5500 STM controller in conjunction with Agilent Picoscan 5.3.3 software. Measurements were completed in both ambient and an ionic liquid medium. Ionic liquid was dried for 12 h prior to use at 120 °C under high vacuum and was used in conjunction with an environmental chamber fitted to the STM head which was under a constant flow of N_2 . The $I(s)$ method was utilised to measure the conductance with a setpoint current (I_0) of 40 nA and a bias voltage (V_{bias}) of + 0.6 V. The tip was withdrawn 4 nm relative to the setpoint and the scan duration was 0.1 s. The initial tip to sample distance (s_0) was approximated using the method described previously in Chapter 1 and, where appropriate, was used in conjunction with the experimental break off (ΔS) to calculate the total break off (S_{total}). Approximately 500 current-distance scans that exhibited a clear current plateau, were plotted into a histogram from which the molecular conductance was calculated.

2.4.2 Cyclic Voltammetry Measurements:

Cyclic voltammetry experiments were completed using an Metrohm Autolab potentiostat PGSTAT30 model utilizing the AutoLab GPES software. For all experiments a three electrode set up was employed, with a gold polycrystalline working electrode and Pt wire counter- and quasi-reference electrodes; referencing was completed to an internal standard of ferrocene. A sealable glass cell was used which was cleaned in 20 % HNO_3 and dried in the oven prior to use. All chemicals were either synthesised in the laboratory or used as received. Acetonitrile was distilled prior to use and ionic liquid was dried for 12 hours at

120 °C under vacuum prior to use. All solutions and experiments were prepared in a glove box in an inert atmosphere.

2.5 Results

2.5.1 Conductance Results:

The $I(s)$ technique was used to measure the conductance of the transition metal complexes. The measurements were completed in either an ambient environment or an ionic liquid medium by rapidly withdrawing the tip at a predetermined setpoint of 40 nA and a bias 0.6 V. Approximately 5 % of the $I(s)$ scans contained a plateau characteristic of a molecule bridging the gap between the tip and the substrate. The conductance was calculated via histogram analysis using the $I(s)$ scans that contained a plateau.

2.5.1.1: Conductance in ambient conditions:

4,4'-Bipyridine was the first molecule to be studied. As the shortest possible molecule employing pyridyl contacts, it represents a benchmark against which the conductances of the pyterpy complexes can be assessed. The compound was initially tested in ambient conditions at a set-point current (I_0) of 40 nA and a bias of 0.6 V following literature procedures.²¹ In ambient conditions a conductance of (7.3 ± 2) nS was determined. The average experimental break off value (Figure 2.9(c)) was calculated to be 0.54 nm and the calculated $d(\ln I)/d(s)$ value was 8.57 nm^{-1} which led to s_0 being 0.8 nm. This gives a total break off distance of (1.34 ± 0.24) nm which was compared to the gold separation distance calculated using Spartan[®], of 1.1 nm for the fully extended molecule. The data are shown in Figure 2.9.

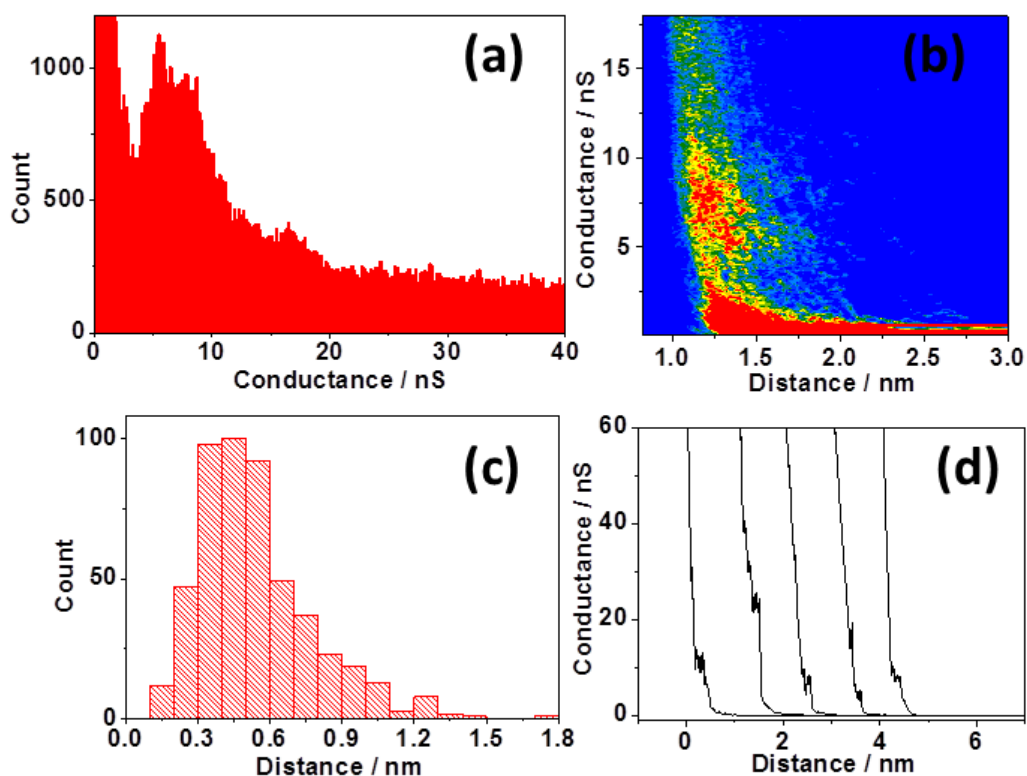


Figure 2.9: Data for 4,4'-bipyridine in ambient conditions $V_{bias} = 0.6$ and $I_0 = 40$ nA (a) Histogram of 505 $I(s)$ scans (b) 2D histogram showing conductance relative to total break-off distance (c) Histogram of the experimental break-off distances (d) example $I(s)$ traces (distance is relative and does not represent actually break-off distance)

Once the technique had been optimised for 4,4'-bipyridine, $[Ru(\text{pyterpy})_2](PF_6)_2$ was measured in ambient conditions. The compound was tested using the same conditions as 4,4'-bipyridine with a set-point current (I_0) of 40 nA and a bias of 0.6 V. In ambient environment the conductance was determined as (3.70 ± 0.9) nS. The average experimental break off value was found to be 0.85 nm (Figure 2.10(c)) and the calculated $d(\ln I)/d(s)$ value was 5.93 nm^{-1} which led to s_0 being 1.19 nm. This gives a total break off distance of (2.04 ± 0.27) nm which was compared to the gold separation distance calculated using Spartan[®], 2.2 nm for the fully extended molecule. The data are shown in Figure 2.10.

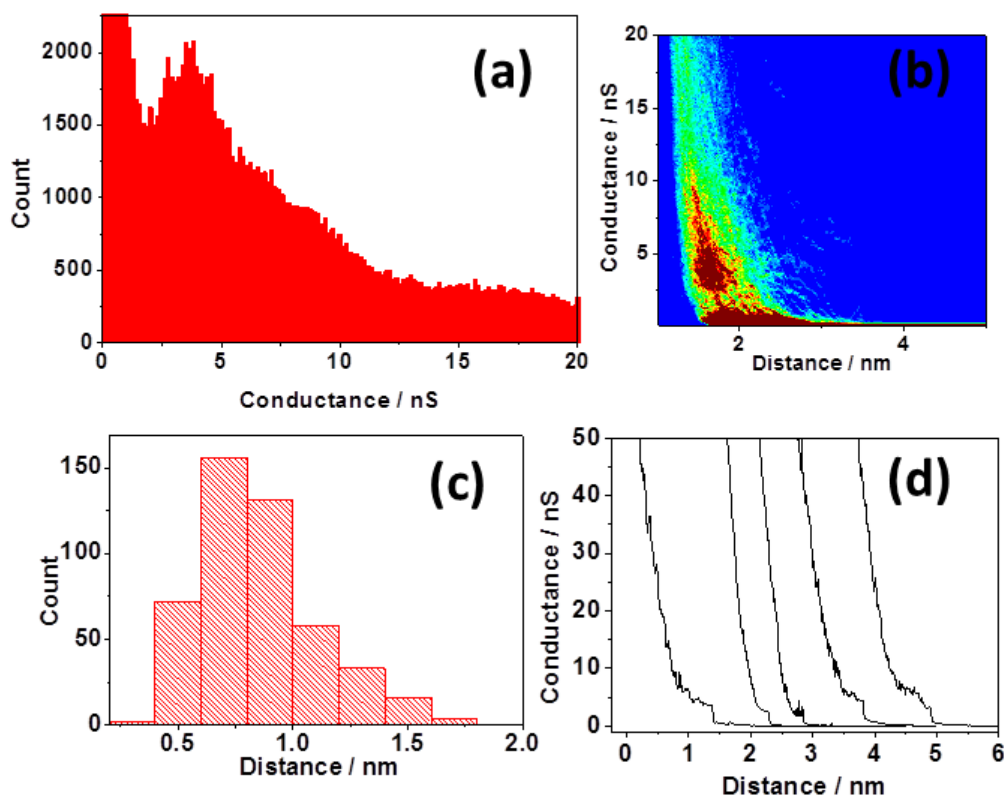


Figure 2.10: Data for [Ru(pyterpy)₂](PF₆)₂ in ambient conditions $V_{bias} = 0.6$ and $I_0 = 40$ nA (a) Histogram of 520 $I(s)$ scans (b) 2D histogram showing conductance relative to total break-off distance (c) Histogram of the experimental break-off distances (d) example $I(s)$ traces (distance is relative and does not represent actually break-off distance)

[Fe(pyterpy)₂](PF₆)₂ was the next molecule to be investigated. The compound was tested in the same conditions as previously described in an ambient environment with a set-point current (I_0) of 40 nA and a bias of 0.6 V. A conductance of (3.42 ± 1) nS was recorded. The average experimental break off value was found to be 1 nm (Figure 2.11(c)) and the calculated $d(\ln I)/d(s)$ value was 7.92 nm^{-1} which resulted in s_0 being 0.89 nm. This gives a total break off distance of (1.89 ± 0.3) nm, compared to the gold separation distance calculated using Spartan[®], which was again 2.2 nm for the fully extended molecule. The data are shown in Figure 2.11.

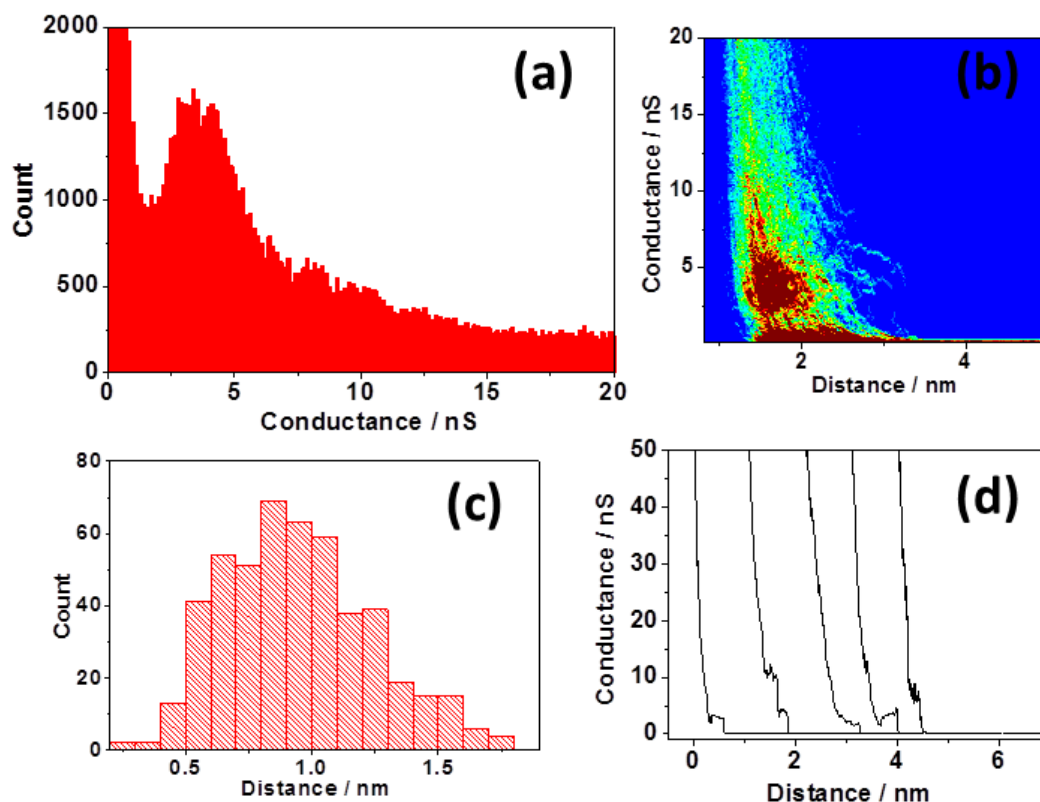


Figure 2.11: Data for [Fe(pyterpy)₂](PF₆)₂ in ambient conditions $V_{bias} = 0.6$ and $I_0 = 40$ nA (a) Histogram of 413 $I(s)$ scans (b) 2D histogram showing conductance relative to total break-off distance (c) Histogram of the experimental break-off distances (d) example $I(s)$ traces (distance is relative and does not represent actually break-off distance)

The conductance of [Co(pyterpy)₂](PF₆)₂ was now investigated in ambient conditions. The compound was measured in the same conditions as previously described with a set-point current (I_0) of 40 nA and a bias of 0.6 V. The conductance was found to be (3.54 ± 1.1) nS. The average experimental break off value was 0.83 nm (Figure 2.12(c)) and the calculated $d(\ln I)/d(s)$ value was 6.25 nm^{-1} which led to s_0 being 1.12 nm. This gives a total break off distance of (1.95 ± 0.25) nm which was compared to the gold separation distance calculated using Spartan®, which was 2.2 nm for the fully extended molecule. The data are shown in Figure 2.12.

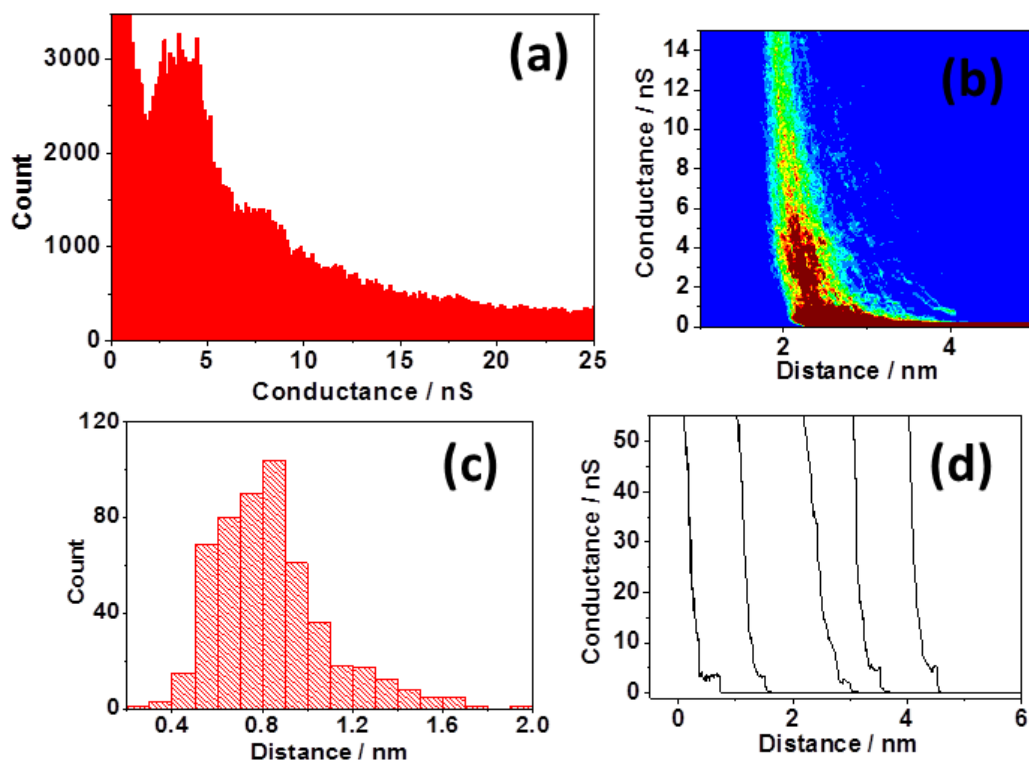


Figure 2.12: Data for [Co(pyterpy)₂](PF₆)₂ in ambient conditions $V_{bias} = 0.6$ and $I_0 = 40$ nA (a) Histogram of 508 $I(s)$ scans (b) 2D histogram showing conductance relative to total break-off distance (c) Histogram of the experimental break-off distances (d) example $I(s)$ traces (distance is relative and does not represent actually break-off distance)

[Cr(pyterpy)₂](PF₆)₃ was the final molecule to be investigated in ambient conditions. The compound was tested in the same conditions as previously described with a set-point current (I_0) of 40 nA and a bias of 0.6 V. A conductance of (2.5 ± 0.42) nS was recorded. The average experimental break off value was calculated to be 1.03 nm (Figure 2.13(c)) and the calculated $d(\ln I)/d(s)$ value was 7.88 nm^{-1} which led to s_0 being 0.89 nm. This gives a total break off distance of (1.92 ± 0.35) nm which was compared to the gold separation distance calculated using Spartan, which was again 2.2 nm for the fully extended molecule. The data are shown in Figure 2.13.

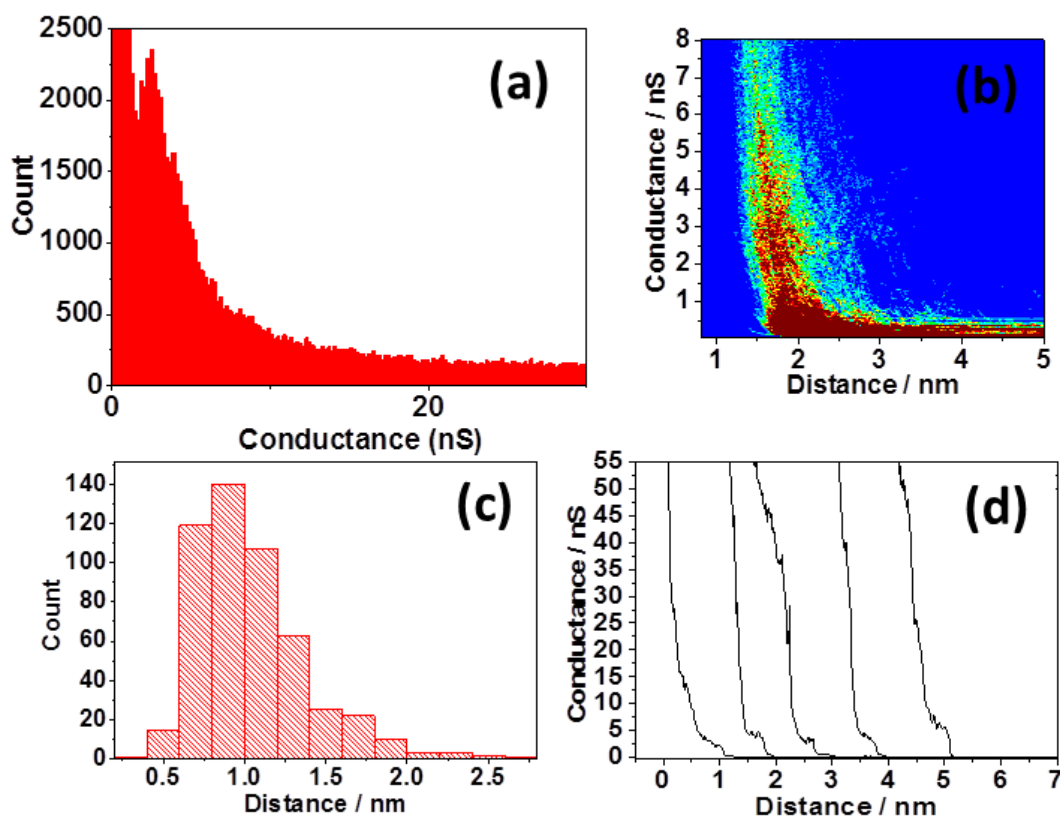


Figure 2.13: Data for $[\text{Cr}(\text{pyterpy})_2](\text{PF}_6)_3$ in ambient conditions $V_{\text{bias}} = 0.6$ and $I_0 = 40$ nA (a) Histogram of 511 $I(s)$ scans (b) 2D histogram showing conductance relative to total break-off distance (c) Histogram of the experimental break-off distances (d) example $I(s)$ traces (distance is relative and does not represent actually break-off distance)

2.5.1.2: Conductance in Ionic Liquid:

Bipyridine was the first molecule to be investigated in ionic liquid. The compound was tested in the same conditions as in an ambient environment with a set-point current (I_0) of 40 nA and a bias of 0.6 V. In ionic liquid a conductance of (5.7 ± 0.88) nS was determined. The average experimental break off value was found to be 1.61 nm (Figure 2.14(c)) and the calculated $d(\ln I)/d(s)$ value was 6.13 nm^{-1} which led to s_0 being 1.15 nm. This gives a total break off distance of (2.76 ± 0.47) nm which was compared to the gold separation distance calculated using Spartan[®], which was 1.1 nm for the fully extended molecule. The data are shown in Figure 2.14.

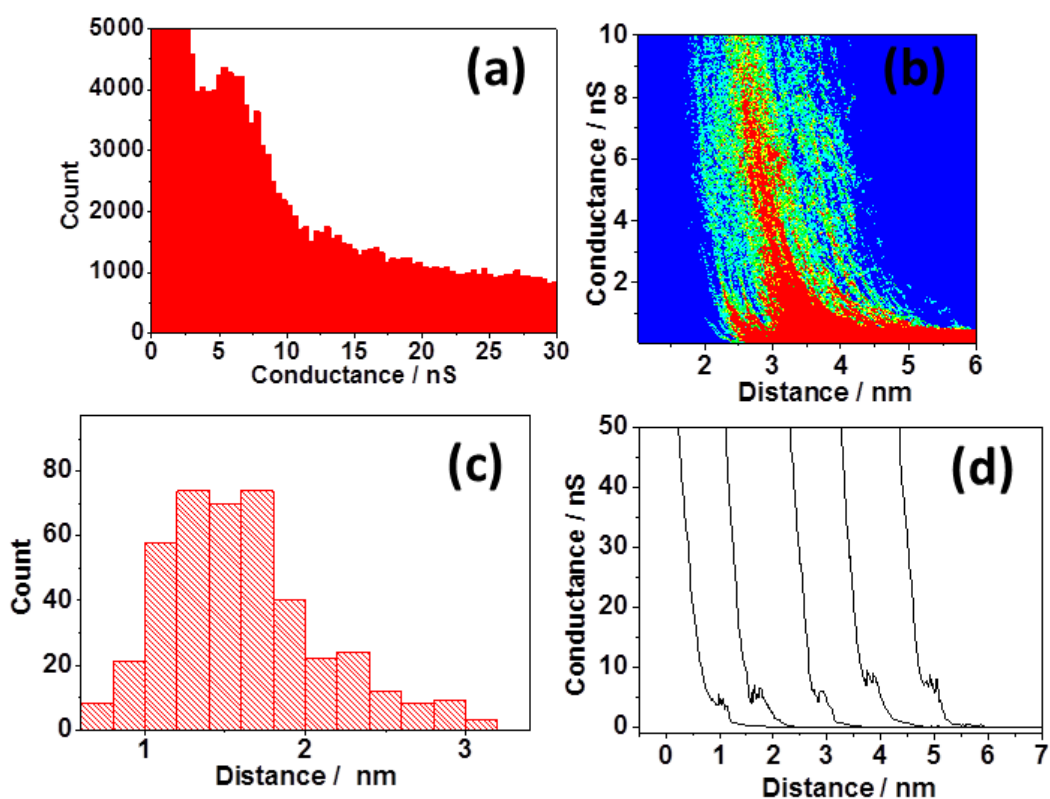


Figure 2.14: Data for 4,4'-bipyridine in ionic liquid $V_{bias} = 0.6$ and $I_0 = 40$ nA (a) Histogram of 440 $I(s)$ scans (b) 2D histogram showing conductance relative to total break-off distance (c) Histogram of the experimental break-off distances (d) example $I(s)$ traces (distance is relative and does not represent actually break-off distance)

The conductance of $[Ru(\text{pyterpy})_2](PF_6)_2$ was then investigated in ionic liquid. The compound was tested in the same conditions as previously described with a set-point current (I_0) of 40 nA and a bias of 0.6 V. In ionic liquid the conductance was found to be (2.61 ± 0.59) nS. The average experimental break off value was 2.18 nm (Figure 2.15(c)) and the calculated $d(\ln I)/d(s)$ value was 2.4 nm^{-1} which led to s_0 being 2.9 nm. This gives a total break off distance of (4.58 ± 0.4) nm, compared to the gold separation distance, calculated using Spartan®, of 2.2 nm for the fully extended molecule. The data are shown in Figure 2.15.

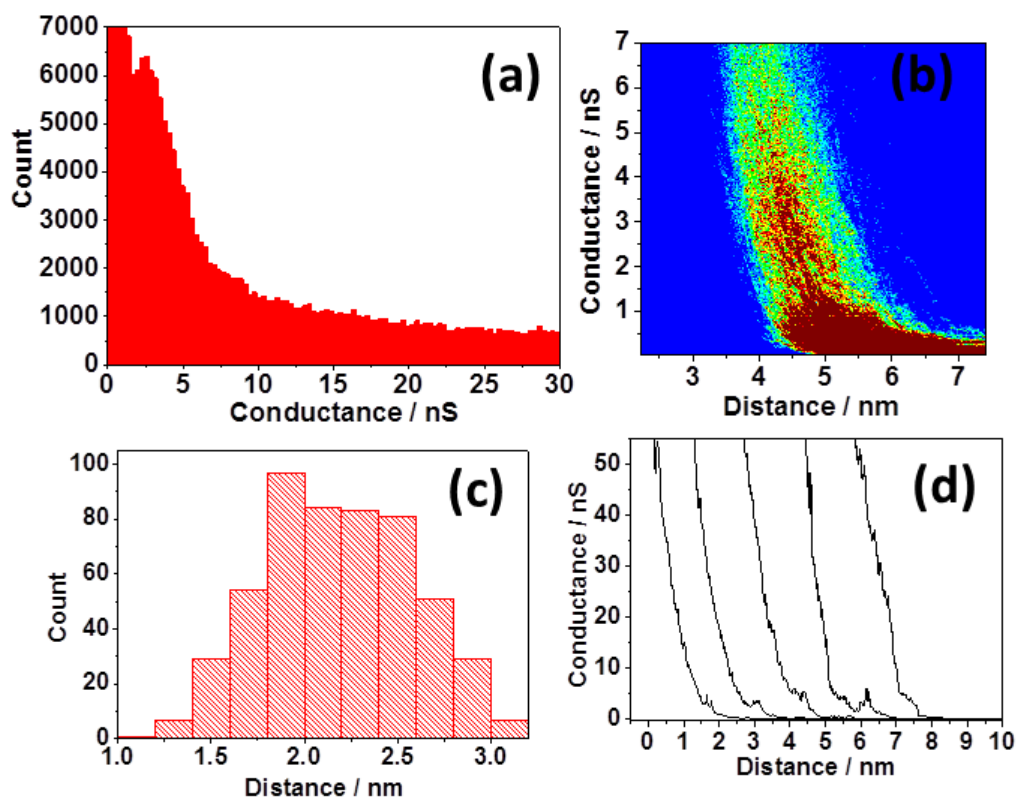


Figure 2.15: Data for $[\text{Ru}(\text{pyterpy})_2](\text{PF}_6)_2$ in ionic liquid $V_{\text{bias}} = 0.6$ and $I_0 = 40$ nA (a) Histogram of 538 $I(s)$ scans (b) 2D histogram showing conductance relative to total break-off distance (c) Histogram of the experimental break-off distances (d) example $I(s)$ traces (distance is relative and does not represent actually break-off distance)

$[\text{Fe}(\text{pyterpy})_2](\text{PF}_6)_2$ was the next molecule to be investigated in ionic liquid. The compound was tested in the same conditions as previously described with a set-point current (I_0) of 40 nA and a bias of 0.6 V. In ionic liquid the conductance was determined to be (3.7 ± 1.05) nS. The average experimental break off value was 1.06 nm (Figure 2.16(c)) and the calculated $d(\ln I)/d(s)$ value was 3.82 nm^{-1} which led to s_0 being 1.84 nm. This gives a total break off distance of (2.9 ± 0.35) nm which is again significantly longer than the gold-gold separation distance for a molecular junction calculated using Spartan[®], 2.2 nm for the fully extended molecule. The data are shown in Figure 2.16.

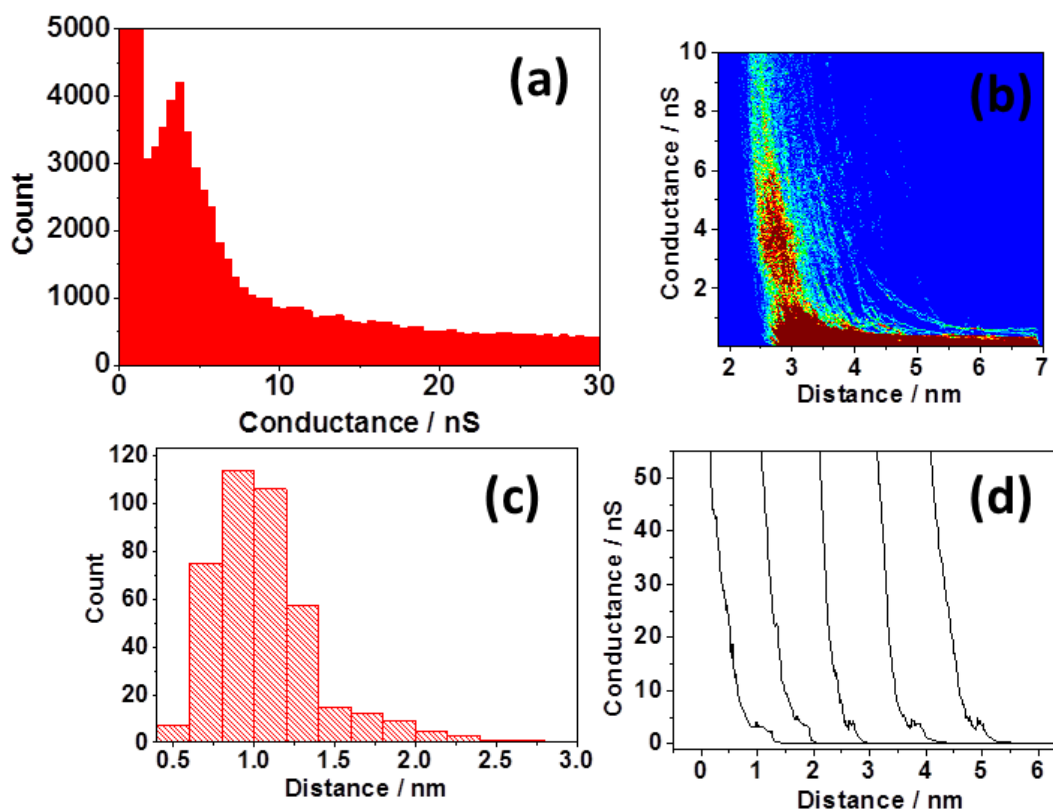


Figure 2.16: Data for [Fe(pyterpy)₂](PF₆)₂ in ionic liquid $V_{bias} = 0.6$ and $I_0 = 40$ nA (a) Histogram of 401 $I(s)$ scans (b) 2D histogram showing conductance relative to total break-off distance (c) Histogram of the experimental break-off distances (d) example $I(s)$ traces (distance is relative and does not represent actually break-off distance)

The conductance of [Co(pyterpy)₂](PF₆)₂ was the next molecule to be investigated in ionic liquid. Under the same conditions as for the Fe(II) complex, the conductance was found to be (2.56 ± 0.72) nS. The average experimental break off value was 1.53 nm (Figure 2.17(c)) and the calculated $d(\ln I)/d(s)$ value was 5.44 nm^{-1} which led to s_0 being 1.29 nm. This gives a total break off distance of (2.82 ± 0.5) nm which is once more longer than the gold separation distance calculated using Spartan[®], which was 2.2 nm for the fully extended molecule. The data are shown in Figure 2.17.

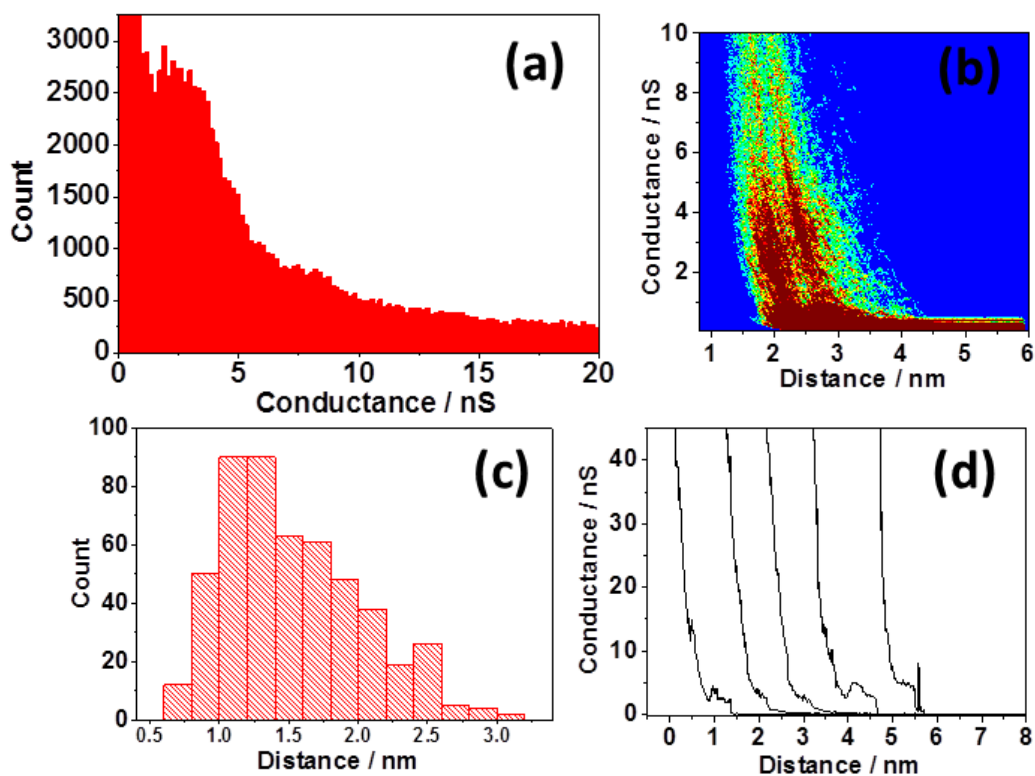


Figure 2.17: Data for $[\text{Co}(\text{pyterpy})_2](\text{PF}_6)_2$ in ionic liquid $V_{\text{bias}} = 0.6$ and $I_0 = 40$ nA (a) Histogram of 508 $I(s)$ scans (b) 2D histogram showing conductance relative to total break-off distance (c) Histogram of the experimental break-off distances (d) example $I(s)$ traces (distance is relative and does not represent actually break-off distance)

$[\text{Cr}(\text{pyterpy})_2](\text{PF}_6)_3$ was the final molecule to be investigated in ionic liquid. The compound was tested in the same conditions as in an ambient environment with a set-point current (I_0) of 40 nA and a bias of 0.6 V. In ionic liquid a conductance of (1.96 ± 0.3) nS was calculated. The average experimental break off value was found to be 2.17 (Figure 2.18(c)) and the calculated $d(\ln I)/d(s)$ value was particularly small, 2.75 nm^{-1} giving an s_0 value of 2.56 nm and hence a total break off distance of (4.73 ± 0.47) nm, compared to the expected junction length of 2.2 nm for the fully extended molecule. The data are shown in Figure 2.18.

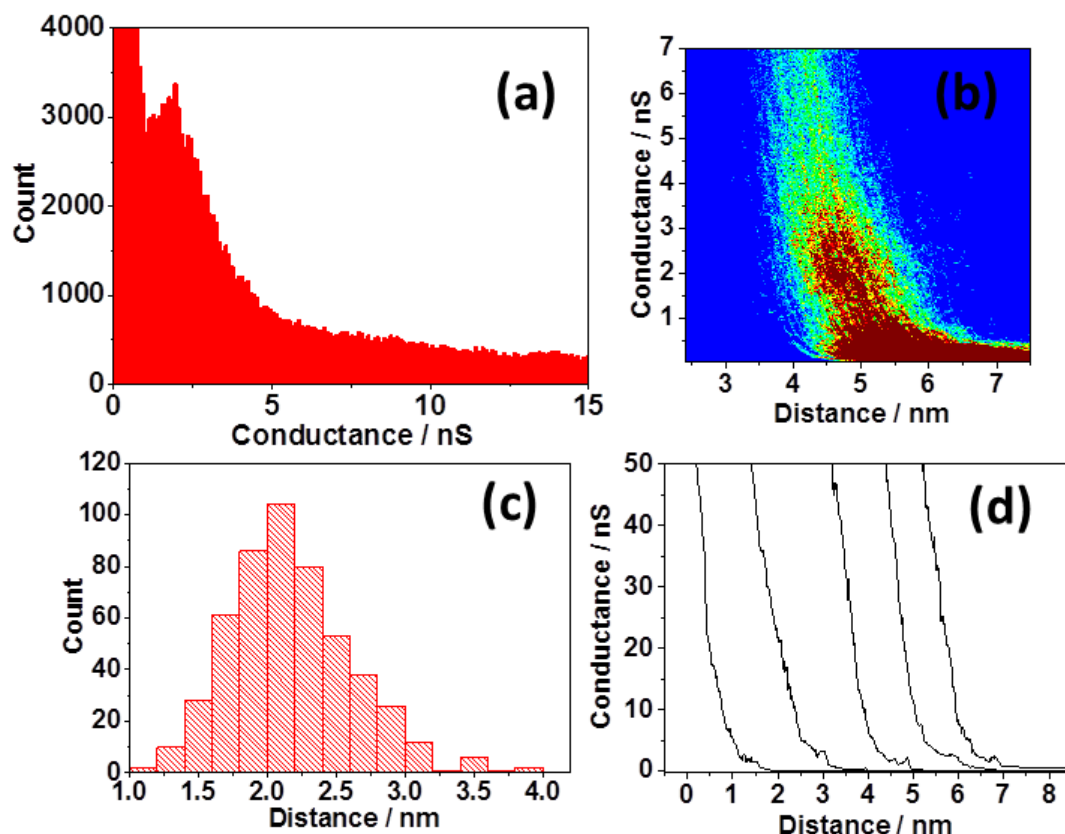


Figure 2.18: Data for $[\text{Cr}(\text{pyterpy})_2](\text{PF}_6)_3$ in ionic liquid $V_{\text{bias}} = 0.6$ and $I_0 = 40$ nA (a) Histogram of 510 $I(s)$ scans (b) 2D histogram showing conductance relative to total break-off distance (c) Histogram of the experimental break-off distances (d) example $I(s)$ traces (distance is relative and does not represent actually break-off distance)

2.5.2 Cyclic Voltammetry

Cyclic Voltammetry was used to observe the M(II)-M(III) redox processes for the metal-organic systems to establish which system would be most promising for conductance measurements under electrochemical control.

2.5.2.1 Cyclic Voltammetry in organic solvent:

The electrolyte utilised was a 0.1 M solution of tetrabutylammonium tetrafluoroborate (TBATFB) in acetonitrile (MeCN), which had been distilled from calcium hydride (CaH_2).

Solution voltammetry of $[\text{Ru}(\text{pyterpy})_2](\text{PF}_6)_2$ was recorded at various scan rates ($0.02 - 1 \text{ Vs}^{-1}$) as shown in Figure 2.19. Once this was complete, 7 mM ferrocene was added and the experiment repeated. The potential scale was then adjusted to the ferrocene redox couple Fc/Fc^+ .

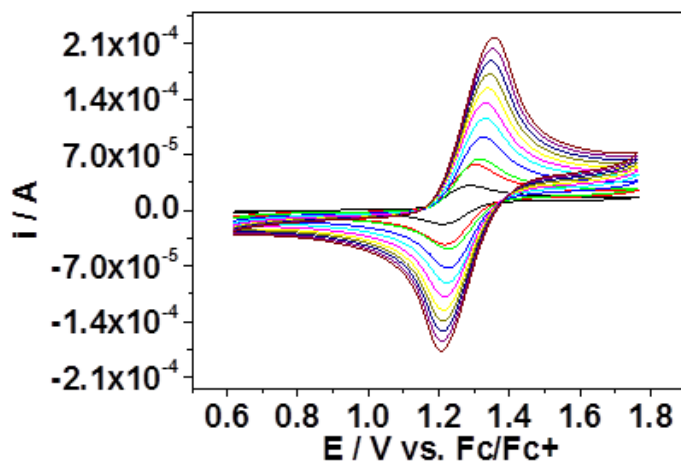


Figure 2.19: Cyclic Voltammogram of 7 mM $[\text{Ru}(\text{pyterpy})_2](\text{PF}_6)_2$ in 0.1 M TBATFB MeCN electrolyte. The potential scale has been calibrated to the Fc/Fc⁺ couple. Scan rates 0.05 Vs⁻¹ to 1 Vs⁻¹.

The M(II)-M(III) redox peak was found to be $E_{1/2} = 1.27$ V vs. Fc/Fc⁺. The data are presented below in Table 2.2.

Table 2.2: The recorded redox potentials $E_{1/2}$ and the difference between the anodic and cathodic peak potentials ΔE_p for 7 mM $[\text{Ru}(\text{pyterpy})_2](\text{PF}_6)_2$ in a 0.1 M TBATFB solution of MeCN. The average redox potential for ferrocene is used to calibrate the potential scale.

Scan Rate / V s ⁻¹	$[\text{Ru}(\text{pyterpy})_2](\text{PF}_6)_2$ V vs. Pt Quasi		Ferrocene V vs. Pt Quasi
	$E_{1/2}/\text{V}$	$\Delta E_p/\text{V}$	$E_{1/2}/\text{V}$
0.05	1.3845	0.069	0.1315
0.10	1.3955	0.081	0.131
0.20	1.407	0.086	0.1315
0.30	1.4105	0.097	0.1315
0.40	1.412	0.104	0.1315
0.50	1.409	0.11	0.139
0.60	1.412	0.124	0.139
0.70	1.412	0.126	0.139
0.80	1.4145	0.131	0.139
0.90	1.415	0.144	0.139
1.0	1.415	0.144	0.1465
Average	1.41		0.136

Cyclic voltammetry data for $[\text{Fe}(\text{pyterpy})_2](\text{PF}_6)_2$ was next recorded as shown in Figure 2.20, Once again, ferrocene was added and the ferrocene redox couple Fc/Fc⁺ determined to provide a reliable reference.

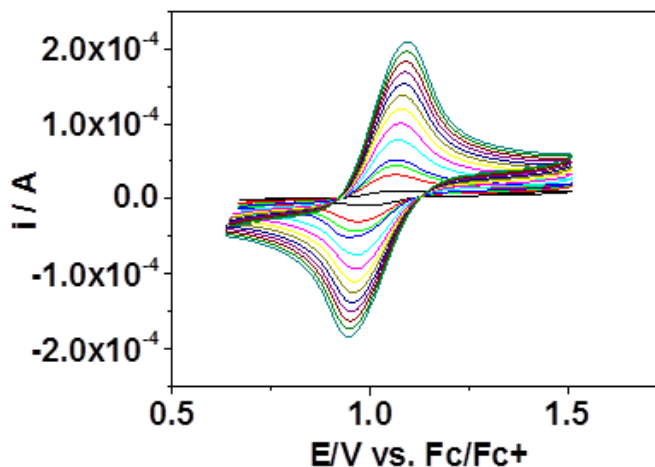


Figure 2.20: Cyclic Voltammogram of 7 mM $[\text{Fe}(\text{pyterpy})_2](\text{PF}_6)_2$ in 0.1 M TBATFB MeCN electrolyte. The potential scale has been calibrated to the Fc/Fc^+ couple. Scan rates 0.02 Vs^{-1} to 1 Vs^{-1} .

$[\text{Fe}(\text{pyterpy})_2](\text{PF}_6)_2$ exhibited a clear M(II)-M(III) redox peak in the organic electrolyte. The calculated redox potential is $E_{1/2} = 1.02 \text{ V vs. Fc}/\text{Fc}^+$. The data are present below in Table 2.3.

Table 2.3: The recorded redox potentials $E_{1/2}$ and the difference between the anodic and cathodic peak potentials ΔE_p for 7 mM $[\text{Fe}(\text{pyterpy})_2](\text{PF}_6)_2$ in a 0.1 M TBATFB solution of MeCN. The average redox potential for ferrocene is used to calibrate the potential scale.

Scan Rate / V s^{-1}	$[\text{Fe}(\text{pyterpy})_2](\text{PF}_6)_2 \text{ V vs. Pt Quasi}$		Ferrocene V vs. Pt Quasi
	$E_{1/2}/\text{V}$	$\Delta E_p/\text{V}$	$E_{1/2}/\text{V}$
0.02	1.1155	0.061	0.081
0.05	1.1055	0.083	0.081
0.08	1.1	0.098	0.081
0.10	1.095	0.11	0.081
0.20	1.1105	0.101	0.0815
0.30	1.11	0.104	0.081
0.40	1.105	0.114	0.091
0.50	1.1095	0.125	0.091
0.60	1.1095	0.125	0.091
0.70	1.11	0.126	0.0915
0.80	1.1095	0.125	0.091
0.90	1.1045	0.135	0.096
1.0	1.11	0.146	0.1065
Average	1.11		0.088

The voltammetry of $[\text{Co}(\text{pyterpy})_2](\text{PF}_6)_2$ was recorded at several scan rates as shown in Figure 2.21, with the ferrocene redox couple Fc/Fc^+ once again subsequently determined to provide the reference scale.

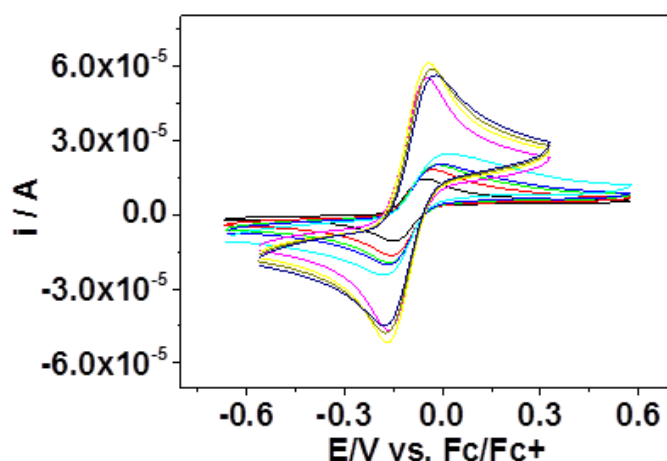


Figure 2.21: Cyclic Voltammogram of 7 mM $[\text{Co}(\text{pyterpy})_2](\text{PF}_6)_2$ in 0.1 M TBATFB MeCN electrolyte. The potential scale has been calibrated to the Fc/Fc^+ couple. Scan rates 0.02 Vs^{-1} to 1 Vs^{-1} .

$[\text{Co}(\text{pyterpy})_2](\text{PF}_6)_2$ exhibited a M(II)-M(III) redox peak in the organic electrolyte. The calculated redox potential is $E_{1/2} = -0.09 \text{ V vs. Fc}/\text{Fc}^+$. The data are present below in Table 2.4.

Table 2.4: The recorded redox potentials $E_{1/2}$ and the difference between the anodic and cathodic peak potentials ΔE_p for 7 mM $[\text{Co}(\text{pyterpy})_2](\text{PF}_6)_2$ in a 0.1 M TBATFB solution of MeCN. The average redox potential for ferrocene is used to calibrate the potential scale.

Scan Rate / V s^{-1}	$[\text{Co}(\text{pyterpy})_2](\text{PF}_6)_2 \text{ V vs. Pt Quasi}$		Ferrocene V vs. Pt Quasi
	$E_{1/2}/\text{V}$	$\Delta E_p/\text{V}$	$E_{1/2}/\text{V}$
0.02	0.0675	0.085	0.1465
0.05	0.0825	0.117	0.159
0.08	0.075	0.136	0.159
0.10	0.0825	0.155	0.1585
0.20	0.09	0.18	0.1665
0.70	0.0665	0.141	0.1815
0.80	0.074	0.156	0.1815
0.90	0.074	0.156	0.174
1.0	0.0665	0.171	0.174
Average	0.075		0.167

Solution voltammetry of $[\text{Cr}(\text{pyterpy})_2](\text{PF}_6)_3$ was recorded at various scan rates as shown in Figure 2.22.

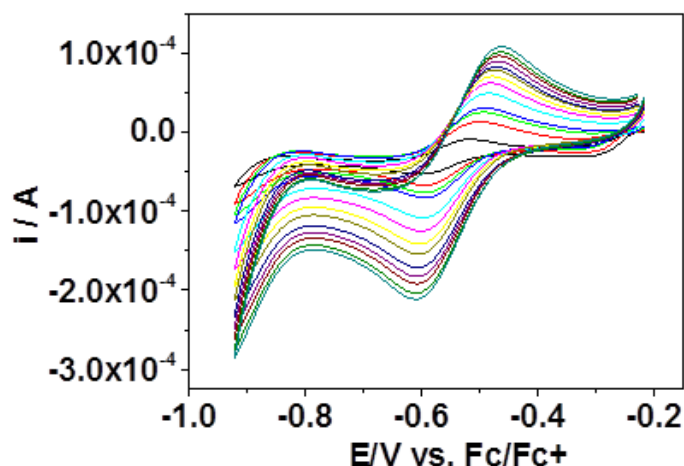


Figure 2.22: Cyclic Voltammogram of 7 mM $[\text{Cr}(\text{pyterpy})_2](\text{PF}_6)_3$ in 0.1 M TBATFB MeCN electrolyte. The potential scale has been calibrated to the Fc/Fc⁺ couple. Scan rates 0.02 Vs⁻¹ to 1 Vs⁻¹.

$[\text{Cr}(\text{pyterpy})_2](\text{PF}_6)_3$ exhibited a clear M(II)-M(III) redox peak in the organic electrolyte.¹⁹ The calculated redox potential is $E_{1/2} = -0.54$ V vs. Fc/Fc⁺. The data are present below in Table 2.5. Scarborough *et al.* have investigated $[\text{Cr}(\text{tbpy})_3]^n(\text{PF}_6)_n$ and found that the seven-membered electron transfer series ($n = 3+, 2+, 1+, 0, 1-, 2-, 3-$) involves one electron ligand based reductions and all seven members contain a central Cr(III) ion.²² This result provides evidence that this redox wave is actually ligand based.

Table 2.5: The recorded redox potentials $E_{1/2}$ and the difference between the anodic and cathodic peak potentials ΔE_p for 7 mM $[\text{Cr}(\text{pyterpy})_2](\text{PF}_6)_3$ in a 0.1 M TBATFB solution of MeCN. The average redox potential for ferrocene is used to calibrate the potential scale.

Scan Rate / V s ⁻¹	$[\text{Cr}(\text{pyterpy})_2](\text{PF}_6)_3$ V vs. Pt Quasi		Ferrocene V vs. Pt Quasi
	$E_{1/2}/\text{V}$	$\Delta E_p/\text{V}$	$E_{1/2}/\text{V}$
0.02	-0.4425	0.081	0.1325
0.05	-0.4325	0.081	0.115
0.08	-0.4275	0.091	0.1
0.10	-0.4225	0.101	0.105
0.20	-0.4225	0.101	0.11
0.30	-0.4275	0.111	0.115
0.40	-0.4225	0.121	0.115
0.50	-0.4225	0.121	0.12
0.60	-0.4225	0.121	0.12
0.70	-0.4225	0.121	0.125
0.80	-0.4225	0.121	0.12
0.90	-0.4175	0.131	0.12
1.0	-0.4175	0.131	0.13
Average	-0.425		0.118

2.5.2.4 Cyclic Voltammetry in ionic liquid

Once the cyclic voltammetry of the metal pyterpy complexes was completed in acetonitrile solvent, the electrochemistry was then investigated in ionic liquid.

Solution voltammetry of $[\text{Ru}(\text{pyterpy})_2](\text{PF}_6)_2$ in ionic liquid was recorded at various scan rates as shown in Figure 2.23; again, once completed 7 mM ferrocene was added and the experiment repeated. The potential scales was then adjusted to the ferrocene redox couple Fc/Fc^+ .

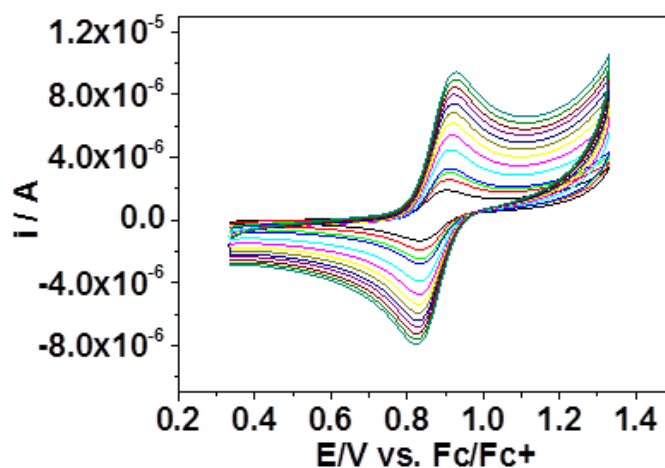


Figure 2.23: Cyclic Voltammogram of 7 mM $[\text{Ru}(\text{pyterpy})_2](\text{PF}_6)_2$ in BMIM-TFSA electrolyte. The potential scale has been calibrated to the Fc/Fc^+ couple. Scan rates 0.02 Vs^{-1} to 1 Vs^{-1} .

$[\text{Ru}(\text{pyterpy})_2](\text{PF}_6)_2$ exhibited a clear M(II)-M(III) redox peak in BMIM-TFSA. The calculated redox potential is $E_{1/2} = 0.87 \text{ V}$ vs. Fc/Fc^+ . The data are presented below in Table 2.6.

Table 2.6: The recorded redox potentials $E_{1/2}$ and the difference between the anodic and cathodic peak potentials ΔE_p for 7 mM $[\text{Ru}(\text{pyterpy})_2](\text{PF}_6)_2$ in BMIM-TFSA. The average redox potential for ferrocene is used to calibrate the potential scale.

Scan Rate / V s^{-1}	$[\text{Ru}(\text{pyterpy})_2]\text{PF}_6)_2$ V vs. Pt Quasi		Ferrocene V vs. Pt Quasi
	$E_{1/2}/\text{V}$	$\Delta E_p/\text{V}$	$E_{1/2}/\text{V}$
0.02	0.934	0.06	0.0615
0.05	0.9395	0.061	0.0675
0.08	0.9395	0.065	0.0705
0.10	0.9425	0.071	0.0705
0.20	0.9395	0.075	0.071
0.30	0.943	0.08	0.0705
0.40	0.943	0.08	0.0705
0.50	0.943	0.08	0.0735
0.60	0.9425	0.081	0.074
0.70	0.943	0.092	0.0705
0.80	0.943	0.09	0.0735
0.90	0.943	0.09	0.075
1.0	0.943	0.092	0.074
Average	0.941		0.071

Cyclic voltammetry data for $[\text{Fe}(\text{pyterpy})_2](\text{PF}_6)_2$ was recorded at various scan rates as shown in Figure 2.24, with the potential scales again adjusted to the ferrocene redox couple Fc/Fc^+ .

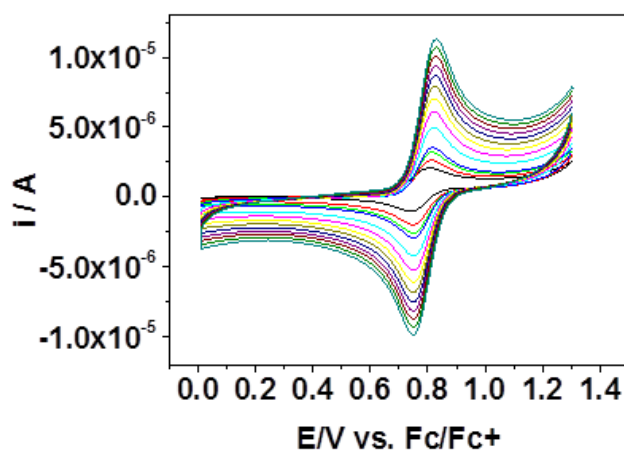


Figure 2.24: Cyclic Voltammogram of 7 mM $[\text{Fe}(\text{pyterpy})_2](\text{PF}_6)_2$ in BMIM-TFSA electrolyte. The potential scale has been calibrated to the Fc/Fc^+ couple. Scan rates 0.02 Vs^{-1} to 1 Vs^{-1} .

$[\text{Fe}(\text{pyterpy})_2](\text{PF}_6)_2$ exhibited a clear $\text{M}(\text{II})-\text{M}(\text{III})$ redox peak in the ionic liquid electrolyte. The redox potential was, $E_{1/2} = 0.78 \text{ V}$ vs. Fc/Fc^+ . The data are presented below in Table 2.7.

Table 2.7: The recorded redox potentials $E_{1/2}$ and the difference between the anodic and cathodic peak potentials ΔE_p for 7 mM $[\text{Fe}(\text{pyterpy})_2](\text{PF}_6)_2$ in BMIM-TFSA. The average redox potential for ferrocene is used to calibrate the potential scale.

Scan Rate / V s^{-1}	$[\text{Fe}(\text{pyterpy})_2](\text{PF}_6)_2$ V vs. Pt Quasi		Ferrocene V vs. Pt Quasi
	$E_{1/2}/\text{V}$	$\Delta E_p/\text{V}$	$E_{1/2}/\text{V}$
0.02	0.8685	0.057	0.098
0.05	0.874	0.062	0.084
0.08	0.877	0.06	0.084
0.10	0.877	0.06	0.081
0.20	0.8795	0.065	0.087
0.30	0.88	0.064	0.0905
0.40	0.88	0.064	0.0905
0.50	0.883	0.07	0.0935
0.60	0.883	0.072	0.096
0.70	0.8825	0.071	0.099
0.80	0.883	0.072	0.1055
0.90	0.883	0.072	0.1085
1.0	0.886	0.074	0.1145
Average	0.880		0.095

Solution voltammetry of $[\text{Co}(\text{pyterpy})_2](\text{PF}_6)_2$ was recorded at various scan rates as shown in Figure 2.25.

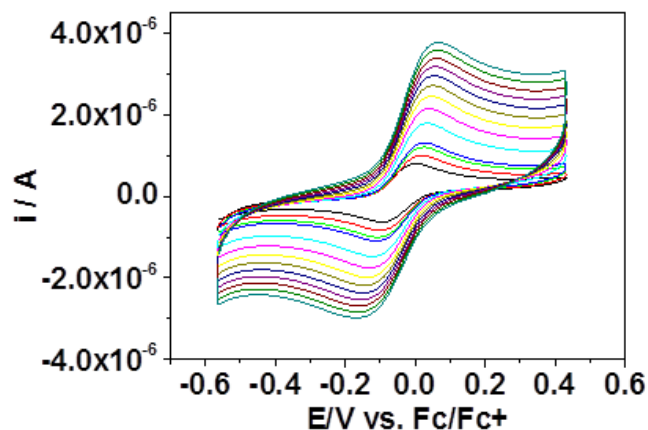


Figure 2.25: Cyclic Voltammogram of 7 mM $[\text{Co}(\text{pyterpy})_2](\text{PF}_6)_2$ in BMIM-TFSA electrolyte. The potential scale has been calibrated to the Fc/Fc^+ couple. Scan rates 0.02 Vs^{-1} to 1 Vs^{-1} .

$[\text{Co}(\text{pyterpy})_2](\text{PF}_6)_2$ exhibited a clear M(II)-M(III) redox peak in the ionic liquid. The redox potential, $E_{1/2} = -0.04 \text{ V}$ vs. Fc/Fc^+ . The data are presented below in Table 2.8.

Table 2.8: The recorded redox potentials $E_{1/2}$ and the difference between the anodic and cathodic peak potentials ΔE_p for 7 mM $[\text{Co}(\text{pyterpy})_2](\text{PF}_6)_2$ in BMIM-TFSA. The average redox potential for ferrocene is used to calibrate the potential scale.

Scan Rate / V s^{-1}	$[\text{Co}(\text{pyterpy})_2](\text{PF}_6)_2$ V vs. Pt Quasi		Ferrocene V vs. Pt Quasi
	$E_{1/2}/\text{V}$	$\Delta E_p/\text{V}$	$E_{1/2}/\text{V}$
0.02	0.0215	0.079	0.0605
0.05	0.0305	0.105	0.0635
0.08	0.0275	0.115	0.0665
0.10	0.0215	0.125	0.0665
0.20	0.022	0.136	0.0665
0.30	0.0125	0.165	0.0695
0.40	0.0125	0.177	0.0695
0.50	0.0125	0.189	0.0695
0.60	0.01	0.196	0.0695
0.70	0.0125	0.201	0.0695
0.80	0.015	0.232	0.0725
0.90	0.0155	0.233	0.0725
1.0	0.1185	0.037	0.0695
Average	0.026		0.0681

Voltammetry of $[\text{Cr}(\text{pyterpy})_2](\text{PF}_6)_3$ was recorded at various scan rates as shown in Figure 2.26, with the potential scale adjusted to the ferrocene redox couple Fc/Fc^+ .

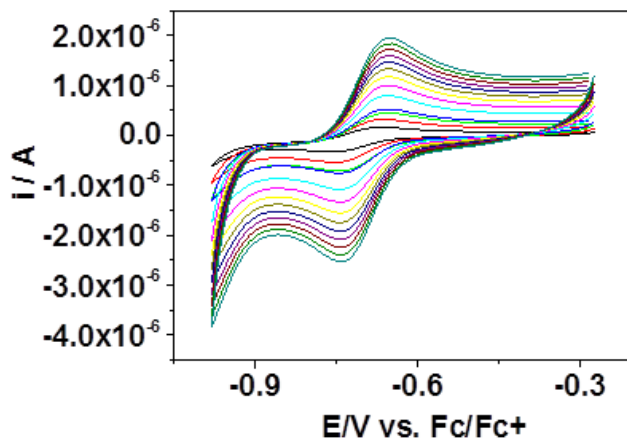


Figure 2.26: Cyclic Voltammogram of 7 mM $[\text{Cr}(\text{pyterpy})_2](\text{PF}_6)_3$ in BMIM-TFSA electrolyte. The potential scale has been calibrated to the Fc/Fc^+ couple. Scan rates 0.02 Vs^{-1} to 1 Vs^{-1} .

$[\text{Cr}(\text{pyterpy})_2](\text{PF}_6)_2$ exhibited a M(II)-M(III) redox peak in ionic liquid at $E_{1/2} = -0.70 \text{ V vs. Fc}/\text{Fc}^+$. The data are presented below in Table 2.9.

Table 2.9: The recorded redox potentials $E_{1/2}$ and the difference between the anodic and cathodic peak potentials ΔE_p for 7 mM $[\text{Cr}(\text{pyterpy})_2](\text{PF}_6)_3$ in BMIM-TFSA. The average redox potential for ferrocene is used to calibrate the potential scale.

Scan Rate / V s^{-1}	$[\text{Cr}(\text{pyterpy})_2](\text{PF}_6)_3$ V vs. Pt Quasi		Ferrocene V vs. Pt Quasi
	$E_{1/2}/\text{V}$	$\Delta E_p/\text{V}$	$E_{1/2}/\text{V}$
0.02	-0.688	0.07	0.027
0.05	-0.678	0.07	0.027
0.08	-0.668	0.07	0.027
0.10	-0.668	0.07	0.027
0.20	-0.668	0.07	0.027
0.30	-0.668	0.07	0.027
0.40	-0.668	0.07	0.022
0.50	-0.668	0.07	0.022
0.60	-0.668	0.07	0.022
0.70	-0.668	0.07	0.022
0.80	-0.668	0.07	0.022
0.90	-0.668	0.07	0.027
1.0	-0.668	0.07	0.027
Average	-0.670		0.025

For comparison with the pyterpy complexes, the voltammetry of ferrocene was also recorded as a function of scan rate as shown in Figure 2.27.

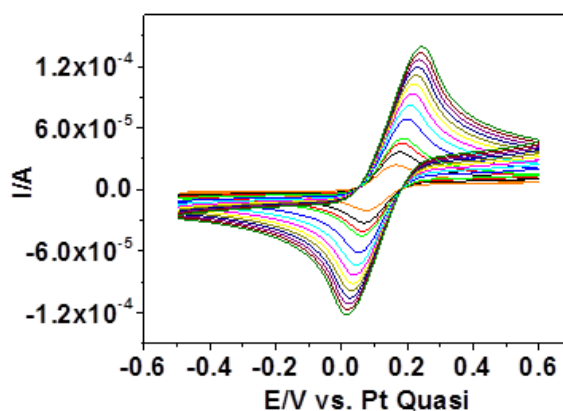


Figure 2.27: Cyclic Voltammogram of 7 mM Ferrocene in BMIM-TFSA electrolyte. Scan rates 0.02 Vs^{-1} to 1 Vs^{-1} .

Ferrocene exhibited a clear redox peak in the organic electrolyte. The calculated redox potential, $E_{1/2} = 0.13$ V vs. Pt Quasi. The data are presented in Table 2.10.

Table 2.10: The recorded redox potentials $E_{1/2}$ and the difference between the anodic and cathodic peak potentials ΔE_p for 7 mM Ferrocene in BMIM-TFSA.

Scan Rate / $V s^{-1}$	Ferrocene V vs. Pt Quasi	
	$E_{1/2}/V$	$\Delta E_p/V$
0.02	0.1215	0.087
0.05	0.1245	0.107
0.08	0.1245	0.109
0.10	0.1245	0.121
0.20	0.1245	0.143
0.30	0.128	0.16
0.40	0.1275	0.173
0.50	0.128	0.184
0.60	0.1305	0.191
0.70	0.1275	0.197
0.80	0.1275	0.209
0.90	0.131	0.216
1.0	0.128	0.22
Average	0.127	0.163

2.6: Discussion

A summary of the conductance data has been presented in Table 2.11.

Table 2.11: Summary of the conductance data.

Complex	Ambient Conditions	Ionic Liquid, BMIM-TFSA
	Conductance / nS	Conductance / nS
4,4'-Bipyridine	(7.3 ± 2)	(5.7 ± 0.88)
[Ru(pyterpy)₂](PF₆)₂	(3.7 ± 0.9)	(2.61 ± 0.59)
[Fe(pyterpy)₂](PF₆)₂	(3.42 ± 1)	(3.7 ± 1.05)
[Co(pyterpy)₂](PF₆)₂	(3.54 ± 1.1)	(2.56 ± 0.72)
[Cr(pyterpy)₂](PF₆)₃	(2.5 ± 0.42)	(1.96 ± 0.3)

The results show the successful formation of molecular junctions in two different environments. 4,4'-Bipyridine showed a greater conductance when compared to the pyterpy complexes, which was expected due to the short length of the molecule. The conductance result for 4,4'-bipyridine in ambient and ionic liquid environment is in good agreement with that reported previously in the literature.²¹ Quek *et al.* report reversible switching of 4,4'-bipyridine by mechanical control of the metal-molecule contact geometry in

1,2,4-trichlorobenzene and recorded a low and a high conductance, ~ 12 and ~ 46 nS respectively.²³ This result is higher than the recorded result in ionic liquid. The ionic liquid result also contradicts that reported by Xu *et al.* who reported a conductance of 774 nS completed in aqueous electrolyte²⁴ and Zhou *et al.* obtained 45 and 371 nS²⁵ using the break junction technique. These results infer that the conductance of 4,4'-bipyridine is medium dependent so further investigations would need to occur using the $I(s)$ method. However, the ionic liquid measurements reported here are in good agreement with the ambient result recorded here and previously.

The conductance of the four pyterpy compounds in ambient conditions was measured successfully; however the ruthenium, iron and cobalt complexes exhibit a conductance very similar to each other. The only complex that exhibits a different conductance is the chromium complex, but still within experimental error. This result that varying the metal centre has little effect on the conductance is at first surprising. The result however could be due to $[\text{Co}(\text{pyterpy})_2](\text{PF}_6)_2$ being oxidised to $[\text{Co}(\text{pyterpy})_2](\text{PF}_6)_3$ in the vicinity of the electrode by ambient air, which would result in a low spin d^6 electron configuration isoelectronic with the Ru(II) and Fe(II) complexes, in which case the Cr(III) d^3 species would be the only complex with a different electron configuration. However, this assumes that the metal d^n configuration is significant. Since there is evidence from Seebeck coefficient measurements²⁶ that the 4-pyridyl contact promotes electron- rather than hole-mediated tunneling in molecular junctions, it is more likely that in all these pyridyl-contact metal complexes, the LUMO-based transport resonance is closer in energy to the contact Fermi energy and, at least for the diamagnetic d^6 species for which the calculations have been performed, the LUMO is essentially ligand-localised according to preliminary DFT calculation (6-31G*, B3LYP; Spartan[®] 08). To investigate this further a series of hole-mediated transition metal complexes could be studied, such as the thioether anchoring group.

The conductance was investigated in ionic liquid as this is the chosen electrolyte for the conductance measurements under electrochemical control. The results showed that all the compounds formed successful molecular

junctions. The conductance results for all of the measured compounds decreased apart from $[\text{Fe}(\text{pyterpy})_2](\text{PF}_6)_2$ which increased very slightly, but within error of the ambient measurement. The other four compounds decreased in conductance, including the stable diamagnetic $[\text{Ru}(\text{pyterpy})_2](\text{PF}_6)_2$ and 4,4'-bipyridine. This suggests the decrease in conductance is due to the ionic liquid environment rather than the electron configuration of the complexes changing.

The conductance recorded for the pyterpy complexes is in good agreement with the conductance recorded by Zhou *et al.* for $[\text{Os}(\text{pyterpy})_2](\text{PF}_6)_2$ measured in aqueous 1 M NaClO_4 under electrochemical control. In the off-state they record a conductance of 2.1 nS, which is in the range of conductance results achieved in this study.

The conductance of these complexes can be compared to that of the oligoporphyrins, presented in Figure 2.28, studied by Sedghi *et al.*^{27, 28}

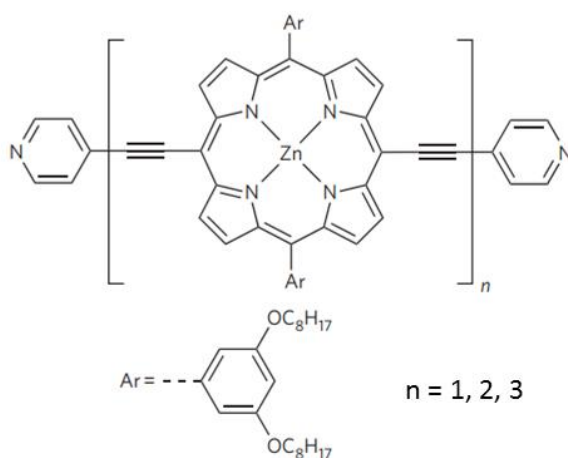


Figure 2.28: Chemical structure of the pyridyl capped oligo-porphyrins studied by Sedghi *et al.*²⁸

The results presented by Sedghi *et al.* investigate the conductance of a pyridyl capped zinc oligo-porphyrin series.²⁸ The result recorded for the pyridyl capped monomer was 2.1 nS which correspond to the results recorded for the investigated transition metal pyterpy complexes. Sedghi *et al.* have also investigated thiol capped oligo-porphyrins of the same structure and the conductance was also found to be 2.1 nS.²⁷ This results ignited interest in

studying terpy based transition metal complexes with different anchoring groups, to see if the conductance is affected which is investigated in chapter 3.

A summary of the calculated break off data has been presented in Table 2.12.

Table 2.12: Summary of the break off data for the conductance measurements

	Environment						Gold Separation as calculated in Spartan® / nm
	Ambient			Ionic Liquid - BMIM-TFSA			
	S_{total} /nm	s_0 / nm	ΔS /nm	S_{total} /nm	s_0 / nm	ΔS /nm	
Bipyridine	(1.34 ± 0.24)	0.8	0.54	(2.76 ± 0.47)	1.15	1.61	1.1
Ru(pyterpy) ₂ (PF ₆) ₂	(2.04 ± 0.27)	1.19	0.85	(4.58 ± 0.4)	2.9	2.18	2.2
Fe(pyterpy) ₂ (PF ₆) ₂	(1.89 ± 0.3)	0.89	1.0	(2.9 ± 0.35)	1.84	1.06	2.2
Co(pyterpy) ₂ (PF ₆) ₂	(1.95 ± 0.25)	1.12	0.83	(2.82 ± 0.5)	1.29	1.53	2.2
Cr(pyterpy) ₂ (PF ₆) ₃	(1.92 ± 0.35)	0.89	1.03	(4.73 ± 0.47)	2.56	2.17	2.2

The total estimated break off distance is usually indicative of the length of molecule bridging the gap between two metal electrodes. The results reported here show for the compounds measured in an ambient environment (highlighted yellow) are in good agreement with the Au-molecule-Au distance as calculated in Spartan®. All of the calculated distances recorded are within the experimental error, or shorter of the measured ones which could be the result of the molecule binding on a step edge of the gold substrate. The break off distances provide good evidence that it is the molecule that is being measured in the molecular junction.

The break off distances calculated from the measurements in the ionic liquid, BMIM-TFSA (highlighted green) do not correlate to the gold separation distance. The recorded results are found to be much higher and outside the range of error. This result can be attributed to the ionic liquid environment. The values of s_0 for the values in ionic liquid are much higher than the values in an ambient environment due to the $d(\ln I)/d(s)$ value being low. As the measurements taken to calculate the $d(\ln I)/d(s)$ value are done so during the experiment the high value could be due to the environment as the s_0 value was

higher in ambient conditions. This can be further investigated by calculating a s_0 value for just the ionic liquid without any of the investigated compounds present, Figure 2.29.

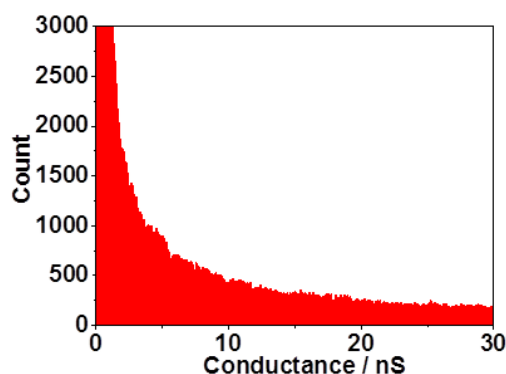


Figure 2.29: Histogram of Ionic Liquid, BMIM-TFSA showing no conductance peaks.

The 1D histogram for the plain ionic liquid shows no conductance peaks, Figure. The s_0 value for the ionic liquid, 1.9 nm is large and suggests that the extended total break off values is due to the medium and not due to the molecule being measured.

Cyclic voltammetry was completed on the four pyterpy complexes, in both organic and ionic liquid solvent. The results will allow the most suitable complex to be selected for conductance measurements under potential control. A summary can be seen in Table 2.13.

Table 2.13: Summary of the cyclic voltammetry results.

Complex	0.1 M TBATFB in MeCN		BMIM-TFSA	
	$E_{1/2}/V$	$\Delta E_p/V$	$E_{1/2}/V$	$\Delta E_p/V$
Ferrocene	0.09	0.14	0.13	0.16
[Ru(pyterpy)₂](PF₆)₂	1.27	0.11	0.87	0.078
[Fe(pyterpy)₂](PF₆)₂	1.02	0.11	0.78	0.066
[Co(pyterpy)₂](PF₆)₂	-0.09	0.14	-0.04	0.15
[Cr(pyterpy)₂](PF₆)₃	-0.54	0.11	-0.70	0.07

All the complexes have shown a clear metal redox peak in both electrolytes. The [Co(pyterpy)₂](PF₆)₂ exhibits a similar quasi-reversible redox potential in both electrolytes. The redox potential is in an easily accessible range to be studied under potential control. This complex will be investigated under electrochemical control. Due to the paramagnetic nature of the

[Co(pyterpy)₂](PF₆)₂ complex it would be of interest to study a complex with diamagnetic nature. This leads to the [Ru(pyterpy)₂](PF₆)₂ and [Fe(pyterpy)₂](PF₆)₂ complex. As the [Fe(pyterpy)₂](PF₆)₂ complex exhibits a lower redox potential it would be more suitable for preliminary investigations into the electrochemical conductance behaviour.

2.7 Conclusions and Future Work

It has been successfully shown that all the complexes form successful molecular junctions. It has been shown that bipyridine has a conductance in ionic liquid which corresponds to literature values for other environments and has a higher conductance than the organometallic compounds, which was expected due to the shorter length.

The conductance of four terpyridine based metal-organic complexes has been shown in two different environments and have shown to be similar to measurements recorded in the literature for similar complex.

Clear metal redox peaks were exhibited in the cyclic voltammetry investigations of the pyterpy complexes. This showed the suitability of the organometallic complexes for conductance measurements under electrochemical control. Future work would be to investigate the conductance of [Co(pyterpy)₂](PF₆)₂ and [Fe(pyterpy)₂](PF₆)₂ under electrochemical control around the M(II)/M(III) redox potential. If these measurements proved successful it would be of interest to investigate multiple transition metal redox processes. The behaviour of this complex could be compared to the 6pTTF6 studied by Kay *et al.*¹⁰

It would also be of interest to investigate the conductance in different environments, such as mesitylene, an inert atmosphere and UHV to see what effect the environment has on the conductance of these organometallic compounds.

The ligand structure could also be tailored and further investigations could occur to see how the ligand affects the conductance.

2.8 References

1. Reed, M. A.; Zhou, C.; Muller, C.; Burgin, T.; Tour, J., Conductance of a molecular junction. *Science* **1997**, *278* (5336), 252-254.
2. Low, P. J., Metal complexes in molecular electronics: progress and possibilities. *Dalton Transactions* **2005**, (17), 2821-2824.
3. Gubin, S.; Gulayev, Y. V.; Khomutov, G.; Kislov, V.; Kolesov, V.; Soldatov, E.; Sulaimankulov, K.; Trifonov, A., Molecular clusters as building blocks for nanoelectronics: the first demonstration of a cluster single-electron tunnelling transistor at room temperature. *Nanotechnology* **2002**, *13* (2), 185; Leary, E.; Van Zalinge, H.; Higgins, S. J.; Nichols, R. J.; Fabrizi de Biani, F.; Leoni, P.; Marchetti, L.; Zanello, P., A molecular wire incorporating a robust hexanuclear platinum cluster. *Physical Chemistry Chemical Physics* **2009**, *11* (25), 5198-5202; Petukhov, K.; Alam, M. S.; Rupp, H.; Strömsdörfer, S.; Müller, P.; Scheurer, A.; Saalfrank, R. W.; Kortus, J.; Postnikov, A.; Ruben, M.; Thompson, L. K.; Lehn, J. M., STM spectroscopy of magnetic molecules. *Coordination Chemistry Reviews* **2009**, *253* (19-20), 2387-2398; Blum, A. S.; Ren, T.; Parish, D. A.; Trammell, S. A.; Moore, M. H.; Kushmerick, J. G.; Xu, G.-L.; Deschamps, J. R.; Pollack, S. K.; Shashidhar, R., Ru₂(ap)₄(σ -oligo(phenyleneethynyl)) Molecular Wires: Synthesis and Electronic Characterization. *Journal of the American Chemical Society* **2005**, *127* (28), 10010-10011; Chae, D.-H.; Berry, J. F.; Jung, S.; Cotton, F. A.; Murillo, C. A.; Yao, Z., Vibrational Excitations in Single Trimetal-Molecule Transistors. *Nano Letters* **2006**, *6* (2), 165-168; Hsu, L.-Y.; Huang, Q.-R.; Jin, B.-Y., Charge Transport Through a Single Molecular Wire Based on Linear Multimetal Complexes: A Non-Equilibrium Green's Function Approach. *The Journal of Physical Chemistry C* **2008**, *112* (28), 10538-10541.
4. Liu, K.; Wang, X.; Wang, F., Probing Charge Transport of Ruthenium-Complex-Based Molecular Wires at the Single-Molecule Level. *ACS Nano* **2008**, *2* (11), 2315-2323.
5. Sauvage, J. P.; Collin, J. P.; Chambron, J. C.; Guillerez, S.; Coudret, C.; Balzani, V.; Barigelletti, F.; De Cola, L.; Flamigni, L., Ruthenium(II) and Osmium(II) Bis(terpyridine) Complexes in Covalently-Linked Multicomponent Systems: Synthesis, Electrochemical Behavior, Absorption Spectra, and Photochemical and Photophysical Properties. *Chemical Reviews* **1994**, *94* (4), 993-1019.
6. Tuccitto, N.; Ferri, V.; Cavazzini, M.; Quici, S.; Zhavnerko, G.; Licciardello, A.; Rampi, M. A., Highly conductive ~ 40-nm-long molecular wires assembled by stepwise incorporation of metal centres. *Nature Materials* **2008**, *8* (1), 41-46.
7. Sikes, H. D.; Smalley, J. F.; Dudek, S. P.; Cook, A. R.; Newton, M. D.; Chidsey, C. E. D.; Feldberg, S. W., Rapid Electron Tunneling Through Oligophenylenevinylene Bridges. *Science* **2001**, *291* (5508), 1519-1523; Salomon, A.; Cahen, D.; Lindsay, S.; Tomfohr, J.; Engelkes, V. B.; Frisbie, C. D., Comparison of electronic transport measurements on organic molecules. *Advanced Materials* **2003**, *15* (22), 1881-1890; He, J.; Chen, F.; Li, J.; Sankey, O. F.; Terazono, Y.; Herrero, C.; Gust, D.; Moore, T. A.; Moore, A. L.; Lindsay, S. M., Electronic Decay Constant of Carotenoid Polyenes from Single-Molecule Measurements. *Journal of the American Chemical Society* **2005**, *127* (5), 1384-1385; Choi, S. H.; Kim, B.; Frisbie, C. D., Electrical resistance of long conjugated molecular wires. *Science* **2008**, *320* (5882), 1482-1486.

8. Zhou, X.-S.; Liu, L.; Fortgang, P.; Lefevre, A.-S.; Serra-Muns, A.; Raouafi, N.; Amatore, C.; Mao, B.-W.; Maisonhaute, E.; Schöllhorn, B., Do molecular conductances correlate with electrochemical rate constants? Experimental insights. *Journal of the American Chemical Society* **2011**, *133* (19), 7509-7516.
9. Kay, N. J.; Nichols, R. J.; Higgins, S. J.; Haiss, W.; Sedghi, G.; Schwarzacher, W.; Mao, B.-W., Ionic Liquids As a Medium for STM-Based Single Molecule Conductance Determination: An Exploration Employing Alkanedithiols. *The Journal of Physical Chemistry C* **2011**, *115* (43), 21402-21408.
10. Kay, N. J.; Higgins, S. J.; Jeppesen, J. O.; Leary, E.; Lycoops, J.; Ulstrup, J.; Nichols, R. J., Single-molecule electrochemical gating in ionic liquids. *Journal of the American Chemical Society* **2012**, *134* (40), 16817-16826.
11. Constable, E. C.; Thompson, A. M. W. C., Pendant-functionalised ligands for metallosupramolecular assemblies; ruthenium(II) and osmium(II) complexes of 4[prime or minute]-(4-pyridyl)-2,2[prime or minute] : 6[prime or minute],2[double prime]-terpyridine. *Journal of the Chemical Society, Dalton Transactions* **1994**, (9), 1409-1418.
12. Constable, E. C.; Thompson, A. M. W. C., Ligand reactivity in iron(II) complexes of 4[prime or minute]-(4[triple prime]-pyridyl)-2,2[prime or minute] : 6[prime or minute],2[double prime]-terpyridine. *Journal of the Chemical Society, Dalton Transactions* **1992**, (20), 2947-2950.
13. Constable, E. C.; Housecroft, C. E.; Neuburger, M.; Phillips, D.; Raithby, P. R.; Schofield, E.; Sparr, E.; Tocher, D. A.; Zehnder, M.; Zimmermann, Y., Development of supramolecular structure through alkylation of pendant pyridyl functionality. *Journal of the Chemical Society, Dalton Transactions* **2000**, (13), 2219-2228; Hutchison, K.; Morris, J. C.; Nile, T. A.; Walsh, J. L.; Thompson, D. W.; Petersen, J. D.; Schoonover, J. R., Spectroscopic and Photophysical Properties of Complexes of 4'-Ferrocenyl-2,2':6',2''-terpyridine and Related Ligands. *Inorganic Chemistry* **1999**, *38* (10), 2516-2523.
14. Albrecht, T.; Moth-Poulsen, K.; Christensen, J. B.; Hjelm, J.; Bjørnholm, T.; Ulstrup, J., Scanning tunneling spectroscopy in an ionic liquid. *Journal of the American Chemical Society* **2006**, *128* (20), 6574-6575.
15. Forster, R. J.; Faulkner, L. R., Electrochemistry of spontaneously adsorbed monolayers. Equilibrium properties and fundamental electron transfer characteristics. *Journal of the American Chemical Society* **1994**, *116* (12), 5444-5452; Albrecht, T.; Guckian, A.; Ulstrup, J.; Vos, J. G., Transistor-like Behavior of Transition Metal Complexes. *Nano Letters* **2005**, *5* (7), 1451-1455.
16. Persaud, L.; Barbiero, G., Synthesis, electrochemical and spectroscopic investigations of 2,2':4,4''-terpyridine and 2,2':4,4'':6,2''-quaterpyridine ligands for metal complex photoelectrochemistry. *Canadian Journal of Chemistry* **1991**, *69* (2), 315-321.
17. CargilláThompson, A. M., Pendant-functionalised ligands for metallosupramolecular assemblies; ruthenium (II) and osmium (II) complexes of 4'-(4-pyridyl)-2, 2': 6', 2''-terpyridine. *Journal of the Chemical Society, Dalton Transactions* **1994**, (9), 1409-1418.
18. Indumathy, R.; Radhika, S.; Kanthimathi, M.; Weyhermuller, T.; Unni Nair, B., Cobalt complexes of terpyridine ligand: Crystal structure and photocleavage of DNA. *Journal of Inorganic Biochemistry* **2007**, *101* (3), 434-443.
19. Scarborough, C. C.; Lancaster, K. M.; DeBeer, S.; Weyhermüller, T.; Sproules, S.; Wieghardt, K., Experimental Fingerprints for Redox-Active

- Terpyridine in $[\text{Cr}(\text{tpy})_2](\text{PF}_6)_n$ ($n = 3-0$), and the Remarkable Electronic Structure of $[\text{Cr}(\text{tpy})_2]^{1-}$. *Inorganic Chemistry* **2012**, *51* (6), 3718-3732.
20. Constable, E. C.; Housecroft, C. E.; Neuburger, M.; Schönle, J.; Zampese, J. A., The surprising lability of bis (2, 2': 6', 2''-terpyridine) chromium (iii) complexes. *Dalton Transactions* **2014**, 43 (19), 7227-7235.
21. Wang, C.; Batsanov, A. S.; Bryce, M. R.; Martín, S.; Nichols, R. J.; Higgins, S. J.; García-Suárez, V. M.; Lambert, C. J., Oligoyne Single Molecule Wires. *Journal of the American Chemical Society* **2009**, *131* (43), 15647-15654.
22. Scarborough, C. C.; Sproules, S.; Weyhermüller, T.; DeBeer, S.; Wieghardt, K., Electronic and Molecular Structures of the Members of the Electron Transfer Series $[\text{Cr}(\text{t bpy})_3]^{n+}$ ($n = 3+, 2+, 1+, 0$): An X-ray Absorption Spectroscopic and Density Functional Theoretical Study. *Inorganic Chemistry* **2011**, *50* (24), 12446-12462.
23. Quek, S. Y.; Kamenetska, M.; Steigerwald, M. L.; Choi, H. J.; Louie, S. G.; Hybertsen, M. S.; Neaton, J. B.; VenkataramanLatha, Mechanically controlled binary conductance switching of a single-molecule junction. *Nat Nano* **2009**, *4* (4), 230-234.
24. Xu, B.; Tao, N. J., Measurement of single-molecule resistance by repeated formation of molecular junctions. *Science* **2003**, *301* (5637), 1221-1223.
25. Zhou, X.-S.; Wei, Y.-M.; Liu, L.; Chen, Z.-B.; Tang, J.; Mao, B.-W., Extending the capability of STM break junction for conductance measurement of atomic-size nanowires: an electrochemical strategy. *Journal of the American Chemical Society* **2008**, *130* (40), 13228-13230.
26. Aradhya, S. V.; Venkataraman, L., Single-molecule junctions beyond electronic transport. *Nature Nanotechnology* **2013**, *8* (6), 399-410.
27. Sedghi, G.; Sawada, K.; Esdaile, L. J.; Hoffmann, M.; Anderson, H. L.; Bethell, D.; Haiss, W.; Higgins, S. J.; Nichols, R. J., Single molecule conductance of porphyrin wires with ultralow attenuation. *Journal of the American Chemical Society* **2008**, *130* (27), 8582-8583.
28. Sedghi, G.; García-Suárez, V. M.; Esdaile, L. J.; Anderson, H. L.; Lambert, C. J.; Martín, S.; Bethell, D.; Higgins, S. J.; Elliott, M.; Bennett, N., Long-range electron tunnelling in oligo-porphyrin molecular wires. *Nature Nanotechnology* **2011**, *6* (8), 517-523.

Chapter 3

Varying the Anchoring Group and Length in Terpyridine Transition Metal Based Molecular Wires

3.1 General Introduction

Charge transport through molecular junctions is one of the most important and interesting matters in molecular electronics. There are many factors that affect the conductance of molecular wires. These factors can be chemical, such as anchoring group, redox state and molecular conformation, or environmental, such as the influence of temperature and solvent environment.

3.1.1 Anchoring group

One of the important factors affecting the conductance of a molecular wire is the anchoring group as it provides a connection between the molecular bridge and the substrate. Anchoring groups play an important role in the electron transport through the molecular junction.^{53, 80} The choice of anchoring group often constitutes a challenge in the design of the molecular wire. The anchoring group determines the strength of the binding to the adjacent substrate as well as the energy and nature of the frontier orbitals. For example, when an electron-withdrawing group is attached to a π -conjugated system the energies of both frontier orbitals decrease and thereby promote electron transfer due a reduction in the difference between the electrode's Fermi level and the molecule's LUMO. Electron-donating substituents result in the frontier orbital energies being lifted and thus favouring hole transport by bringing the molecule's HOMO closer to the Fermi level.^{47b}

If the anchoring group has a high affinity for the required substrate the metal-molecule-metal junctions can self-assemble *in situ*. Thiols have been extensively studied as anchoring groups for use in molecular electronics, as they form a strong covalent bond with the gold substrate.^{21a, 46b, 81} However variability between junctions has been noted;⁸² it has been shown that the conductance of thiolated molecules are sensitive to binding geometry.^{82c, 83} This has led to investigations into how different anchoring groups conductance results compare to the thiol anchoring group.

The selection of the anchoring group is of great importance and the ideal anchoring group would exhibit reproducible well-defined binding, strong anchoring and a high conductance. Different anchoring groups possess different coupling strengths and contact geometries, which will affect the charge

transport properties of the molecular junction,⁸⁴ the exponential decay of the conductance with molecular length,^{46c} the length that a junction can be stretched.⁸⁵ The anchoring group also affects the ability to tune the current rectification⁸⁶ and modify the charge transport⁸⁷ in a junction.

Various anchoring groups other than thiolates have been shown to form successful molecular junctions including amine,⁴⁶ nitrile,⁴⁷ pyridyl,^{48 49 46b, 50} methyl sulphide,^{46c, 51} carboxylic acid^{46d, 52} and nitro.^{47b} In this study we investigate the anchoring group effect on transition metal complexes by investigating the pyridyl and methyl sulphide based anchoring group an example is shown in Figure 3.1.

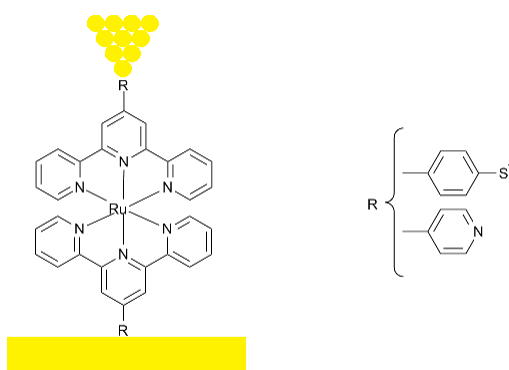


Figure 3.1: The chemical structure of the transition metal complexes to be investigated to see the variation of anchoring group vs. conductance

Li *et al.*⁵³ have investigated the conductance of a highly conjugated porphyrin template terminated with a range of anchoring groups, the molecular structure is shown in Figure 3.2.

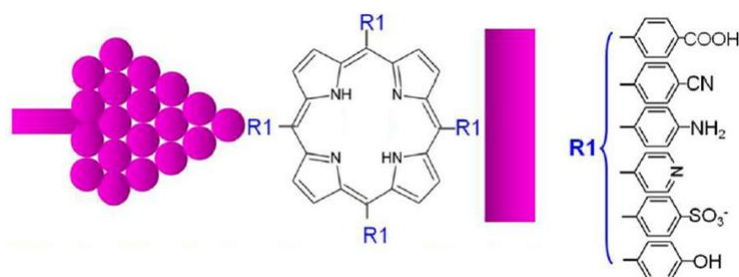


Figure 3.2: Molecular structure of the porphyrin studied by Li *et al.*⁵³ Figure adapted from reference ⁵³

They found that the conductances varied significantly with anchoring group. The conductance of the studied porphyrins followed the sequence pyridyl > amine > sulfonate > nitrile > carboxylic acid with pyridyl anchoring group having a conductance much greater than that of the carboxylic acid anchoring group as shown in Table 3.1.

Table 3.1: Summary of Single Molecule Conductance results of Porphyrins measured using the STM Break Junction method and DFT calculation results. Taken from reference 53.

Anchoring Group	Single Molecule Conductance (nS)	End-to-end length (nm)	Binding Energy (eV)
Pyridyl	(20.5 ± 3.50)	1.56	-1.1
Amine	(5.91 ± 0.40)	1.84	-0.8
Sulfonate	(5.20 ± 0.40)	2.01	-0.3
Nitrile	(4.11 ± 0.48)	2.08	-0.9
Carboxylic Acid	(2.67 ± 0.26)	1.98	-0.6

The pyridyl anchoring group exhibited the highest and broadest conductance peak out of the series. This higher recorded conductance could be due to the anchoring atom being directly part of the π -system which would explain the better anchoring group to the gold electrode. This study concluded that the conductance of a molecule is dependent on a collection of factors including the interaction between the anchoring group and the electrodes, the length of the molecule and the alignment of the LUMO level with the E_F of the electrode. The result shows a clear anchoring group effect present in the conductance measurements of highly conjugated molecular junctions. This result makes it particularly interesting to investigate the effect of anchoring group on the highly conjugated terpyridine based transition metal complexes and forming a comparison to the porphyrin molecule.

An important factor to consider, when investigating the anchoring group, is the contact geometry. The varying geometry from junction to junction can cause a large variation of conductance values and inconsistencies seen in some results. Kamenetska *et al.*⁴⁸ have investigated the conductance and geometry of pyridyl based molecular junctions. The group investigated four different molecules, all

with pyridyl anchoring groups, and found that all four pyridyl compounds exhibit two conductances, low and high, which are dependent on the contact geometry as seen in Figure 3.3.

They established that electrode separation played a key part in both conductance states with the low conductance being consistent with the molecule being bound to the apex atom on each electrode in a vertical geometry, whilst the high conductance corresponds to the electrode separation being smaller than the length of the molecule.

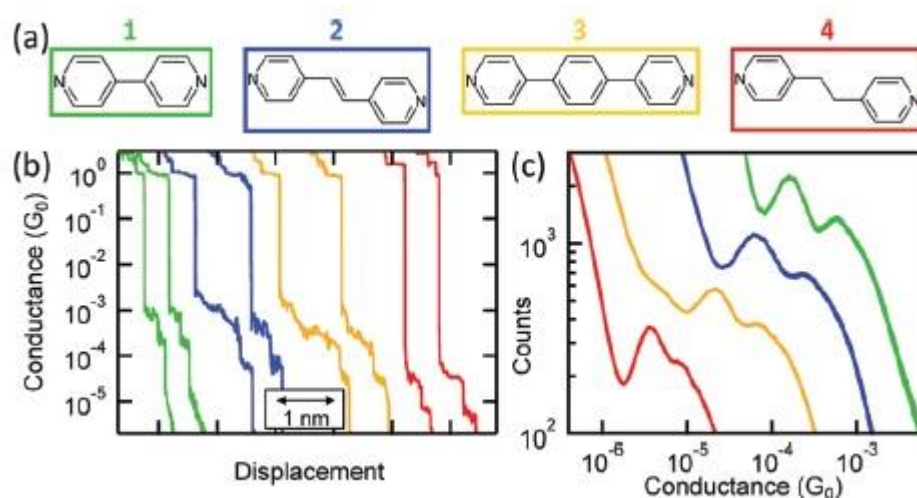


Figure 3.3: a) shows the compounds investigated in the study b) and c) show the clear presence of two conductances, high and low for each of the four compounds. Figure taken from reference 48.

DFT calculations show that the N-Au bonds in the low conductance state are aligned with the molecular backbone in a vertical geometry which results in them being perpendicular to the π -system, while the high conductance state has a geometry in which the molecule is tilted, resulting in an increased coupling between the electrode and molecular π -system.⁵⁶

Due to ease of synthesis a series of thiomethyl-substituted compounds were prepared. Methyl thioethers have been investigated to a lesser extent than pyridyl and thiol anchoring groups but have been shown to form successful contacts to gold substrate.^{46c, 51} Park *et al.*^{46c} report that the sulphur forms a donor-acceptor bond through donation of a lone pair to an uncoordinated gold atom. DFT calculations showed that the Au-SMeR bond has a binding energy of

0.6 eV. This is lower than the binding energy recorded by Quek *et al.* for Au-pyridylR which was reported to be 1.36 eV⁵⁶ but the sulfur will have a high affinity for the gold substrate so it will be interesting to investigate the effect of anchoring group for these transition metal complexes.

3.1.2 Molecular Length

Many groups have studied the effect that the length of the molecular wire has on the measured conductance. Series of molecules, for example, oligothiophenes,¹⁶ alkanes⁸⁸ and oligophenylenes⁸⁹ have been studied; the most common finding is that the conductance decays exponentially with the length of the molecule (L), described in Equation 3.1.

$$G(L) = Ae^{-\beta L} \quad \text{Equation 3.1}$$

Where the attenuation factor, β is dependent on the type of molecule, A is a prefactor that determines the order of magnitude of the conductance. Typical values of β range from 0.2-0.4 Å⁻¹ for conjugated molecules to 0.8-1.2 Å⁻¹ for aromatic compounds.⁴⁰

Attenuation factors for a variety of systems have been reported. It has been shown that the longer the molecular wire the lower the conductance.⁸⁸ Haiss *et al.* have shown an exponential decay of the conductance for alkanedithiols when the number of CH₂ groups is greater than 8 as shown below in Figure 3.4.⁸⁸ The results show less of a conductance change for alkanedithiols with a chain length less than 8 CH₂ groups.

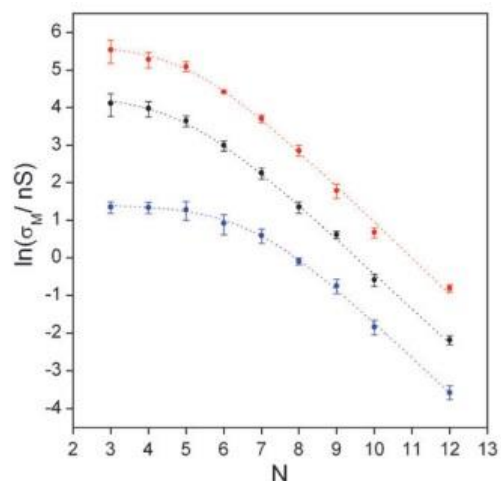


Figure 3.4: Logarithm of the low (blue), medium and high conductance group for alkanedithiols as a function of number of CH₂ groups (N) in ambient conditions and a bias of +0.6 V. Taken from reference 88.

Linear fitting for compounds with more than 8 CH₂ group showed an attenuation factor (β) of (0.89 ± 0.03) per CH₂ group for the low conductance state, (0.89 ± 0.03) per CH₂ group for the medium conductance state and (0.93 ± 0.05) per CH₂ group for the high conductance state.

Kim *et al.* have investigated the conductance for compounds that contain multiple ruthenium metal centres as shown in Figure 3.5.⁹⁰

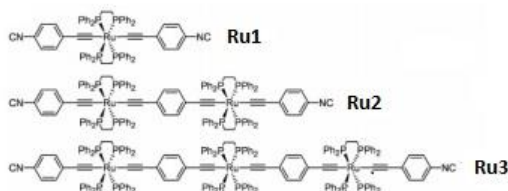


Figure 3.5: The ruthenium complexes investigated by Kim *et al.* Figure taken from reference 90.

The ruthenium complexes showed weak length dependence due to an efficient charge transport through the molecular backbone. The calculated β -factor for the series was 0.9 nm^{-1} compared to the values for conjugated organic wires which generally have values between $2\text{-}7 \text{ nm}^{-1}$.^{67c, 91} This result ignites interest in the β -factor when the ligand is changed with just one ruthenium metal centre present as shown in Figure 3.6.

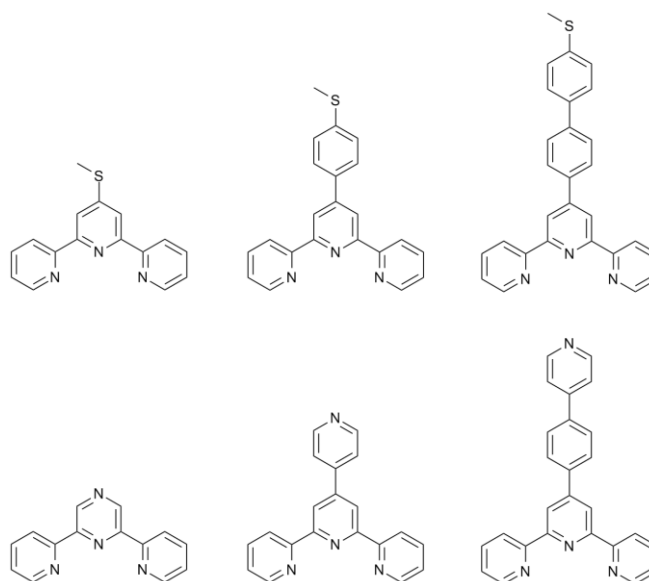


Figure 3.6: The chemical structure of the ligands investigated in this study

3.1.3 Aim

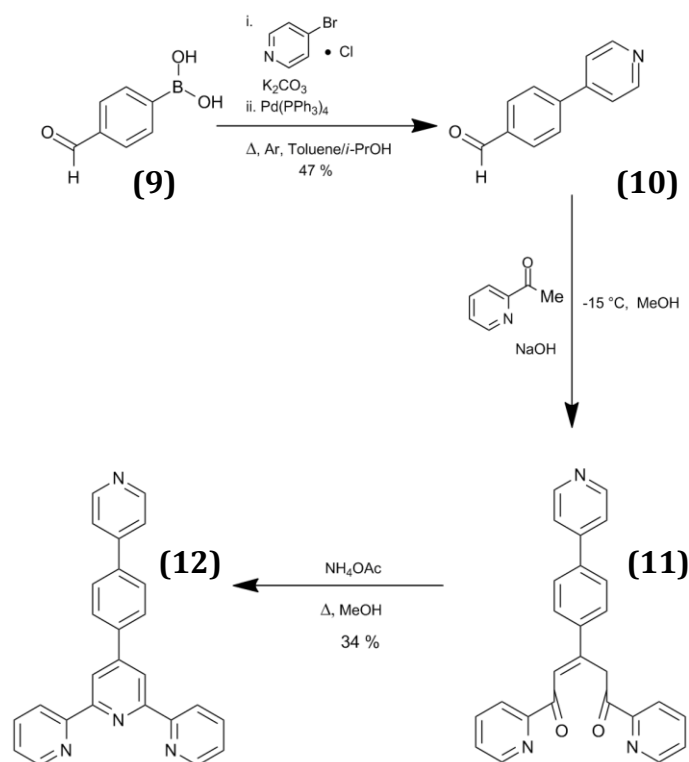
This study has two aims. Firstly, to investigate the change in anchoring group on the measured conductance. Secondly, to study the effect of varying the ligand length on the conductance for both the methyl sulphide and pyridyl anchoring groups.

3.2 Synthesis

All complexes were synthesised from commercially available starting materials apart from 2,6-di(pyridin-2-yl)pyrazine ligand and $[\text{Co}(2,6\text{-di}(\text{pyridin-2-yl})\text{pyrazine})_2](\text{BF}_4)_2$ which were used as received from the group of Professor Malcolm Halcrow at the University of Leeds, UK. $[\text{Co}(4'\text{-}(\text{pyridin-4-yl})\text{-}2,2':6',2''\text{-terpyridine})_2](\text{PF}_6)_2$ and $[\text{Ru}(4'\text{-}(\text{pyridin-4-yl})\text{-}2,2':6',2''\text{-terpyridine})_2](\text{PF}_6)_2$ were synthesised as described previously in Chapter 2.

3.3.1 Synthesis of 4'-[4-(pyridin-4-yl)phenyl]-2,2':6',2''-terpyridine (12)

The synthesis of the 4'-[4-(pyridin-4-yl)phenyl]-2,2':6',2''-terpyridine ligand was as shown in Scheme 3.1. A Suzuki coupling between 4-formylphenylboronic acid and 4-bromopyridine hydrochloride yielded 4-(pyridin-4-yl)benzaldehyde. Subsequent reaction with two equivalents of 2-acetyl pyridine gave an enedione intermediate which, after an *in situ* ring closure with ammonium acetate, afforded the target molecule in a yield of 34 %.



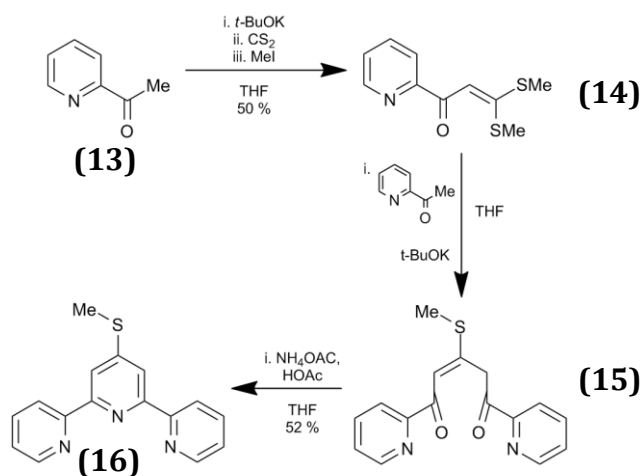
Scheme 3.1: Synthesis of 4'-[4-(pyridin-4-yl)phenyl]-2,2':6',2''-terpyridine

The literature reaction pathway was different to achieve the target molecule.⁹² Goodall *et al.* completed the synthesis of 4'-[4-(pyridin-4-yl)phenyl]-2,2':6',2''-terpyridine *via* the Suzuki coupling of 4'-(4-bromophenyl)-2,2':6',2''-terpyridine with pyridin-4-ylboronic acid in dimethoxyethane (DME) with the catalyst being Pd(PPh₃)₄, and sodium carbonate used as the base. The reported literature yield was 36 %.^{92a} The reported reaction yield was only slightly higher than the experimental yield reported here, this suggests the experimental pathway could be a suitable alternative to the literature.

3.3.2 Synthesis of 4'-(methylthio)-2,2':6',2''-terpyridine (16)

The synthesis of the 4'-(methylthio)-2,2':6',2''-terpyridine ligand shown in Scheme 3.2 was a straightforward two step literature procedure as described by Potts *et al.*⁹³ The first step was the reaction of carbon disulphide with the potassium enolate of 2-acetylpyridine followed by methyl iodide provides the intermediate 3,3-bis(methylthio)-1-(pyridin-2-yl)prop-2-en-1-one, with a yield of 50 %. Subsequent reaction with another equivalent of the potassium enolate of 2-acetyl pyridine yields an enedione intermediate which after an *in situ* ring

closure with ammonium acetate in glacial acetic acid affords the target molecule.

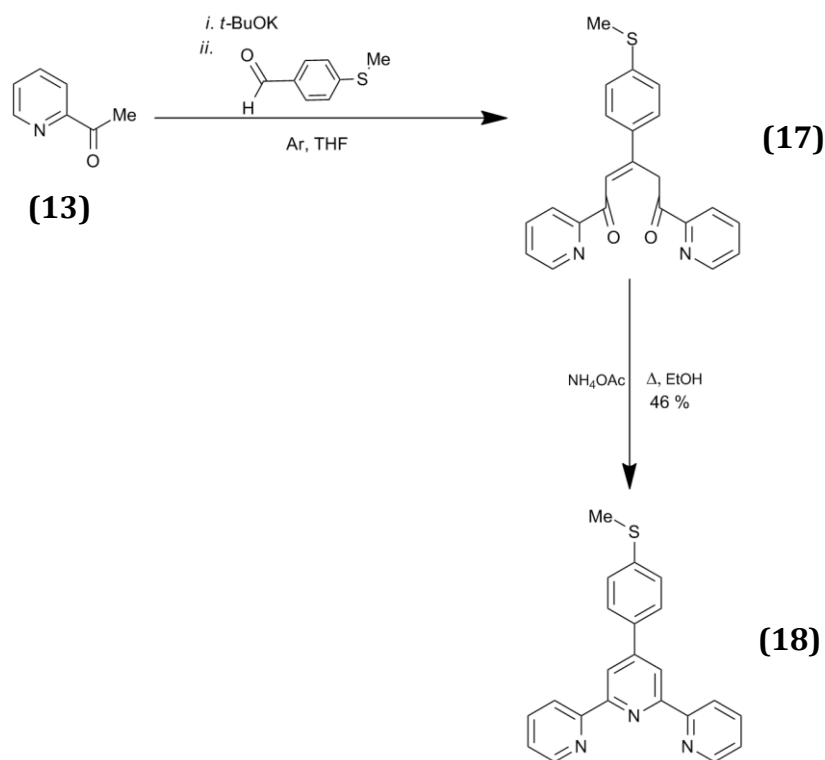


Scheme 3.2: Synthetic pathway to 4'-(methylthio)-2,2':6',2''-terpyridine

The final product was reached with a reasonable yield, 52 % compared to the literature yield of 74 % for the Potts method,⁹³ and was subsequently taken on to produce the ruthenium complex. Jameson *et al.* reported an alternative two step procedure by condensation of an *N,N*-dimethylaminoenone with 2-acetylpyridinenolate, resulting in an overall yield of 47 %.⁹⁴ Although the number of reaction steps was reduced, so was the achieved yield.

3.3.3 Synthesis of 4'-(4-(methylthio)phenyl)-2,2':6',2''-terpyridine (**18**)

The synthesis of 4'-(4-(methylthio)phenyl)-2,2':6',2''-terpyridine was completed, using commercially available compounds, following the route shown in Scheme 3.3. Reaction of 4-(methylthio)benzaldehyde with two equivalents of the potassium enolate of 2-acetylpyridine yields an enedione intermediate which followed by an *in situ* ring closure with ammonium acetate affords the target molecule.

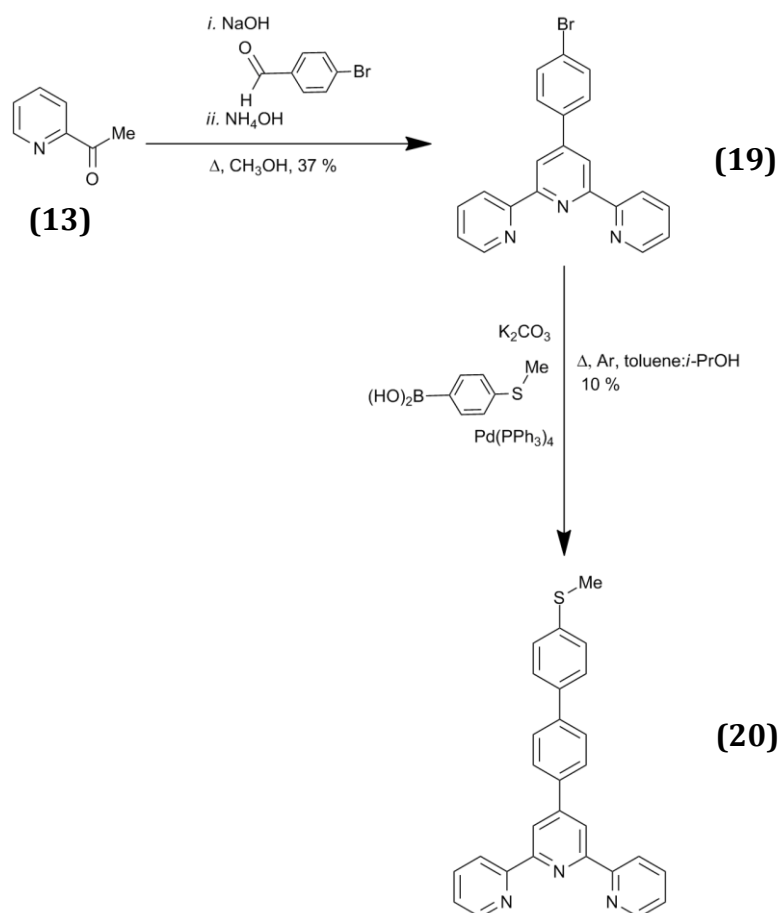


Scheme 3.3: Synthetic pathway to 4'-(4-(methylthio)phenyl)-2,2':6',2''-terpyridine

Constable *et al.* reported the synthesis of 4'-(4-(methylthio)phenyl)-2,2':6',2''-terpyridine via the reaction of 2-acetylpyridine with 4-methylthiobenzaldehyde in ethanolic KOH at room temperature, with a reported yield of 53 %.⁹⁵

3.3.4 Synthesis of 4'-(4'-(methylthio)-[1,1'-biphenyl]-4-yl)-2,2':6',2''-terpyridine (20)

The synthesis of 4'-(4'-(methylthio)-[1,1'-biphenyl]-4-yl)-2,2':6',2''-terpyridine was more protracted (Scheme 3.4). The first step was the synthesis of 4'-(4-bromophenyl)-2,2':6',2''-terpyridine following a literature procedure⁹⁶ which was achieved by the reaction of 4-bromobenzaldehyde with two equivalents of 2-acetylpyridine yields an enedione intermediate which after an *in situ* ring closure with ammonium acetate affords the 4'-(4-bromophenyl)-2,2':6',2''-terpyridine intermediate. Utilising a Suzuki coupling between the intermediate and (4-(methylthio)phenyl)boronic acid yields the target compound, in a 10 % yield.



Scheme 3.4: Synthetic pathway to 4'-(4'-(methylthio)-[1,1'-biphenyl]-4-yl)-2,2':6',2''-terpyridine

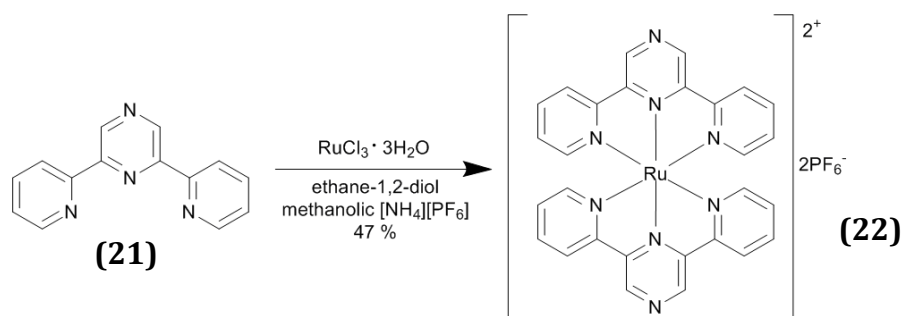
This is the first reported synthesis of 4'-(4'-(methylthio)-[1,1'-biphenyl]-4-yl)-2,2':6',2''-terpyridine to our knowledge. Although the yield is low, the extended complex allowed the investigation of the single molecule conductance of the ruthenium complex.

3.3.5 Synthesis of Ruthenium Complexes

The synthesis of the ruthenium complexes was completed by adapting literature procedures.

3.3.6 Synthesis of [Ru(2,6-di(pyridin-2-yl)pyrazine)₂](PF₆)₂ (22)

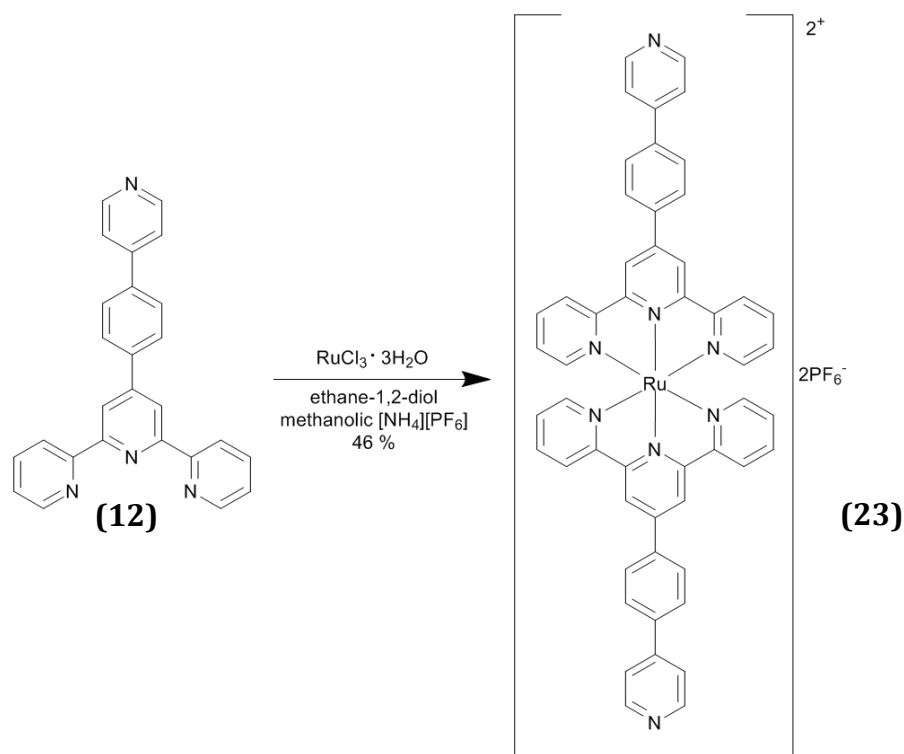
The synthesis of [Ru(2,6-di(pyridin-2-yl)pyrazine)₂](PF₆)₂ was completed by heating RuCl₃·3H₂O with two equivalents of 2,6-di(pyridin-2-yl)pyrazine to reflux in ethane-1,2-diol. Purification and counter ion exchange resulted with the title compound being recovered as a red solid in a 47 % yield, as shown in Scheme 3.5.



Scheme 3.5: Synthesis of $[\text{Ru}(2,6\text{-di}(\text{pyridin-2-yl})\text{pyrazine})_2](\text{PF}_6)_2$

3.3.7 Synthesis of $[\text{Ru}(4'\text{-}[4\text{-}(\text{pyridin-4-yl})\text{phenyl}]\text{-}2,2':6',2''\text{-terpyridine})_2](\text{PF}_6)_2$ (23)

The synthesis of $[\text{Ru}(4'\text{-}[4\text{-}(\text{pyridin-4-yl})\text{phenyl}]\text{-}2,2':6',2''\text{-terpyridine})_2](\text{PF}_6)_2$ was completed by heating $\text{RuCl}_3 \cdot 3\text{H}_2\text{O}$ with two equivalents of 4'-[4-(pyridin-4-yl)phenyl]-2,2':6',2''-terpyridine to reflux in ethane-1,2-diol. Purification and counter ion exchange resulted with the title compound being recovered as a red solid in a 46 % yield, Scheme 3.6

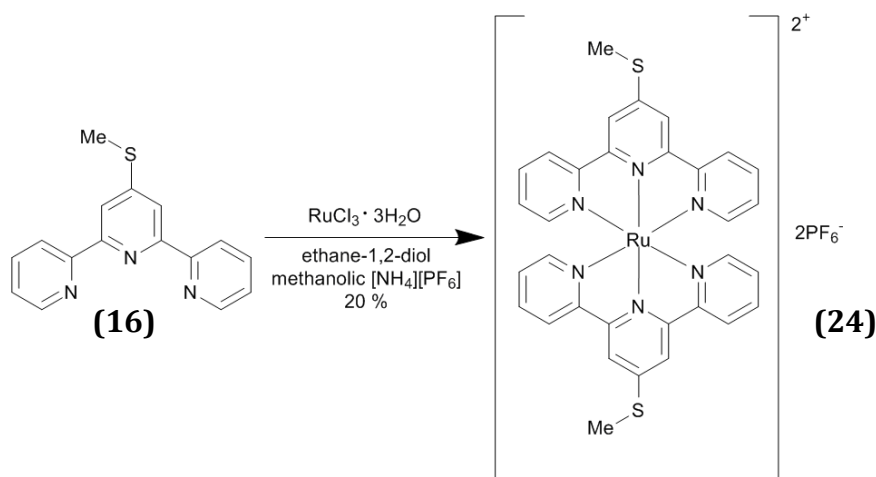


Scheme 3.6: Synthesis of $[\text{Ru}(4'\text{-}[4\text{-}(\text{pyridin-4-yl})\text{phenyl}]\text{-}2,2':6',2''\text{-terpyridine})_2](\text{PF}_6)_2$

3.3.8 Synthesis of $[\text{Ru}(4'\text{-}(\text{methylthio})\text{-}2,2':6',2''\text{-terpyridine})_2](\text{PF}_6)_2$ (24)

The synthesis of $[\text{Ru}(4'\text{-}(\text{methylthio})\text{-}2,2':6',2''\text{-terpyridine})_2](\text{PF}_6)_2$ was completed by heating $\text{RuCl}_3 \cdot 3\text{H}_2\text{O}$ with two equivalents of 4'-(methylthio)-

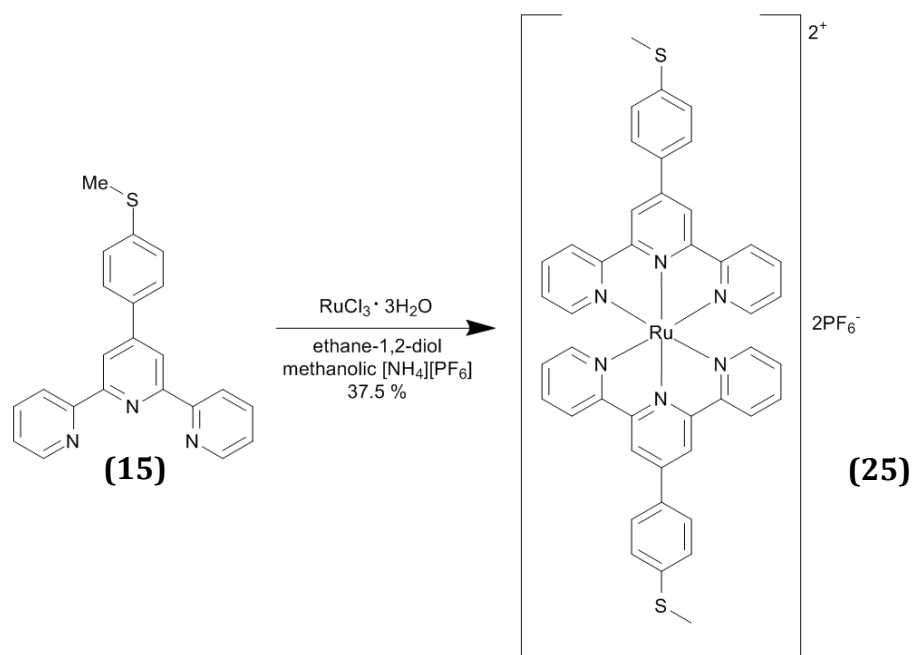
2,2':6',2''-terpyridine to reflux in ethane-1,2-diol. Purification and counter ion exchange resulted with the title compound being recovered as a red solid in a 20 % yield, as shown in Scheme 3.7.



Scheme 3.7: Synthesis of [Ru(4'-(methylthio)-2,2':6',2''-terpyridine)₂](PF₆)₂

3.3.9 Synthesis of [Ru(4'-(4-(methylthio)phenyl)-2,2':6',2''-terpyridine)₂](PF₆)₂ (25)

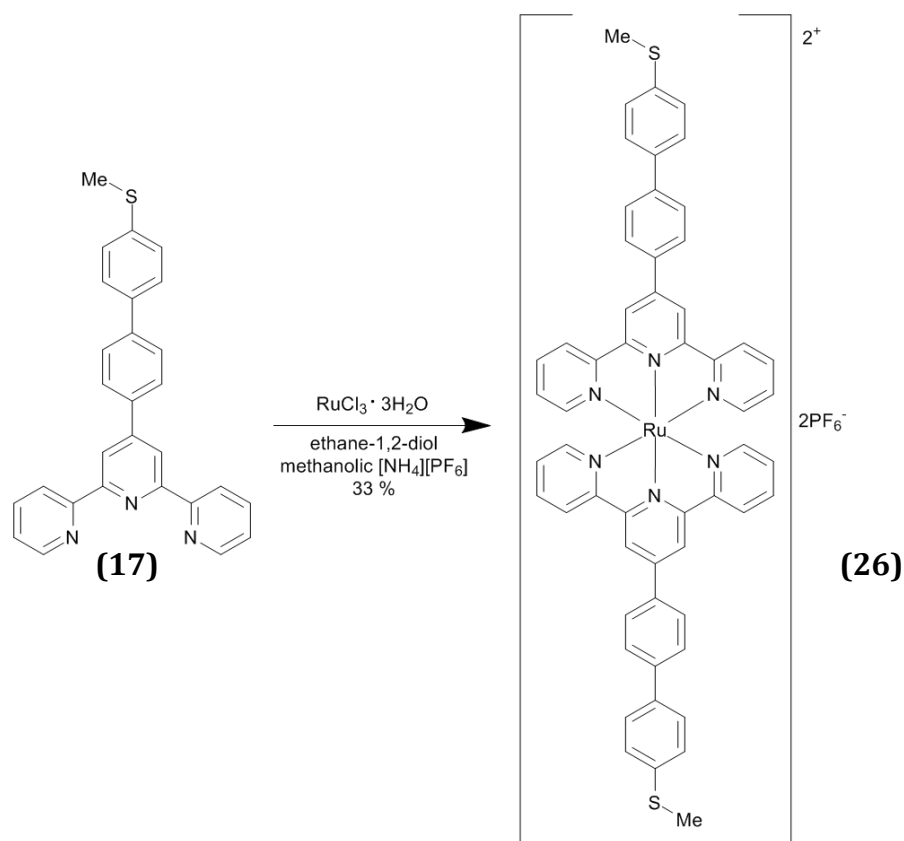
The synthesis of [Ru(4'-(4-(methylthio)phenyl)-2,2':6',2''-terpyridine)₂](PF₆)₂ was completed by heating RuCl₃·3H₂O with two equivalents of 4'-(4-(methylthio)phenyl)-2,2':6',2''-terpyridine to reflux in ethane-1,2-diol. Purification and counter ion exchange resulted with the title compound being recovered as a red solid in a 37.5 % yield, as shown in Scheme 3.8.



Scheme 3.8: $[\text{Ru}(4'-(4-(\text{methylthio})\text{phenyl})-2,2':6',2''\text{-terpyridine})_2](\text{PF}_6)_2$

3.3.10 Synthesis of $[\text{Ru}(4'-(4'-(\text{methylthio})-[1,1'\text{-biphenyl}]-4\text{-yl})-2,2':6',2''\text{-terpyridine})_2](\text{PF}_6)_2$ (26)

The synthesis of $[\text{Ru}(4'-(4'-(\text{methylthio})-[1,1'\text{-biphenyl}]-4\text{-yl})-2,2':6',2''\text{-terpyridine})_2](\text{PF}_6)_2$ was completed following Scheme 3.9. This was completed by heating $\text{RuCl}_3 \cdot 3\text{H}_2\text{O}$ with two equivalents of 4'-(4'-(methylthio)-[1,1'-biphenyl]-4-yl)-2,2':6',2''-terpyridine to reflux in ethane-1,2-diol. Purification and counter ion exchange resulted with the title compound being recovered as a red solid in a 33 % yield.



Scheme 3.9: $[\text{Ru}(4'-(4'-(\text{methylthio})-[1,1'\text{-biphenyl}]-4\text{-yl})-2,2':6',2''\text{-terpyridine})_2](\text{PF}_6)_2$

3.3 Experimental Methods

3.3.1 Sample Preparation

The samples were prepared using commercial gold on glass slides (Arrandee®) which were flame annealed using a Bunsen burner immediately prior to use. The freshly annealed slide was immersed into a 5×10^{-5} M dichloromethane solution of the appropriate complex for 1 min to allow the molecules to adsorb to the surface. The slide was then rinsed with EtOH and dried with a blast of N_2 to remove any physisorbed material. Au STM tips were prepared by cutting 0.25 mm Au wire (99.99 %, Goodfellow).

Conductance measurements were completed using an Agilent 5500 STM controller in conjunction with Agilent Picoscan 5.3.3 software. Measurements were completed in an ambient environment. The $I(s)$ method was utilised to measure the conductance with setpoint currents (I_0) of 20 or 40 nA depending on the length of the molecular wire, and a bias voltage (V_{bias}) of + 0.6 V. The tip was withdrawn 4 nm relative to the setpoint and the scan duration was 0.1 s.

The initial tip to sample distance (s_0) was approximated using the method described previously in Chapter 1 and, where appropriate, used in conjunction with the experimental break off (ΔS) to calculate the total break off (S_{total}). Approximately 500 current-distance scans that exhibited a current plateau were plotted into a histogram from which the molecular conductance was calculated.

3.4 Results

3.4.1 Conductance Results

The $I(s)$ technique was used to measure the conductance of the transition metal complexes. Approximately 5 % of the $I(s)$ scans contained a plateau characteristic of a molecule bridging the gap between the tip and the substrate. The conductance was calculated via histogram analysis using the $I(s)$ scans that contained a plateau.

3.4.1.1 Pyridyl anchoring group analogues

$[\text{Ru}(\text{2,6-di(pyridin-2-yl)pyrazine})_2](\text{PF}_6)_2$ was the first complex to be measured, using a set point of 40 nA and a bias of 0.6 V. The data are presented in Figure 3.7. The conductance was calculated using the 1D histogram (Figure 3.7 (a)) to be (6.6 ± 1.5) nS. The average experimental break off value (Figure 3.7 (c)) was calculated to be 1.0 nm and $d(\ln I)/d(s)$ was 6.5 nm^{-1} which gave a s_0 value of 1.1 nm respectively. This gives an estimated total break off distance of (2.1 ± 0.4) nm which relates to the gold separation distance calculated using Spartan[®], which was 1.36 nm for the fully extended molecule.

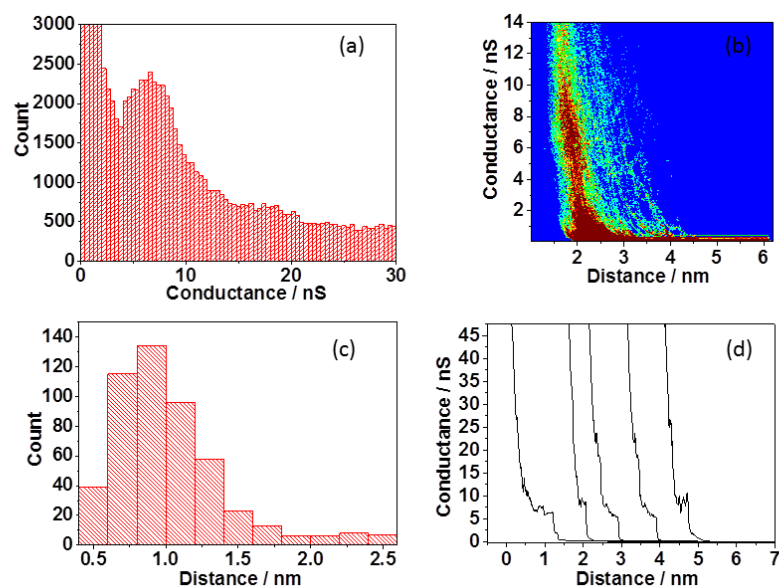


Figure 3.7: Data for [Ru(2,6-di(pyridin-2-yl)pyrazine)₂PF₆]₂ in ambient conditions $V_{bias} = 0.6$ V and $I_0 = 40$ nA (a) Histogram of 506 $I(s)$ scans (b) 2D histogram showing conductance relative to total break-off distance (c) Histogram of the experimental break-off distances (d) example $I(s)$ traces (distance is relative and does not represent actually break-off distance)

The results for [Ru(pyterpy)₂](PF₆)₂ can be seen in Figure 3.8. The conductance was measured using the same conditions as previously described, and determined to be (3.70 ± 0.54) nS using the 1D histogram in Figure 3.8(a). The average experimental break off value (Figure 3.8(c)) was calculated to be 0.85 nm and $d(\ln I)/d(s)$ was 5.99 nm^{-1} which gave a s_0 value of 1.19 nm respectively, giving an estimated total break off distance of (2.04 ± 0.27) nm. This corresponds to the distance calculated using Spartan[®], which was 2.2 nm for the fully extended molecule sandwiched between two gold atoms.

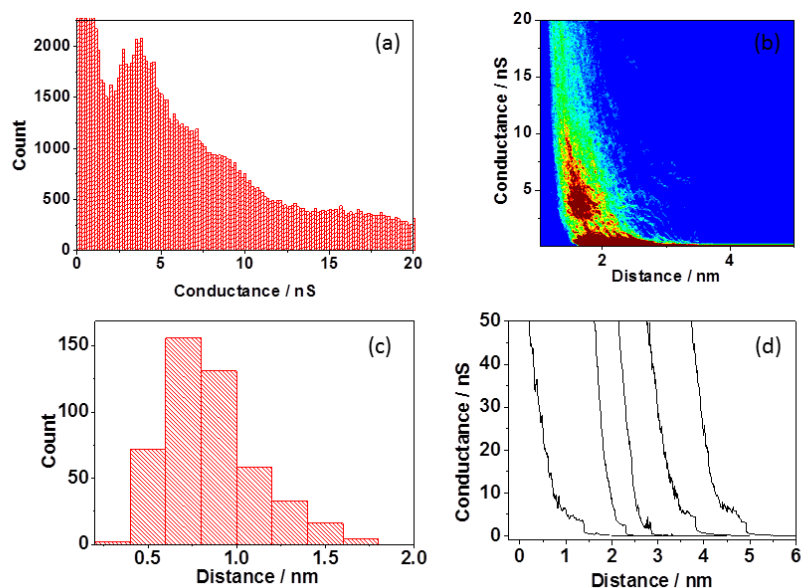


Figure 3.8: Data for [Ru(pyterpy)₂](PF₆)₂ in ambient conditions $V_{bias} = 0.6$ V and $I_0 = 40$ nA (a) Histogram of 520 $I(s)$ scans (b) 2D histogram showing conductance relative to total break-off distance (c) Histogram of the experimental break-off distances (d) example $I(s)$ traces (distance is relative and does not represent actually break-off distance)

[Ru(PPT)₂](PF₆)₂ was measured using the same conditions as previously described but with a setpoint of 20 nA to account for the longer length of the molecule; the data are presented in Figure 3.9. The conductance was calculated using the histogram in Figure 3.9(a) to be (1.05 ± 0.22) nS. The average experimental break off value (Figure 3.9(c)) was calculated to be 1.10 nm and $d(\ln I)/d(s)$ was 4.09 nm^{-1} which gave a s_0 of 1.90 nm. This gives an estimated total break off distance of (3.0 ± 0.4) nm which corresponds to the gold separation distance calculated using Spartan[®], which was 3.08 nm for the fully extended molecule.

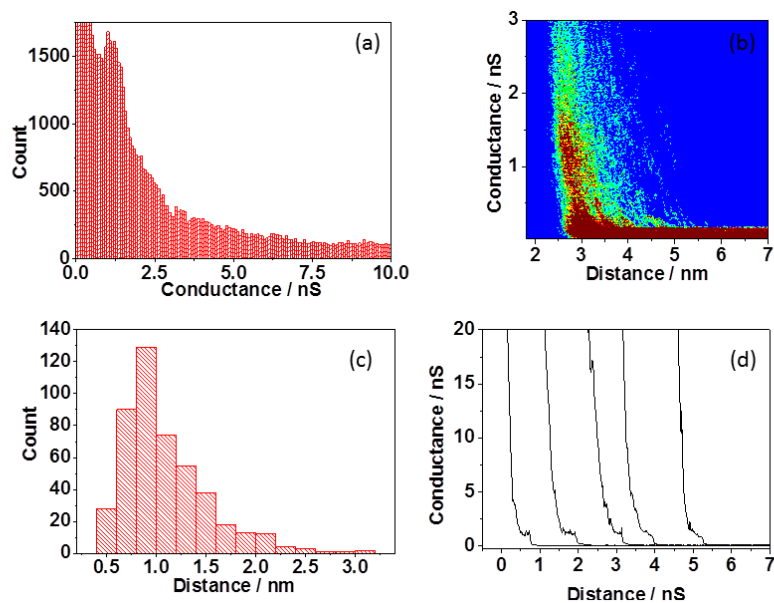


Figure 3.9: Data for $[\text{Ru}(\text{PPT})_2](\text{PF}_6)_2$ in ambient conditions $V_{\text{bias}} = 0.6 \text{ V}$ and $I_0 = 20 \text{ nA}$ (a) Histogram of 468 $I(s)$ scans (b) 2D histogram showing conductance relative to total break-off distance (c) Histogram of the experimental break-off distances (d) example $I(s)$ traces (distance is relative and does not represent actually break-off distance)

This recorded result for $[\text{Ru}(\text{PPT})_2](\text{PF}_6)_2$ is lower than that of $[\text{Ru}(\text{pyrazine})_2](\text{PF}_6)_2$ and $[\text{Ru}(\text{pyterpy})_2](\text{PF}_6)_2$. This shows for the ruthenium pyridyl series that there is a clear decrease in conductance as the length of molecule increases as shown in Figure 3.10.

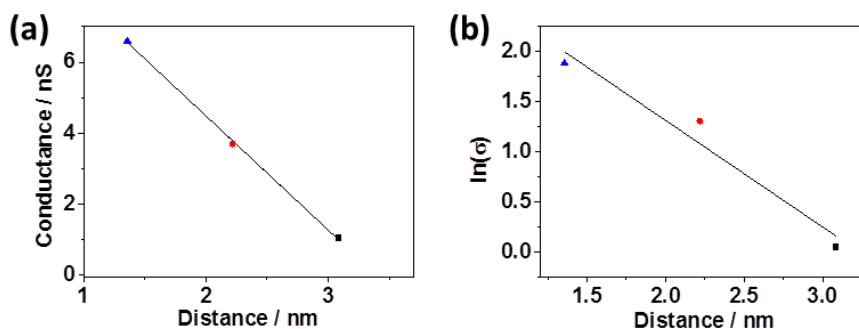


Figure 3.10: (a) Plot of the conductance vs. distance (Au-Molecule-Au) of the ruthenium pyridyl series. (b) Plot of the $\ln(\sigma)$ vs. distance (Au-Molecule-Au) of the ruthenium pyridyl series. Where blue triangle is $[\text{Ru}(\text{pyrazine})_2](\text{PF}_6)_2$, red circle is $[\text{Ru}(\text{pyterpy})_2](\text{PF}_6)_2$ and black square is $[\text{Ru}(\text{PPT})_2](\text{PF}_6)_2$.

The attenuation factor was determined by initially calculating the separation between two gold atoms for each molecule using Spartan[®] in the extended conformation and energy minimised. A plot of $\ln(\text{conductance})$ vs. distance was

then produced (Figure 3.10(b)). Linear regression was used to calculate the slope and therefore the attenuation factor. The attenuation factor for the ruthenium pyridyl series was calculated using Figure 3.10 to be 1.06 nm^{-1} . This result is comparable to the one recorded by Kim *et al.* for a series with multiple metal centres.⁹⁰

The next complexes investigated were the cobalt (II) pyridyl analogues. This would enable it to be seen if changing the metal centre has an effect on the conductance result.

The first complex measured was $[\text{Co}(2,6\text{-di}(\text{pyridin-2-yl})\text{pyrazine})_2](\text{BF}_4)_2$. The complex was measured in ambient conditions with a setpoint of 40 nA and a bias of 0.6 V; the data are presented in Figure 3.11. The conductance was calculated using the 1D histogram (Figure 3.11(a)) to be $(7.05 \pm 1.34) \text{ nS}$. The average experimental break off value (Figure 3.11(c)) was calculated to be 1.35 nm and $d(\ln I)/d(s)$ was 3.71 nm^{-1} which gave a s_0 value of 0.9 nm respectively. This gives an estimated total break off distance of $(2.25 \pm 0.4) \text{ nm}$ which corresponds to the gold separation distance calculated using Spartan[®], which was 1.35 nm for the fully extended molecule. This recorded result is within experimental error of the result recorded for $[\text{Ru}(2,6\text{-di}(\text{pyridin-2-yl})\text{pyrazine})_2](\text{PF}_6)_2$.

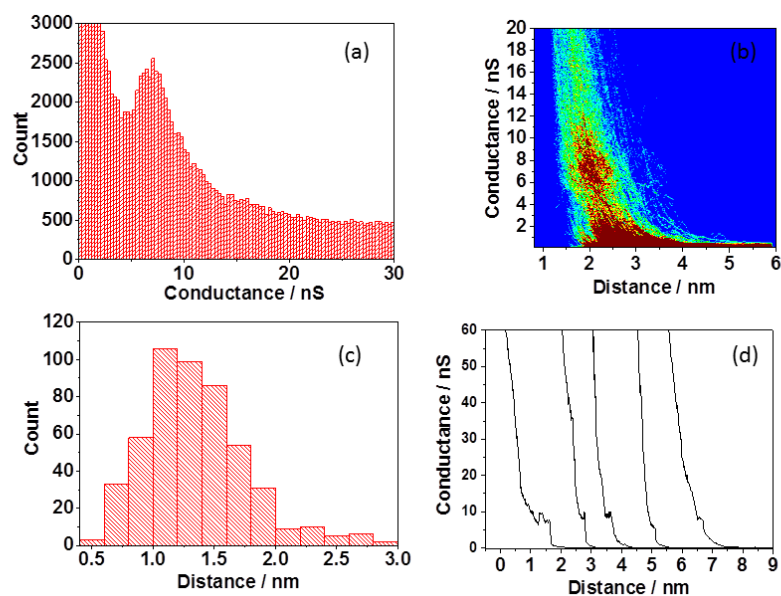


Figure 3.11: Data for [Co(2,6-di(pyridin-2-yl)pyrazine)₂](BF₄)₂ in ambient conditions $V_{bias} = 0.6$ V and $I_0 = 40$ nA (a) Histogram of 502 $I(s)$ scans (b) 2D histogram showing conductance relative to total break-off distance (c) Histogram of the experimental break-off distances (d) example $I(s)$ traces (distance is relative and does not represent actually break-off distance)

The next molecule to be measured was [Co(pyterpy)₂](PF₆)₂. The complex was measured using the conditions described previously, the data are presented in Figure 3.12. The conductance was calculated to be (3.54 ± 1.1) nS. The average experimental break off value was 0.83 nm (Figure 3.12(c)) and the calculated $d(\ln I)/d(s)$ value was 6.25 nm^{-1} which led to s_0 being 1.12 nm. This gives a total break off distance of (1.95 ± 0.25) nm which was compared to the gold separation distance calculated using Spartan[®], which was 2.2 nm for the fully extended molecule.

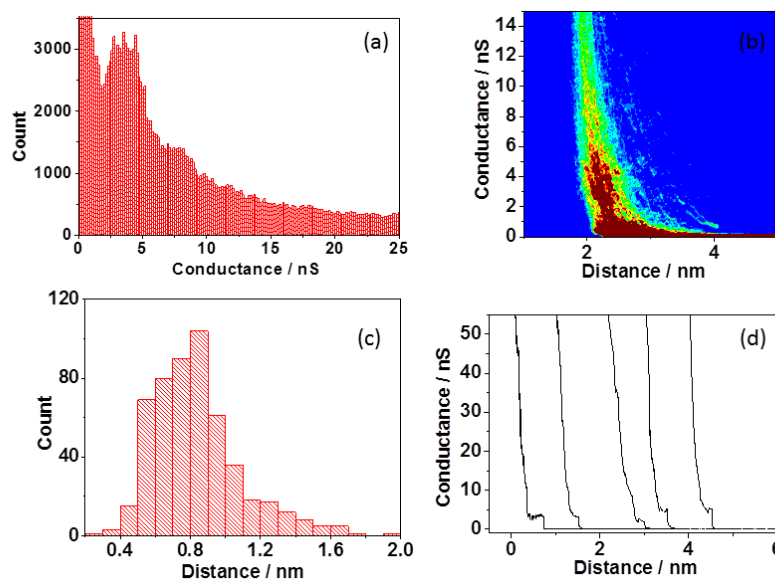


Figure 3.12: Data for $[\text{Co}(\text{pyterpy})_2](\text{PF}_6)_2$ in ambient conditions $V_{\text{bias}} = 0.6 \text{ V}$ and $I_0 = 40 \text{ nA}$ (a) Histogram of 508 $I(s)$ scans (b) 2D histogram showing conductance relative to total break-off distance (c) Histogram of the experimental break-off distances (d) example $I(s)$ traces (distance is relative and does not represent actually break-off distance)

As discussed in Chapter 2 the conductance of the $[\text{Co}(\text{pyterpy})_2](\text{PF}_6)_2$ complex is similar to that of the $[\text{Ru}(\text{pyterpy})_2](\text{PF}_6)_2$ complex. It can clearly be seen that the conductance once again decreases linearly with length (Figure 3.13(a)). When compared to the ruthenium pyridyl complexes it can be seen that a similar decrease in conductance is followed (Figure 3.13(a) although not enough points are present for the $[\text{Co}(\text{pyterpy})_2](\text{PF}_6)_2$ complex to calculate an accurate β -value.

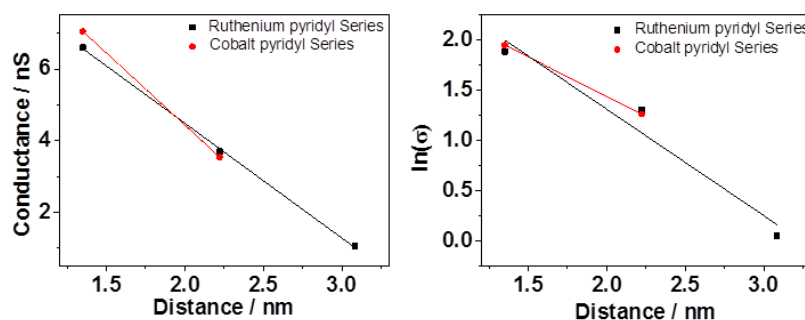


Figure 3.13: (a) Plot showing conductance vs. distance for the cobalt series. (b) plot of $\ln(\text{conductance})$ vs. distance for both the cobalt and ruthenium series.

3.4.1.2 Methyl Sulphide Anchoring Group Analogues.

$[\text{Ru}(\text{TT})_2](\text{PF}_6)_2$ was measured in ambient conditions with a set point of 40 nA and a bias of 0.6 V. the data are presented in Figure 3.14. The conductance was

calculated to be (7.35 ± 1.78) nS. The average experimental break off value was calculated to be 1.5 nm, $d(\ln I)/d(s)$ was 7.08 nm^{-1} which gave a s_0 value of 1.0 nm. This gives an estimated total break off distance of (2.5 ± 0.5) nm which corresponds to the gold separation distance calculated using Spartan[®], which was 1.55 nm for the fully extended molecule.

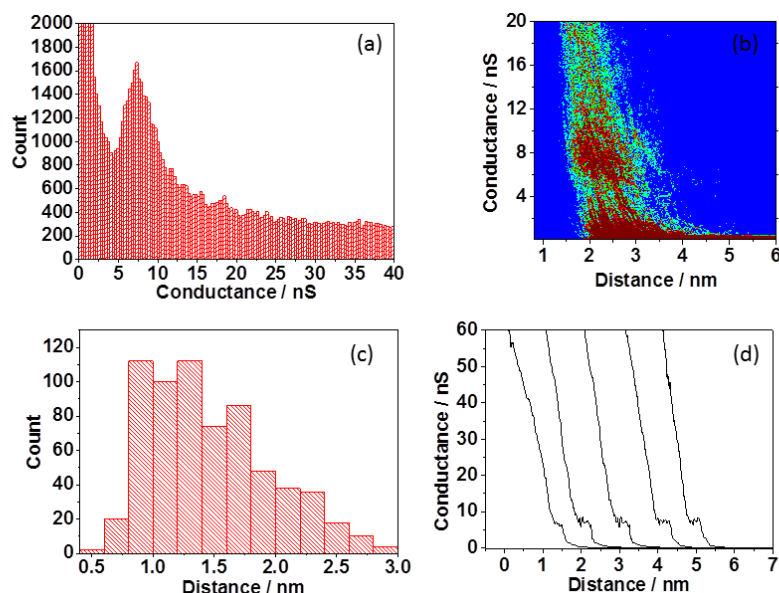


Figure 3.14: Data for $[\text{Ru}(\text{TT})_2](\text{PF}_6)_2$ in ambient conditions $V_{\text{bias}} = 0.6 \text{ V}$ and $I_0 = 40 \text{ nA}$ (a) Histogram of 542 $I(s)$ scans (b) 2D histogram showing conductance relative to total break-off distance (c) Histogram of the experimental break-off distances (d) example $I(s)$ traces (distance is relative and does not represent actually break-off distance)

The same conditions were used to measure the conductance of $[\text{Ru}(\text{TPT})_2](\text{PF}_6)_2$ the data are presented in Figure 3.15. The conductance was calculated to be (4.03 ± 1.48) nS. The average experimental break off value was 1.2 nm and $d(\ln I)/d(s)$ was 6.99 nm^{-1} so s_0 was calculated 1.0 nm respectively. This gives an estimated total break off distance of (2.2 ± 0.4) nm which corresponds to the gold separation distance calculated using Spartan[®], which was 2.39 nm for the molecule.

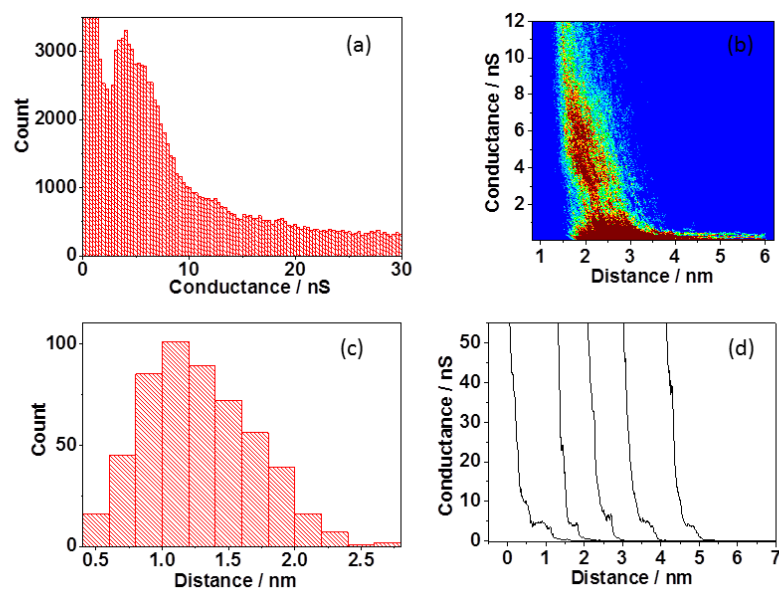


Figure 3.15: Data for $[\text{Ru}(\text{TPT})_2](\text{PF}_6)_2$ in ambient conditions $V_{\text{bias}} = 0.6$ and $I_0 = 40$ nA (a) Histogram of 528 $I(s)$ scans (b) 2D histogram showing conductance relative to total break-off distance (c) Histogram of the experimental break-off distances (d) example $I(s)$ traces (distance is relative and does not represent actually break-off distance)

The conductance recorded for the methyl sulphide complex was slightly higher than that of the pyridyl head group. This could be due to the sulphur forming a strong bond with the gold substrate. It was then interesting to see if this increase continued for molecules of different length.

The final molecule to be measured was $[\text{Ru}(\text{TPPT})_2](\text{PF}_6)_2$. It was measured in the same conditions as previously described but with a set point of 20 nA to account for the longer length of the molecule, the data are presented in Figure 3.16. The conductance was calculated to be (1.14 ± 0.40) nS. The average experimental break off value was 1.0 nm, $d(\ln I)/d(s)$ was 3.59 nm^{-1} and s_0 was calculated to be 2.2 nm. This gives an estimated total break off distance of (3.2 ± 0.3) nm which corresponds to the gold separation distance calculated using Spartan[®], which was 3.27 nm.

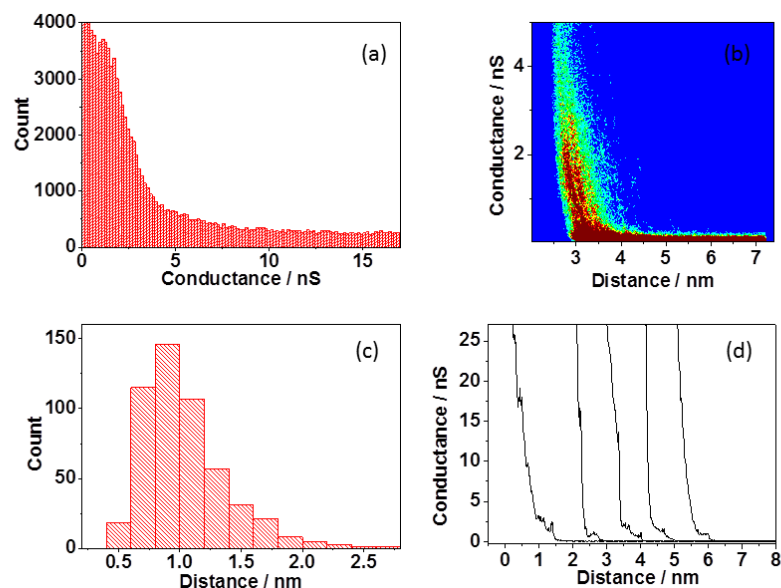


Figure 3.16: Data for $[\text{Ru}(\text{TPPT})_2](\text{PF}_6)_2$ in ambient conditions $V_{\text{bias}} = 0.6 \text{ V}$ and $I_0 = 20 \text{ nA}$ (a) Histogram of 550 $I(s)$ scans (b) 2D histogram showing conductance relative to total break-off distance (c) Histogram of the experimental break-off distances (d) example $I(s)$ traces (distance is relative and does not represent actually break-off distance)

The conductance results show a lower conductance for the longer methyl sulphide complex than the shorter analogues. This result confirms again for the methyl sulphide series that as the length of the molecule is increased the conductance decreases, the data are presented in Figure 3.17.

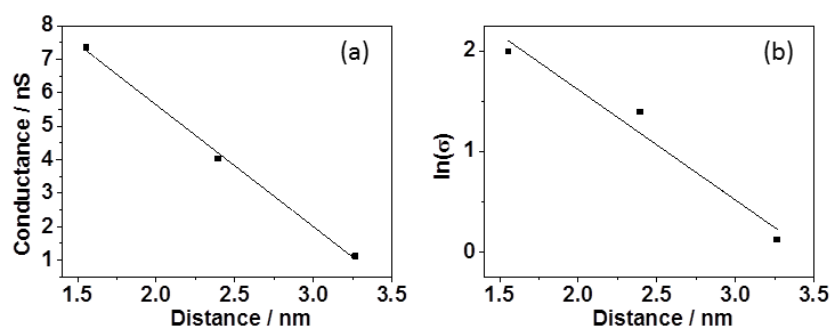


Figure 3.17: (a) plot of conductance vs. distance for the methyl sulphide series. (b) plot of $\ln(\sigma)$ vs. distance for the methyl sulphide series.

The attenuation factor for the methyl sulphide series was calculated to using Figure 3.17(b) to be 1.09 nm^{-1} . This is comparable to the value calculated for the ruthenium pyridyl complexes, the data can be seen in Figure 3.18.

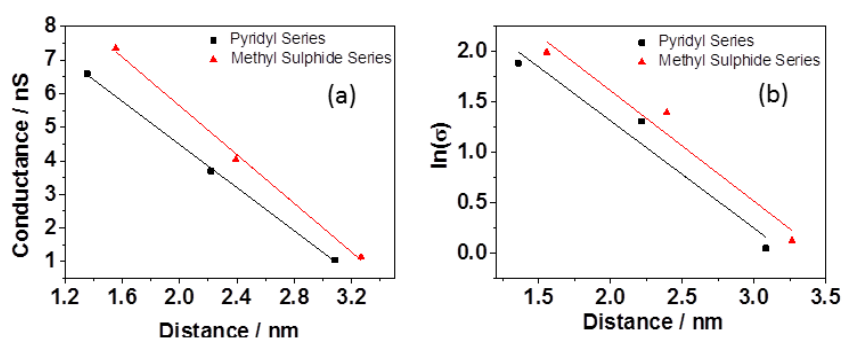


Figure 3.18: (a) Plot of conductance vs. distance for both ruthenium pyridyl and methyl sulphide series. (b) plot of $\ln(\sigma)$ vs. distance for the two series.

Both series show a clear decrease in conductance as the length of the molecule increases and exhibit similar β -values (Figure 3.18).

3.5 Discussion

All of the collected conductance, break-off data and calculated attenuation factors are presented in Table 3.2.

Table 3.2: Estimate of the total break-off distance for all the measured complexes compared to the length of the molecule sandwiched between two gold electrodes.

Complex	Conductance / nS	Au-Au separation calculated in Spartan® / nm	Break-off distance / nm	Attenuation Factor β / nm ⁻¹	
				nm ⁻¹	Å ⁻¹
[Ru(2,6-di(pyridin-2-yl)pyrazine) ₂](PF ₆) ₂	(6.60 ± 1.5)	1.36	(2.10 ± 0.4)	1.06	0.106
[Ru(pyterpy) ₂](PF ₆) ₂	(3.70 ± 0.54)	2.22	(2.20 ± 0.3)		
[Ru(PPT) ₂](PF ₆) ₂	(1.05 ± 0.22)	3.08	(3.00 ± 0.4)		
[Co(2,6-di(pyridin-2-yl)pyrazine) ₂](BF ₄) ₂	(7.05 ± 1.34)	1.35	(2.30 ± 0.4)	n/a	
[Co(pyterpy) ₂](PF ₆) ₂	(3.54 ± 1.1)	2.22	(1.95 ± 0.25)	n/a	
[Ru(TT) ₂](PF ₆) ₂	(7.35 ± 1.78)	1.55	(2.50 ± 0.5)	1.09	0.109
[Ru(TPT) ₂](PF ₆) ₂	(4.03 ± 1.48)	2.39	(2.20 ± 0.4)		
[Ru(TPPT) ₂](PF ₆) ₂	(1.14 ± 0.40)	3.27	(3.20 ± 0.3)		

The total break-off distances generally correspond well to the Au-Au distance calculated in Spartan® and provide further evidence that successful molecular junctions are being formed. The conductance values for the methyl sulphide series are increased than the pyridyl series, this change in conductance was expected due to the pyridyl anchoring group being LUMO driven and the thioether anchoring group being HOMO orientated. However, both series follow a distinct pattern in their conductance results. This suggests that changing the anchoring group will have an effect on the conductance but when the length of the molecule is increased the conductance will follow a set pattern.

The attenuation factors for the two series, pyridyl and thioether are close in value, $\beta = 0.106$ and 0.109 \AA^{-1} respectively. The series shows a shallow length dependence of the conductance. The calculated attenuation factors for the two series correspond to the attenuation factor for conjugated systems. The similar attenuation factor suggests that changing the anchoring group as well as the length does not have an effect on the attenuation factor for transition metal complexes. The low attenuation factor is usually characteristic of a hopping charge transport regime further investigations into the temperature dependence of the series would allow this to be explored.

Sedghi *et al.* presented an attenuation factor of $\beta = 0.04 \text{ \AA}^{-1}$ for pyridyl terminated oligo-porphyrins.^{79b} This is evidenced by the shallow length dependence of the conductance. This behaviour was also seen in analogous compounds, however, with a thiol end group and an attenuation factor of $\beta = 0.04 \text{ \AA}^{-1}$. This reported result provides evidence that the attenuation factor does not change with anchoring group which agrees with the experimental results for the terpyridine based complexes studied here. The reported attenuation factor for the pyridyl and thioether terpyridine series is higher than the attenuation factors reported for the porphyrin system however the porphyrins studied have multiple metal centres, yet the terpyridine transition metal complexes only have one centre. This could be further explored by investigating multiple metal centred transition metal complexes and provide a direct comparison.

This result is also comparable to the one recorded by Kim *et al.* for a series with multiple ruthenium metal centres (Figure 3.5) which was found to have a attenuation factor of 0.9 nm^{-1} .⁹⁰ Once again, it would be of interest to study multiple transition metal terpyridine based complexes to see if that has an effect on the attenuation factor.

3.6 Conclusion and Future Work

The conductance data in this study presented two low attenuation factors for the pyridyl and thioether series; the values found to be 0.106 and 0.109 \AA^{-1} respectively. This suggests a hopping mediated charge transport in these systems. To further investigate a temperature dependence study could be completed. A series of multiple transition metal centred terpyridine based complexes could also be investigated to see how the attenuation factor is affected by the addition of further transition metal centres.

The conductance of different anchoring groups was investigated with an evident change in conductance between the two anchoring groups. For both the methyl sulphide and pyridyl series length dependence is observed with a β -factor calculated for the methyl sulphide series and pyridyl series. Future work would be to complete the cobalt series, investigate different anchoring groups, different environments.

3.7 References

1. Basch, H.; Cohen, R.; Ratner, M. A., Interface Geometry and Molecular Junction Conductance: Geometric Fluctuation and Stochastic Switching. *Nano Letters* **2005**, *5* (9), 1668-1675; Beebe, J. M.; Engelkes, V. B.; Miller, L. L.; Frisbie, C. D., Contact Resistance in Metal–Molecule–Metal Junctions Based on Aliphatic SAMs: Effects of Surface Linker and Metal Work Function. *Journal of the American Chemical Society* **2002**, *124* (38), 11268-11269.
2. Li, Z.; Smeu, M.; Ratner, M. A.; Borguet, E., Effect of Anchoring Groups on Single Molecule Charge Transport through Porphyrins. *The Journal of Physical Chemistry C* **2013**, *117* (29), 14890-14898.
3. Zotti, L. A.; Kirchner, T.; Cuevas, J. C.; Pauly, F.; Huhn, T.; Scheer, E.; Erbe, A., Revealing the Role of Anchoring Groups in the Electrical Conduction Through Single-Molecule Junctions. *Small* **2010**, *6* (14), 1529-1535.
4. Dulić, D.; Pump, F.; Campidelli, S.; Lavie, P.; Cuniberti, G.; Filoramo, A., Controlled Stability of Molecular Junctions. *Angewandte Chemie* **2009**, *121* (44), 8423-8426; Lörtscher, E.; Cho, C. J.; Mayor, M.; Tschudy, M.; Rettner, C.; Riel, H., Influence of the Anchor Group on Charge Transport through Single-Molecule Junctions. *ChemPhysChem* **2011**, *12* (9), 1677-1682; Ke, S.-H.; Baranger, H. U.; Yang, W., Molecular Conductance: Chemical Trends of Anchoring Groups. *Journal of the American Chemical Society* **2004**, *126* (48), 15897-15904; Ulman, A., Formation and structure of self-assembled monolayers. *Chemical reviews* **1996**, *96* (4), 1533-1554.
5. Hong, W.; Manrique, D. Z.; Moreno-García, P.; Gulcur, M.; Mishchenko, A.; Lambert, C. J.; Bryce, M. R.; Wandlowski, T., Single Molecular Conductance of Tolanes: Experimental and Theoretical Study on the Junction Evolution Dependent on the Anchoring Group. *Journal of the American Chemical Society* **2011**, *134* (4), 2292-2304.
6. Ulrich, J.; Esrail, D.; Pontius, W.; Venkataraman, L.; Millar, D.; Doerr, L. H., Variability of Conductance in Molecular Junctions. *The Journal of Physical Chemistry B* **2006**, *110* (6), 2462-2466; Li, X.; He, J.; Hihath, J.; Xu, B.; Lindsay, S. M.; Tao, N., Conductance of Single Alkanedithiols: Conduction Mechanism and Effect of Molecule–Electrode Contacts. *Journal of the American Chemical Society* **2006**, *128* (6), 2135-2141.
7. Li, C.; Pobelov, I.; Wandlowski, T.; Bagrets, A.; Arnold, A.; Evers, F., Charge Transport in Single Au | Alkanedithiol | Au Junctions: Coordination Geometries and Conformational Degrees of Freedom. *Journal of the American Chemical Society* **2007**, *130* (1), 318-326.
8. Lee, M. H.; Speyer, G.; Sankey, O. F., Electron transport through single alkane molecules with different contact geometries on gold. *Physica Status Solidi (b)* **2006**, *243* (9), 2021-2029; Müller, K. H., Effect of the atomic configuration of gold electrodes on the electrical conduction of alkanedithiol molecules. *Physical Review B* **2006**, *73* (4), 045403.
9. Kaliginedi, V.; Rudnev, A. V.; Moreno-García, P.; Baghernejad, M.; Huang, C.; Hong, W.; Wandlowski, T., Promising anchoring groups for single-molecule conductance measurements. *Physical Chemistry Chemical Physics* **2014**, *16* (43), 23529-23539.
10. Park, Y. S.; Whalley, A. C.; Kamenetska, M.; Steigerwald, M. L.; Hybertsen, M. S.; Nuckolls, C.; Venkataraman, L., Contact Chemistry and Single-Molecule

Conductance: A Comparison of Phosphines, Methyl Sulfides, and Amines. *Journal of the American Chemical Society* **2007**, *129* (51), 15768-15769.

11. Kamenetska, M.; Koentopp, M.; Whalley, A.; Park, Y.; Steigerwald, M.; Nuckolls, C.; Hybertsen, M.; Venkataraman, L., Formation and evolution of single-molecule junctions. *Physical Review Letters* **2009**, *102* (12), 126803.

12. Kushmerick, J. G.; Whitaker, C. M.; Pollack, S. K.; Schull, T. L.; Shashidhar, R., Tuning current rectification across molecular junctions. *Nanotechnology* **2004**, *15* (7), S489.

13. Danilov, A.; Kubatkin, S.; Kafanov, S.; Hedegård, P.; Stuhr-Hansen, N.; Moth-Poulsen, K.; Bjørnholm, T., Electronic transport in single molecule junctions: Control of the molecule-electrode coupling through intramolecular tunneling barriers. *Nano letters* **2008**, *8* (1), 1-5.

14. Arroyo, C. R.; Leary, E.; Castellanos-Gómez, A.; Rubio-Bollinger, G.; González, M. T.; Agraït, N., Influence of Binding Groups on Molecular Junction Formation. *Journal of the American Chemical Society* **2011**, *133* (36), 14313-14319; Venkataraman, L.; Klare, J. E.; Nuckolls, C.; Hybertsen, M. S.; Steigerwald, M. L., Dependence of single-molecule junction conductance on molecular conformation. *Nature* **2006**, *442* (7105), 904-907.

15. Chen, F.; Li, X.; Hihath, J.; Huang, Z.; Tao, N., Effect of Anchoring Groups on Single-Molecule Conductance: Comparative Study of Thiol-, Amine-, and Carboxylic-Acid-Terminated Molecules. *Journal of the American Chemical Society* **2006**, *128* (49), 15874-15881.

16. Mishchenko, A.; Zotti, L. A.; Vonlanthen, D.; Bürkle, M.; Pauly, F.; Cuevas, J. C.; Mayor, M.; Wandlowski, T., Single-Molecule Junctions Based on Nitrile-Terminated Biphenyls: A Promising New Anchoring Group. *Journal of the American Chemical Society* **2010**, *133* (2), 184-187.

17. Kamenetska, M.; Quek, S. Y.; Whalley, A. C.; Steigerwald, M. L.; Choi, H. J.; Louie, S. G.; Nuckolls, C.; Hybertsen, M. S.; Neaton, J. B.; Venkataraman, L., Conductance and Geometry of Pyridine-Linked Single-Molecule Junctions. *Journal of the American Chemical Society* **2010**, *132* (19), 6817-6821.

18. Tam, E. S.; Parks, J. J.; Shum, W. W.; Zhong, Y.-W.; Santiago-Berríos, M. E. B.; Zheng, X.; Yang, W.; Chan, G. K. L.; Abruña, H. D.; Ralph, D. C., Single-Molecule Conductance of Pyridine-Terminated Dithienylethene Switch Molecules. *ACS Nano* **2011**, *5* (6), 5115-5123.

19. Xu, B.; Xiao, X.; Tao, N. J., Measurements of Single-Molecule Electromechanical Properties. *Journal of the American Chemical Society* **2003**, *125* (52), 16164-16165.

20. Capozzi, B.; Dell, E. J.; Berkelbach, T. C.; Reichman, D. R.; Venkataraman, L.; Campos, L. M., Length-Dependent Conductance of Oligothiophenes. *Journal of the American Chemical Society* **2014**, *136* (29), 10486-10492; Dell, E. J.; Capozzi, B.; DuBay, K. H.; Berkelbach, T. C.; Moreno, J. R.; Reichman, D. R.; Venkataraman, L.; Campos, L. M., Impact of Molecular Symmetry on Single-Molecule Conductance. *Journal of the American Chemical Society* **2013**, *135* (32), 11724-11727.

21. Martín, S.; Haiss, W.; Higgins, S.; Cea, P.; López, M. C.; Nichols, R. J., A Comprehensive Study of the Single Molecule Conductance of α,ω -Dicarboxylic Acid-Terminated Alkanes. *The Journal of Physical Chemistry C* **2008**, *112* (10), 3941-3948.

22. Quek, S. Y.; Kamenetska, M.; Steigerwald, M. L.; Choi, H. J.; Louie, S. G.; Hybertsen, M. S.; Neaton, J. B.; VenkataramanLatha, Mechanically controlled binary conductance switching of a single-molecule junction. *Nat Nano* **2009**, *4* (4), 230-234.
23. Leary, E.; Höbenreich, H.; Higgins, S. J.; Van Zalinge, H.; Haiss, W.; Nichols, R. J.; Finch, C.; Grace, I.; Lambert, C.; McGrath, R., Single-molecule solvation-shell sensing. *Physical Review Letters* **2009**, *102* (8), 086801.
24. Haiss, W.; Martin, S.; Scullion, L. E.; Bouffier, L.; Higgins, S. J.; Nichols, R. J., Anomalous length and voltage dependence of single molecule conductance. *Physical Chemistry Chemical Physics* **2009**, *11* (46), 10831-10838.
25. Quek, S. Y.; Choi, H. J.; Louie, S. G.; Neaton, J. B., Length Dependence of Conductance in Aromatic Single-Molecule Junctions. *Nano Letters* **2009**, *9* (11), 3949-3953.
26. Scheer, E., *Molecular electronics: an introduction to theory and experiment*. World Scientific: 2010; Vol. 1.
27. Kim; Beebe, J. M.; Olivier, C.; Rigaut, S.; Touchard, D.; Kushmerick, J. G.; Zhu, X. Y.; Frisbie, C. D., Temperature and Length Dependence of Charge Transport in Redox-Active Molecular Wires Incorporating Ruthenium(II) Bis(σ -arylacetylde) Complexes. *The Journal of Physical Chemistry C* **2007**, *111* (20), 7521-7526.
28. He, J.; Chen, F.; Li, J.; Sankey, O. F.; Terazono, Y.; Herrero, C.; Gust, D.; Moore, T. A.; Moore, A. L.; Lindsay, S. M., Electronic Decay Constant of Carotenoid Polyenes from Single-Molecule Measurements. *Journal of the American Chemical Society* **2005**, *127* (5), 1384-1385; Kim; Beebe, J. M.; Jun, Y.; Zhu, X. Y.; Frisbie, C. D., Correlation between HOMO Alignment and Contact Resistance in Molecular Junctions: Aromatic Thiols versus Aromatic Isocyanides. *Journal of the American Chemical Society* **2006**, *128* (15), 4970-4971; Seferos, D. S.; Blum, A. S.; Kushmerick, J. G.; Bazan, G. C., Single-Molecule Charge-Transport Measurements that Reveal Technique-Dependent Perturbations. *Journal of the American Chemical Society* **2006**, *128* (34), 11260-11267.
29. Goodall, W.; Wild, K.; Arm, K. J.; Williams, J. A. G., The synthesis of 4[prime or minute]-aryl substituted terpyridines by Suzuki cross-coupling reactions: substituent effects on ligand fluorescence. *Journal of the Chemical Society, Perkin Transactions 2* **2002**, (10), 1669-1681.
30. Kubota, E.; Lee, Y. H.; Fuyuhiko, A.; Kawata, S.; Harrowfield, J. M.; Kim, Y.; Hayami, S., Synthesis, structure, and luminescence properties of arylpyridine-substituted terpyridine Zn(II) and Cd(II) complexes. *Polyhedron* **2013**, *52* (0), 435-441.
31. Potts, K. T.; Ralli, P.; Theodoridis, G.; Winslow, P., 2, 2': 6', 2'-Terpyridine. *Organic Syntheses* **1986**, 189-189.
32. Jameson, D. L.; Guise, L. E., An improved, two-step synthesis of 2,2':6',2''-terpyridine. *Tetrahedron Letters* **1991**, *32* (18), 1999-2002.
33. Constable, E. C.; Housecroft, C. E.; Medlycott, E.; Neuburger, M.; Reinders, F.; Reymann, S.; Schaffner, S., The first complex of 4'-(4-methylthiophenyl)-2,2':6',2''-terpyridine – A model for terpylated self-assembled monolayers. *Inorganic Chemistry Communications* **2008**, *11* (5), 518-520.
34. Korall, P.; Borje, A.; Norrby, P.; Åkermark, B., High Yield Preparation of 4'-(4-Bromophenyl)-2, 2': 6', 2''-terpyridine by a Condensation Reaction.

Determination of the Stereochemistry of Two Complex By-products by a Combination of Molecular Mechanics and NMR Spectroscopy. *Acta Chemica Scandinavica* **1997**, *51* (6), 760-766.

35. Sedghi, G.; García-Suárez, V. M.; Esdaile, L. J.; Anderson, H. L.; Lambert, C. J.; Martín, S.; Bethell, D.; Higgins, S. J.; Elliott, M.; Bennett, N., Long-range electron tunnelling in oligo-porphyrin molecular wires. *Nature Nanotechnology* **2011**, *6* (8), 517-523.

Chapter 4

Conductance of **transition metal based** **molecular wires under** **electrochemical control**

4.1 General Introduction

Much attention in molecular electronics has focused on utilizing different backbones and anchoring groups to maximise the conductance properties of a molecular wire.⁹⁷ However, it has now become of interest to investigate molecules with properties that can be switched reversibly.^{10c, 34b, 61} The electrochemical gating of two transition metal complexes is investigated in this chapter.

4.1.1 Introduction

The control of single molecule conductance using electrochemical gating is of great interest. The use of a bipotentiostat and an electrolyte solution in conjunction with the STM allows these measurements to take place, see Chapter 1 for detailed description of EC-STM. Using this technique, a range of varied redox molecules (e.g. functionalised viologens,^{10c, 61, 98} functionalised pyrrolotetrathiafulvalene^{34b, 61} and oligoanilines⁹⁹) have been studied as a function of electrochemical potential.

The molecules so far studied results exhibit two types of typical behaviour, as shown in Figure 4.1. In the first case the conductance changes in an off-on behaviour as the redox potential is passed, Figure 4.1(a).^{10c, 100} The second type of behaviour exhibits an off conductance as the redox potential is approached at which it peaks into an on conductance and then falls back to the off conductance as the redox potential is passed, Figure 4.1(b).^{34b, 61, 99a}

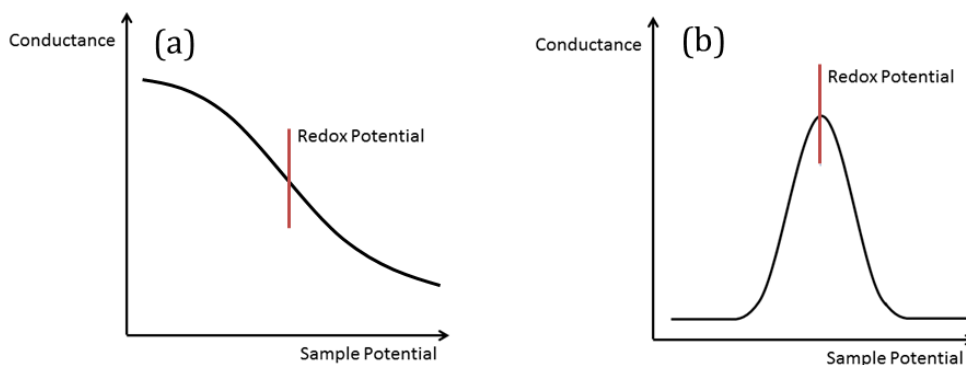


Figure 4.1 Schematic of the conductance behaviours exhibited when redox active molecules are measured as a function of potential (a) on-off type behaviour. (b) off-on-off type behaviour.

Structure property relationships are still not fully understood and there is currently no understanding of the structural factors that result in a certain behaviour. This makes further investigations into the conductance behaviour under potential control of particular interest.

There have so far been few investigations into the single molecule conductance measurements of metal terpyridine complexes. Osario *et al.* have demonstrated the ability to control the spin state (high-spin to low-spin) by using a three-terminal device incorporating a Mn^{2+} ion coordinated by two terpyridine ligands, chemical structure and schematic can be seen below in Figure 4.2.¹⁰¹ This result shows the potential for further manipulation of transition metal complexes in molecular devices.

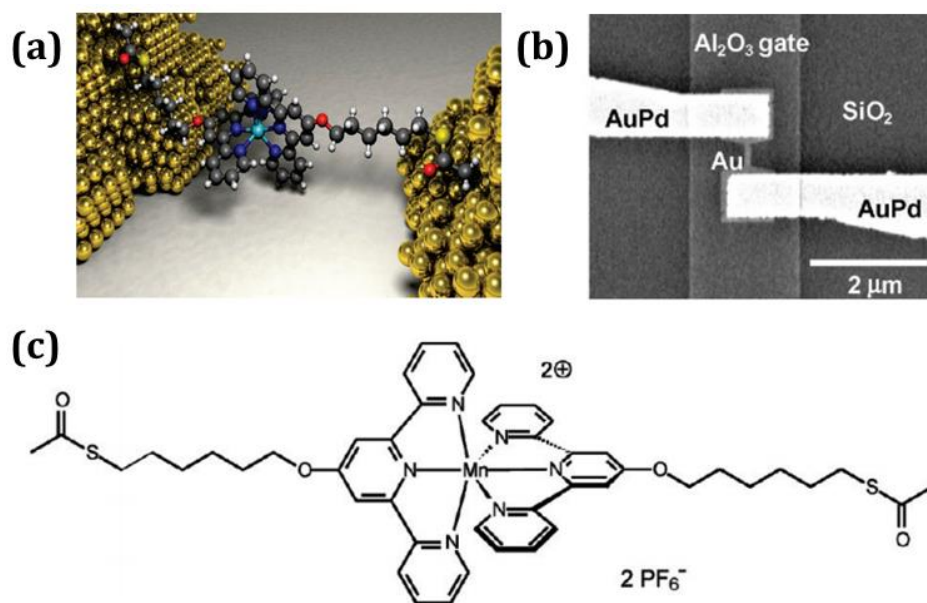


Figure 4.2: (a) Schematic of the Mn²⁺ complex attached to gold electrodes. (b) Fabricated three-terminal device. (c) Molecular structure of the Mn²⁺ complex. Figure adapted from reference ¹⁰¹

As briefly discussed in Chapter 1, Albrecht *et al.* have investigated the cyclic voltammetry properties of an osmium bis-terpyridine complex monolayer formed on Au(111) followed by investigations into the conductance as a function of potential, Figure 4.3.^{33b} The conductance was measured on a monolayer of the osmium bis-terpyridine complex and was completed using constant tip height mode.

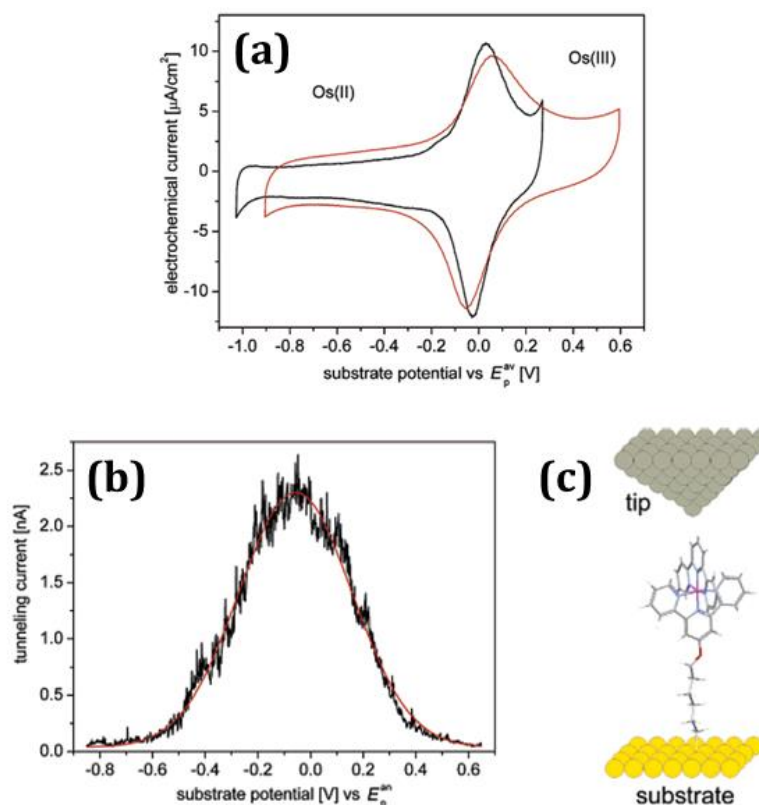


Figure 4.3: (a) Cyclic voltammetry results for the Osmium Bisterpyridine complex in BMIM-PF₆ (red line) and aqueous HClO₄ (black line). Scan Rate 0.1 V/s (b) Tunneling current enhancement in ionic liquid measured using an EC-STM (c) Schematic of the Os complex between the tip and substrate. Figure adapted from reference 33b.

The cyclic voltammetry on a monolayer show clear metal redox peaks for both the aqueous and ionic liquid electrolyte, Figure 4.3(a). The CV measured in BMIM-PF₆ shows broader signals with a larger peak separation; this result is typical for an ionic liquid due to its lower diffusion coefficient. The EC-STM results show that as the redox potential is reached, there is a clear increase in the tunneling current observed, which decreases again as the redox potential is passed, Figure 4.3(b). This increase from 0.05 nA to 2.3 nA at the maximum shows an increase factor of ~ 50 . Albrecht *et al.* have previously shown that electron hopping most likely dominates at small V_{bias} ,^{62, 70b} which causes this noticeable change in conductance.

Zhou *et al.* have studied the relationship between molecular conductance and electrochemical rate constants for a set of redox active molecules.⁶⁸ The conductance of [Os(pyterpy)₂](PF₆)₂ in aqueous 1 M NaClO₄ was studied as a

function of potential using the break junction technique, shown below in Figure 4.4.

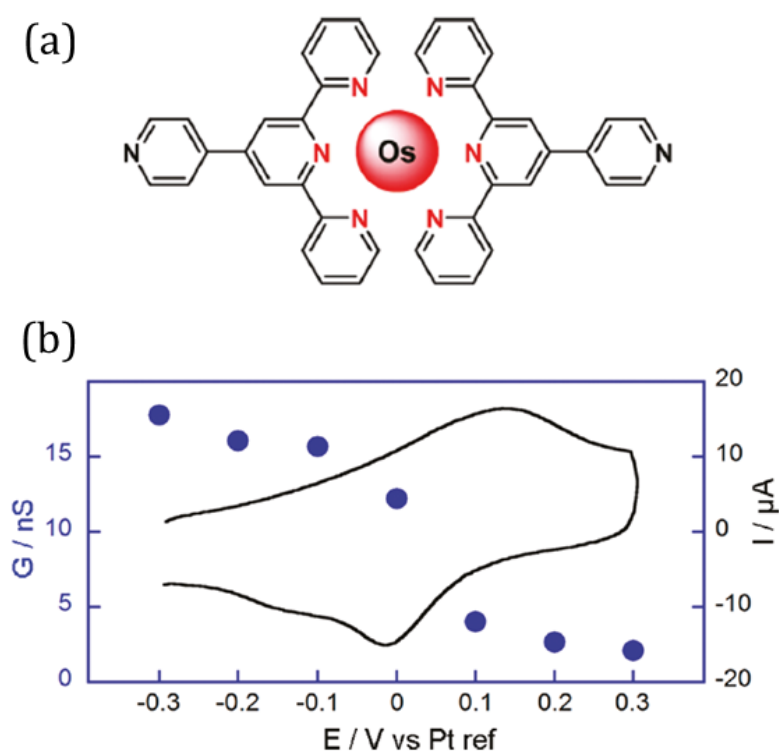


Figure 4.4: (a) Molecular system investigated. (b) Conductance (blue dots) and cyclic voltammetry (black line) for [Os(pyterpy)₂](PF₆)₂] as recorded by Zhou *et al.*⁶⁸ Figure adapted from reference 68.

The [Os(pyterpy)₂](PF₆)₂ exhibits an on-off conductance switching, Figure 4.4(b). The clear change in switching can be seen with a conductance of 17.8 nS at -0.3 V and a conductance of 2.1 nS at +0.3 V. The determined heterogeneous rate constant (k_{ET}) for [Os(pyterpy)₂](PF₆)₂] was calculated to be $k_{ET} = (2.0 \times 10^6 \pm 0.5 \times 10^6 \text{ s}^{-1})$. The group observe that fast electron transfer rate constants correspond to high conductance. The conductance variation with potential suggests that the charge transport mechanism for the investigated molecules is superexchange, not electron hopping.

This makes the investigations into the two transition metal complexes here particularly interesting. The two complexes to be studied are [Co(pyterpy)₂](PF₆)₂ and [Fe(pyterpy)₂](PF₆)₂ (Figure 4.5) these complexes were chosen due to their suitability from the solution cyclic voltammetry in ionic liquid and their ability to form successful molecular junctions in both ambient and ionic liquid medium.

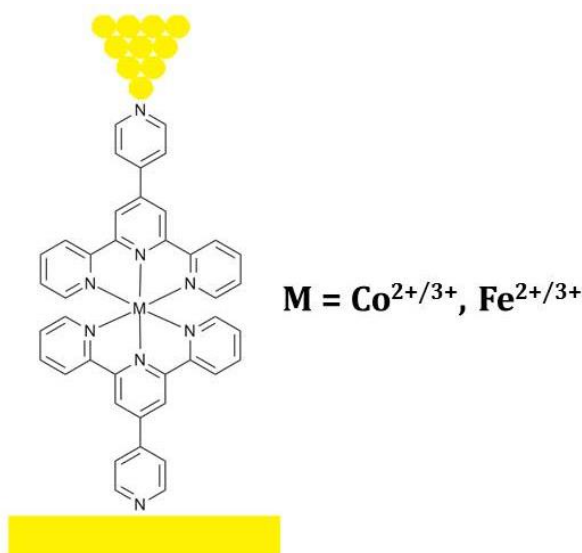


Figure 4.5: Schematic of the investigated complexes between two electrodes.

4.2 Aim

The aim of this study is to investigate the M(II)/M(III) monolayer voltammetry results of the two pyterpy complexes, [Co(pyterpy)₂](PF₆)₂ and [Fe(pyterpy)₂](PF₆)₂ in ionic liquid. Conductance studies of two different transition metal complex molecular junctions under electrochemical control in ionic liquid were then undertaken with a view to investigating whether the complexes showed ‘off-on’ (sigmoidal) or ‘off-on-off’ behaviour of the junction conductance as a function of electrochemical potential.

4.3 Methods

4.3.1 Synthesis

The transition metal complexes were synthesised in the laboratory as previously described in Chapter 2.

4.3.2 Conductance Measurements

The samples were prepared using commercial gold on glass slides (Arrandee®) which were flame annealed using a Bunsen burner immediately prior to use. The freshly annealed slide was then used immediately. A weak solution (1 mM) of the appropriate transition metal complex was prepared in dry BMIM-TFSA and immediately put into the STM cell utilising the environmental chamber purged with nitrogen and left for 1 h. Au STM tips were prepared by cutting 0.25 mm Au wire (99.99 %, Goodfellow).

Conductance measurements were completed using an Agilent 5500 STM controller in conjunction with Agilent Picoscan 5.3.3 software. Measurements were completed in both ambient and an ionic liquid medium. Ionic liquid was dried for 12 h prior to use at 120 °C under high vacuum and was used in conjunction with an environmental chamber fitted to the STM head which was under a constant flow of N₂. The $I(s)$ method was utilised to measure the conductance with a setpoint current (I_0) of 40 nA and a bias voltage (V_{bias}) of + 0.6 V. The tip was withdrawn 4 nm relative to the setpoint and the scan duration was 0.1 s. The initial tip to sample distance (s_0) was approximated using the method described previously in Chapter 1 and, where appropriate, was used in conjunction with the experimental break off (ΔS) to calculate the total break off (S_{total}). Approximately 500 current-distance scans that exhibited a clear current plateau, were plotted into a histogram from which the molecular conductance was calculated.

4.3.3 Cyclic Voltammetry

Cyclic voltammetry experiments were completed using a Metrohm Autolab potentiostat PGSTAT30 model utilizing the AutoLab GPES software. For all experiments a three electrode set up was employed, with a Au(111) bead working electrode and Pt Wire counter and reference electrodes, referencing was completed to an internal standard of ferrocene. A sealable glass cell was used which was cleaned in 20 % HNO₃ and dried in the oven prior to use. All chemicals were either synthesised in the laboratory or used as received. Ionic liquid was dried for 12 hours at 120 °C under vacuum prior to use. All solutions and experiments were prepared in a glove box in an inert atmosphere.

4.4 Results

4.4.1 Cyclic Voltammetry

The experimental procedure was completed by forming a monolayer of the transition metal complex on the Au(111) working electrode (WE). This was completed by immersing the Au(111) WE into a 1 mM solution of the transition metal complex in BMIM-TFSA solution for approximately 18 hours. The Au(111) WE was then rinsed with BMIM-TFSA to remove any physisorbed material and inserted into the sealable cell, containing clean BMIM-TFSA as the

electrolyte. Pt Wire was used as reference (RE) and counter (CE) electrodes. At the end of each experiment ferrocene was added to calibrate the potential scale.

4.4.1.1 Cyclic voltammetry of $\text{Fe}(\text{pyterpy})_2(\text{PF}_6)_2$

Initially monolayer investigations were completed on $[\text{Fe}(\text{pyterpy})_2](\text{PF}_6)_2$, Figure 4.6. This involved forming a monolayer on the Au(111) working electrode and inserting it into a clean glass cell with BMIM-TFSA present. Pt Wire was the quasi-reference and counter electrode. Voltammograms were taken at various scan rates (0.1 – 50 V/s^{-1}) and once completed ferrocene was added and the scale was calibrated to the Fc/Fc^+ reference.

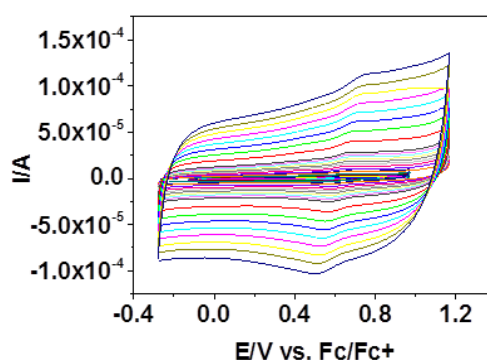


Figure 4.6: Cyclic voltammogram of $[\text{Fe}(\text{pyterpy})_2](\text{PF}_6)_2$ monolayer in BMIM-TFSA electrolyte. The potential scale has been calibrated to the Fc/Fc^+ couple. Scan rates 0.1 Vs^{-1} to 50 Vs^{-1}

The determination of the electron transfer rate constant, k_{ET} , was completed using the Laviron method as described in Chapter 1. By applying the constraint of $\eta = 0$ to Equation 4.1, it can be reduced to Equation 4.2.²⁹

$$\log k_{APP} = \alpha \log(1 - \alpha) + (1 - \alpha) \log \alpha - \log \left(\frac{RT}{nFv} \right) - \frac{\alpha(1-\alpha)nF\eta}{2.3RT} \quad \text{Equation 4.1}$$

$$k_{ET} = \frac{\alpha n F v_c}{RT} = (1 - \alpha) \frac{n F v_a}{RT} \quad \text{Equation 4.2}$$

Where F is Faradays constant (96485 C mol^{-1}), R is the gas constant (8.314 J mol^{-1}), T is temperature (298 K), α is the electron transfer coefficient (0.5) and v_a and v_c are the x values at which the anodic and cathodic branches intercept. The determination of v_a and v_c is completed by plotting the peak potential E_p vs. $\ln(v)$ scan rate. E_p^a and E_p^c are plotted separately. Figure 4.7 shows the plot of E_p vs. $\ln(v)$ scan rate and a close up of the area used to calculate v_a and v_c

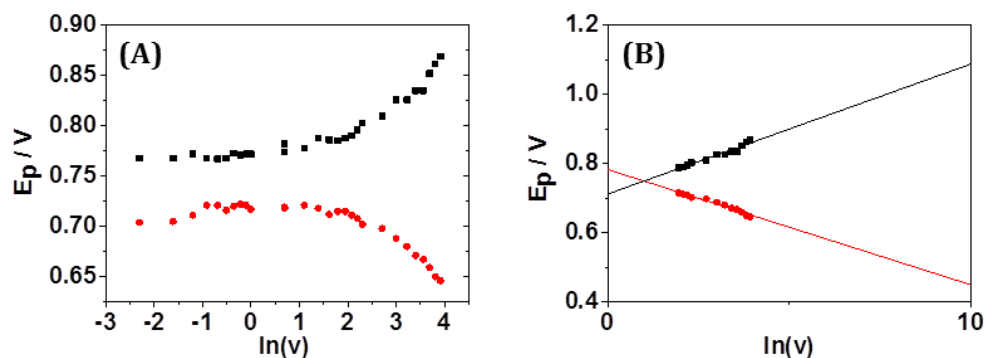


Figure 4.7: (A) Plot of E_p (V) vs. $\ln(v)$ for $[\text{Fe}(\text{pyterpy})_2](\text{PF}_6)_2$ (B) The section utilised to calculate v . Black is E_p^c and Red is E_p^a .

The k_{ET} was calculated to be $1.9 \times 10^1 \text{ s}^{-1}$. This is lower than the value calculated for the $[\text{Os}(\text{pyterpy})_2](\text{PF}_6)_2$ complex measured by Zhou *et al.*⁶⁸ and will be discussed in further detail in Section 4.5.

4.4.1.2 Cyclic voltammetry of $[\text{Co}(\text{pyterpy})_2](\text{PF}_6)_2$

The monolayer of $[\text{Co}(\text{pyterpy})_2](\text{PF}_6)_2$ was investigated using the same technique as the $[\text{Fe}(\text{pyterpy})_2](\text{PF}_6)_2$ complex and calibrated to the Fc/Fc^+ internal reference. The voltammogram can be seen in Figure 4.8.

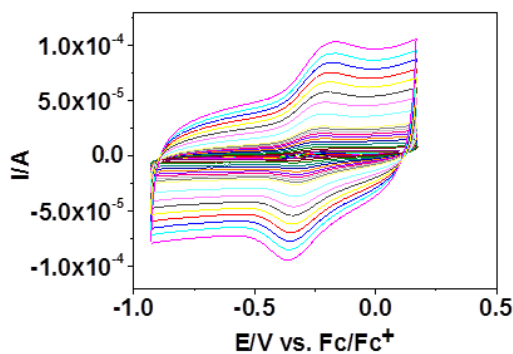


Figure 4.8: Cyclic Voltammogram of $[\text{Co}(\text{pyterpy})_2](\text{PF}_6)_2$ monolayer in BMIM-TFSA electrolyte. The potential scale has been calibrated to the Fc/Fc^+ couple.

The determination of the electron transfer rate constant, k_{ET} , was completed using the Laviron method as shown above in Equation 4.1 and 4.2 using the plots shown in Figure 4.9.

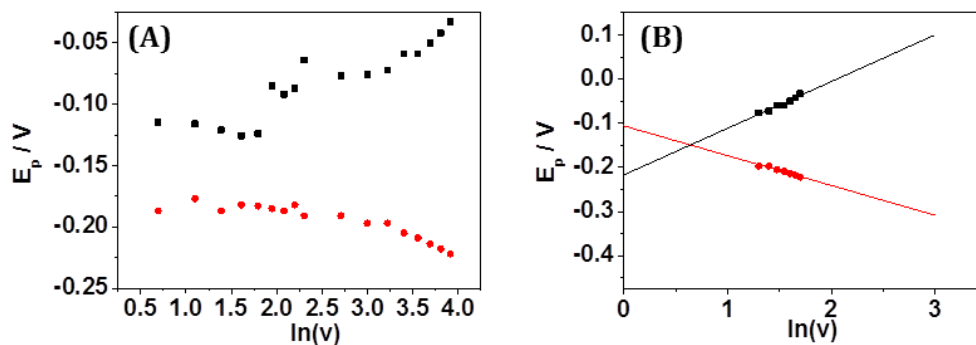


Figure 4.9: Plot of E_p (V) vs. $\ln(v)$ for $[\text{Co}(\text{pyterpy})_2](\text{PF}_6)_2$ (B) The section utilised to calculate v . Black is E_p^c and Red is E_p^a .

The k_{ET} was calculated to be $1.2 \times 10^1 \text{ s}^{-1}$. The rate constant for the $[\text{Co}(\text{pyterpy})_2](\text{PF}_6)_2$ complex is lower than the $[\text{Fe}(\text{pyterpy})_2](\text{PF}_6)_2$ the reasons for this will be discussed in Section 4.5.

4.4.2: Conductance Measurements

The $I(s)$ technique was used to measure the conductance of the two transition metal complexes at different sample potentials. The measurements were completed in an ionic liquid medium by rapidly withdrawing the tip at a predetermined of 40 nA and a bias 0.6 V. Approximately 5 % of the $I(s)$ scans contained a plateau characteristic of a molecule bridging the gap between the tip and the substrate. The conductance was calculated via histogram analysis using the $I(s)$ scans that contained a plateau. The conductance was measured at a bias of 0.6 V and a setpoint current of 40 nA.

4.4.3: Conductance Studies of $[\text{Fe}(\text{pyterpy})_2](\text{PF}_6)_2$ under electrochemical control

All $I(s)$ scans that contained a plateau were used in the histogram analysis. The histograms for sample potentials of 1, 0.95, 0.9, 0.85, 0.8, 0.75, 0.7 and 0.65 V vs. Pt quasi reference at least 400 scans were included, and the histograms for sample potentials 1.05, 0.6, 0.55 and 0.45 V vs. Pt quasi reference contained at least 250 scans, Figure 4.10 and 4.11.

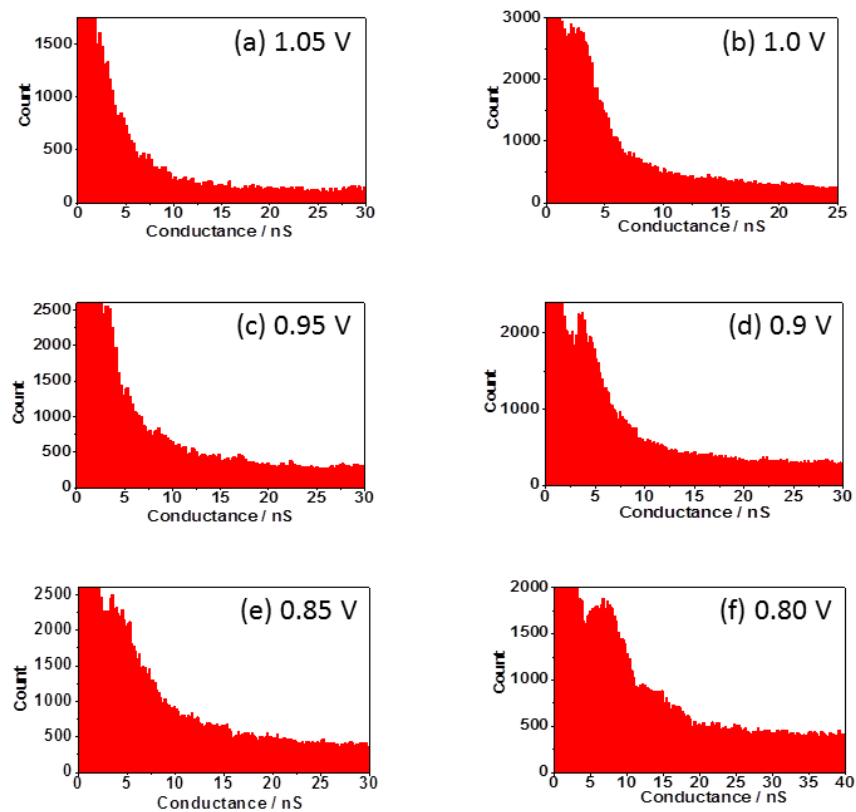


Figure 4.10: Conductance histograms of $[\text{Fe}(\text{pyterpy})_2](\text{PF}_6)_2$ using sample potentials of (a) 1.05 V, (b) 1 V, (c) 0.95 V, (d) 0.9 V, (e) 0.85 V and (f) 0.8 V, obtained using the $I(s)$ method; $V_{\text{BIAS}} = +0.6 \text{ V}$; $I_0 = 40 \text{ nA}$; 257, 516, 533, 502, 535 and 501 scans were analysed respectively. Sample potentials are with respect to the Pt quasi reference.

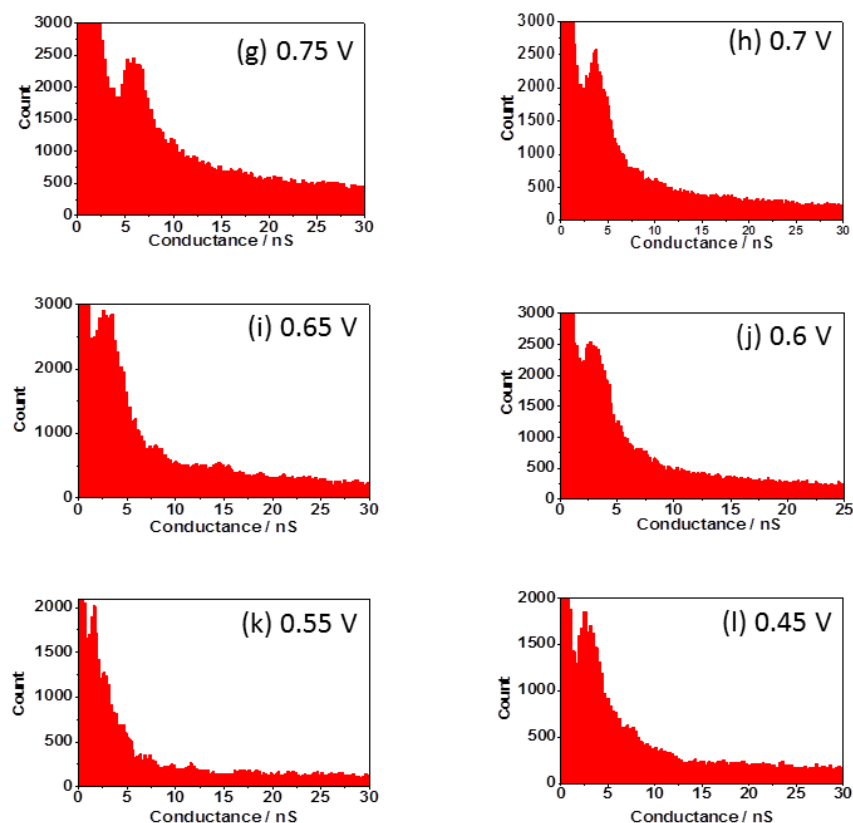


Figure 4.11: Conductance histograms of $[\text{Fe}(\text{pyterpy})_2](\text{PF}_6)_2$ using sample potentials of (g) 0.75 V, (h) 0.7 V, (i) 0.65 V, (j) 0.6 V, (k) 0.55 V and (l) 0.45 V, obtained using the $I(s)$ method; $V_{\text{BIAS}} = +0.6 \text{ V}$; $I_0 = 40 \text{ nA}$; 507, 501, 512, 303, 253 and 255 scans were analysed respectively. Sample potentials are with respect to the Pt quasi reference.

A summary of the conductance results obtained for $[\text{Fe}(\text{pyterpy})_2](\text{PF}_6)_2$ is presented below in Table 4.1.

Table 4.1: Summary of the conductance data

Sample Potential, V vs. Pt quasi	Conductance / nS
1.05	(2.25 ± 0.59)
1	(2.1 ± 0.67)
0.95	(3.3 ± 0.59)
0.9	(3.7 ± 0.86)
0.85	(4.5 ± 0.90)
0.8	(6.75 ± 1.95)
0.75	(5.85 ± 1.050)
0.7	(3.7 ± 0.96)
0.65	(3.45 ± 1.1)
0.6	(2.7 ± 0.71)
0.55	(1.65 ± 0.89)
0.45	(2.55 ± 0.78)

The break off distance was calculated as described in Chapter 1 for each sample potential for $[\text{Fe}(\text{pyterpy})_2](\text{PF}_6)_2$. This value was compared to the gold separation distance calculated in Spartan[®] which was 2.2 nm. A summary of the data can be seen in Table 4.2.

Table 4.2: Summary of break off distance

Sample Potential, V vs. Pt quasi	Experimental Break off - ΔS , nm	$d(\ln I)/d(s)$, nm^{-1}	s_0 , nm	Total break off, nm
1.05	1.04	6.772	1	(2.04 ± 0.5)
1	1.41	3.816	1.8	(3.21 ± 0.5)
0.95	1.04	5.461	1.3	(2.34 ± 0.4)
0.9	1.55	3.174	2.2	(3.75 ± 0.3)
0.85	1.80	5.168	1.4	(3.20 ± 0.7)
0.8	1.33	3.351	2.1	(3.43 ± 0.44)
0.75	1.61	3.202	2.2	(3.81 ± 0.3)
0.7	1.37	3.4729	2	(3.37 ± 0.25)
0.65	1.22	9.195	0.8	(2.02 ± 0.4)
0.6	1.19	4.165	1.7	(2.89 ± 0.4)
0.55	1.20	6.738	1.0	(2.20 ± 0.4)
0.45	1.3	4.69	1.5	(2.8 ± 0.4)

2D histograms were plotted relative to the break off distance and can be seen below in Figure 4.12 and 4.13.

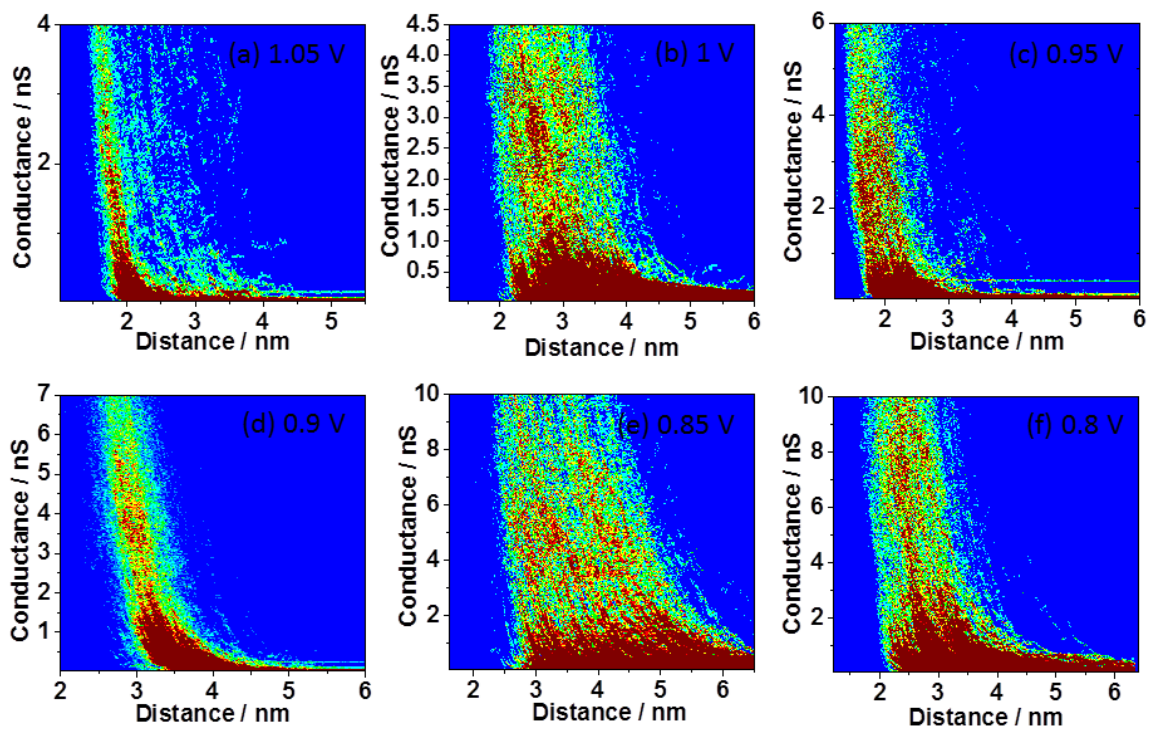


Figure 4.12: 2D Conductance histograms of $[\text{Fe}(\text{pyterpy})_2](\text{PF}_6)_2$ relative to break off distance using sample potentials of (a) 1.05 V, (b) 1 V, (c) 0.95 V, (d) 0.9 V, (e) 0.85 V and (f) 0.8 V. Sample potentials are with respect to the Pt quasi reference.

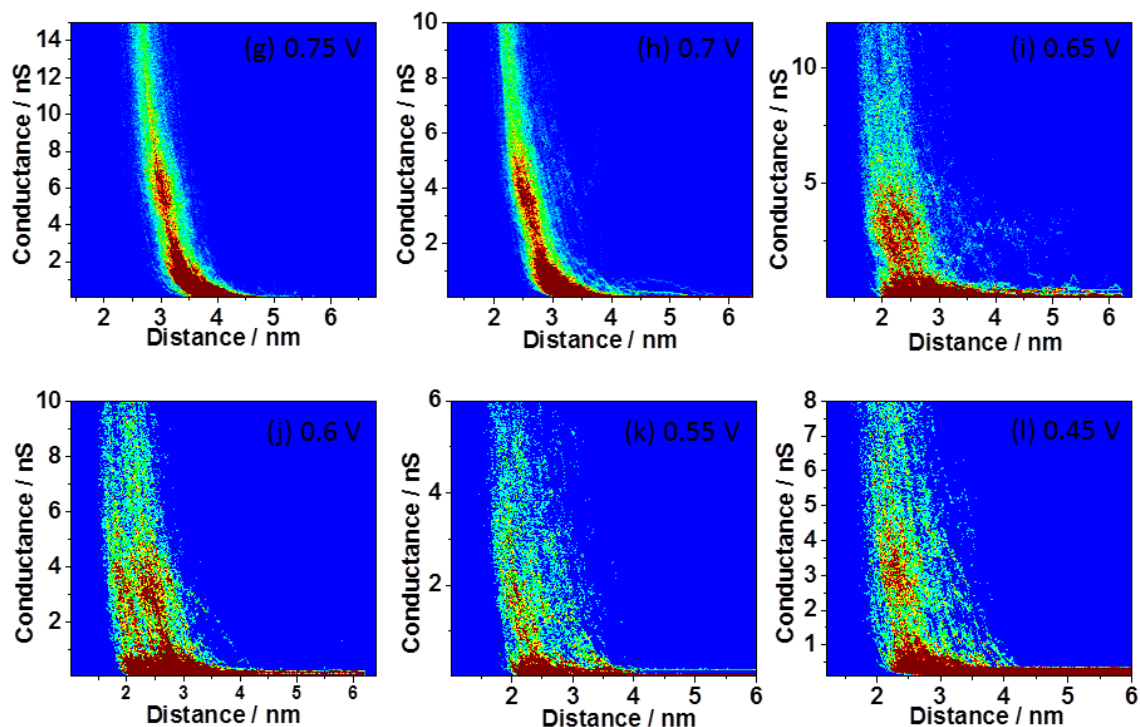


Figure 4.13: 2D Conductance histograms of $[\text{Fe}(\text{pyterpy})_2](\text{PF}_6)_2$ relative to break off distance using sample potentials of (g) 0.75 V, (h) 0.7 V, (i) 0.65 V, (j) 0.6 V, (k) 0.55 V and (l) 0.45 V. Sample potentials are with respect to the Pt quasi reference.

The conductance is plotted as a function of sample potential. The result for $[\text{Fe}(\text{pyterpy})_2](\text{PF}_6)_2$ is shown below in Figure 4.14.

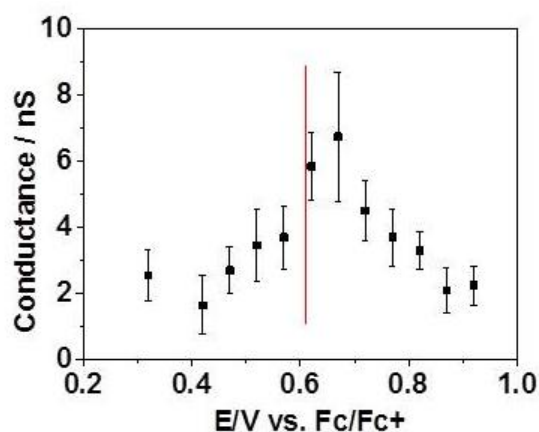


Figure 4.14: Conductance of $[\text{Fe}(\text{pyterpy})_2](\text{PF}_6)_2$ vs. Sample potential, V vs. Fc/Fc⁺. Redox potential given by red line.

A clear off-on-off profile is exhibited as the conductance passes the redox potential. The conductance increases from ~ 2 nS in the off state to 6.75 nS in the on state. This threefold increase in conductance and then drop back off after

the redox potential has passed is interesting as it contradicts the results reported by Zhou *et al.* where the $[\text{Os}(\text{pyterpy})_2](\text{PF}_6)_2$ exhibits an on-off profile.⁶⁸ This will be discussed further in Section 4.5.

4.4.4: Conductance Studies of $\text{Co}(\text{pyterpy})_2(\text{PF}_6)_2$ under electrochemical control

The conductance of $[\text{Co}(\text{pyterpy})_2](\text{PF}_6)_2$ was now investigated as a function of potential. Sample potentials of -0.35, -0.25, -0.15, -0.05, 0, 0.05, 0.15 and 0.25 V vs. Pt quasi reference at least 400 scans were included in the histogram, and the histograms for sample potentials -0.8, -0.6, -0.4, 0.4, 0.6 and 0.8 V vs. Pt quasi reference contained at least 250 scans. The 1D histograms can be seen below in Figure 4.15 and 4.16.

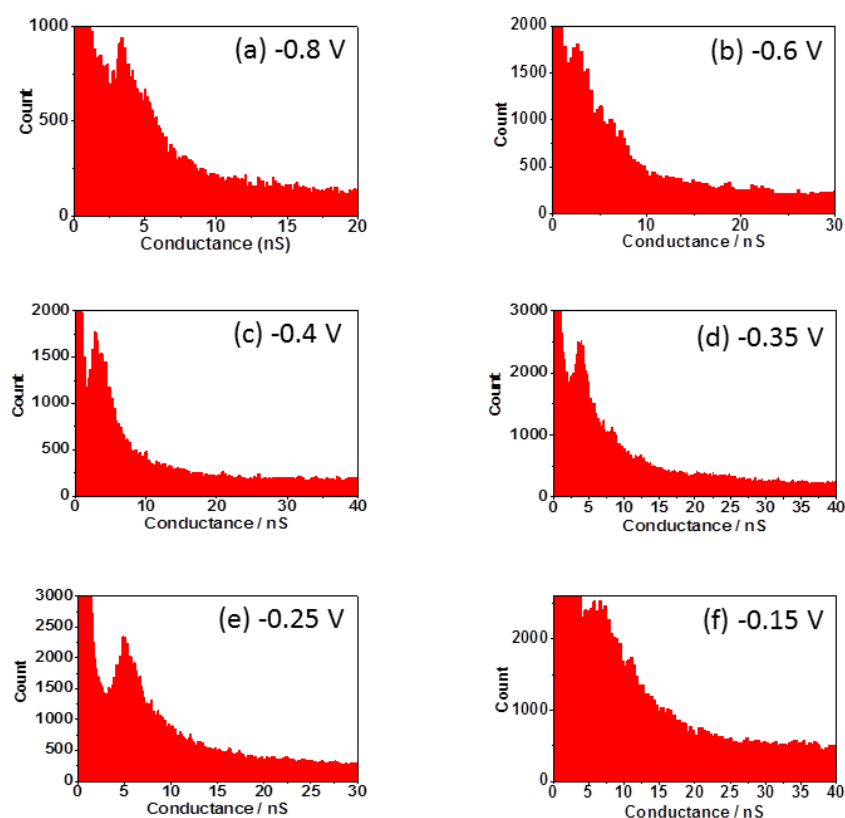


Figure 4.15: Conductance histograms of $[\text{Co}(\text{pyterpy})_2](\text{PF}_6)_2$ using sample potentials of (a) -0.8 V, (b) -0.6 V, (c) -0.4 V, (d) -0.35 V, (e) -0.25 V and (f) -0.15 V, obtained using the $I(s)$ method; $V_{\text{BIAS}} = +0.6$ V ; $I_0 = 40$ nA ; 258, 309, 265, 510, 508 and 562 scans were analysed respectively. Sample potentials are with respect to the Pt quasi reference.

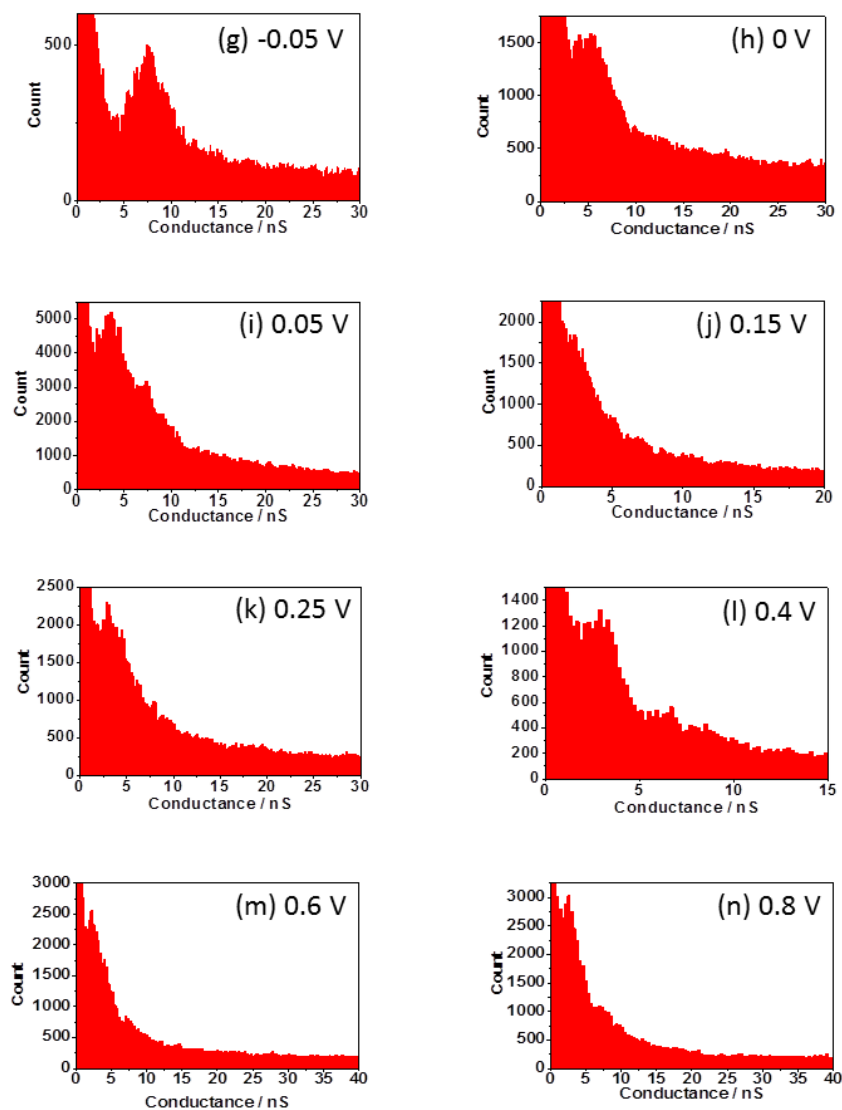


Figure 4.16: Conductance histograms of $[\text{Co}(\text{pyterpy})_2](\text{PF}_6)_2$ using sample potentials of (g) -0.05 V, (h) 0 V, (i) 0.05 V, (j) 0.15 V, (k) 0.25 V, (l) 0.4 V, (m) 0.6 V and (n) 0.8 V, obtained using the $I(s)$ method; $V_{\text{BIAS}} = +0.6$ V; $I_0 = 40$ nA; 491, 540, 502, 425, 421, 365, 323 and 329 scans were analysed respectively. Sample potentials are with respect to the Pt quasi reference

A summary of the conductance data for $[\text{Co}(\text{pyterpy})_2](\text{PF}_6)_2$ under potential control has been recorded in Table 4.3.

Table 4.3: Summary of the conductance data

Sample Potential, V vs. Pt quasi	Conductance / nS
-0.8	(3.3 ± 0.62)
-0.6	(2.6 ± 0.82)
-0.4	(2.85 ± 0.63)
-0.35	(4.05 ± 0.39)
-0.25	(4.95 ± 0.95)
-0.15	(5.8 ± 1.1)
-0.05	(7.65 ± 1.32)
0	(5.3 ± 1.31)
0.05	(3.75 ± 0.66)
0.15	(2.3 ± 0.72)
0.25	(3.15 ± 0.83)
0.4	(2.9 ± 0.61)
0.6	(2.25 ± 0.54)
0.8	(2.55 ± 0.65)

The break off distance was calculated for each conductance set at different sample potentials and compared to the gold separation distance calculated in Spartan[®] to be 2.2nm. The data are summarised in Table 4.4.

Table 4.4: Summary of the break off distance data calculated.

Sample Potential, V vs. Pt quasi	Experimental Break off - ΔS , nm	$d(\ln I)/d(s)$, nm ⁻¹	s_0 , nm	Total break off, nm
-0.8	1.45	4.33	1.6	(3.05 ± 0.5)
-0.6	1.30	3.41	2.1	(3.4 ± 0.4)
-0.4	1.30	3.99	1.8	(3.1 ± 0.9)
-0.35	2.01	4.46	1.6	(3.61 ± 0.7)
-0.25	1.30	4.85	1.5	(2.80 ± 0.5)
-0.15	1.00	6.44	1.1	(2.1 ± 0.4)
-0.05	1.21	7.67	0.9	(2.11 ± 0.4)
0	1.59	3.97	1.8	(3.39 ± 0.5)
0.05	1.43	5.43	1.3	(2.73 ± 0.6)
0.15	1.3	6.20	1.1	(2.4 ± 0.3)
0.25	1.22	6.17	1.2	(2.42 ± 0.3)
0.4	1.15	2.72	2.6	(3.75 ± 0.4)
0.6	1.3	4.14	1.7	(3.0 ± 0.5)
0.8	1.18	3.47	2.0	(3.18 ± 0.4)

2D histograms relative to the break off distance were plotted for each measured sample potential for [Co(pyterpy)₂](PF₆)₂, Figure 4.17 and 4.18.

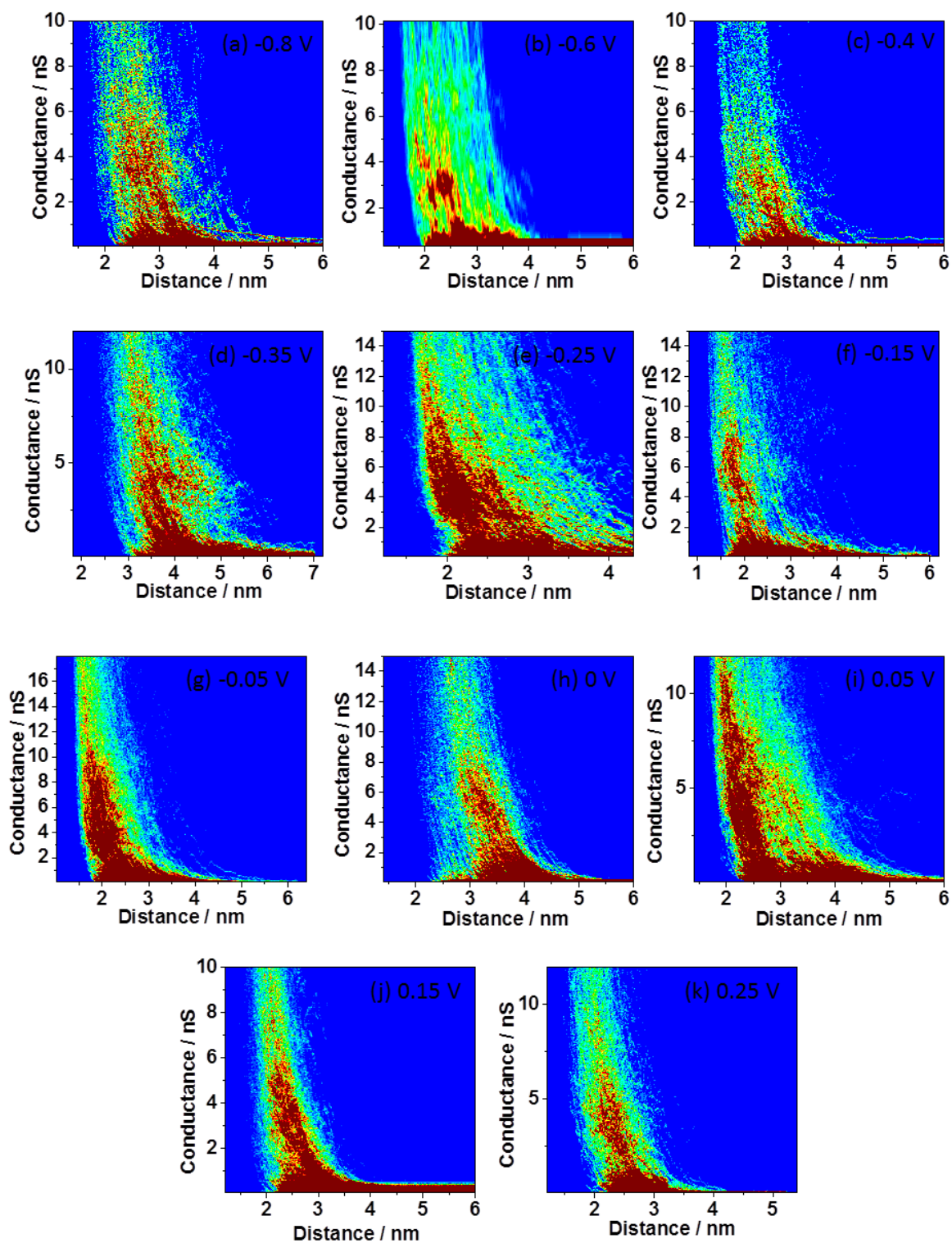


Figure 4.17: 2D Conductance histograms of $[\text{Co}(\text{pyterpy})_2](\text{PF}_6)_2$ relative to break off distance using sample potentials of (a) -0.8 V, (b) -0.6 V, (c) -0.4 V, (d) -0.35 V, (e) -0.25 V, (f) -0.15 V, (g) -0.05 V, (h) 0 V, (i) 0.05 V, (j) 0.15 V and (k) 0.25 V. Sample potentials are with respect to the Pt quasi reference.

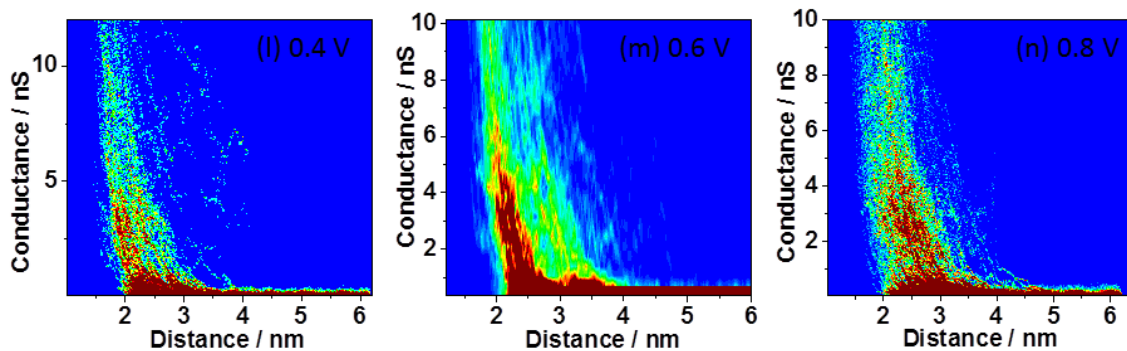


Figure 4.18: 2D Conductance histograms of $[\text{Co}(\text{pyterpy})_2](\text{PF}_6)_2$ relative to break off distance using sample potentials of (l) 0.4 V, (m) 0.6 V and (n) 0.8 V. Sample potentials are with respect to the Pt quasi reference.

The conductance of $[\text{Co}(\text{pyterpy})_2](\text{PF}_6)_2$ can now be plotted as a function of sample potential. This can be seen below in Figure 4.19.

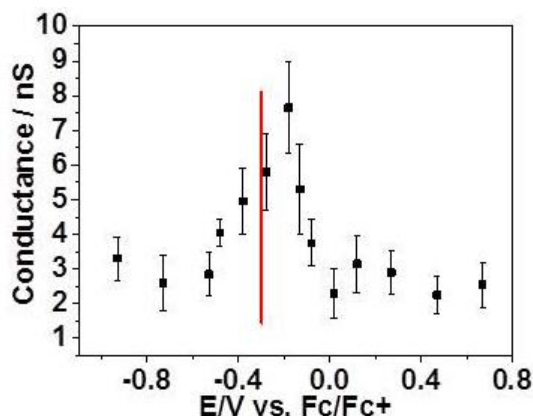


Figure 4.19: Conductance of $[\text{Co}(\text{pyterpy})_2](\text{PF}_6)_2$ vs. Sample potential, V vs. Fc/Fc⁺. Redox potential position given by the red line.

The conductance shows a clear off-on-off profile, with the conductance increasing threefold from ~ 2.5 nS in the off-state to ~ 7.5 nS in the on-state. This behaviour is the same as exhibited by the $[\text{Fe}(\text{pyterpy})_2](\text{PF}_6)_2$ this result is discussed in further detail in Section 4.5.

4.5: Discussion

The cyclic voltammograms of the monolayer formation of the two transition metal complexes exhibit a redox peak assigned as M(II)/M(III) in each case by analogy with the literature on terpy complexes (see Chapter 2). The redox potential for both complexes has shifted to less positive potentials compared to solution voltammetry, as seen in Table 4.5.

Table 4.5: The recorded redox potentials $E_{1/2}$ for $M(\text{pyterpy})_2(\text{PF}_6)_2$ complexes in BMIM-TFSA for solution and monolayer voltammetry results calibrated to ferrocene reference.

	Solution Voltammetry $E_{1/2} / \text{V vs. Fc/Fc}^+$	Monolayer Voltammetry $E_{1/2} / \text{V vs. Fc/Fc}^+$
[Fe(pyterpy)₂](PF₆)₂	0.78 V	0.61 V
[Co(pyterpy)₂](PF₆)₂	-0.04 V	-0.30 V

This is due to the different environments felt by the complexes when they are in a SAM compared to when they are 'free' in a solution.

The calculated rate constants for [Fe(pyterpy)₂](PF₆)₂ and [Co(pyterpy)₂](PF₆)₂ were found to be $1.9 \times 10^1 \text{ s}^{-1}$ and $1.2 \times 10^1 \text{ s}^{-1}$ respectively. Both the calculated rate constants for [Co(pyterpy)₂](PF₆)₂ and [Fe(pyterpy)₂](PF₆)₂ are lower than the rate constant calculated by Zhou *et al.* for [Os(pyterpy)₂](PF₆)₂ which was reported to be $2.0 \times 10^6 \text{ s}^{-1}$, in 0.1 M NaClO₄ aqueous solution.⁶⁸ This low rate constant can be attributed to the ionic liquid medium. The ionic liquid is highly viscous which results in a lower diffusion coefficient which will result in a lower rate constant. Also a higher reorganisation energy is reported for ionic liquids.^{34b}

The conductance measurements for both [Co(pyterpy)₂](PF₆)₂ and [Fe(pyterpy)₂](PF₆)₂ exhibit a clear off-on-off profile as the redox potential is passed. The conductance for both complexes is found to increase threefold from the off-state to the on-state. This behaviour is similar to that recorded for 6pTTF6 by Kay *et al.* in ionic liquid, BMIM-OTf.^{34b} They reported a similar off-on-off profile in the ionic liquid medium, with the conductance going from ~ 0.5 nS in the off state to ~ 2 nS in the on state similarly Leary *et al.* report for an aqueous electrolyte an increase in conductance from ~ 0.5 nS in the off state to ~ 2.5 nS in the on state.⁶¹ The recorded result for [Fe(pyterpy)₂](PF₆)₂ and [Co(pyterpy)₂](PF₆)₂ however contradicts the result recorded by Zhou *et al.* for [Os(pyterpy)₂](PF₆)₂ which was found to exhibit an on-off conductance profile in 0.1 M NaClO₄ aqueous solution but the rate constant calculated for the [Os(pyterpy)₂](PF₆)₂ was much greater, which could suggest the off-on-off

profile is exhibited at low rate constants for the transition metal complexes in ionic liquid. This would need to be further investigated by studying the conductance of $[\text{Os}(\text{pyterpy})_2](\text{PF}_6)_2$ in ionic liquid to confirm the reason.

4.6 Conclusions and Future work

It has been successfully shown that $[\text{Co}(\text{pyterpy})_2](\text{PF}_6)_2$ and $[\text{Fe}(\text{pyterpy})_2](\text{PF}_6)_2$ form stable monolayers on Au(111) substrate which can be investigated with cyclic voltammetry successfully up to a scan rate of up to 50 Vs^{-1} . The rate constant k_{ET} was calculated for both complexes and was found to be lower than a $[\text{Os}(\text{pyterpy})_2](\text{PF}_6)_2$ recorded in the literature, this can be attributed to the ionic liquid solvent.

The conductance results as a function of sample potential exhibited an off-on-off profile as the redox potential is passed. This was exhibited in both the $[\text{Fe}(\text{pyterpy})_2](\text{PF}_6)_2$ and $[\text{Co}(\text{pyterpy})_2](\text{PF}_6)_2$ complexes. This result showed a profile similar to that recorded by Kay *et al.* for an organic molecule in ionic liquid.^{34b} This result shows the promise of using transition metal complexes in single molecule electronics. However, Zhou *et al.* have shown $[\text{Os}(\text{pyterpy})_2](\text{PF}_6)_2$ to have an on-off conductance profile in an aqueous solvent. This result could be due to the differing rate constants and the medium. To clarify further investigations are necessary to see how the $[\text{Os}(\text{pyterpy})_2](\text{PF}_6)_2$ behaves in ionic liquid and the $[\text{Fe}(\text{pyterpy})_2](\text{PF}_6)_2$ and $[\text{Co}(\text{pyterpy})_2](\text{PF}_6)_2$ behave in aqueous solvent.

In this study, the successful use of transition metal complexes in single molecule electronics has been shown and the stability of the complexes under electrochemical control has been confirmed.

4.7 References

1. Nichols, R. J.; Haiss, W.; Higgins, S. J.; Leary, E.; Martin, S.; Bethell, D., The experimental determination of the conductance of single molecules. *Physical Chemistry Chemical Physics* **2010**, *12* (12), 2801-2815.
2. Kay, N. J.; Higgins, S. J.; Jeppesen, J. O.; Leary, E.; Lycoops, J.; Ulstrup, J.; Nichols, R. J., Single-molecule electrochemical gating in ionic liquids. *Journal of the American Chemical Society* **2012**, *134* (40), 16817-16826.
3. Haiss, W.; van Zalinge, H.; Higgins, S. J.; Bethell, D.; Höbenreich, H.; Schiffrin, D. J.; Nichols, R. J., Redox state dependence of single molecule conductivity. *Journal of the American Chemical Society* **2003**, *125* (50), 15294-15295.
4. Leary, E.; Higgins, S. J.; van Zalinge, H.; Haiss, W.; Nichols, R. J.; Nygaard, S.; Jeppesen, J. O.; Ulstrup, J., Structure– Property Relationships in Redox-Gated Single Molecule Junctions– A Comparison of Pyrrolo-Tetrathiafulvalene and Viologen Redox Groups. *Journal of the American Chemical Society* **2008**, *130* (37), 12204-12205.
5. Li, Z.; Pobelov, I.; Han, B.; Wandlowski, T.; Błaszczuk, A.; Mayor, M., Conductance of redox-active single molecular junctions: an electrochemical approach. *Nanotechnology* **2007**, *18* (4), 044018.
6. Chen, F.; He, J.; Nuckolls, C.; Roberts, T.; Klare, J. E.; Lindsay, S., A molecular switch based on potential-induced changes of oxidation state. *Nano Letters* **2005**, *5* (3), 503-506.
7. He, J.; Chen, F.; Lindsay, S.; Nuckolls, C., Length dependence of charge transport in oligoanilines. *Applied Physics Letters* **2007**, *90* (7), 072112.
8. Li, X.; Hihath, J.; Chen, F.; Masuda, T.; Zang, L.; Tao, N., Thermally activated electron transport in single redox molecules. *Journal of the American Chemical Society* **2007**, *129* (37), 11535-11542; Li, C.; Mishchenko, A.; Li, Z.; Pobelov, I.; Wandlowski, T.; Li, X.; Würthner, F.; Bagrets, A.; Evers, F., Electrochemical gate-controlled electron transport of redox-active single perylene bisimide molecular junctions. *Journal of Physics: Condensed Matter* **2008**, *20* (37), 374122.
9. Osorio, E. A.; Moth-Poulsen, K.; van der Zant, H. S. J.; Paaske, J.; Hedegård, P.; Flensberg, K.; Bendix, J.; Bjørnholm, T., Electrical Manipulation of Spin States in a Single Electrostatically Gated Transition-Metal Complex. *Nano Letters* **2009**, *10* (1), 105-110.
10. Albrecht, T.; Moth-Poulsen, K.; Christensen, J. B.; Hjelm, J.; Bjørnholm, T.; Ulstrup, J., Scanning tunneling spectroscopy in an ionic liquid. *Journal of the American Chemical Society* **2006**, *128* (20), 6574-6575.
11. Albrecht, T.; Guckian, A.; Ulstrup, J.; Vos, J. G., Transistor-like Behavior of Transition Metal Complexes. *Nano Letters* **2005**, *5* (7), 1451-1455; Albrecht, T.; Moth-Poulsen, K.; Christensen, J. B.; Guckian, A.; Bjørnholm, T.; Vos, J. G.; Ulstrup, J., In situ scanning tunnelling spectroscopy of inorganic transition metal complexes. *Faraday Discussions* **2006**, *131*, 265-279.
12. Zhou, X.-S.; Liu, L.; Fortgang, P.; Lefevre, A.-S.; Serra-Muns, A.; Raouafi, N.; Amatore, C.; Mao, B.-W.; Maisonhaute, E.; Schöllhorn, B., Do molecular conductances correlate with electrochemical rate constants? Experimental insights. *Journal of the American Chemical Society* **2011**, *133* (19), 7509-7516.

13. Eckermann, A. L.; Feld, D. J.; Shaw, J. A.; Meade, T. J., Electrochemistry of redox-active self-assembled monolayers. *Coordination Chemistry Reviews* **2010**, *254* (15), 1769-1802.

Chapter 5
Conductance of
Porphyrin Nanoring
Based Molecular
Nanowires

5.1 General Introduction

As the interest in charge transport through a molecular junction increases, the ability to manipulate the system has been developed.^{57, 97} Quantum interference is of great interest to molecular electronics because it can be used to control the molecular devices. This can be achieved through manipulation of the chemical structure or by electrostatic gating via a third electrode.^{78, 102} Here, a preliminary investigation into chemical design of porphyrin based nanorings is presented with the aim of investigating possible quantum interference effects.

5.1.1 Introduction

Porphyrin complexes are of particular interest for molecular electronics. Porphyrin macrocycles are highly conjugated and the basic structure (Figure 5.1) is composed of four pyrrole units linked by =CH- connections; the structure is able to coordinate with various metal ions such as iron, magnesium and zinc in the central cavity to form a stable structure where the ligands can be further functionalised. These characteristics make porphyrins an attractive molecule for single molecule conductance investigations.



Figure 5.1: Molecular structure of the simplest porphyrin, porphine.

The charge transport properties of (oligo-)porphyrin molecules can be investigated by direct electrical measurements.^{79, 103} This is where the molecule is attached to two electrodes and the charge flow through the molecule is measured. The oligo-porphyrins have been found to be capable of efficient long-range charge transport.

Sedghi *et al.* have shown that a series of oligo-porphyrin molecules can be trapped between two electrodes and the charge flow through the porphyrin molecule can be measured, Figure 5.2.^{79a}

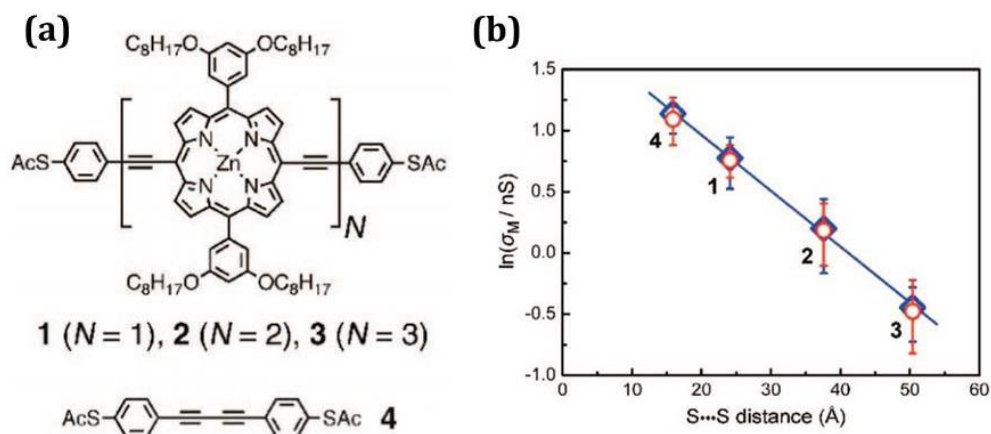


Figure 5.2: (a) Chemical structure of the oligo-porphyrin (1-3) and reference (5) molecules to be investigated. (b) $\ln(\text{conductance})$ vs. calculated sulfur-sulfur distance of the molecule. Figure adapted from reference 79a.

The chemical structure of the investigated oligo-porphyrins and reference molecule can be seen in Figure 5.2 (a). The results show clear length dependence for the oligo-porphyrin molecules with a very low calculated attenuation factor of $\beta = (0.04 \pm 0.006) \text{ \AA}^{-1}$. Similar behaviour has been recorded for analogous compounds with a pyridyl anchoring group rather than a thiol anchoring group.^{79b} The summary of the conductance and length data are shown in Table 5.1

Table 5.1: Conductance results and calculated length for the oligo-porphyrin and reference molecules investigated by Sedghi *et al.* Data taken from reference 79b.

Molecule	Conductance / nS	Length / nm
1	(2.1 ± 0.3)	2.47
2	(1.2 ± 0.3)	3.82
3	(0.6 ± 0.2)	5.10
4	(3.0 ± 0.6)	1.65

The results in Table 1 confirm the capability of the oligo-porphyrin molecule to exhibit efficient charge transport for both shorter and longer porphyrins with a sulfur-sulfur distance of 5.10 nm. This result shows the potential of oligo-porphyrins for investigation into their interesting properties.

Ferreira *et al.* have shown that molecular wires with a length of up to 14 nm can exhibit efficient electrical charge transport, Figure 5.3.^{103d}

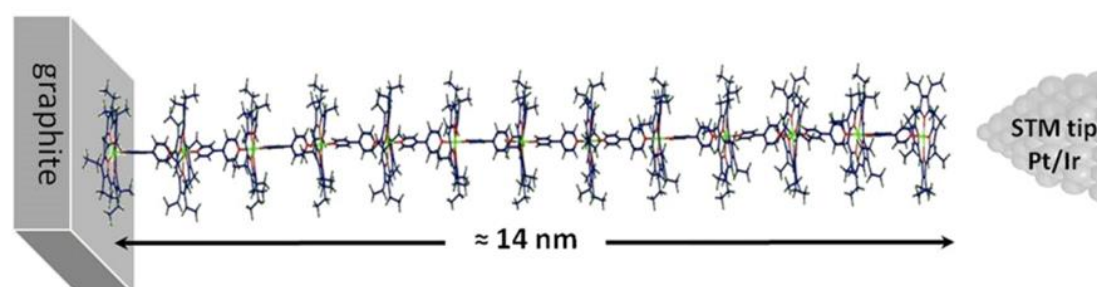


Figure 5.3: Scheme of 14 nm long porphyrin based molecular wire. Figure adapted from reference 103d.

The self-assembled molecular wires were prepared stepwise *in situ* by alternate binding of 4,4'-bipyridine and the zinc porphyrin with the longest molecular wire containing a total of 13 porphyrins separated by 12 bipyridine units. The conductance was investigated using scanning tunneling spectroscopy (tip height remains constant). From the conductance, an attenuation factor of $\beta = (0.015 \pm 0.006) \text{ \AA}^{-1}$ was calculated for molecules with a length of up to 6.5 nm, even lower than the one reported by Sedghi *et al.* This could be due to the porphyrins being linked via metal centre axial coordination, rather than via positions in the porphyrin rings as reported by Sedghi *et al.*⁷⁹ This result once again confirms the suitability of larger porphyrins for investigations into quantum interference.

Sprafke *et al.* have developed a synthetic strategy for preparing fully π -conjugated six-porphyrin nanorings.¹⁰⁴ The Anderson group have further functionalised a six-porphyrin nanoring suitable for connection to metal contacts (Figure 5.4).

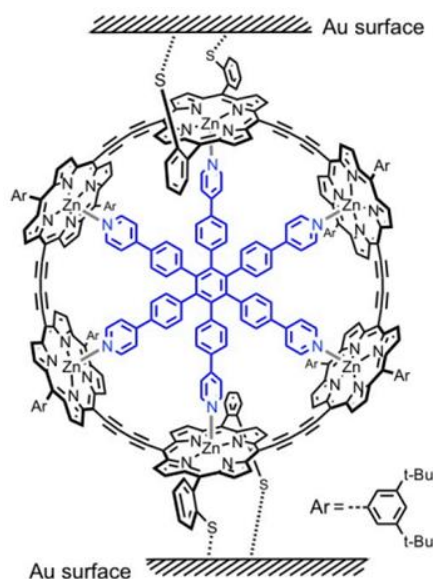


Figure 5.4: Chemical structure of six-porphyrin nanoring bound to gold electrode.

The complex has been developed with sulfur atoms ortho to the porphyrin moieties to ensure that the oligoporphyrin ring stands up rather than binding on its side (Figure 5.4). The thioester straps hold the sulfur atoms in place and are then removed *in situ* on the gold surface during single molecule conductance measurements. With these sulfur contacts, the conductance properties of these complexes could be investigated.

There is great interest in developing a single molecule switch that can operate at room temperature with a very high ON/OFF ratio. One possible way to achieve this, is to exploit quantum mechanical interference within the molecule so that the electron pathway from the source to drain is effectively broken. Quantum interference can be simply described by imagining a molecule which can allow charge transport between two points, A and B, by two different pathways, route 1 and 2 (Figure 5.5).⁵⁷

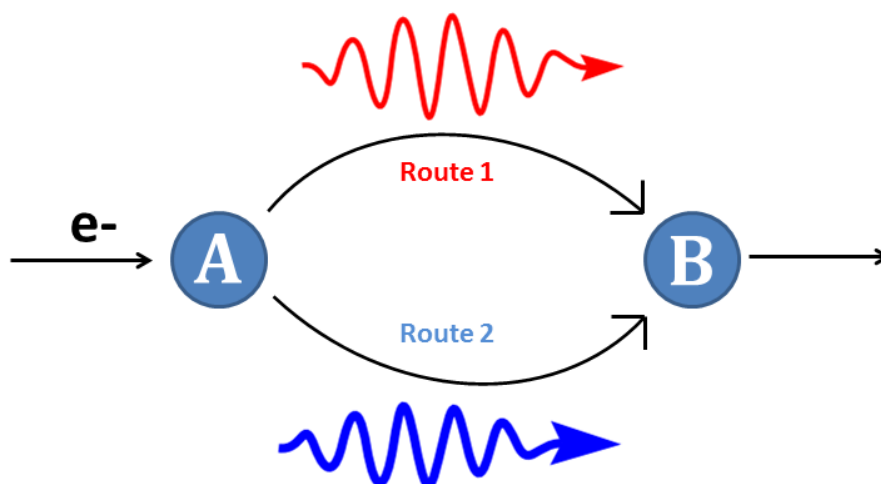


Figure 5.5: Schematic of quantum interference.

Constructive interference occurs when the wavefunctions for the two pathways are in phase, resulting in efficient transport and the system having a high conductance. Destructive interference occurs if the wavefunctions are out of phase so transport is blocked. Interference will only occur if the wavefunction simultaneously explores both routes, i.e. coherent transport. If the transport is incoherent hopping, then interference will not occur.

Investigations into charge transport are required to optimise this effect. In Figure 5.5, if the external environment is changed and effects the phase of wavefunction in route 1, relative to route 2 then route 2 will change whether interference is constructive or destructive. This phase shift could be created by changing the energy levels in one route, by the electric field of a nearby molecule or by the presence of a gate electrode.

Aradhya et al. have shown the effect of interference in molecular junctions by investigating *para*-stilbene and its *meta*-counterpart capped with thiol anchoring groups, Figure 5.6.¹⁰⁵

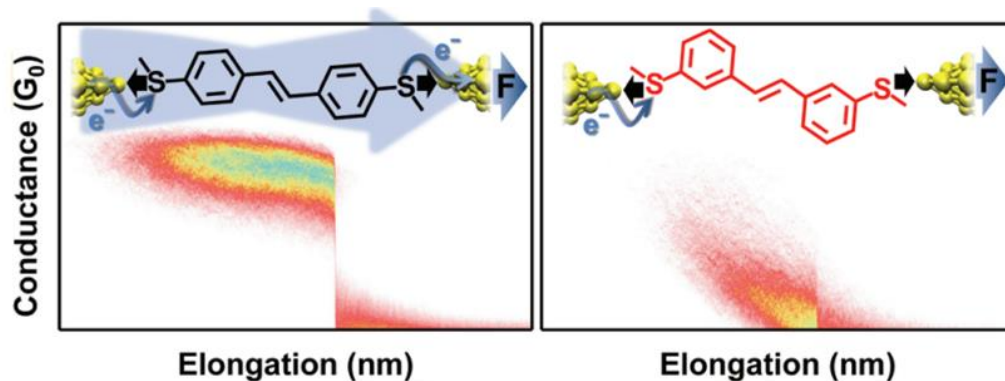


Figure 5.6: Schematic of the para-stilbene and meta-counterpart as reported by Aradhya *et al.*¹⁰⁵

The para-stilbene showed a conductance two orders of magnitude larger than the meta-stilbene. The meta-stilbene was expected to show a low transmission due to interference effects. Several other investigations into quantum interference effects have been completed.^{57, 102} Guédon *et al.* have investigated the conductance of linearly and cross conjugated molecules.¹⁰⁶ The conductance of the cross conjugated molecule was found to be two orders of magnitude lower than the linear conjugated molecule. Quantum interference effects have been found to be the cause for decreased conductance in a *meta*-coupled benzene compared to a *para*-coupled benzene.¹⁰⁷ Conductance measurements on a *meta*-oligo(3)-phenylenevinylene derivative was found to be an order of magnitude smaller than the corresponding *para*-oligo(3)-phenylenevinylene derivative.¹⁰⁸

These quantum interference investigations provide motivation for studying larger molecules such as the porphyrin based nanoring systems investigated in this study. Initially two nanorings will be investigated, the complete nanoring (Figure 5.7(A)) and the broken nanoring (Figure 5.7(B)). The conductance results will allow further development in the structure to further investigate quantum interference effects using the porphyrin based nanoring structure.

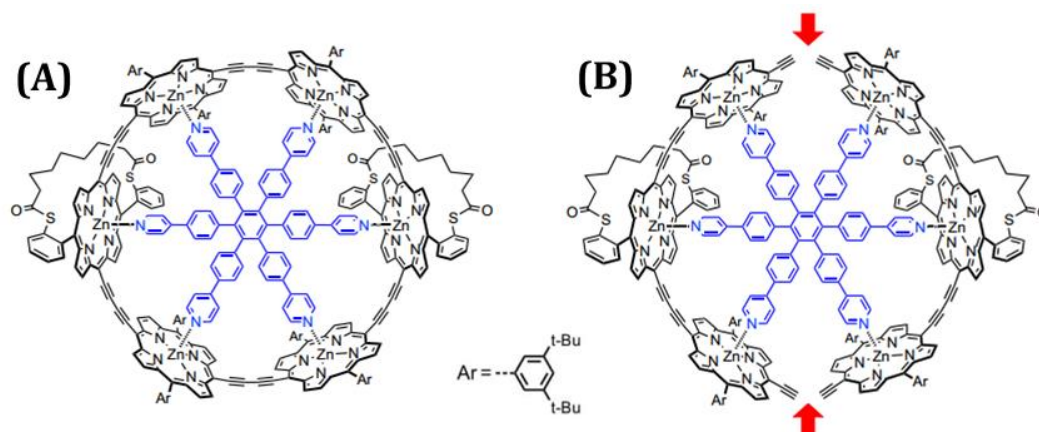


Figure 5.7: Chemical structure of the porphyrin based nanorings to be studied. (A) The complete nanoring (B) The broken nanoring, with the two breaks being signalled by the red arrows.

5.2 Aim

Conductance studies of these nanoring systems have not been previously been completed. The aim of this study is to demonstrate the conductance of two different nanorings can be measured using an STM in ambient and a mesitylene environment. This study acts as a preliminary investigation with the wider aim of developing the structure and performing conductance measurements on a range of nanorings to investigate the effect of quantum interference.

5.3 Methods

The nanorings were used as received from the group of Professor Harry Anderson of the University of Oxford, UK. The samples were prepared using commercial gold on glass slides (Arrandee®) which was flame annealed using a Bunsen burner immediately prior to use. The freshly annealed slide was immersed into a 6.9×10^{-6} M chloroform solution of the required nanoring for 2 min to allow the molecules to adsorb to the surface. The slide was then rinsed with EtOH and dried with N_2 to remove any physisorbed material. Au STM tips were prepared by cutting 0.25 mm Au wire (99.99 %, Goodfellow).

Conductance measurements were completed using an Agilent 5500 STM controller in conjunction with Agilent Picoscan 5.3.3 software. Measurements were completed in both ambient and a mesitylene environment. Mesitylene was distilled from sodium prior to use and was used in conjunction with an environmental chamber fitted to the STM head which was purged with N_2 . The

$I(s)$ method was utilised to measure the conductance with a setpoint currents (I_0) of 8, 20 and 60 nA and a bias voltage (V_{bias}) of + 0.6 V. The tip was withdrawn 4 nm relative to the setpoint and the scan duration was 0.1 s. The initial tip to sample distance (s_0) was approximated using the method described previously in Chapter 1 and, where appropriate, was used in conjunction with the experimental break off (ΔS) to calculate the total break off (S_{total}). Approximately 500 current-distance scans that exhibited a clear current plateau, were plotted into a histogram from which the molecular conductance was calculated.

5.4 Results

5.4.1 Conductance Measurements

The $I(s)$ technique was used to measure the conductance of the transition metal complexes. The measurements were completed in either an ambient environment or an mesitylene medium by rapidly withdrawing the tip at a predetermined setpoint of 8, 20 or 60 nA and a bias 0.6 V. Approximately 7 % of the $I(s)$ scans contained a plateau characteristic of a molecule bridging the gap between the tip and the substrate. The conductance was calculated via histogram analysis using the $I(s)$ scans that contained a plateau.

5.4.1.1: Complete Nanoring

The complete nanoring was the first complex to be studied. The compound was tested in two different environments, in air and in mesitylene and at three different setpoints 8, 20 and 60 nA.

In ambient conditions a conductance of (0.55 ± 0.11) nS was recorded at a bias of 0.6 V and a setpoint current of 8 nA. The average experimental break off value (Figure 5.8(c)) was calculated to be 1.6 nm and the calculated $d(\ln I)/d(s)$ value was 3.14 nm^{-1} which led to s_0 being 2.8 nm. This gives a total break off distance of (4.4 ± 0.54) nm which was compared to the gold separation distance calculated using Spartan®, which was 3.6 nm for the fully extended molecule. The data are shown in Figure 5.8.

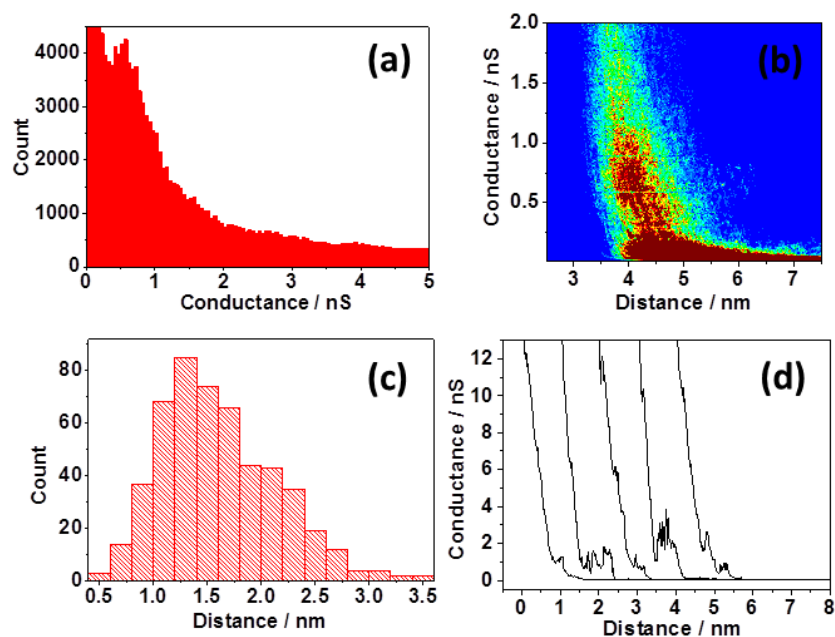


Figure 5.8: Data for Complete Nanoring in ambient conditions $V_{bias} = 0.6$ and $I_0 = 8$ nA (a) Histogram of 513 $I(s)$ scans (b) 2D histogram showing conductance relative to total break-off distance (c) Histogram of the experimental break-off distances (d) example $I(s)$ traces (distance is relative and does not represent actually break-off distance)

The complete nanoring was then measured with a set point of 20 nA and a tip bias of 0.6 V in an ambient environment. The data are shown in Figure 5.9. The measured conductance was calculated to be (2.45 ± 0.72) nS using the 1D histogram shown in Figure (a). The average experimental break off value (Figure 5.9(c)) was calculated to be 1.5 nm and the calculated $d(\ln I)/d(s)$ nm^{-1} value was 3.24 which led to s_0 being 2.4 nm. This gives a total break off distance of (3.9 ± 0.6) nm which was once again compared to the calculated gold separation distance of 3.6 nm for the fully extended molecule.

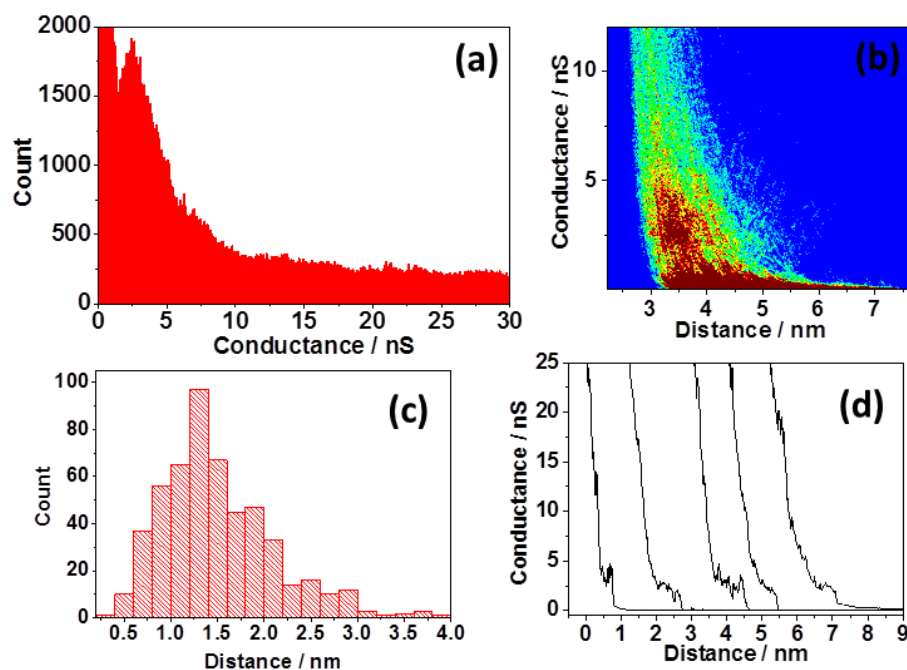


Figure 5.9: Data for Complete Nanoring in ambient conditions $V_{bias} = 0.6$ and $I_0 = 20$ nA (a) Histogram of 520 $I(s)$ scans (b) 2D histogram showing conductance relative to total break-off distance (c) Histogram of the experimental break-off distances (d) example $I(s)$ traces (distance is relative and does not represent actually break-off distance)

Finally the complete nanoring was measured in an ambient environment with a set point of 60 nA and a tip bias of 0.6 V, the data are presented in Figure 5.10. The measured conductance was (5.25 ± 1.15) nS calculated using the 1D histogram shown in Figure 5.10(a). The average experimental break off value (Figure 5.10(c)) was calculated to be 1.5 nm and the calculated $d(\ln I)/d(s)$ value was 4.07 nm^{-1} which led to s_0 being 1.6 nm. This gives a total break off distance of (3.1 ± 0.5) nm which was compared to the gold separation distance value for the fully extended molecule, 3.6 nm. This value corresponded well to the measured total break off distance; providing good evidence that nanoring molecular junctions were being formed.

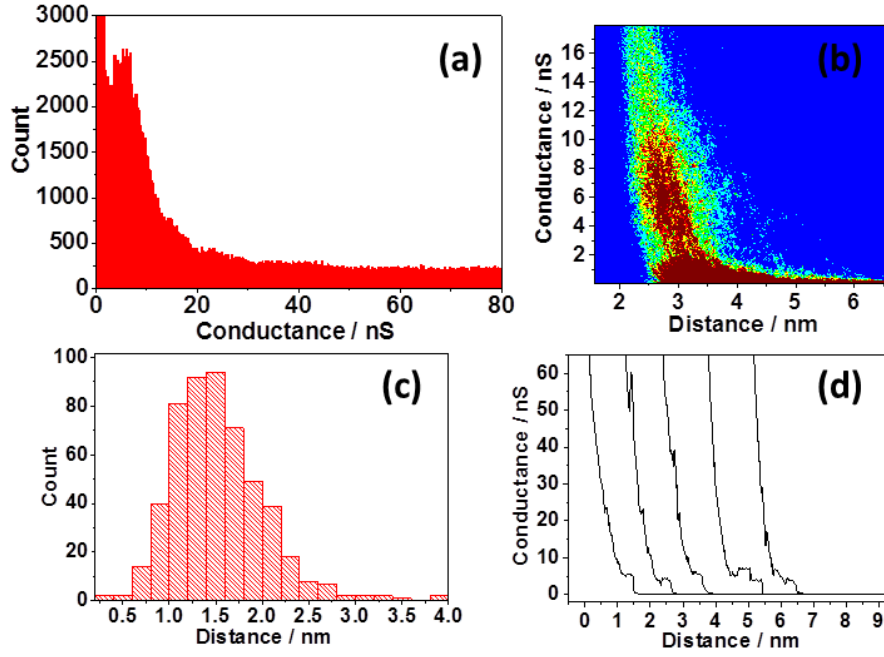


Figure 5.10: Data for Complete Nanoring in ambient conditions $V_{bias} = 0.6$ and $I_0 = 60$ nA
(a) Histogram of 526 $I(s)$ scans (b) 2D histogram showing conductance relative to total break-off distance (c) Histogram of the experimental break-off distances (d) example $I(s)$ traces (distance is relative and does not represent actually break-off distance)

A summary of the data for the complete nanoring in ambient conditions can be seen below in Table 5.2. It can be seen that there are three different conductance values measured and although the $d(\ln I)/d(s)$ values are low, the estimated total break off distance is in good agreement with the gold separation distance as calculated in Spartan®.

Table 5.2: Summary of the complete nanoring in ambient environment conductance data and estimated break off distance.

Set Point / nA	Conductance / nS	$d(\ln I)/d(s)$	s_0	Break off / nm	Estimated total Break off distance / nm	Gold separation as calculated by Spartan® / nm
8	(0.55 ± 0.11)	3.14	2.8	1.6	(4.4 ± 0.5)	3.6
20	(2.45 ± 0.72)	3.24	2.4	1.5	(3.9 ± 0.6)	
60	(5.25 ± 1.15)	4.07	1.6	1.5	(3.1 ± 0.5)	

The complex was then measured in mesitylene to see if this affected the conductance and the estimated total break off distance.

The complete nanoring was measured in an mesitylene environment with a set point of 8 nA and a tip bias of 0.6 V, the data are presented in Figure 5.11. The conductance was calculated to be (0.65 ± 0.15) nS using the 1D histogram shown in Figure 5.11(a). The average experimental break off value (Figure 5.11 (c)) was calculated to be 1.6 nm and the calculated $d(\ln I)/d(s)$ value was 7.39 nm^{-1} which led to s_0 being 1.2 nm. This gives a total break off distance of (2.8 ± 0.54) nm, compared to the gold separation distance for the fully extended molecule calculated using Spartan[®], of 3.6 nm.

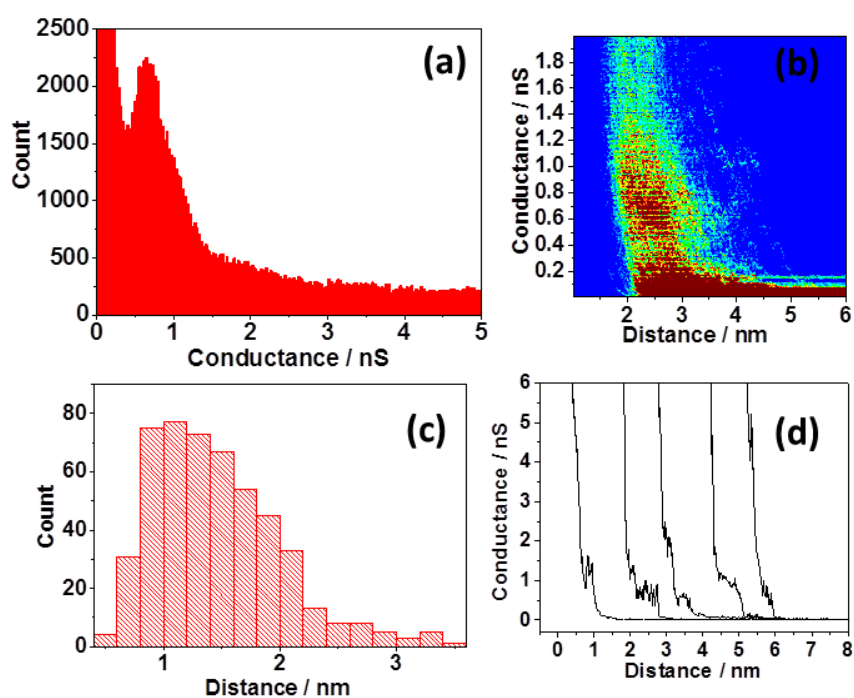


Figure 5.11: Data for Complete Nanoring in mesitylene conditions $V_{bias} = 0.6$ and $I_0 = 8$ nA
 (a) Histogram of 502 $I(s)$ scans (b) 2D histogram showing conductance relative to total break-off distance (c) Histogram of the experimental break-off distances (d) example $I(s)$ traces (distance is relative and does not represent actually break-off distance)

The nanoring was then measured in mesitylene at a set point of 20 nA and a tip bias of 0.6 V, the data can be seen in Figure 5.12. The measured conductance was (1.35 ± 0.29) nS, calculated using the 1D histogram shown in Figure 5.12(a). The average experimental break off value (Figure 5.12(c)) was calculated to be 1.5 nm and the calculated $d(\ln I)/d(s)$ value was 7.04 nm^{-1} which

led to s_0 being 1.1 nm. This gives a total break off distance of (2.6 ± 0.56) nm which was then compared to the gold separation distance of 3.6 nm for the fully extended molecule.

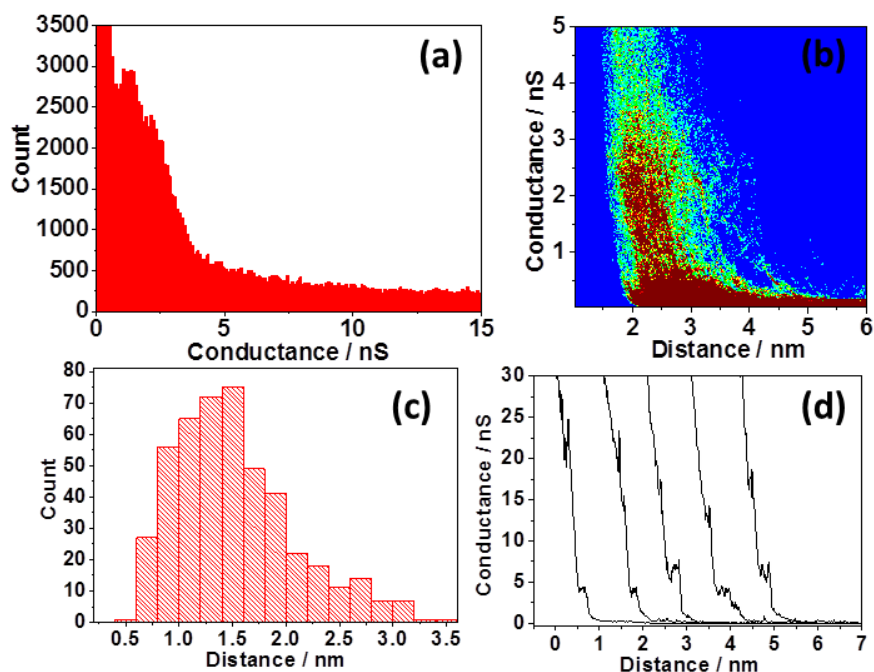


Figure 5.12: Data for Complete Nanoring in mesitylene conditions $V_{bias} = 0.6$ and $I_0 = 20$ nA (a) Histogram of 467 $I(s)$ scans (b) 2D histogram showing conductance relative to total break-off distance (c) Histogram of the experimental break-off distances (d) example $I(s)$ traces (distance is relative and does not represent actually break-off distance)

Finally the complete nanoring was measured in mesitylene with a set point of 60 nA and a tip bias of 0.6 V, the can be seen in Figure 5.13. Using the 1D histogram shown in Figure 5.13(a) the conductance was calculated to be (3.75 ± 1.2) nS. The average experimental break off value (Figure 1 5.13(c)) was calculated to be 1.5 nm and the calculated $d(\ln I)/d(s)$ value was 5.91 nm^{-1} which led to s_0 being 1.1 nm. This gives a total break off distance of (2.6 ± 0.59) nm which was compared to the gold separation distance calculated using Spartan[®], which was 3.6 nm for the fully extended molecule.

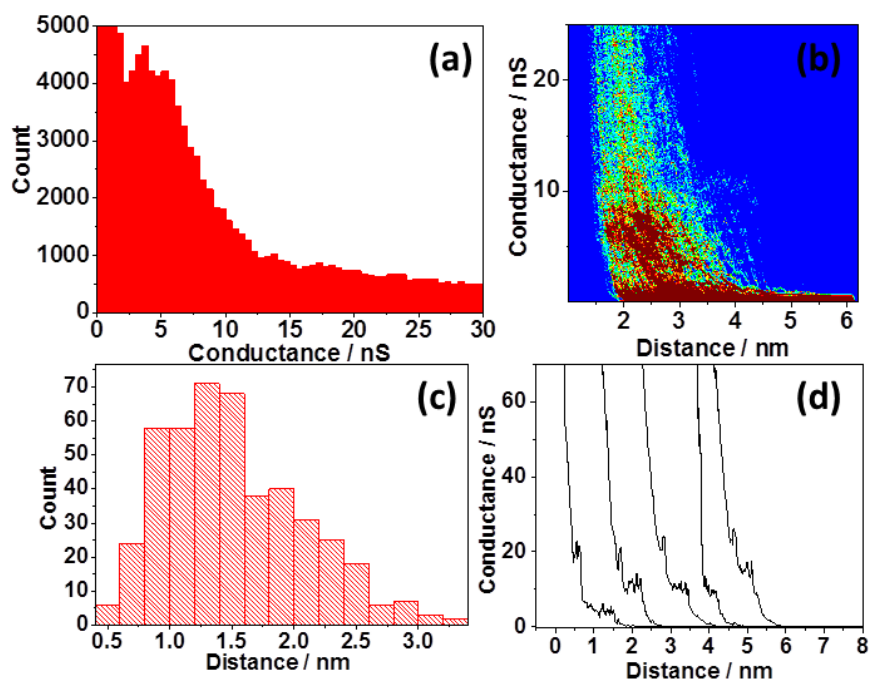


Figure 5.13: Data for Complete Nanoring in mesitylene conditions $V_{bias} = 0.6$ and $I_0 = 60$ nA
(a) Histogram of 455 $I(s)$ scans (b) 2D histogram showing conductance relative to total break-off distance (c) Histogram of the experimental break-off distances (d) example $I(s)$ traces (distance is relative and does not represent actually break-off distance)

A summary of the data recorded for the complete nanoring in ambient and a mesitylene environment can be seen below in Table 5.3. The break off distance is lower for the mesitylene environment which is due to higher $d(\ln I)/d(s)$ values being recorded.

Table 5.3: Summary of the complete nanoring data, including conductance and estimated break off distance.

Set Point / nA	Conductance / nS		Estimated Break off Distance / nm		Gold separation as calculated by Spartan [®] / nm
	Ambient	Mesitylene	Ambient	Mesitylene	
8	(0.55 ± 0.11)	(0.65 ± 0.15)	(4.4 ± 0.5)	(2.8 ± 0.54)	3.6
20	(2.45 ± 0.72)	(1.35 ± 0.29)	(3.9 ± 0.6)	(2.6 ± 0.56)	
60	(5.25 ± 1.15)	(3.75 ± 1.2)	(3.1 ± 0.5)	(2.6 ± 0.59)	

5.4.1.2: Broken Nanoring

The broken nanoring was initially measured in ambient environment with a set point of 8 nA and a tip bias of 0.6 V, the results can be seen in Figure 5.14. The conductance was calculated using the 1D histogram (Figure 5.14(a)) to be (0.27

± 0.09) nS. The average experimental break off value (Figure 5.14(c)) was calculated to be 1.4 nm and the calculated $d(\ln I)/d(s)$ value was 3.3 nm^{-1} which led to s_0 being 2.6 nm. This gives a total break off distance of $(4.0 \pm 0.55) \text{ nm}$ which was compared to the gold separation distance calculated using Spartan[®], which was 3.6 nm for the fully extended molecule.

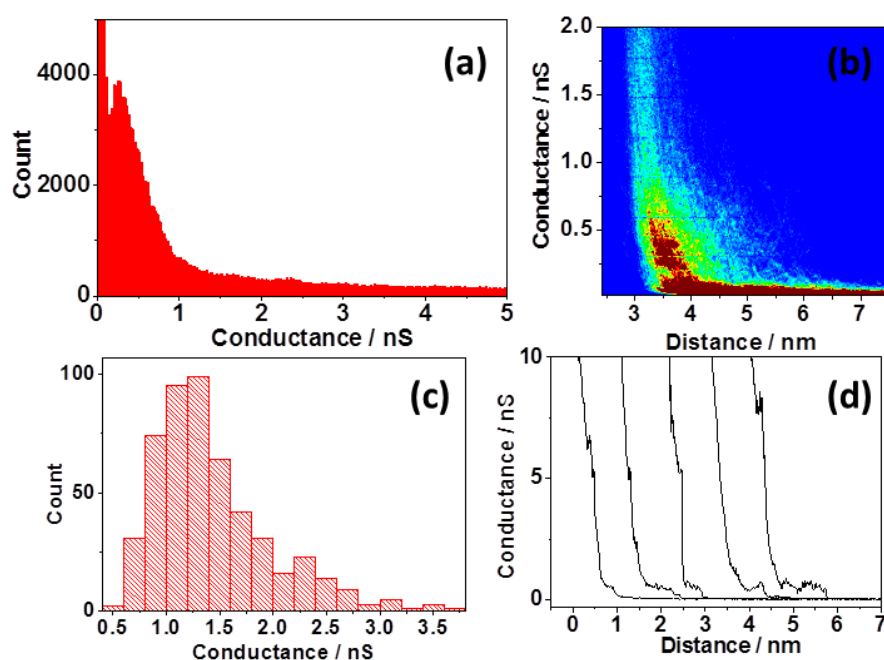


Figure 5.14: Data for Broken Nanoring in ambient conditions $V_{\text{bias}} = 0.6$ and $I_0 = 8 \text{ nA}$ (a) Histogram of 571 $I(s)$ scans (b) 2D histogram showing conductance relative to total break-off distance (c) Histogram of the experimental break-off distances (d) example $I(s)$ traces (distance is relative and does not represent actually break-off distance)

The broken nanoring was then measured in ambient environment with a set point of 20 nA and a tip bias of 0.6 V. The conductance was calculated to be $(1.5 \pm 0.56) \text{ nS}$ using the 1D histogram (Figure 5.15(a)). The average experimental break off value (Figure 5.15(c)) was calculated to be 1.2 nm and the calculated $d(\ln I)/d(s)$ value was 2.85 nm^{-1} which led to s_0 being 2.7 nm. A total break off distance of $(3.9 \pm 0.45) \text{ nm}$ was calculated which was then compared to the gold separation distance calculated using Spartan[®], which was 3.6 nm for the fully extended molecule.

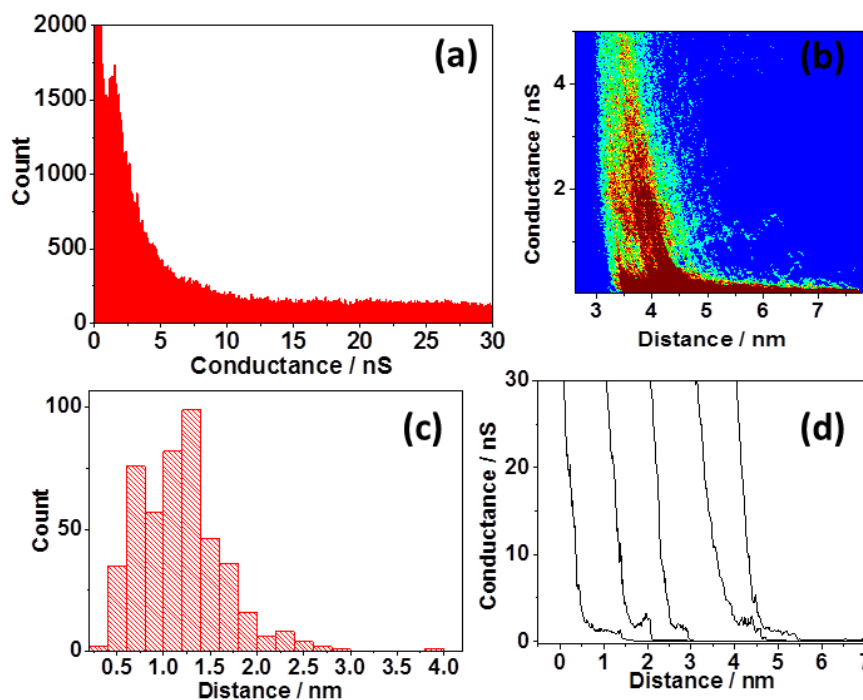


Figure 5.15: Data for Broken Nanoring in ambient conditions $V_{bias} = 0.6$ and $I_0 = 20$ nA (a) Histogram of 502 $I(s)$ scans (b) 2D histogram showing conductance relative to total break-off distance (c) Histogram of the experimental break-off distances (d) example $I(s)$ traces (distance is relative and does not represent actually break-off distance)

The broken nanoring was measured in ambient environment with a set point of 60 nA and a tip bias of 0.6 V, the data can be seen in Figure 5.16. The conductance was calculated using the 1D histogram (Figure 5.16(a)) to be (4.35 ± 1.05) nS. The average experimental break off value (Figure 5.16(c)) was calculated to be 1.1 nm and the $d(\ln I)/d(s)$ value was 3.3 nm^{-1} giving a s_0 of 2.0 nm. This gives a total break off distance of (3.1 ± 0.4) nm which was compared to the gold separation distance calculated using Spartan[®], which was 3.6 nm for the fully extended molecule.

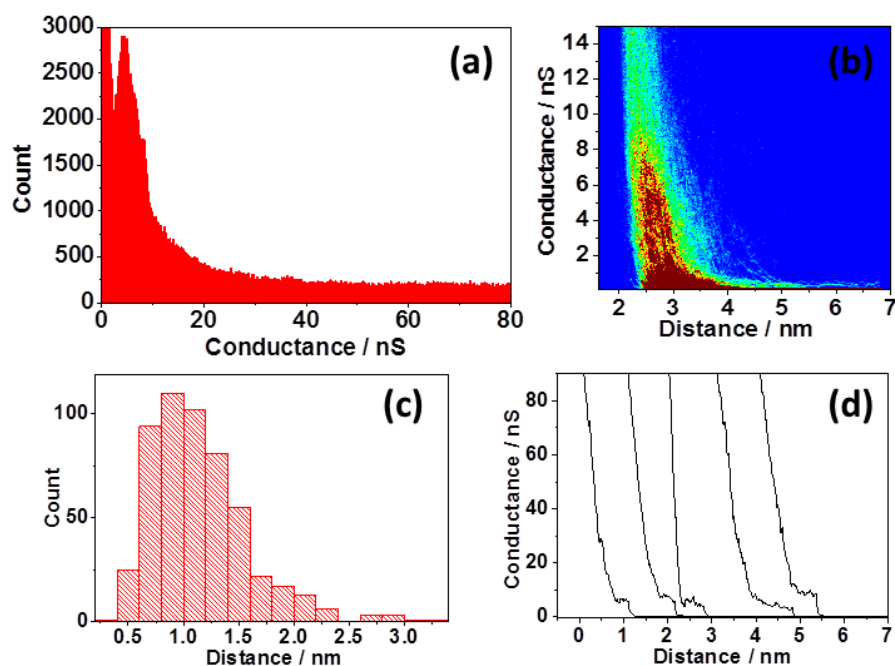


Figure 5.16: Data for broken Nanoring in ambient conditions $V_{bias} = 0.6$ and $I_0 = 60$ nA (a) Histogram of 582 $I(s)$ scans (b) 2D histogram showing conductance relative to total break-off distance (c) Histogram of the experimental break-off distances (d) example $I(s)$ traces (distance is relative and does not represent actually break-off distance)

A summary of the data recorded for the broken nanoring in ambient conditions is presented in Table 5.4. Three conductance values are observed. The total break off distance corresponds to the Au-Au separation in Spartan®.

Table 5.4: Summary of the broken nanoring in ambient environment conductance data and estimated break off distance.

Set Point / nA	Conductance / nS	Estimated total Break off distance / nm	Gold separation as calculated by Spartan® / nm
8	(0.27 ± 0.09)	(4.0 ± 0.55)	3.6
20	(1.5 ± 0.56)	(3.9 ± 0.45)	
60	(4.35 ± 1.05)	(3.1 ± 0.4)	

The broken nanoring was now measured in mesitylene environment with a set point of 8 nA and a tip bias of 0.6 V, the data are shown in Figure 5.17. The conductance was calculated using the 1D histogram (Figure 5.17(a)) to be (0.31 ± 0.08) nS. The average experimental break off value (Figure 5.17(c)) was calculated to be 1.5 nm and the calculated $d(\ln I)/d(s)$ value was 4.57 nm^{-1} giving a s_0 of 1.9 nm. This gives a total break off distance of (3.4 ± 0.54) nm which was

compared to the gold separation distance calculated using Spartan[®], which was 3.6 nm for the fully extended molecule.

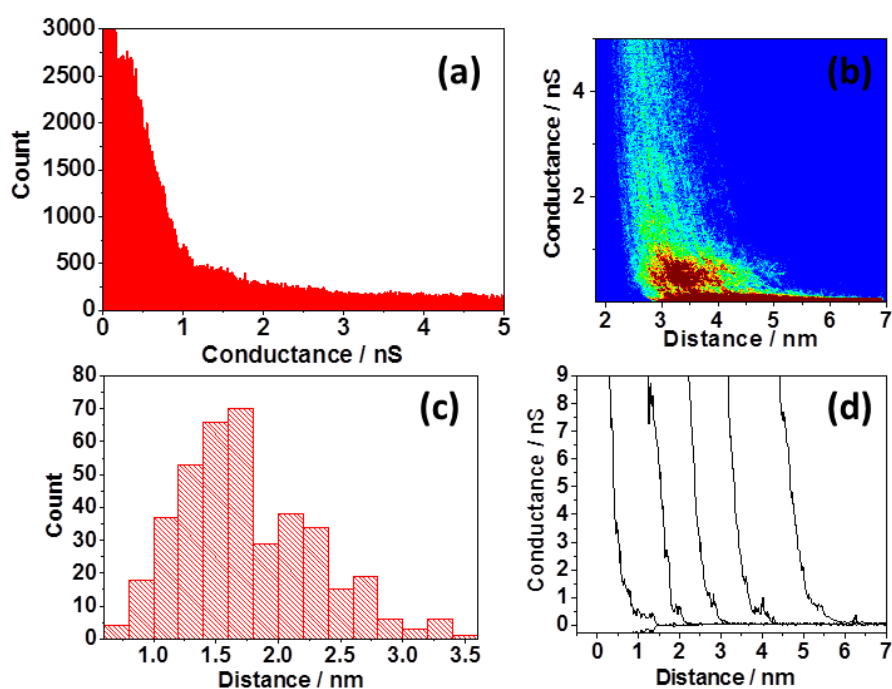


Figure 5.17: Data for Broken Nanoring in mesitylene conditions $V_{bias} = 0.6$ and $I_0 = 8$ nA
(a) Histogram of 399 $I(s)$ scans (b) 2D histogram showing conductance relative to total break-off distance (c) Histogram of the experimental break-off distances (d) example $I(s)$ traces (distance is relative and does not represent actually break-off distance)

The broken nanoring was now measured in mesitylene environment with a set point of 20 nA and a tip bias of 0.6 V; the data are shown in Figure 5.18. The conductance was calculated using the 1D histogram (Figure 5.18(a)) to be (1.25 ± 0.31) nS. The average experimental break off value (Figure 5.18(c)) was calculated to be 1.6 nm and the calculated $d(\ln I)/d(s)$ value was 3.99 nm^{-1} giving a s_0 of 1.9 nm. This gives a total break off distance of (3.5 ± 0.46) nm which was compared to the gold separation distance calculated using Spartan[®], which was 3.6 nm for the fully extended molecule.

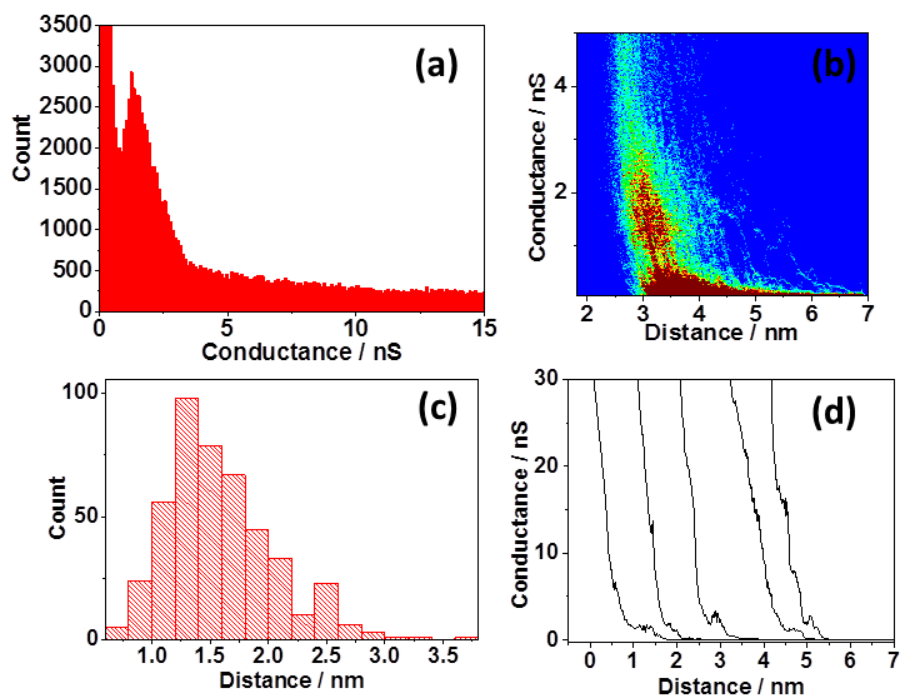


Figure 5.18: Data for broken Nanoring in mesitylene conditions $V_{bias} = 0.6$ and $I_0 = 20$ nA
(a) Histogram of 452 $I(s)$ scans (b) 2D histogram showing conductance relative to total break-off distance (c) Histogram of the experimental break-off distances (d) example $I(s)$ traces (distance is relative and does not represent actually break-off distance)

The broken nanoring was now measured in mesitylene environment with a set point of 60 nA and a tip bias of 0.6 V, as shown in Figure 5.19. The conductance was calculated using the 1D histogram (Figure 5.19(a)) to be (3.68 ± 0.94) nS. The average experimental break off value (Figure 5.19(c)) was calculated to be 2.0 nm and the calculated $d(\ln I)/d(s)$ value was 3.76 nm^{-1} giving an s_0 of 1.8 nm. This translates to a total break off distance of (3.8 ± 0.53) nm, compared to the gold separation distance calculated using Spartan[®] of, 3.6 nm for the fully extended molecule.

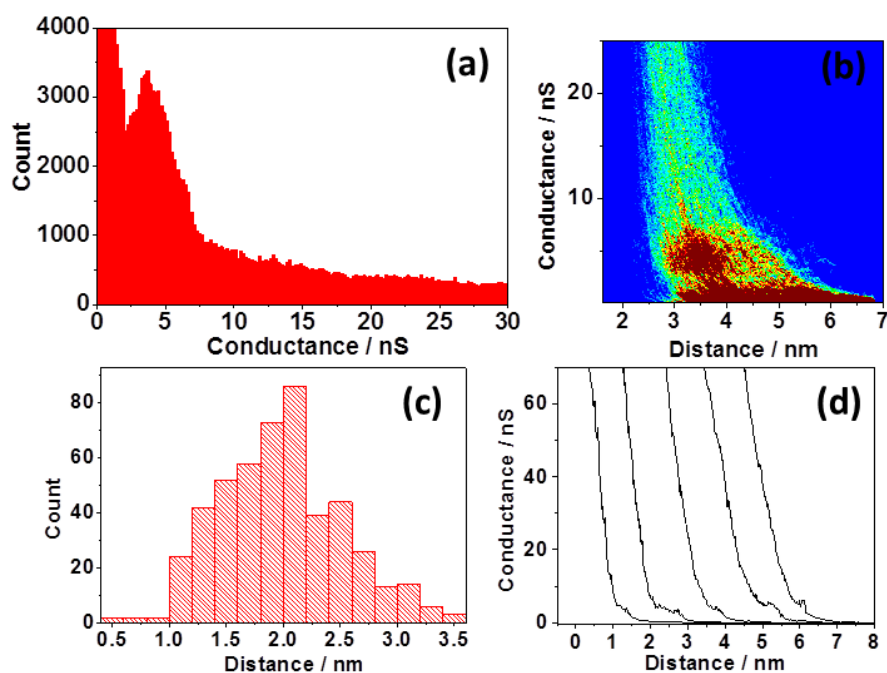


Figure 5.19: Data for broken Nanoring in mesitylene conditions $V_{bias} = 0.6$ and $I_0 = 60$ nA
(a) Histogram of 486 $I(s)$ scans (b) 2D histogram showing conductance relative to total break-off distance (c) Histogram of the experimental break-off distances (d) example $I(s)$ traces (distance is relative and does not represent actually break-off distance)

A summary of the broken nanoring data in ambient and a mesitylene environment is presented in Table 5.5.

Table 5.5: Summary of the broken nanoring data, including conductance and estimated break off distance.

Set Point / nA	Conductance / nS		Total Break off Distance / nm		Gold separation as calculated by Spartan® / nm
	Ambient	Mesitylene	Ambient	Mesitylene	
8	(0.27 ± 0.09)	(0.31 ± 0.08)	(4.0 ± 0.55)	(3.4 ± 0.54)	3.6
20	(1.5 ± 0.56)	(1.25 ± 0.31)	(3.9 ± 0.45)	(3.5 ± 0.46)	
60	(4.35 ± 1.05)	(3.68 ± 0.94)	(3.1 ± 0.4)	(3.8 ± 0.53)	

5.5: Discussion

A summary of the recorded single molecule conductance results can be seen in Table 5.6.

The results show that despite the porphyrin nanorings size (3.6 nm) and complex structure they have both proven successful at forming gold-molecule-gold junctions in two different environments. Both nanorings exhibited a low,

medium and high conductance group in the different environments. This result was unexpected as with four sulfur anchoring groups being able to bind in one of two ways (step edge or flat) several different conductance values would be expected if the system behaved as described in Chapter 1. It would be of interest to investigate how a differing amount of anchoring groups influences the conductance.

The low conductance results (set point 8 nA) correspond to the conductance result recorded for the oligo-porphyrins as seen in Table by Sedghi *et al.*^{79b} Although the two oligo-porphyrin is closer in length to the porphyrin ring, the three oligoporphyrin exhibits a conductance, 0.6 nS comparable to the low conductance recorded for the nanoring. This could be due to the oligoporphyrin having a direct straight pathway were as the nanoring has a circular porphyrin nanoring.

Table 5.6: Summary of the conductance data for porphyrin based Nanoring complexes.

Setpoint I(o) / nA	Conductance / nS			
	Ambient Environment		Mesitylene Environment	
	Complete	Broken	Complete	Broken
8	(0.55 ± 0.11)	(0.27 ± 0.09)	(0.65 ± 0.15)	(0.31 ± 0.08)
20	(2.45 ± 0.72)	(1.5 ± 0.56)	(1.35 ± 0.29)	(1.25 ± 0.31)
60	(5.25 ± 1.15)	(4.35 ± 1.05)	(3.75 ± 1.2)	(3.68 ± 0.94)

The conductance of the histograms for the measurements completed in mesitylene showed a clearer conductance peak than those recorded in ambient conditions. Previous literature investigations have shown mesitylene to be a good solvent for single molecule conductance measurements, and to remove any contamination that may be recorded in ambient conditions.⁶⁰ Both sets of conductance results are within experimental error of each other.

It can be seen from Table 5.6 that while the conductance of the complete nanoring is slightly higher than the broken nanoring under ambient conditions. This was not as great a difference as was expected from breaking two pathways through the molecule. The reason for this decrease in conductance has not yet been fully established but three possible ideas are:

1. The majority of charge transport flows through the template in the middle of the system for both nanorings resulting in the little change in conductance. The presence of the template could influence charge transport by holding the whole structure in a regular geometry, or by providing extra coupling pathways, however the π - π^* gap of the template is much larger than that of the porphyrin oligomer perimeter, so it is not expected to contribute directly to charge transport.
2. The broken nanoring is in fact binding to the gold surface through the broken acetylene moieties rather than the sulfur which would result in a conductance similar to the complete nanoring.
3. The “broken” acetylenes are close enough in proximity, so that the charge still flows, resulting in a similar conductance to the complete nanoring.

To establish whether the template is participating in the charge transport going through the nanoring, the template could be removed to see how this would affect the measured conductance.

Acetylene has been shown to be an effective anchoring group for single molecule conductance measurements.¹⁰⁹ The coordination of acetylene to metal atoms is well-known¹¹⁰ and they have a rich surface chemistry.¹¹¹ By developing the structure of the nanoring, the acetylene group could be eliminated and further investigations could occur.

A summary of the break off data are shown in Table 5.7.

Table 5.7: Summary of the estimated total break off distances for both nanorings.

Setpoint $I(0)$ / nA	Calculated Total Break-off / nm				Gold separation distance as calculated by Spartan [®] / nm
	Ambient Environment		Mesitylene Environment		
	Complete	Broken	Complete	Broken	
8	(4.4 ± 0.54)	(4.0 ± 0.55)	(2.8 ± 0.54)	(3.4 ± 0.54)	3.6
20	(3.9 ± 0.6)	(3.9 ± 0.45)	(2.6 ± 0.56)	(3.5 ± 0.46)	
60	(3.1 ± 0.5)	(3.1 ± 0.4)	(2.6 ± 0.59)	(3.8 ± 0.53)	

The calculated total break off distance corresponds to the length of both nanorings sandwiched between two gold atoms. The results in mesitylene are lower than the ambient measurements, this is due to the $d(\ln I)/d(s)$ value being higher in mesitylene resulting in a lower s_0 value.

The recorded results provide good evidence that it is the nanorings that are being measured and provide a basis to further investigate their transport properties.

5.6 Conclusions and Future Work

The single molecule conductance data has successfully shown that both nanorings can form molecular junctions. These results are the first conductance measurements of porphyrin nanorings and it has shown efficient charge transport through the system.

It is still not known what the electron pathway is through the molecule. Although the effects of quantum interference cannot be clearly defined with these preliminary investigation measurements on porphyrin based nanoring systems, the knowledge developed will assist in the development of the nanoring structure to allow quantum interference effects to be investigated which will help to contribute to the understanding of electronic transmission through single molecule devices.

Future work would be to develop the structure of the nanoring and then investigate the single molecule conductance. The structure could be changed by removing the template in the middle of the nanoring and comparing it to the complete nanoring system. The conductance of a half of a nanoring could be compared to the complete nanoring. The resulting acetylene could be changed to remove any chances of it interfering in the recorded result. The metal centre could also be varied from zinc to see if it also had any effect on the conductance.

This knowledge can eventually be used to assist the design and synthesis of other molecules where substituents added to the molecular structure enhance the operation of single molecule devices based on physical phenomena other than quantum interference.

5.7 References

1. Nichols, R. J.; Haiss, W.; Higgins, S. J.; Leary, E.; Martin, S.; Bethell, D., The experimental determination of the conductance of single molecules. *Physical Chemistry Chemical Physics* **2010**, *12* (12), 2801-2815.
2. Sun, L.; Diaz-Fernandez, Y. A.; Gschneidner, T. A.; Westerlund, F.; Lara-Avila, S.; Moth-Poulsen, K., Single-molecule electronics: from chemical design to functional devices. *Chemical Society Reviews* **2014**, *43* (21), 7378-7411.
3. Nichols, R. J.; Higgins, S. J., Molecular junctions: Interference comes into view. *Nat Nano* **2012**, *7* (5), 281-282.
4. Aradhya, S. V.; Venkataraman, L., Single-molecule junctions beyond electronic transport. *Nature Nanotechnology* **2013**, *8* (6), 399-410.
5. Sedghi, G.; Sawada, K.; Esdaile, L. J.; Hoffmann, M.; Anderson, H. L.; Bethell, D.; Haiss, W.; Higgins, S. J.; Nichols, R. J., Single molecule conductance of porphyrin wires with ultralow attenuation. *Journal of the American Chemical Society* **2008**, *130* (27), 8582-8583.
6. Kang, B. K.; Aratani, N.; Lim, J. K.; Kim, D.; Osuka, A.; Yoo, K.-H., Length and temperature dependence of electrical conduction through dithiolated porphyrin arrays. *Chemical Physics Letters* **2005**, *412* (4), 303-306; Yoon, D. H.; Lee, S. B.; Yoo, K.-H.; Kim, J.; Lim, J. K.; Aratani, N.; Tsuda, A.; Osuka, A.; Kim, D., Electrical conduction through linear porphyrin arrays. *Journal of the American Chemical Society* **2003**, *125* (36), 11062-11064; Kiguchi, M.; Takahashi, T.; Kanehara, M.; Teranishi, T.; Murakoshi, K., Effect of end group position on the formation of a single porphyrin molecular junction. *The Journal of Physical Chemistry C* **2009**, *113* (21), 9014-9017.
7. Sedghi, G.; García-Suárez, V. M.; Esdaile, L. J.; Anderson, H. L.; Lambert, C. J.; Martín, S.; Bethell, D.; Higgins, S. J.; Elliott, M.; Bennett, N., Long-range electron tunnelling in oligo-porphyrin molecular wires. *Nature Nanotechnology* **2011**, *6* (8), 517-523.
8. Ferreira, Q.; Bragança, A. M.; Alcácer, L.; Morgado, J., Conductance of Well-Defined Porphyrin Self-Assembled Molecular Wires up to 14 nm in Length. *The Journal of Physical Chemistry C* **2014**, *118* (13), 7229-7234.
9. Sprafke, J. K.; Kondratuk, D. V.; Wykes, M.; Thompson, A. L.; Hoffmann, M.; Drevinskas, R.; Chen, W.-H.; Yong, C. K.; Kärnbratt, J.; Bullock, J. E.; Malfois, M.; Wasielewski, M. R.; Albinsson, B.; Herz, L. M.; Zigmantas, D.; Beljonne, D.; Anderson, H. L., Belt-Shaped π -Systems: Relating Geometry to Electronic Structure in a Six-Porphyrin Nanoring. *Journal of the American Chemical Society* **2011**, *133* (43), 17262-17273.
10. Aradhya, S. V.; Meisner, J. S.; Krikorian, M.; Ahn, S.; Parameswaran, R.; Steigerwald, M. L.; Nuckolls, C.; Venkataraman, L., Dissecting Contact Mechanics from Quantum Interference in Single-Molecule Junctions of Stilbene Derivatives. *Nano Letters* **2012**, *12* (3), 1643-1647.
11. Guedon, C. M.; Valkenier, H.; Markussen, T.; Thygesen, K. S.; Hummelen, J. C.; van der Molen, S. J., Observation of quantum interference in molecular charge transport. *Nat Nano* **2012**, *7* (5), 305-309.
12. Arroyo, C. R.; Tarkuc, S.; Frisenda, R.; Seldenthuis, J. S.; Woerde, C. H. M.; Elkema, R.; Grozema, F. C.; van der Zant, H. S. J., Signatures of Quantum Interference Effects on Charge Transport Through a Single Benzene Ring. *Angewandte Chemie International Edition* **2013**, *52* (11), 3152-3155.

13. Arroyo, C.; Frisenda, R.; Moth-Poulsen, K.; Seldenthuis, J.; Bjornholm, T.; van der Zant, H., Quantum interference effects at room temperature in OPV-based single-molecule junctions. *Nanoscale Research Letters* **2013**, *8* (1), 234.
14. Nakashima, S.; Takahashi, Y.; Kiguchi, M., Effect of the environment on the electrical conductance of the single benzene-1, 4-diamine molecule junction. *Beilstein Journal of Nanotechnology* **2011**, *2* (1), 755-759.
15. Ballesteros, L. M.; Martín, S.; Momblona, C.; Marqués-González, S.; López, M. C.; Nichols, R. J.; Low, P. J.; Cea, P., Acetylene Used as a New Linker for Molecular Junctions in Phenylene–Ethynylene Oligomer Langmuir–Blodgett Films. *The Journal of Physical Chemistry C* **2012**, *116* (16), 9142-9150.
16. Buschbeck, R.; Low, P. J.; Lang, H., Homoleptic transition metal acetylides. *Coordination Chemistry Reviews* **2011**, *255* (1–2), 241-272.
17. Tao, F.; Xu, G. Q., Attachment Chemistry of Organic Molecules on Si(111)- 7×7 . *Accounts of Chemical Research* **2004**, *37* (11), 882-893.

Chapter 6

Conclusion

There is a huge amount of interest in the synthesis and electrical characterisation of molecules that have the potential for use in electronic devices. In order for this technology to move forward it is necessary to gain insights into structure-property relationships at the nanoscale, as well as a basic understanding of the charge transport through various molecular architectures. The main focus of this research project was to investigate the application of transition metal complexes for application in molecular electronics.

The conductance of bipyridine was initially investigated and the conductance was found to be the same in ambient and ionic liquid environment. The result corresponded to some literature values but a wide range has been reported due to different techniques and sample preparation. The investigation of the conductance of a series of $[M(\text{pyterpy})_2](\text{PF}_6)_n$ where $n = 2$ with $M = \text{Co}, \text{Fe}, \text{Ru}$ and $n = 3$ for $M = \text{Cr}$ sought to investigate the variation of transition metal centre and the effect on the single molecule conductance. These results showed the successful formation of a molecular junction. However, the results showed a remarkably small change of conductance upon variation of the transition metal centre. This was investigated in a different medium, ionic liquid BMIM-TFSA to explore whether this had any effect on the recorded conductance and to assess the suitability for conductance measurements as a function of potential. The conductance of the transition metal complexes was found to decrease slightly but did not change dramatically. The S_0 value was much higher in ionic liquid this could be due to the molecule also being measured, to counteract this just the experimentally measured break off distance could be used. Due to the pyridyl anchoring group having LUMO based transport resonance it is essentially ligand localised, confirming the result of the data presented here that the metal centre does not play a part in the conductance being dominated by hopping mechanism. This could be investigated by investigating a series of HOMO based transport molecules.

The electrochemistry of the series of $[M(\text{pyterpy})_2](\text{PF}_6)_n$ was investigated to establish the suitability for conductance measurements under potential control. This was done by locating the $M(\text{II})$ - $M(\text{III})$ redox potentials. The molecules were

measured in an acetonitrile solvent first and compared to literature values. The complexes were then investigated in ionic liquid.

The effect of the anchoring group on the conductance of transition metal complexes was investigated by measuring the single molecule conductance of pyridyl and methyl sulphide terminated bis-terpyridine transition metal complexes. The single molecule conductance of the methyl sulphide anchoring group complex was found to be higher than the pyridyl anchoring group, the anchoring group did not have as much of an effect as expected because the ligands are the limiting factor in the transport. The relationship between length and conductance was then probed by adjusting the structure of the ligand to incorporate more phenyl rings as the systems length increased. The data presented an attenuation factor of $\beta = 0.106$ and 0.109 \AA^{-1} for the pyridyl and thioether anchoring group respectively. This result is in the range reported for conjugated systems and infers a hopping transport mechanism.⁴⁰ This needs to be further investigated with a temperature controlled study. The difference in results reported for the multiple metal-terpyridine molecular wires reported by Kim *et al.* can be explained by the higher metal to ligand ratio, which allows the metallic properties to have a stronger influence on the charge transport.⁹⁰

The next study detailed the conductance results of $[\text{M}(\text{pyterpy})_2](\text{PF}_6)_n$ with $\text{M} = \text{Co}$ and Fe , under potential control. The first part was the study of the electrochemical behaviour of a monolayer of each of the complexes formed on an Au(111) surface. $\text{M}(\text{II})$ - $\text{M}(\text{III})$ redox peaks were seen and the rate constants were calculated. The single molecule conductance measurements were investigated as a function of potential control, and showed a clear increase in potential at the redox potential of the $[\text{M}(\text{pyterpy})_2](\text{PF}_6)_n$ complex. This behaviour is somewhat unexpected due to the behaviour previously reported in the literature by Zhou *et al.*⁶⁸ but could be due to the much slower rate constant of the $[\text{M}(\text{pyterpy})_2](\text{PF}_6)_n$ complexes in ionic liquid or could be due to the differing sample preparation. Due to this experiment being completed in different medium, direct comparisons cannot be made. Further investigation is required to see how the cobalt and iron complexes behave in 1 M NaClO_4 and how the osmium complex behaves in ionic liquid. Another variation between

the two results is the sample preparation, Zhou et al. use a acetonitrile adsorbate solution which has been shown to form molecular bridges.¹¹² A dichloromethane solution is used in this study, experiments with different sample preparations could be performed to eliminate any difference.

Porphyrins have been shown to form molecular junctions and exhibit efficient charge transport.⁷⁹ Two 6-porphyrin nanoring have been investigated, one complete and one with two breaks in the 6-porphyrin ring with the aim of investigating quantum interference effects. This preliminary investigation showed the ability of the nanoring to form successful molecular junctions, but surprisingly the broken 6-porphyrin nanoring did not exhibit a conductance significantly different from the complete 6-porphyrin nanoring. This result showed the capability of the procedure to measure complex molecules and allowed the idea of the development of the structure to investigate quantum interference effects.

The result of the research in this thesis shows that transition metal complexes are an interesting molecule for single molecule conductance measurements and it is expected the study of these complexes will continue to grow substantially with the ease of synthesis, accessible redox potential and ligand variability.

6.1 References

1. Scheer, E., *Molecular electronics: an introduction to theory and experiment*. World Scientific: 2010; Vol. 1.
2. Kim; Beebe, J. M.; Olivier, C.; Rigaut, S.; Touchard, D.; Kushmerick, J. G.; Zhu, X. Y.; Frisbie, C. D., Temperature and Length Dependence of Charge Transport in Redox-Active Molecular Wires Incorporating Ruthenium(II) Bis(σ -arylacetylide) Complexes. *The Journal of Physical Chemistry C* **2007**, *111* (20), 7521-7526.
3. Zhou, X.-S.; Liu, L.; Fortgang, P.; Lefevre, A.-S.; Serra-Muns, A.; Raouafi, N.; Amatore, C.; Mao, B.-W.; Maisonhaute, E.; Schöllhorn, B., Do molecular conductances correlate with electrochemical rate constants? Experimental insights. *Journal of the American Chemical Society* **2011**, *133* (19), 7509-7516.
4. Solomun, T.; Christmann, K.; Baumgaertel, H., Interaction of acetonitrile and benzonitrile with the gold (100) surface. *The Journal of Physical Chemistry* **1989**, *93* (20), 7199-7208.
5. Sedghi, G.; García-Suárez, V. M.; Esdaile, L. J.; Anderson, H. L.; Lambert, C. J.; Martín, S.; Bethell, D.; Higgins, S. J.; Elliott, M.; Bennett, N., Long-range electron tunnelling in oligo-porphyrin molecular wires. *Nature Nanotechnology* **2011**, *6* (8), 517-523; Sedghi, G.; Sawada, K.; Esdaile, L. J.; Hoffmann, M.; Anderson, H. L.; Bethell, D.; Haiss, W.; Higgins, S. J.; Nichols, R. J., Single molecule conductance of porphyrin wires with ultralow attenuation. *Journal of the American Chemical Society* **2008**, *130* (27), 8582-8583.

Chapter 7

Experimental

7.1 General Experimental Procedures

7.1.1 Purification

All compounds and solvents were used as received unless described otherwise. If required, purification was completed to standard procedures according to Armarego and Perrin.¹¹³ Experiments required anhydrous conditions were performed using glassware that had been dried in the oven for 12 hrs, and solvent was degassed by bubbling with Ar for at least 15 minutes.

Acetonitrile was dried over 3Å molecular sieves followed by distillation under nitrogen atmosphere from calcium hydride.

2-acetylpyridine was freshly distilled under reduced pressure and used immediately.

Mesitylene was freshly distilled from Na under reduced pressure.

Tetrahydrofuran was freshly distilled under a nitrogen atmosphere from sodium/benzophenone ketyl radical anion.

Ionic Liquid was dried according to literature procedures by heating to 120 °C under a high-vacuum.¹¹⁴

7.1.2 Chromatography

Flash chromatography was completed using various solvents on Sigma-Aldrich technical grade silica gel used with an airline to apply pressure. Thin layer chromatography was completed on Merck silica gel 60 F-254 plates and the separation was visualised using UV light where possible. UV inactive compounds were visualised by staining with KMnO₄.

7.1.3 Analytical Data

NMR spectra were obtained using a Bruker AMX 400 (¹H, 400 MHz; ¹³C, 100 MHz) and referenced to an internal standard, tetramethylsilane.

Mass spectra were recorded on a Fisons Trio-1000 spectrometer using electrospray, electron or chemical ionization, dependent on the compound.

CHN analyses were recorded on a Fisons elemental analyser for fluorinated samples and an Isoprime Elemental Analyser for non-fluorinated samples.

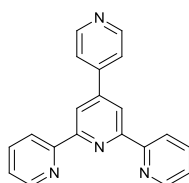
UV-Vis spectra were recorded in acetonitrile using a Perkin Elmer UV/Vis Lambda 5 spectrometer utilising UV WinLab software with a 1 cm path length in the range of 200-1100 nm.

IR was completed neat using a Bruker FTIR in the range of 4000 – 400 cm⁻¹.

Melting points were determined using Griffin melting point apparatus.

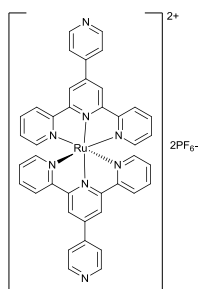
7.4 Syntheses

Preparation of 4'-(pyridin-4-yl)-2,2':6',2''-terpyridine.⁷¹ (3)



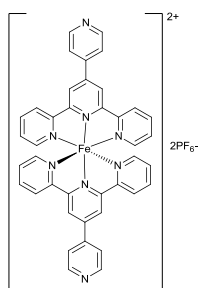
A solution of 4-pyridinecarboxaldehyde (5.76 g, 53.80 mmol) in MeOH (40 mL) was cooled to -15 °C, and solutions of 2-acetylpyridine (12.6 g, 104.7 mmol) in MeOH (20 mL) and 20 % aq NaOH (40 mL) were added simultaneously over a period of 20 minutes. The reaction mixture was then further stirred for 3 h at -10 °C. The solution was warmed to room temperature and filtered. The filtrate was then treated with NH₄OAc (1.0 g, 12.97 mmol) and heated to reflux for 4 h. The resulting solution was filtered and washed several times with hot water and hot ethanol. The title compound was recovered as a white solid (2.66 g, 15.9 %); m.p: 212-215 °C; ¹H-NMR (400 MHz, CDCl₃): 8.73 (d, J = 4.0 Hz, 4H, *aromatic*), 8.76 (dd, J = 5.0, 2.0 Hz, 2H, *aromatic*), 8.66 (d, J = 7.9 Hz, 2H, *aromatic*), 7.88 (td, J = 7.6, 1.76 Hz, 2H, *aromatic*), 7.78 (dd, J = 4.4, 1.6 Hz, 2H, *aromatic*), 7.37 (ddd, J = 7.3, 4.8, 1.0 Hz, 2H, *aromatic*); ¹³C-NMR (100 MHz, CDCl₃): 156.7, 156.1, 150.9, 149.6, 147.8, 146.3, 137.3, 124.5, 122.0, 121.7, 119.0; MS (ES⁺): m/z: 311 [M]⁺; Anal. Calc. C₂₀H₁₄N₄ (310.35): C, 77.40 %; H, 4.55 %; N, 18.05 %. Found: C, 76.48 %; H, 4.59 %; N, 18.04 %; UV/Vis (CH₃CN, 1.2 x 10⁻⁵ mol dm⁻³) λ_{max}/nm (ε_{max}/10³ dm³ mol⁻¹ cm⁻¹): 316 (sh), 278 (67.1), 239 (104.5).

Preparation of Ru(4'-(pyridin-4-yl)-2,2':6',2''-terpyridine)₂(PF₆)₂.⁷² (4)



A solution of $\text{RuCl}_3 \cdot 3\text{H}_2\text{O}$ (0.019g, 0.120 mmol) and 4'-(pyridin-4-yl)-2,2':6',2''-terpyridine (0.098 g, 0.316 mmol) in ethane-1,2-diol (10 mL) was heated to reflux for 3 h. The solution was allowed to cool, and water (10 mL) and an excess of methanolic $[\text{NH}_4][\text{PF}_6]$ were added. The resulting dark brown precipitate was collected on Celite by filtration and then redissolved in CH_3CN . The CH_3CN was evaporated to minimum volume, and purification was by flash column chromatography (SiO_2 , eluting with acetonitrile: saturated potassium nitrate: water (7:1:0.5)). The first major orange fraction was collected, an excess of methanolic $[\text{NH}_4][\text{PF}_6]$ was added, and the solution reduced in volume to precipitate $[\text{Ru}(4'-(\text{pyridin-4-yl})-2,2':6',2''\text{-terpyridine})_2][\text{PF}_6]_2$. The compound was filtered and dried in air to yield the title compound as a red solid (0.05 g, 40 %). $^1\text{H-NMR}$ (CD_3CN), 400 MHz): 9.06 (s, 4H), 8.97 (dd, $J = 4.4, 1.7$ Hz, 4H), 8.66 (d, $J = 8.1$ Hz, 4H), 8.13 (dd, $J = 1.6, 4.4$ Hz, 4H), 7.97 (td, $J = 7.8, 1.4$ Hz, 4H), 7.42 (d, $J = 4.8$ Hz, 4H), 7.19 (m, 4H); $^{13}\text{C-NMR}$ (100 MHz, CD_3CN): 158.4, 156.3, 153.1, 151.3, 138.8, 128.2, 125.3, 124.7, 122.6, 122.4; MS (ES^+ , CH_3OH): m/z : 722 $[\text{M} - 2\text{PF}_6]^+$, 868 $[\text{M} - \text{PF}_6]^+$; UV/Vis (CH_3CN , 1.2×10^{-5} mol dm^{-3}) $\lambda_{\text{max}}/\text{nm}$ ($\epsilon_{\text{max}}/10^3 \text{ dm}^3 \text{ mol}^{-1} \text{ cm}^{-1}$): 490 (25.1), 313 (56), 275 (84.3).

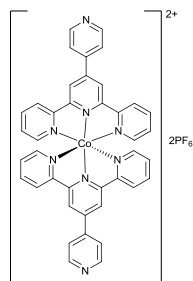
Preparation of $\text{Fe}(4'-(\text{pyridin-4-yl})-2,2':6',2''\text{-terpyridine})_2(\text{PF}_6)_2$.^{69b} (5)



A solution of $\text{FeCl}_2 \cdot 4\text{H}_2\text{O}$ (0.064g, 0.32 mmol) and 4'-(pyridin-4-yl)-2,2':6',2''-terpyridine (0.20 g, 0.64 mmol) in methanol (30 mL) was stirred at room temperature for 30 minutes. Excess aqueous $[\text{NH}_4][\text{PF}_6]$ was added. The

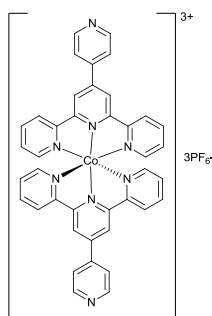
resulting purple precipitate was collected on celite by filtration, washed with H₂O, EtOH and Et₂O and redissolved in CH₃CN. The solvent was removed *in vacuo* to yield the title compound as a purple solid. (0.2 g, 64 %); ¹H-NMR (CD₃CN), 400 MHz): 9.24 (s, 4H), 9.02 (dd, J = 4.5, 1.5 Hz, 4H), 8.63 (d, J = 8.0 Hz, 4H), 8.24 (dd, J = 4.4, 1.5 Hz, 4H), 7.91 (td, J = 7.8, 1.2 Hz, 4H), 7.18 (d, J = 5.1 Hz, 4H), 7.10 (td, J = 6.2, 1.1 Hz, 4H); ¹³C-NMR (100 MHz, CD₃CN): 161.24, 158.30, 153.67, 151.77, 139.51, 128.06, 124.65, 122.58, 122.32; MS (ES⁺, CH₃OH): m/z: 821.2 (-PF₆), 695.2 (-P₂F₁₁); UV/Vis (CH₃CN, 1.2 x 10⁻⁵ mol dm⁻³) λ_{max}/nm (ε_{max}/10³ dm³ mol⁻¹ cm⁻¹): 569 (14.6), 324 (29.2), 284 (59.6), 276 (sh).

Preparation of Co(4'-(pyridin-4-yl)-2,2':6',2''-terpyridine)₂(PF₆)₂⁷³ (6)



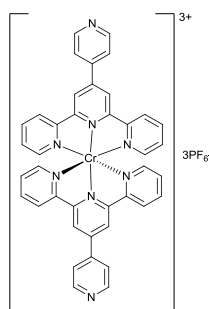
4'-(Pyridin-4-yl)-2,2':6',2''-terpyridine (0.093 g, 0.3 mmol) was partially dissolved in acetone (15 mL). In a separate flask, an excess of CoCl₂·6H₂O (0.142g, 0.597 mmol) was completely dissolved in water (20 mL). The two solutions were combined resulting in an immediate colour change to reddish-orange. The reaction mixture was allowed to stand in open air at room temperature for 1 h. Water (80 mL) was next added to the reaction mixture to dilute the acetone. The solution was filtered to remove any insolubles such as free ligand. The remaining filtrate was collected and an excess of NH₄PF₆ (0.30 g, 1.84 mmol) was added resulting in the precipitation of the desired product. The isolated solid was washed with water, and washed/dried with diethyl-ether yielding the product as a red solid. (0.148 g, 50 %); MS (ES⁺, CH₃OH): m/z: 824.2 (-PF₆), 698.2 (-P₂F₁₁); UV/Vis (CH₃CN, 1.2 x 10⁻⁵ mol dm⁻³) λ_{max}/nm (ε_{max}/10³ dm³ mol⁻¹ cm⁻¹): 323 (60.8), 283 (sh), 276 (145.1).

Preparation of Co(4'-(pyridin-4-yl)-2,2':6',2''-terpyridine)₂(PF₆)₃⁷³ (7)



Co(4'-(pyridin-4-yl)-2,2':6',2''-terpyridine)₂(PF₆)₂ (0.01 g, 0.010 mmol) was suspended in H₂O (1 mL) and a saturated solution of aqueous Br₂ (1 drop neat Br₂ in 1 mL H₂O) was added to give a bright orange suspension. The reaction mixture was stirred at room temperature for 20 h, whereupon an excess of aqueous NH₄PF₆ was added. The orange precipitate that formed was collected by filtration through celite, washed well with H₂O, EtOH and Et₂O, and then redissolved in CH₃CN. The solvent was removed *in vacuo* and Co(4'-(pyridin-4-yl)-2,2':6',2''-terpyridine)₂(PF₆)₃ was isolated. ¹H-NMR (CD₃CN), 400 MHz): δ = 9.31 (s, 4H), 9.11 (d, J = 6.33 Hz, 4H), 8.71 (d, J = 8.63 Hz, 4H), 8.40 (d, J = 6.29, 4H), 8.29 (td, J = 7.82, 1.07 Hz, 4H), 7.48 (td, J = 5.97, 1.24 Hz, 4H), 7.39 (d, J = 5.227, 4H).

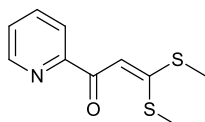
Preparation of Cr(4'-(pyridin-4-yl)-2,2':6',2''-terpyridine)₂(PF₆)₃.^{74b, 115} (8)



To degassed water (30 mL) was added 4'-(pyridin-4-yl)-2,2':6',2''-terpyridine (0.67 g, 2.19 mmol) and CrCl₂ (0.135 g, 1.10 mmol). The solution was stirred at room temperature for 20 h during which time the colour changed from light blue to dark brown. A degassed solution of aqueous NH₄PF₆ (5 mL; 0.44 M, 2.20 mmol) was added and a precipitate formed. The solid was filtered through a Schlenk frit and the solid was washed with 50 mL of degassed water. The solid was dried under vacuum, reconstituted in dry CH₃CN and filtered. Cr(4'-(pyridin-4-yl)-2,2':6',2''-terpyridine)₂(PF₆)₂ was dissolved in CH₃CN (2 mL).

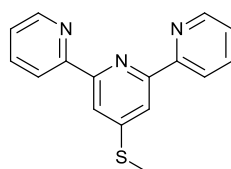
Separately AgPF₆ (30 mg, 0.12 mmol) was dissolved in CH₃CN (1 mL) and this solution was added over 20 s to the stirring solution. After 15 minutes the CH₃CN was removed under vacuum to afford a brown residue. The product was reconstituted in CH₃CN and filtered through Celite, and the solvent was removed under vacuum. The residue was triturated, then washed with THF, and dried under vacuum to give the title compound as an orange solid. (0.45 g, 37 %); UV/Vis (CH₃CN, 1.2 x 10⁻⁵ mol dm⁻³) λ_{max}/nm (ε_{max}/10³ dm³ mol⁻¹ cm⁻¹): 368 (21), 318 (sh), 282 (89.2).

Preparation of 3,3-bis(methylthio)-1-(pyridin-2-yl)prop-2-en-1-one.⁹³ (14)



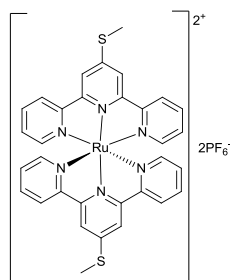
2-Acetylpyridine (4.97 g, 41.0 mmol) was added dropwise over a period of 5-10 minutes to a stirring solution of potassium *tert*-butoxide (9.65 g, 85.9 mmol) in anhydrous THF (100 mL) under N₂ at room temperature. Carbon disulfide (3.17 g, 41.6 mmol) was added to the stirring solution over a period of 3 minutes. Once the addition was complete methyl iodide (12.31 g, 86.7 mmol) was added over a period of 10 minutes. The mixture was stirred for a further 12 h. The reaction mixture was cooled in an ice bath for 4 h after which time a yellow precipitate had formed. The precipitate was collected by filtration, dried and recrystallised from EtOH to yield the title compound as yellow crystals (4.61 g, 50 %); m.p: 100-104 °C; ¹H NMR (400 MHz, CDCl₃) δ = 8.63 (m, 1H), 8.18 (dt, J = 7.8, 1.1 Hz, 1H), 7.83 (dt, J = 7.6, 1.7 Hz, 1H), 7.64 (s, 1H, C-H), 7.39 (ddd, J = 7.5, 4.76, 1.2 Hz, 1H), 2.64 (s, 3H, S-CH₃), 2.56 (s, 3H, S-CH₃); ¹³C NMR (100MHz, CDCl₃) δ =184.77 (C=O), 168.2 (HC=C-S), 155.4, 148.9, 137.4, 126.3, 123.0, 109.2 (HC=C-S₂), 17.9 (H₃C-S), 15.5 (H₃C-S); MS (CI+ (NH₃)): m/z 226 [M]⁺; Anal. Calc. for C₁₀H₁₁NOS₂ (225.33): C, 53.30 %; H, 4.92 %; N, 6.22 %; Found: C, 53.19 %; H, 4.84 %; N, 6.07 %; IR (neat) ν_{max} cm⁻¹: 1619.91 (C=O).

Preparation of 4'-(methylthio)-2,2':6',2''-terpyridine.⁹³ (16)



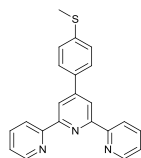
Added to a solution of potassium tert-butoxide (0.1 g, 0.89 mmol) in anhydrous THF (10 mL) under N₂ at room temperature was 2-acetylpyridine (0.54 g, 4.4 mmol). The resultant solution was stirred for 10 minutes prior to the addition of 3,3-bis(methylthio)-1-(pyridin-2-yl)prop-2-en-1-one (1.0 g, 4.4 mmol). The reaction mixture was stirred for 12 h at room temperature during which time a red solid precipitated. The mixture was treated with ammonium acetate (3.42 g, 44.37 mmol) and glacial acetic acid (11.1 mL). The THF was removed by distillation. The remaining grey solution was chilled to 15 °C and allowed to stand for 3 h. A grey material precipitated and was collected by filtration, washed with cold water and dried in air. The crude product was taken up in boiling EtOH, filtered and the filter cake rinsed with hot EtOH. The combined filtrates were diluted with water and allowed to cool to room temperature. The resulting precipitate was collected by filtration, washed with 50 % aqueous EtOH and dried in vacuo to yield the title compound as grey crystals (0.64 g, 52 %); m.p: 105-110 °C; ¹H NMR (400 MHz, CDCl₃) δ = 8.61 (m, 4H), 8.32 (s, 2H, C-H), 7.85 (dt, J = 7.8, 1.8 Hz, 2H), 7.34 (ddd, J = 7.4, 4.8, 1.2 Hz, 2H), 2.66 (s, 3H, S-CH₃); ¹³C NMR (100 MHz, CDCl₃) δ = 156.4, 155.3, 152.9 (C-S-CH₃), 149.5, 137.3, 124.3, 121.8, 117.3, 14.4 (S-CH₃); MS (CI⁺ (NH₃)): m/z: 280 [M]⁺; Anal. Calc. C₁₆H₁₃N₃S (279.36): C, 68.79 %; H, 4.69 %; N, 15.04 %; Found: C, 69.03 %; H, 4.21 %; N, 14.55 %; IR (neat) ν_{max} cm⁻¹: 1558, 1392; UV/Vis (CH₃CN, 9 x 10⁻⁶ mol dm⁻³) λ_{max}/nm (ε_{max}/10³ dm³ mol⁻¹ cm⁻¹): 277 (103.7)

Preparation of Ru(4'-(methylthio)-2,2':6',2''-terpyridine)₂(PF₆)₂ (24)



A solution of $\text{RuCl}_3 \cdot 3\text{H}_2\text{O}$ (0.19 g, 1.20 mmol) and 4'-(methylthio)-2,2':6',2''-terpyridine (0.66 g, 2.4 mmol) in ethane-1,2-diol (100 mL) was heated to reflux for 12 h. The solution was allowed to cool, and water (10 mL) and an excess of methanolic $[\text{NH}_4][\text{PF}_6]$ were added. The resulting dark brown precipitate was collected on Celite by filtration and then redissolved in CH_3CN . The CH_3CN was evaporated to minimum volume, and purification was by flash column chromatography (SiO_2 , eluting with acetonitrile: saturated potassium nitrate: water (7:1:0.5)). The first major orange fraction was collected, an excess of methanolic $[\text{NH}_4][\text{PF}_6]$ were added, and the solution reduced in volume to precipitate $[\text{Ru}(4'-(\text{methylthio})-2,2':6',2''\text{-terpyridine})_2][\text{PF}_6]_2$. The compound was filtered and dried in air to yield the title compound as a red solid (0.21 g, 20 %); $^1\text{H-NMR}$ (CD_3CN , 400 MHz): 8.54 (s, 4H), 8.51 (d, $J = 8.0$ Hz, 4H), 7.90 (td, $J = 9.1, 1.3$ Hz, 4H), 7.38 (d, $J = 5.0$ Hz, 4H), 7.16-7.14 (m, $J = 14.3$ Hz, 4H), 2.93 (s, *S-CH₃*, 6H); $^{13}\text{C-NMR}$ (100 MHz, CD_3CN): 158.41, 155.09, 153.08, 138.43, 128.03, 124.98, 120.14, 14.84 (*S-CH₃*); MS (ES+, CH_3OH): m/z : 805.0 (- PF_6), 679.1 (- P_2F_{11}); UV/Vis (CH_3CN , 9×10^{-6} mol dm^{-3}) $\lambda_{\text{max}}/\text{nm}$ ($\epsilon_{\text{max}}/10^3$ $\text{dm}^3 \text{mol}^{-1} \text{cm}^{-1}$): 491 (11.2), 301 (sh), 281 (115.6).

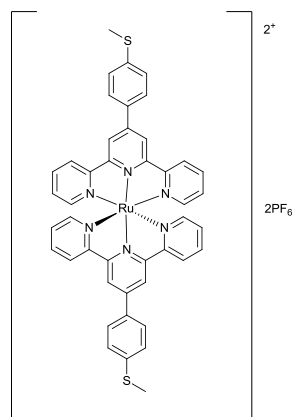
Synthesis of 4'-(4-(methylthio)phenyl)-2,2':6',2''-terpyridine (18)



To a solution of *t*BuOK (3.70 g, 33 mmol) in dry THF (50 mL) added was 2-acetylpyridine (2.66 g, 22 mmol). The reaction mixture was stirred for 2 h under argon. After this time a solution of 4-(methylthio)benzaldehyde (1.52 g, 10 mmol) in dry THF (10 mL) was added and the reaction mixture was stirred overnight. During this time a dark red colour developed. Ammonium acetate (26 g, 337 mmol) and ethanol (180 mL) were added and the reaction mixture was heated to reflux for 4 h. The solvent was reduced in vacuo to 30 % to precipitate the crude yellow product. Recrystallisation from EtOH yielded the title compound as yellow crystals (1.63 g, 46 %); m.p: 165-170 °C; $^1\text{H-NMR}$ (CDCl_3 , 400 MHz): 8.84 (s, 2H), 8.79 (d, $J = 4.51$ Hz, 4H), 8.00 (t, $J = 7.54$ Hz, 2H), 7.93 (d, $J = 8.39$ Hz, 2H), 7.46 (t, $J = 6.58$ Hz, 2H), 7.37 (d, $J = 8.45$ Hz, 2H), 2.55

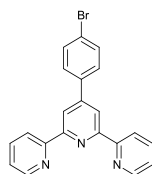
(s, *S-CH*₃, 3H); ¹³C-NMR (100 MHz, CDCl₃): 148.5, 127.6, 126.5, 124.0, 121.7, 118.9, 15.5 (*S-CH*₃); MS (CI+ (CH₄)): m/z: 356; UV/Vis (CH₃CN, 9 x 10⁻⁶ mol dm⁻³) λ_{max}/nm (ε_{max}/10³ dm³ mol⁻¹ cm⁻¹): 280 (244.3), 231 (135.1).

Preparation of Ru(4'-(4-(methylthio)phenyl)-2,2':6',2''-terpyridine)₂(PF₆)₂ (25)



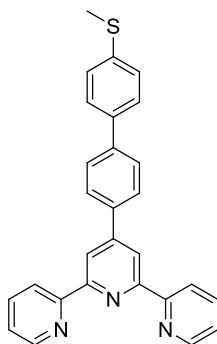
A solution of RuCl₃·3H₂O (0.019g, 0.120 mmol) and 4'-(4-(methylthio)phenyl)-2,2':6',2''-terpyridine (0.085 g, 0.240 mmol) in ethane-1,2-diol (10 mL) was heated to reflux for 3 h, The solution was allowed to cool, and water (10 mL) and an excess of methanolic [NH₄][PF₆] were added. The resulting dark brown precipitate was collected on celite by filtration and then redissolved in CH₃CN. The CH₃CN was reduced to minimum volume, and purification was by flash column chromatography (SiO₂, eluting with acetonitrile: saturated potassium nitrate: water (7:1:0.5). The first major orange fraction was collected, an excess of methanolic [NH₄][PF₆] were added, and the solution reduced in volume to precipitate [Ru(4-(methylthio)phenyl)-2,2':6',2''-terpyridine]₂[PF₆]₂. The compound was filtered and dried in air to yield the title compound as a red solid (0.049 g, 37.5 %); ¹H-NMR (CD₃CN), 400 MHz): (s, 2H), (dd, J= 4.4, 1.7 Hz, H), (d, J = 8.1 Hz, H), (dd, J = 1.6, 4.4 Hz, H), (td, J = 7.8, 1.4 Hz, H), (d, J = 4.8 Hz, H), (m, H); ¹³C-NMR (100 MHz, CD₃CN): 158.82, 156.00, 153.02, 148.23, 143.22, 138.58, 133.40, 128.64, 128.02, 127.01, 125.07, 121.65, 14.80 (*S-CH*₃); MS (ES+, CH₃OH): m/z: 813 (-2PF₆), 957 (-PF₆); UV/Vis (CH₃CN, 9 x 10⁻⁶ mol dm⁻³) λ_{max}/nm (ε_{max}/10³ dm³ mol⁻¹ cm⁻¹): 494 (76.3), 308 (169.7), 283 (137.3), 275 (sh).

Synthesis of 4'-(4-bromophenyl)-2,2':6',2''-terpyridine (19)



To 4-bromobenzaldehyde (1.0 g, 5.40 mmol) in 120 mL CH₃OH was added 2-acetylpyridine (1.3 g, 10.80 mmol), NaOH (0.22 g, 5.4 mmol) and 30 mL concentrated NH₄OH. The reaction mixture was refluxed for 72 h, and then stirred at room temperature for another 3 h. The formed slight yellow precipitate was filtered and washed sequentially with H₂O and CH₃OH. White powder could be obtained after recrystallization from EtOH (0.783 g, 37.2 %); m.p: 109-113 °C; ¹H-NMR (CDCl₃), 400 MHz): 8.76 (s, 2H), 8.75 (d, J= 0.81 Hz, 2H), 8.71 (d, J = 7.9 Hz, 2H), 7.94 (td, J = 7.7, 1.5 Hz, 2H), 7.82 (dd, J = 6.7, 1.8 Hz, 2H), 7.65 (dd, J = 6.6, 1.9 Hz, 2H), 7.42-7.39 (m, J = 12.2 Hz, 2H); ¹³C-NMR (100 MHz, CDCl₃): 155.77, 149.22, 148.87, 137.33, 132.16, 128.95, 124.08, 123.6, 121.59, 118.82; MS (EI+): m/z: 387 (⁷⁹Br), 389 (⁸¹Br).

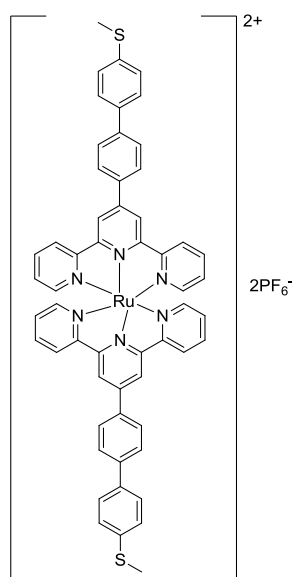
4'-(4'-(methylthio)-[1,1'-biphenyl]-4-yl)-2,2':6',2''-terpyridine (20)



Added to a solution of 4'-(4-bromophenyl)-2,2':6',2''-terpyridine (0.23 g, 0.59 mmol) in toluene:*i*-PrOH (50:50, 4 mL) was (4-(methylthio)phenyl)boronic acid (0.1 g, mmol) and 2 M aqueous K₂CO₃ (2.6 mL). After degassing the solution for 15 mins with Ar, Pd(PPh₃)₄ (0.016 g, mmol) was added and the mixture was refluxed for 7 h under Ar. After this time the reaction mixture was diluted with water and extracted with EtOAc. The combined organic layers were dried with MgSO₄ and the solvent evaporated. Recrystallisation from EtOAc yielded the title compound as white needles (0.025 g, 0.058 mmol, 9.8 %); m.p: 190-195°C; ¹H-NMR (CDCl₃), 400 MHz): 8.817 (s, 2H), 8.71 (d, J= 3.74 Hz, 4H), 7.99 (d, J =

8.27 Hz, 2H), 7.92 (t, $J = 7.73$ Hz, 2H), 7.65 (d, $J = 8.32$ Hz, 2H), 7.53 (d, $J = 8.38$ Hz, 2H), 7.37 (t, $J = 5.6$ Hz, 2H), 7.29 (d, $J = 8.38$ Hz, 2H), 2.47 (s, 3H); ^{13}C -NMR (100 MHz, CDCl_3): 148.39, 141.33, 138.23, 137.04, 127.85, 127.42, 127.30, 126.95, 124.12, 121.87, 119.20, 14.77 ($S\text{-CH}_3$); MS (CI^+ (CH_4)): m/z : 432; UV/Vis (CH_3CN , 9×10^{-6} mol dm^{-3}) $\lambda_{\text{max}}/\text{nm}$ ($\epsilon_{\text{max}}/10^3 \text{ dm}^3 \text{ mol}^{-1} \text{ cm}^{-1}$): 279 (163.2).

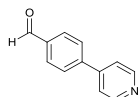
Ru(4'-(4'-(methylthio)-[1,1'-biphenyl]-4-yl)-2,2':6',2''-terpyridine) $_2$ (PF $_6$) $_2$ (26)



A solution of $\text{RuCl}_3 \cdot 3\text{H}_2\text{O}$ (0.007g, 0.03 mmol) and 4'-(4'-(methylthio)-[1,1'-biphenyl]-4-yl)-2,2':6',2''-terpyridine (0.025 g, 0.06 mmol) in ethane-1,2-diol (2.5 mL) was heated to reflux for 3 h, The solution was allowed to cool, and water (2.5 mL) and an excess of methanolic $[\text{NH}_4][\text{PF}_6]$ were added. The resulting dark brown precipitate was collected on celite by filtration and then redissolved in CH_3CN . The CH_3CN was reduced to minimum volume, and purification was by flash column chromatography (SiO_2 , eluting with acetonitrile: saturated potassium nitrate: water (7:1:0.5)). The first major orange fraction was collected, an excess of methanolic $[\text{NH}_4][\text{PF}_6]$ were added, and the solution reduced in volume to precipitate $[\text{Ru}(4'-(4'-(methylthio)-[1,1'-biphenyl]-4-yl)-2,2':6',2''\text{-terpyridine})_2][\text{PF}_6]_2$. The compound was filtered and dried in air to yield the title compound as a red solid (0.012 g, 33 %); ^1H -NMR (CD_3CN , 400 MHz): 9.07 (s, 4H), 8.68 (d, $J = 7.99$ Hz, 3H), 8.34 (d, $J = 8.39$ Hz, 3H), 8.10 (d, $J = 8.12$ Hz, 4H), 8.03 (d, $J = 8.37$ Hz, 4H), 7.96 (t, $J = 7.31$ Hz, 6H), 7.85 (d, $J = 8.2$ Hz, 4H), 7.45 (d, $J = 4.58$ Hz, 4H), 7.19 (t, $J = 6.06$ Hz, 4H), 2.76 (s,

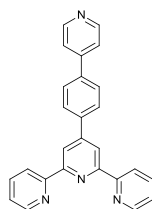
*S-CH*₃, 6H); ¹³C-NMR (100 MHz, CD₃CN): (*aromatic*), (*aromatic*), (*aromatic*), (*aromatic*), (*aromatic*), (*aromatic*), (*aromatic*), (*aromatic*); MS (ES+, CH₃OH): m/z: 995 (-PF₁₂), 1141 (-F₆); UV/Vis (CH₃CN, 9 x 10⁻⁶ mol dm⁻³) λ_{max}/nm (ε_{max}/10³ dm³ mol⁻¹ cm⁻¹): 494 (9.9), 311 (38.9), 287 (sh).

Synthesis of 4-(pyridin-4-yl)benzaldehyde (10)



Added to a solution of 4-bromopyridine hydrochloride (0.2 g, 1.34 mmol) in toluene:*i*-PrOH (50:50, 4 mL) was (4-formylphenyl)boronic acid (0.16 g, 1.06 mmol) and 2 M aqueous K₂CO₃ (2.6 mL). After degassing the solution for 15 mins using Ar, Pd(PPh₃)₄ (0.036g, 0.030 mmol) was added and the mixture was refluxed for 7 h under Ar. After this time the reaction mixture was diluted with water and extracted with EtOAc. The combined organic layers were dried with MgSO₄ and the solvent evaporated. Recrystallisation from EtOAc yielded the title compound as white needles (0.116 g, 47 %); m.p: 85-88 °C; ¹H-NMR (400 MHz, CDCl₃): 10.11 (s, 1H, *O*-H), 8.75 (dd, J = 4.6, 1.6 Hz, 2H), 8.03 (dd, J = 6.5, 1.7 Hz, 2H), 7.83 (dd, J = 7.2, 1.6 Hz, 2H), 7.65 (dd, J = 4.65, 1.6 Hz, 2H); ¹³C-NMR (100 MHz, CDCl₃): 191.47 (C=O), 148.94, 143.25, 136.83, 130.52, 127.88, 122.27; MS (CI+ (NH₃)): m/z: 184.3.

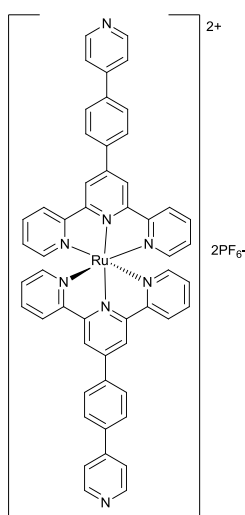
Synthesis of 4'-[4-(pyridin-4-yl)phenyl]-2,2':6',2''-terpyridine (12)



A solution of 4-(pyridin-4-yl)benzaldehyde (0.05 g, 0.273 mmol) in methanol (4 mL) was cooled to -15°C. Solutions of 2-acetylpyridine (0.066 g, 0.54 mmol) in MeOH (2 mL) and 20 % aq NaOH (4 mL) were added simultaneously over a period of 20 minutes. The reaction mixture was then further stirred for 3 h at -10 °C. The solution was warmed to room temperature and filtered. The filtrate was then treated with NH₄OAc (0.1 g, 1.297 mmol) and heated to reflux for 4 h.

The resulting solution was filtered and washed several times with hot water and hot ethanol. The title compound was recovered as a white solid (0.036 g, 34 %); m.p: 220-225 °C; $^1\text{H-NMR}$ (400 MHz, CDCl_3): 8.82 (s, 2H), 8.76-8.70 (m, $J = 26.0$ Hz, 6H), 8.09 (d, $J = 8.3$ Hz, 2H), 7.92 (td, $J = 7.7, 1.55$ Hz, 2H), 7.84 (d, $J = 8.3$ Hz, 2H), 7.75 (d, $J = 6.2$ Hz, 2H), 7.41-7.38 (m, $J = 12.1$ Hz, 2H); $^{13}\text{C-NMR}$ (100 MHz, CDCl_3): 156.08, 156.04, 149.21, 149.13, 149.12, 139.64, 138.14, 137.04, 128.21, 127.64, 124.01, 121.89, 121.46, 118.80; MS (EI+): m/z : 386.5; UV/Vis (CH_3CN , 1.2×10^{-5} mol dm^{-3}) $\lambda_{\text{max}}/\text{nm}$ ($\epsilon_{\text{max}}/10^3 \text{ dm}^3 \text{ mol}^{-1} \text{ cm}^{-1}$): 285 (209.4).

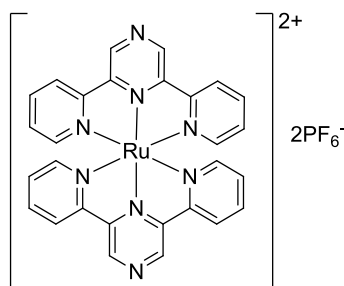
Preparation of Ru(4'-[4-(pyridin-4-yl)phenyl]-2,2':6',2''-terpyridine) $_2$ (PF $_6$) $_2$ (23)



A solution of $\text{RuCl}_3 \cdot 3\text{H}_2\text{O}$ (0.019g, 0.120 mmol) and 4'-[4-(pyridin-4-yl)phenyl]-2,2':6',2''-terpyridine (0.092 g, 0.240 mmol) in ethane-1,2-diol (10 mL) was heated to reflux for 3 h. The solution was allowed to cool, and water (10 mL) and an excess of methanolic $[\text{NH}_4][\text{PF}_6]$ were added. The resulting dark brown precipitate was collected on Celite by filtration and then redissolved in CH_3CN . The CH_3CN was reduced to minimum volume *in vacuo*, and purification was by flash column chromatography (SiO_2 , eluting with acetonitrile: saturated potassium nitrate: water (7:1:0.5)). The first major orange fraction was collected, an excess of methanolic $[\text{NH}_4][\text{PF}_6]$ was added, and the solution was evaporated to low volume to precipitate $[\text{Ru}(4'-[4-(\text{pyridin-4-yl})\text{phenyl}]-2,2':6',2''\text{-terpyridine})_2][\text{PF}_6]_2$. The compound was filtered and dried in air to yield the title compound as a red solid (0.048 g, 46 %); $^1\text{H-NMR}$ (CD_3CN), 400

MHz): 9.08 (s, 4H), 8.77 (dd, $J = 4.7, 1.5$ Hz, 4H), 8.68 (d, $J = 7.95$ Hz, 4H), 8.38 (d, $J = 8.43$ Hz, 4H), 8.18 (d, $J = 8.45$ Hz, 4H), 7.99-7.94 (m, $J = 19.6$ Hz, 8H), 7.45 (d, $J = 5.5$ Hz, 4H), 7.22-7.94 (m, $J = 14.3$ Hz, H); $^{13}\text{C-NMR}$ (100 MHz, CD_3CN): ; MS (ES+, CH_3OH): m/z : 873 (- 2PF_6), 1019 (- PF_6); UV/Vis (CH_3CN , 1.2×10^{-5} mol dm^{-3}) $\lambda_{\text{max}}/\text{nm}$ ($\epsilon_{\text{max}}/10^3 \text{ dm}^3 \text{ mol}^{-1} \text{ cm}^{-1}$): 493 (24.3), 310 (60.8), 287 (sh).

Ru(2,6-di(pyridin-2-yl)pyrazine)₂(PF₆)₂ (22)



A solution of $\text{RuCl}_3 \cdot 3\text{H}_2\text{O}$ (0.027 g, 0.105 mmol) and 2,6-di(pyridin-2-yl)pyrazine (0.05 g, 0.214 mmol) in ethane-1,2-diol (10 mL) was heated to reflux for 3 h. The solution was allowed to cool, and water (10 mL) and an excess of methanolic $[\text{NH}_4][\text{PF}_6]$ were added. The resulting dark brown precipitate was collected on Celite by filtration and then redissolved in CH_3CN . The CH_3CN was evaporated to minimum volume, and purification was by flash column chromatography (SiO_2 , eluting with acetonitrile: saturated potassium nitrate: water (7:1:0.5)). The first major orange fraction was collected, an excess of methanolic $[\text{NH}_4][\text{PF}_6]$ was added, and the solution reduced in volume to precipitate $[\text{Ru}(2,6\text{-di}(\text{pyridin-2-yl})\text{pyrazine})_2][\text{PF}_6]_2$. The compound was filtered and dried in air to yield the title compound as a red solid (0.04 g, 47 %); $^1\text{H-NMR}$ (CD_3CN), 400 MHz): 9.86 (s, 1H), 8.62 (d, $J = 8.09$ Hz, 1H), 7.99 (td, $J = 7.93, 1.32$ Hz, 1H), 7.36 (d, $J = 5.51$ Hz, 1H), 7.20 (td, $J = 5.66, 1.13$ Hz, 1H); $^{13}\text{C-NMR}$ (100 MHz, CD_3CN): 153.76, 150.44, 144.39, 139.41, 128.56, 125.62; MS (ES+, CH_3OH): m/z : 569 (- 2PF_6), 715 (- PF_6); UV/Vis (CH_3CN , 1.2×10^{-5} mol dm^{-3}) $\lambda_{\text{max}}/\text{nm}$ ($\epsilon_{\text{max}}/10^3 \text{ dm}^3 \text{ mol}^{-1} \text{ cm}^{-1}$): 469 (9.5), 340 (sh), 308 (26.8), 269 (23.5).

7.5 Scanning Tunneling Microscopy Measurements

Measurements were completed using an Agilent 2500 or 5500 controller utilizing Agilent PicoScan 5.3.3 software. Gold on glass substrates (Arrandee®)

were flame annealed prior to use for approximately 2 minutes. Gold tips for use in the STM were prepared by cutting 0.25 mm gold wire (99.99%, Goodfellows). A monolayer of the required substrate was formed by immersing the gold substrate into a solution of the required molecule for a set amount of time. The substrate was then washed with ethanol and dried with nitrogen. For conductance measurements in solution an environmental chamber was used and for measurements under electrochemical control Pt quasi reference and counter electrodes were employed. Once the ionic liquid was added to the cell the system was purged with nitrogen for 1 h prior to use.

The I(s) method was used throughout these measurements with a constant bias of + 0.6 V and various set point currents. The scans were performed with duration of 0.1 second and from 0 – 4 nm relative to the set point current. For each molecule set around 500 scans were taken and the data plotted into a histogram to calculate the conductance. The total break off distance was calculated using the method described in chapter 1.

7.6 Cyclic Voltammetry

Cyclic voltammetry experiments were completed using an EcoChemie Autolab potentiostat PGSTAT30 model utilizing the AutoLab GPES software. For all experiments a three electrode set up was employed.

The gold working electrodes were tested prior to use following standard literature procedures.^{26, 30a} The resulting voltammograms can be seen in Figure 7.1 and 7.2.

The quality of the Au(111) working electrode was tested following literature procedures.^{30a} The Au(111) electrode was tested in 0.1 M H₂SO₄ using a saturated calomel electrode as the reference electrode and a Pt wire counter electrode. The butterfly peak occurs due to sulfate anion adsorption, Figure 7.1.

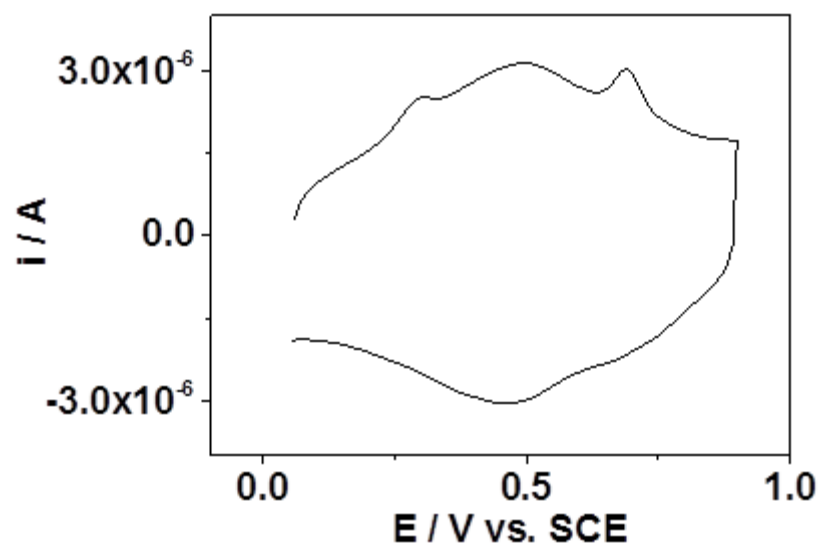


Figure 7.1: Cyclic Voltammogram of Au(111) surface in a 0.1 M H₂SO₄ electrolyte referenced to SCE. Scan Rate 0.1 V/s

The electrochemical surface area of the Au polycrystalline working electrode was calculated following literature procedures.²⁶ The Au(111) electrode was tested in 0.1 M phosphate buffer (pH 7.4) using a saturated calomel electrode as the reference electrode and a Pt wire counter electrode at a scan rate of 0.05 V/s. The voltammogram can be seen in Figure 7.2.

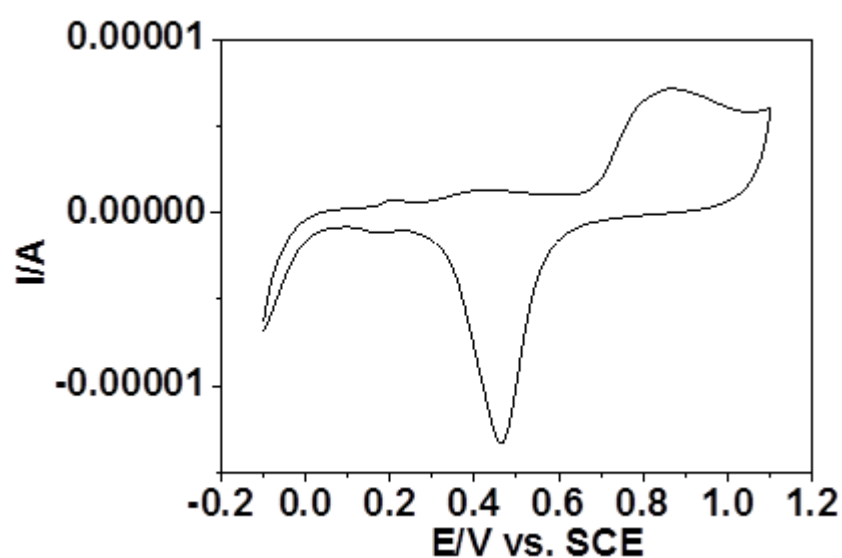


Figure 7.2: Cyclic voltammogram of Au polycrystalline electrode in 0.1 M phosphate buffer referenced to SCE. Scan rate 0.05 V/s.

The area of the gold oxide reduction peak is then calculated. This is then divided by the standard adsorption charge associated with the polycrystalline gold, $390 \mu\text{C cm}^{-2}$

$$A_{ec} = Q_{Ad}/Q_m \quad \text{Equation 7.1}$$

Where A_{ec} is the electrochemical surface area, Q_{Ad} is the adsorption charge of a known adsorbate on the electrode surface and Q_m is the charge associated with the monolayer coverage of the adsorbate from the experiment.

Solution voltammetry experiments of the transition metal complexes were completed using a sealed cell prepared in the glove box using either dried ionic liquid BMIM-TFSA or dry acetonitrile, which contained 0.1 M TBATFB as the electrolyte. The electrodes used for all experiments were gold polycrystalline working electrode, Pt Wire counter and reference. The experiments were referenced to an internal standard, ferrocene.

Monolayer voltammetry experiments were completed using a sealed cell prepared in the glove box using dried ionic liquid BMIM-TFSA. The electrodes used for all experiments were gold (111) working electrode, Pt Wire counter and reference. The experiments were referenced to an internal standard, ferrocene.

7.7 References

1. Moore, G. E., Cramming more components onto integrated circuits. McGraw-Hill New York, NY, USA: 1965.
2. Moore, G. E., Progress in digital integrated electronics. *IEDM Tech. Digest* **1975**, 11.
3. Balzani, V.; Credi, A.; Venturi, M., Molecular devices and machines. *Nano Today* **2007**, 2 (2), 18-25.
4. Moore, G. E. In *Lithography and the future of Moore's law*, SPIE's 1995 Symposium on Microlithography, International Society for Optics and Photonics: 1995; pp 2-17.
5. Tour, J. M., Molecular electronics. Synthesis and testing of components. *Accounts of Chemical Research* **2000**, 33 (11), 791-804.
6. Feynman, R. P., There's plenty of room at the bottom. *Engineering and Science* **1960**, 23 (5), 22-36.
7. Aviram, A.; Ratner, M. A., Molecular rectifiers. *Chemical Physics Letters* **1974**, 29 (2), 277-283.
8. Aviram, A.; Joachim, C.; Pomerantz, M., Evidence of switching and rectification by a single molecule effected with a scanning tunneling microscope. *Chemical Physics Letters* **1988**, 146 (6), 490-495.
9. Reed, M. A.; Zhou, C.; Muller, C.; Burgin, T.; Tour, J., Conductance of a molecular junction. *Science* **1997**, 278 (5336), 252-254.
10. (a) Xu, B.; Tao, N. J., Measurement of single-molecule resistance by repeated formation of molecular junctions. *Science* **2003**, 301 (5637), 1221-1223; (b) Haiss, W.; Nichols, R. J.; Higgins, S. J.; Bethell, D.; Höbenreich, H.; Schiffrin, D. J., Wiring nanoparticles with redox molecules. *Faraday Discussions* **2004**, 125, 179-194; (c) Haiss, W.; van Zalinge, H.; Higgins, S. J.; Bethell, D.; Höbenreich, H.; Schiffrin, D. J.; Nichols, R. J., Redox state dependence of single molecule conductivity. *Journal of the American Chemical Society* **2003**, 125 (50), 15294-15295.
11. Cui, X.; Primak, A.; Zarate, X.; Tomfohr, J.; Sankey, O.; Moore, A.; Moore, T.; Gust, D.; Harris, G.; Lindsay, S., Reproducible measurement of single-molecule conductivity. *Science* **2001**, 294 (5542), 571-574.
12. Weber, H.; Reichert, J.; Weigend, F.; Ochs, R.; Beckmann, D.; Mayor, M.; Ahlrichs, R.; Löhneysen, H., Electronic transport through single conjugated molecules. *Chemical Physics* **2002**, 281 (2), 113-125.
13. Binnig, G.; Rohrer, H.; Gerber, C.; Weibel, E., Surface studies by scanning tunneling microscopy. *Physical Review Letters* **1982**, 49 (1), 57.
14. Binnig, G.; Rohrer, H., Scanning tunneling microscopy—from birth to adolescence (Nobel Lecture). *Angewandte Chemie International Edition in English* **1987**, 26 (7), 606-614.
15. Fujihira, M.; Suzuki, M.; Fujii, S.; Nishikawa, A., Currents through single molecular junction of Au/hexanedithiolate/Au measured by repeated formation of break junction in STM under UHV: Effects of conformational change in an alkylene chain from gauche to trans and binding sites of thiolates on gold. *Physical Chemistry Chemical Physics* **2006**, 8 (33), 3876-3884.
16. Leary, E.; Höbenreich, H.; Higgins, S. J.; Van Zalinge, H.; Haiss, W.; Nichols, R. J.; Finch, C.; Grace, I.; Lambert, C.; McGrath, R., Single-molecule solvation-shell sensing. *Physical Review Letters* **2009**, 102 (8), 086801.
17. Li, X.; He, J.; Hihath, J.; Xu, B.; Lindsay, S. M.; Tao, N., Conductance of single alkanedithiols: Conduction mechanism and effect of molecule-electrode contacts. *Journal of the American Chemical Society* **2006**, 128 (6), 2135-2141.
18. Haiss, W.; van Zalinge, H.; Bethell, D.; Ulstrup, J.; Schiffrin, D. J.; Nichols, R. J., Thermal gating of the single molecule conductance of alkanedithiols. *Faraday Discussions* **2006**, 131, 253-264.

19. Halbritter, J., Tunnel channels, spectroscopy and imaging in STM. *Applied Physics A* **1998**, *66* (1), S181-S186.
20. Landauer, R., Spatial variation of currents and fields due to localized scatterers in metallic conduction. *IBM Journal of Research and Development* **1957**, *1* (3), 223-231.
21. (a) Ulman, A., Formation and structure of self-assembled monolayers. *Chemical Reviews* **1996**, *96* (4), 1533-1554; (b) Vericat, C.; Vela, M.; Benitez, G.; Carro, P.; Salvarezza, R., Self-assembled monolayers of thiols and dithiols on gold: new challenges for a well-known system. *Chemical Society Reviews* **2010**, *39* (5), 1805-1834; (c) Nuzzo, R. G.; Allara, D. L., Adsorption of bifunctional organic disulfides on gold surfaces. *Journal of the American Chemical Society* **1983**, *105* (13), 4481-4483.
22. Compton, R. G.; Sanders, G. H., *Electrode potentials*. Oxford Univ. Press: 1996.
23. Compton, R. G.; Banks, C. E., *Understanding voltammetry*. World Scientific: 2007.
24. Oldham, K. B., Analytical expressions for the reversible Randles-Sevcik function. *Journal of Electroanalytical Chemistry and Interfacial Electrochemistry* **1979**, *105* (2), 373-375.
25. Nicholson, R. S., Theory and Application of Cyclic Voltammetry for Measurement of Electrode Reaction Kinetics. *Analytical Chemistry* **1965**, *37* (11), 1351-1355.
26. Carvalhal, R. F.; Sanches Freire, R.; Kubota, L. T., Polycrystalline Gold Electrodes: A Comparative Study of Pretreatment Procedures Used for Cleaning and Thiol Self-Assembly Monolayer Formation. *Electroanalysis* **2005**, *17* (14), 1251-1259.
27. Finklea, H. O.; Snider, D. A.; Fedyk, J.; Sabatani, E.; Gafni, Y.; Rubinstein, I., Characterization of octadecanethiol-coated gold electrodes as microarray electrodes by cyclic voltammetry and ac impedance spectroscopy. *Langmuir* **1993**, *9* (12), 3660-3667.
28. Laviron, E., General expression of the linear potential sweep voltammogram in the case of diffusionless electrochemical systems. *Journal of Electroanalytical Chemistry and Interfacial Electrochemistry* **1979**, *101* (1), 19-28.
29. Eckermann, A. L.; Feld, D. J.; Shaw, J. A.; Meade, T. J., Electrochemistry of redox-active self-assembled monolayers. *Coordination Chemistry Reviews* **2010**, *254* (15), 1769-1802.
30. (a) Hamelin, A., Cyclic voltammetry at gold single-crystal surfaces. Part 1. Behaviour at low-index faces. *Journal of Electroanalytical Chemistry* **1996**, *407* (1-2), 1-11; (b) Hamelin, A.; Martins, A., Cyclic voltammetry at gold single-crystal surfaces. Part 2. Behaviour of high-index faces. *Journal of Electroanalytical Chemistry* **1996**, *407* (1), 13-21.
31. Kolthoff, I., A review of electrochemistry in non-aqueous solvents. *Pure and Applied Chemistry* **1971**, *25* (2), 305-326.
32. Balula, Maria S.; Gamelas, José A.; Carapuça, Helena M.; Cavaleiro, Ana M. V.; Schlindwein, W., Electrochemical Behaviour of First Row Transition Metal Substituted Polyoxotungstates: A Comparative Study in Acetonitrile. *European Journal of Inorganic Chemistry* **2004**, *2004* (3), 619-628.
33. (a) Buzzeo, M. C.; Evans, R. G.; Compton, R. G., Non-haloaluminate room-temperature ionic liquids in electrochemistry—A review. *ChemPhysChem* **2004**, *5* (8), 1106-1120; (b) Albrecht, T.; Moth-Poulsen, K.; Christensen, J. B.; Hjelm, J.; Bjørnholm, T.; Ulstrup, J., Scanning tunneling spectroscopy in an ionic liquid. *Journal of the American Chemical Society* **2006**, *128* (20), 6574-6575.
34. (a) Kay, N. J.; Nichols, R. J.; Higgins, S. J.; Haiss, W.; Sedghi, G.; Schwarzacher, W.; Mao, B.-W., Ionic Liquids As a Medium for STM-Based Single Molecule Conductance Determination: An Exploration Employing Alkanedithiols. *The Journal of Physical Chemistry C* **2011**, *115* (43), 21402-21408; (b) Kay, N. J.; Higgins, S. J.; Jeppesen, J. O.; Leary, E.; Lycoops, J.; Ulstrup, J.; Nichols, R. J., Single-molecule electrochemical gating in ionic liquids. *Journal of the American Chemical Society* **2012**, *134* (40), 16817-16826.

35. Zalinge, H., Measurement of single molecule conductivity using the spontaneous formation of molecular wires. *Physical Chemistry Chemical Physics* **2004**, *6* (17), 4330-4337.
36. Leary, E. Single Molecule Conductance of Dithiahexyl-Aryl Compounds. University of Liverpool, 2008.
37. Moreland, J.; Ekin, J., Electron tunneling experiments using Nb-Sn "break" junctions. *Journal of Applied Physics* **1985**, *58* (10), 3888-3895.
38. Muller, C.; Van Ruitenbeek, J.; De Jongh, L., Experimental observation of the transition from weak link to tunnel junction. *Physica C: Superconductivity* **1992**, *191* (3), 485-504.
39. (a) Kaliginedi, V.; Moreno-García, P.; Valkenier, H.; Hong, W.; García-Suárez, V. M.; Buitter, P.; Otten, J. L.; Hummelen, J. C.; Lambert, C. J.; Wandlowski, T., Correlations between molecular structure and single-junction conductance: A case study with oligo (phenylene-ethynylene)-type wires. *Journal of the American Chemical Society* **2012**, *134* (11), 5262-5275; (b) Hong, W.; Manrique, D. Z.; Moreno-Garcia, P.; Gulcur, M.; Mishchenko, A.; Lambert, C. J.; Bryce, M. R.; Wandlowski, T., Single molecular conductance of tolans: experimental and theoretical study on the junction evolution dependent on the anchoring group. *Journal of the American Chemical Society* **2012**, *134* (4), 2292-2304.
40. Scheer, E., *Molecular electronics: an introduction to theory and experiment*. World Scientific: 2010; Vol. 1.
41. (a) Karthäuser, S., Control of molecule-based transport for future molecular devices. *Journal of Physics: Condensed Matter* **2011**, *23* (1), 013001; (b) Wang, W.; Lee, T.; Reed, M. A., Mechanism of electron conduction in self-assembled alkanethiol monolayer devices. *Physical Review B* **2003**, *68* (3), 035416.
42. McConnell, H. M., Intramolecular charge transfer in aromatic free radicals. *The Journal of Chemical Physics* **1961**, *35* (2), 508-515.
43. Simmons, J. G., Generalized formula for the electric tunnel effect between similar electrodes separated by a thin insulating film. *Journal of Applied Physics* **1963**, *34* (6), 1793-1803.
44. (a) Zhang, J.; Kuznetsov, A. M.; Medvedev, I. G.; Chi, Q.; Albrecht, T.; Jensen, P. S.; Ulstrup, J., Single-molecule electron transfer in electrochemical environments. *Chemical Reviews* **2008**, *108* (7), 2737-2791; (b) Schmickler, W.; Widrig, C., The investigation of redox reactions with a scanning tunneling microscope: experimental and theoretical aspects. *Journal of Electroanalytical Chemistry* **1992**, *336* (1), 213-221.
45. Choi, S. H.; Kim, B.; Frisbie, C. D., Electrical resistance of long conjugated molecular wires. *Science* **2008**, *320* (5882), 1482-1486.
46. (a) Arroyo, C. R.; Leary, E.; Castellanos-Gómez, A.; Rubio-Bollinger, G.; González, M. T.; Agraït, N., Influence of Binding Groups on Molecular Junction Formation. *Journal of the American Chemical Society* **2011**, *133* (36), 14313-14319; (b) Hong, W.; Manrique, D. Z.; Moreno-García, P.; Gulcur, M.; Mishchenko, A.; Lambert, C. J.; Bryce, M. R.; Wandlowski, T., Single Molecular Conductance of Tolans: Experimental and Theoretical Study on the Junction Evolution Dependent on the Anchoring Group. *Journal of the American Chemical Society* **2011**, *134* (4), 2292-2304; (c) Park, Y. S.; Whalley, A. C.; Kamenetska, M.; Steigerwald, M. L.; Hybertsen, M. S.; Nuckolls, C.; Venkataraman, L., Contact Chemistry and Single-Molecule Conductance: A Comparison of Phosphines, Methyl Sulfides, and Amines. *Journal of the American Chemical Society* **2007**, *129* (51), 15768-15769; (d) Chen, F.; Li, X.; Hihath, J.; Huang, Z.; Tao, N., Effect of Anchoring Groups on Single-Molecule Conductance: Comparative Study of Thiol-, Amine-, and Carboxylic-Acid-Terminated Molecules. *Journal of the American Chemical Society* **2006**, *128* (49), 15874-15881; (e) Venkataraman, L.; Klare, J. E.; Nuckolls, C.; Hybertsen, M. S.; Steigerwald, M. L., Dependence of single-molecule junction conductance on molecular conformation. *Nature* **2006**, *442* (7105), 904-907.

47. (a) Mishchenko, A.; Zotti, L. A.; Vonlanthen, D.; Bürkle, M.; Pauly, F.; Cuevas, J. C.; Mayor, M.; Wandlowski, T., Single-Molecule Junctions Based on Nitrile-Terminated Biphenyls: A Promising New Anchoring Group. *Journal of the American Chemical Society* **2010**, *133* (2), 184-187; (b) Zotti, L. A.; Kirchner, T.; Cuevas, J. C.; Pauly, F.; Huhn, T.; Scheer, E.; Erbe, A., Revealing the Role of Anchoring Groups in the Electrical Conduction Through Single-Molecule Junctions. *Small* **2010**, *6* (14), 1529-1535.
48. Kamenetska, M.; Quek, S. Y.; Whalley, A. C.; Steigerwald, M. L.; Choi, H. J.; Louie, S. G.; Nuckolls, C.; Hybertsen, M. S.; Neaton, J. B.; Venkataraman, L., Conductance and Geometry of Pyridine-Linked Single-Molecule Junctions. *Journal of the American Chemical Society* **2010**, *132* (19), 6817-6821.
49. Tam, E. S.; Parks, J. J.; Shum, W. W.; Zhong, Y.-W.; Santiago-Berríos, M. E. B.; Zheng, X.; Yang, W.; Chan, G. K. L.; Abruña, H. D.; Ralph, D. C., Single-Molecule Conductance of Pyridine-Terminated Dithienylethene Switch Molecules. *ACS Nano* **2011**, *5* (6), 5115-5123.
50. Xu, B.; Xiao, X.; Tao, N. J., Measurements of Single-Molecule Electromechanical Properties. *Journal of the American Chemical Society* **2003**, *125* (52), 16164-16165.
51. (a) Capozzi, B.; Dell, E. J.; Berkelbach, T. C.; Reichman, D. R.; Venkataraman, L.; Campos, L. M., Length-Dependent Conductance of Oligothiophenes. *Journal of the American Chemical Society* **2014**, *136* (29), 10486-10492; (b) Dell, E. J.; Capozzi, B.; DuBay, K. H.; Berkelbach, T. C.; Moreno, J. R.; Reichman, D. R.; Venkataraman, L.; Campos, L. M., Impact of Molecular Symmetry on Single-Molecule Conductance. *Journal of the American Chemical Society* **2013**, *135* (32), 11724-11727.
52. Martín, S.; Haiss, W.; Higgins, S.; Cea, P.; López, M. C.; Nichols, R. J., A Comprehensive Study of the Single Molecule Conductance of α,ω -Dicarboxylic Acid-Terminated Alkanes. *The Journal of Physical Chemistry C* **2008**, *112* (10), 3941-3948.
53. Li, Z.; Smeu, M.; Ratner, M. A.; Borguet, E., Effect of Anchoring Groups on Single Molecule Charge Transport through Porphyrins. *The Journal of Physical Chemistry C* **2013**, *117* (29), 14890-14898.
54. (a) Pauly, F.; Viljas, J. K.; Cuevas, J. C.; Schön, G., Density-functional study of tilt-angle and temperature-dependent conductance in biphenyl dithiol single-molecule junctions. *Physical Review B* **2008**, *77* (15), 155312; (b) Jones, D. R.; Troisi, A., Single Molecule Conductance of Linear Dithioalkanes in the Liquid Phase: Apparently Activated Transport Due to Conformational Flexibility. *The Journal of Physical Chemistry C* **2007**, *111* (39), 14567-14573.
55. Bagrets, A.; Arnold, A.; Evers, F., Conduction Properties of Bipyridinium-Functionalized Molecular Wires. *Journal of the American Chemical Society* **2008**, *130* (28), 9013-9018.
56. Quek, S. Y.; Kamenetska, M.; Steigerwald, M. L.; Choi, H. J.; Louie, S. G.; Hybertsen, M. S.; Neaton, J. B.; Venkataraman, L., Mechanically controlled binary conductance switching of a single-molecule junction. *Nat Nano* **2009**, *4* (4), 230-234.
57. Sun, L.; Diaz-Fernandez, Y. A.; Gschneidner, T. A.; Westerlund, F.; Lara-Avila, S.; Moth-Poulsen, K., Single-molecule electronics: from chemical design to functional devices. *Chemical Society Reviews* **2014**, *43* (21), 7378-7411.
58. Haiss, W.; Martín, S.; Leary, E.; Zalinge, H. v.; Higgins, S. J.; Bouffier, L.; Nichols, R. J., Impact of junction formation method and surface roughness on single molecule conductance. *The Journal of Physical Chemistry C* **2009**, *113* (14), 5823-5833.
59. Fatemi, V.; Kamenetska, M.; Neaton, J.; Venkataraman, L., Environmental control of single-molecule junction transport. *Nano letters* **2011**, *11* (5), 1988-1992.
60. Nakashima, S.; Takahashi, Y.; Kiguchi, M., Effect of the environment on the electrical conductance of the single benzene-1, 4-diamine molecule junction. *Beilstein Journal of Nanotechnology* **2011**, *2* (1), 755-759.

61. Leary, E.; Higgins, S. J.; van Zalinge, H.; Haiss, W.; Nichols, R. J.; Nygaard, S.; Jeppesen, J. O.; Ulstrup, J., Structure– Property Relationships in Redox-Gated Single Molecule Junctions– A Comparison of Pyrrolo-Tetrathiafulvalene and Viologen Redox Groups. *Journal of the American Chemical Society* **2008**, *130* (37), 12204-12205.
62. Albrecht, T.; Moth-Poulsen, K.; Christensen, J. B.; Guckian, A.; Bjørnholm, T.; Vos, J. G.; Ulstrup, J., In situ scanning tunnelling spectroscopy of inorganic transition metal complexes. *Faraday Discussions* **2006**, *131*, 265-279.
63. Low, P. J., Metal complexes in molecular electronics: progress and possibilities. *Dalton Transactions* **2005**, (17), 2821-2824.
64. (a) Gubin, S.; Gulayev, Y. V.; Khomutov, G.; Kislov, V.; Kolesov, V.; Soldatov, E.; Sulaimankulov, K.; Trifonov, A., Molecular clusters as building blocks for nanoelectronics: the first demonstration of a cluster single-electron tunnelling transistor at room temperature. *Nanotechnology* **2002**, *13* (2), 185; (b) Leary, E.; Van Zalinge, H.; Higgins, S. J.; Nichols, R. J.; Fabrizi de Biani, F.; Leoni, P.; Marchetti, L.; Zanello, P., A molecular wire incorporating a robust hexanuclear platinum cluster. *Physical Chemistry Chemical Physics* **2009**, *11* (25), 5198-5202; (c) Petukhov, K.; Alam, M. S.; Rupp, H.; Strömsdörfer, S.; Müller, P.; Scheurer, A.; Saalfrank, R. W.; Kortus, J.; Postnikov, A.; Ruben, M.; Thompson, L. K.; Lehn, J. M., STM spectroscopy of magnetic molecules. *Coordination Chemistry Reviews* **2009**, *253* (19–20), 2387-2398; (d) Blum, A. S.; Ren, T.; Parish, D. A.; Trammell, S. A.; Moore, M. H.; Kushmerick, J. G.; Xu, G.-L.; Deschamps, J. R.; Pollack, S. K.; Shashidhar, R., Ru₂(ap)₄(σ-oligo(phenyleneethynyl)) Molecular Wires: Synthesis and Electronic Characterization. *Journal of the American Chemical Society* **2005**, *127* (28), 10010-10011; (e) Chae, D.-H.; Berry, J. F.; Jung, S.; Cotton, F. A.; Murillo, C. A.; Yao, Z., Vibrational Excitations in Single Trimetal-Molecule Transistors. *Nano Letters* **2006**, *6* (2), 165-168; (f) Hsu, L.-Y.; Huang, Q.-R.; Jin, B.-Y., Charge Transport Through a Single Molecular Wire Based on Linear Multimetal Complexes: A Non-Equilibrium Green's Function Approach. *The Journal of Physical Chemistry C* **2008**, *112* (28), 10538-10541; (g) Liu, K.; Wang, X.; Wang, F., Probing Charge Transport of Ruthenium-Complex-Based Molecular Wires at the Single-Molecule Level. *ACS Nano* **2008**, *2* (11), 2315-2323.
65. Sauvage, J. P.; Collin, J. P.; Chambron, J. C.; Guillerez, S.; Coudret, C.; Balzani, V.; Barigelletti, F.; De Cola, L.; Flamigni, L., Ruthenium(II) and Osmium(II) Bis(terpyridine) Complexes in Covalently-Linked Multicomponent Systems: Synthesis, Electrochemical Behavior, Absorption Spectra, and Photochemical and Photophysical Properties. *Chemical Reviews* **1994**, *94* (4), 993-1019.
66. Tuccitto, N.; Ferri, V.; Cavazzini, M.; Quici, S.; Zhavnerko, G.; Licciardello, A.; Rampi, M. A., Highly conductive~ 40-nm-long molecular wires assembled by stepwise incorporation of metal centres. *Nature Materials* **2008**, *8* (1), 41-46.
67. (a) Sikes, H. D.; Smalley, J. F.; Dudek, S. P.; Cook, A. R.; Newton, M. D.; Chidsey, C. E. D.; Feldberg, S. W., Rapid Electron Tunneling Through Oligophenylenevinylene Bridges. *Science* **2001**, *291* (5508), 1519-1523; (b) Salomon, A.; Cahen, D.; Lindsay, S.; Tomfohr, J.; Engelkes, V. B.; Frisbie, C. D., Comparison of electronic transport measurements on organic molecules. *Advanced Materials* **2003**, *15* (22), 1881-1890; (c) He, J.; Chen, F.; Li, J.; Sankey, O. F.; Terazono, Y.; Herrero, C.; Gust, D.; Moore, T. A.; Moore, A. L.; Lindsay, S. M., Electronic Decay Constant of Carotenoid Polyenes from Single-Molecule Measurements. *Journal of the American Chemical Society* **2005**, *127* (5), 1384-1385.
68. Zhou, X.-S.; Liu, L.; Fortgang, P.; Lefevre, A.-S.; Serra-Muns, A.; Raouafi, N.; Amatore, C.; Mao, B.-W.; Maisonhaute, E.; Schöllhorn, B., Do molecular conductances correlate with electrochemical rate constants? Experimental insights. *Journal of the American Chemical Society* **2011**, *133* (19), 7509-7516.
69. (a) Constable, E. C.; Thompson, A. M. W. C., Pendant-functionalised ligands for metallosupramolecular assemblies; ruthenium(II) and osmium(II) complexes of 4[prime or

minute]-(4-pyridyl)-2,2[prime or minute] : 6[prime or minute],2[double prime]-terpyridine. *Journal of the Chemical Society, Dalton Transactions* **1994**, (9), 1409-1418; (b) Constable, E. C.; Thompson, A. M. W. C., Ligand reactivity in iron(II) complexes of 4[prime or minute]-(4[triple prime]-pyridyl)-2,2[prime or minute] : 6[prime or minute],2[double prime]-terpyridine. *Journal of the Chemical Society, Dalton Transactions* **1992**, (20), 2947-2950; (c) Constable, E. C.; Housecroft, C. E.; Neuburger, M.; Phillips, D.; Raithby, P. R.; Schofield, E.; Sparr, E.; Tocher, D. A.; Zehnder, M.; Zimmermann, Y., Development of supramolecular structure through alkylation of pendant pyridyl functionality. *Journal of the Chemical Society, Dalton Transactions* **2000**, (13), 2219-2228; (d) Hutchison, K.; Morris, J. C.; Nile, T. A.; Walsh, J. L.; Thompson, D. W.; Petersen, J. D.; Schoonover, J. R., Spectroscopic and Photophysical Properties of Complexes of 4'-Ferrocenyl-2,2':6',2''-terpyridine and Related Ligands. *Inorganic Chemistry* **1999**, *38* (10), 2516-2523.

70. (a) Forster, R. J.; Faulkner, L. R., Electrochemistry of spontaneously adsorbed monolayers. Equilibrium properties and fundamental electron transfer characteristics. *Journal of the American Chemical Society* **1994**, *116* (12), 5444-5452; (b) Albrecht, T.; Guckian, A.; Ulstrup, J.; Vos, J. G., Transistor-like Behavior of Transition Metal Complexes. *Nano Letters* **2005**, *5* (7), 1451-1455.

71. Persaud, L.; Barbiero, G., Synthesis, electrochemical and spectroscopic investigations of 2,2':4,4''-terpyridine and 2,2':4,4'':6,2''-quaterpyridine ligands for metal complex photoelectrochemistry. *Canadian Journal of Chemistry* **1991**, *69* (2), 315-321.

72. Cargill-Thompson, A. M., Pendant-functionalised ligands for metallosupramolecular assemblies; ruthenium (II) and osmium (II) complexes of 4'-(4-pyridyl)-2, 2': 6', 2''-terpyridine. *Journal of the Chemical Society, Dalton Transactions* **1994**, (9), 1409-1418.

73. Indumathy, R.; Radhika, S.; Kanthimathi, M.; Weyhermüller, T.; Unni Nair, B., Cobalt complexes of terpyridine ligand: Crystal structure and photocleavage of DNA. *Journal of Inorganic Biochemistry* **2007**, *101* (3), 434-443.

74. (a) Scarborough, C. C.; Lancaster, K. M.; DeBeer, S.; Weyhermüller, T.; Sproules, S.; Wieghardt, K., Experimental Fingerprints for Redox-Active Terpyridine in [Cr(tpy)₂](PF₆)_n (n = 3–0), and the Remarkable Electronic Structure of [Cr(tpy)₂]^{1–}. *Inorganic Chemistry* **2012**, *51* (6), 3718-3732; (b) Constable, E. C.; Housecroft, C. E.; Neuburger, M.; Schönle, J.; Zampese, J. A., The surprising lability of bis (2, 2': 6', 2''-terpyridine) chromium (iii) complexes. *Dalton Transactions* **2014**, *43* (19), 7227-7235.

75. Wang, C.; Batsanov, A. S.; Bryce, M. R.; Martín, S.; Nichols, R. J.; Higgins, S. J.; García-Suárez, V. M.; Lambert, C. J., Oligoynne Single Molecule Wires. *Journal of the American Chemical Society* **2009**, *131* (43), 15647-15654.

76. Scarborough, C. C.; Sproules, S.; Weyhermüller, T.; DeBeer, S.; Wieghardt, K., Electronic and Molecular Structures of the Members of the Electron Transfer Series [Cr (t bpy) ₃]ⁿ (n= 3+, 2+, 1+, 0): An X-ray Absorption Spectroscopic and Density Functional Theoretical Study. *Inorganic Chemistry* **2011**, *50* (24), 12446-12462.

77. Zhou, X.-S.; Wei, Y.-M.; Liu, L.; Chen, Z.-B.; Tang, J.; Mao, B.-W., Extending the capability of STM break junction for conductance measurement of atomic-size nanowires: an electrochemical strategy. *Journal of the American Chemical Society* **2008**, *130* (40), 13228-13230.

78. Aradhya, S. V.; Venkataraman, L., Single-molecule junctions beyond electronic transport. *Nature Nanotechnology* **2013**, *8* (6), 399-410.

79. (a) Sedghi, G.; Sawada, K.; Esdaile, L. J.; Hoffmann, M.; Anderson, H. L.; Bethell, D.; Haiss, W.; Higgins, S. J.; Nichols, R. J., Single molecule conductance of porphyrin wires with ultralow attenuation. *Journal of the American Chemical Society* **2008**, *130* (27), 8582-8583; (b) Sedghi, G.; García-Suárez, V. M.; Esdaile, L. J.; Anderson, H. L.; Lambert, C. J.; Martín, S.;

Bethell, D.; Higgins, S. J.; Elliott, M.; Bennett, N., Long-range electron tunnelling in oligoporphyrin molecular wires. *Nature Nanotechnology* **2011**, *6* (8), 517-523.

80. (a) Basch, H.; Cohen, R.; Ratner, M. A., Interface Geometry and Molecular Junction Conductance: Geometric Fluctuation and Stochastic Switching. *Nano Letters* **2005**, *5* (9), 1668-1675; (b) Beebe, J. M.; Engelkes, V. B.; Miller, L. L.; Frisbie, C. D., Contact Resistance in Metal-Molecule-Metal Junctions Based on Aliphatic SAMs: Effects of Surface Linker and Metal Work Function. *Journal of the American Chemical Society* **2002**, *124* (38), 11268-11269.

81. (a) Dulić, D.; Pump, F.; Campidelli, S.; Lavie, P.; Cuniberti, G.; Filoramo, A., Controlled Stability of Molecular Junctions. *Angewandte Chemie* **2009**, *121* (44), 8423-8426; (b) Lörtscher, E.; Cho, C. J.; Mayor, M.; Tschudy, M.; Rettner, C.; Riel, H., Influence of the Anchor Group on Charge Transport through Single-Molecule Junctions. *ChemPhysChem* **2011**, *12* (9), 1677-1682; (c) Ke, S.-H.; Baranger, H. U.; Yang, W., Molecular Conductance: Chemical Trends of Anchoring Groups. *Journal of the American Chemical Society* **2004**, *126* (48), 15897-15904.

82. (a) Ulrich, J.; Esrail, D.; Pontius, W.; Venkataraman, L.; Millar, D.; Doerrer, L. H., Variability of Conductance in Molecular Junctions. *The Journal of Physical Chemistry B* **2006**, *110* (6), 2462-2466; (b) Li, X.; He, J.; Hihath, J.; Xu, B.; Lindsay, S. M.; Tao, N., Conductance of Single Alkanedithiols: Conduction Mechanism and Effect of Molecule-Electrode Contacts. *Journal of the American Chemical Society* **2006**, *128* (6), 2135-2141; (c) Li, C.; Pobelov, I.; Wandlowski, T.; Bagrets, A.; Arnold, A.; Evers, F., Charge Transport in Single Au | Alkanedithiol | Au Junctions: Coordination Geometries and Conformational Degrees of Freedom. *Journal of the American Chemical Society* **2007**, *130* (1), 318-326.

83. (a) Lee, M. H.; Speyer, G.; Sankey, O. F., Electron transport through single alkane molecules with different contact geometries on gold. *Physica Status Solidi (b)* **2006**, *243* (9), 2021-2029; (b) Müller, K. H., Effect of the atomic configuration of gold electrodes on the electrical conduction of alkanedithiol molecules. *Physical Review B* **2006**, *73* (4), 045403.

84. Kaliginedi, V.; Rudnev, A. V.; Moreno-García, P.; Baghernejad, M.; Huang, C.; Hong, W.; Wandlowski, T., Promising anchoring groups for single-molecule conductance measurements. *Physical Chemistry Chemical Physics* **2014**, *16* (43), 23529-23539.

85. Kamenetska, M.; Koentopp, M.; Whalley, A.; Park, Y.; Steigerwald, M.; Nuckolls, C.; Hybertsen, M.; Venkataraman, L., Formation and evolution of single-molecule junctions. *Physical Review Letters* **2009**, *102* (12), 126803.

86. Kushmerick, J. G.; Whitaker, C. M.; Pollack, S. K.; Schull, T. L.; Shashidhar, R., Tuning current rectification across molecular junctions. *Nanotechnology* **2004**, *15* (7), S489.

87. Danilov, A.; Kubatkin, S.; Kafanov, S.; Hedegård, P.; Stuhr-Hansen, N.; Moth-Poulsen, K.; Bjørnholm, T., Electronic transport in single molecule junctions: Control of the molecule-electrode coupling through intramolecular tunneling barriers. *Nano Letters* **2008**, *8* (1), 1-5.

88. Haiss, W.; Martin, S.; Scullion, L. E.; Bouffier, L.; Higgins, S. J.; Nichols, R. J., Anomalous length and voltage dependence of single molecule conductance. *Physical Chemistry Chemical Physics* **2009**, *11* (46), 10831-10838.

89. Quek, S. Y.; Choi, H. J.; Louie, S. G.; Neaton, J. B., Length Dependence of Conductance in Aromatic Single-Molecule Junctions. *Nano Letters* **2009**, *9* (11), 3949-3953.

90. Kim; Beebe, J. M.; Olivier, C.; Rigaut, S.; Touchard, D.; Kushmerick, J. G.; Zhu, X. Y.; Frisbie, C. D., Temperature and Length Dependence of Charge Transport in Redox-Active Molecular Wires Incorporating Ruthenium(II) Bis(σ -arylacetylide) Complexes. *The Journal of Physical Chemistry C* **2007**, *111* (20), 7521-7526.

91. (a) Kim; Beebe, J. M.; Jun, Y.; Zhu, X. Y.; Frisbie, C. D., Correlation between HOMO Alignment and Contact Resistance in Molecular Junctions: Aromatic Thiols versus Aromatic Isocyanides. *Journal of the American Chemical Society* **2006**, *128* (15), 4970-4971; (b) Seferos, D. S.; Blum, A. S.; Kushmerick, J. G.; Bazan, G. C., Single-Molecule Charge-Transport Measurements that Reveal Technique-Dependent Perturbations. *Journal of the American Chemical Society* **2006**, *128* (34), 11260-11267.
92. (a) Goodall, W.; Wild, K.; Arm, K. J.; Williams, J. A. G., The synthesis of 4[prime or minute]-aryl substituted terpyridines by Suzuki cross-coupling reactions: substituent effects on ligand fluorescence. *Journal of the Chemical Society, Perkin Transactions 2* **2002**, (10), 1669-1681; (b) Kubota, E.; Lee, Y. H.; Fuyuhiko, A.; Kawata, S.; Harrowfield, J. M.; Kim, Y.; Hayami, S., Synthesis, structure, and luminescence properties of arylpyridine-substituted terpyridine Zn(II) and Cd(II) complexes. *Polyhedron* **2013**, *52* (0), 435-441.
93. Potts, K. T.; Ralli, P.; Theodoridis, G.; Winslow, P., 2, 2': 6', 2'-Terpyridine. *Organic Syntheses* **1986**, 189-189.
94. Jameson, D. L.; Guise, L. E., An improved, two-step synthesis of 2,2':6',2"-terpyridine. *Tetrahedron Letters* **1991**, *32* (18), 1999-2002.
95. Constable, E. C.; Housecroft, C. E.; Medlycott, E.; Neuburger, M.; Reinders, F.; Reymann, S.; Schaffner, S., The first complex of 4'-(4-methylthiophenyl)-2,2':6',2"-terpyridine – A model for terpylated self-assembled monolayers. *Inorganic Chemistry Communications* **2008**, *11* (5), 518-520.
96. Korall, P.; Borje, A.; Norrby, P.; Åkermark, B., High Yield Preparation of 4'-(4-Bromophenyl)-2, 2': 6', 2"-terpyridine by a Condensation Reaction. Determination of the Stereochemistry of Two Complex By-products by a Combination of Molecular Mechanics and NMR Spectroscopy. *Acta Chemica Scandinavica* **1997**, *51* (6), 760-766.
97. Nichols, R. J.; Haiss, W.; Higgins, S. J.; Leary, E.; Martin, S.; Bethell, D., The experimental determination of the conductance of single molecules. *Physical Chemistry Chemical Physics* **2010**, *12* (12), 2801-2815.
98. Li, Z.; Pobelov, I.; Han, B.; Wandlowski, T.; Błaszczak, A.; Mayor, M., Conductance of redox-active single molecular junctions: an electrochemical approach. *Nanotechnology* **2007**, *18* (4), 044018.
99. (a) Chen, F.; He, J.; Nuckolls, C.; Roberts, T.; Klare, J. E.; Lindsay, S., A molecular switch based on potential-induced changes of oxidation state. *Nano Letters* **2005**, *5* (3), 503-506; (b) He, J.; Chen, F.; Lindsay, S.; Nuckolls, C., Length dependence of charge transport in oligoanilines. *Applied Physics Letters* **2007**, *90* (7), 072112.
100. (a) Li, X.; Hihath, J.; Chen, F.; Masuda, T.; Zang, L.; Tao, N., Thermally activated electron transport in single redox molecules. *Journal of the American Chemical Society* **2007**, *129* (37), 11535-11542; (b) Li, C.; Mishchenko, A.; Li, Z.; Pobelov, I.; Wandlowski, T.; Li, X.; Würthner, F.; Bagrets, A.; Evers, F., Electrochemical gate-controlled electron transport of redox-active single perylene bisimide molecular junctions. *Journal of Physics: Condensed Matter* **2008**, *20* (37), 374122.
101. Osorio, E. A.; Moth-Poulsen, K.; van der Zant, H. S. J.; Paaske, J.; Hedegård, P.; Flensberg, K.; Bendix, J.; Bjørnholm, T., Electrical Manipulation of Spin States in a Single Electrostatically Gated Transition-Metal Complex. *Nano Letters* **2009**, *10* (1), 105-110.
102. Nichols, R. J.; Higgins, S. J., Molecular junctions: Interference comes into view. *Nat Nano* **2012**, *7* (5), 281-282.
103. (a) Kang, B. K.; Aratani, N.; Lim, J. K.; Kim, D.; Osuka, A.; Yoo, K.-H., Length and temperature dependence of electrical conduction through dithiolated porphyrin arrays. *Chemical Physics Letters* **2005**, *412* (4), 303-306; (b) Yoon, D. H.; Lee, S. B.; Yoo, K.-H.; Kim, J.; Lim, J. K.; Aratani, N.; Tsuda, A.; Osuka, A.; Kim, D., Electrical conduction through linear porphyrin arrays. *Journal of the American Chemical Society* **2003**, *125* (36), 11062-11064; (c) Kiguchi, M.; Takahashi, T.; Kanehara, M.; Teranishi, T.; Murakoshi, K., Effect of end group

- position on the formation of a single porphyrin molecular junction. *The Journal of Physical Chemistry C* **2009**, *113* (21), 9014-9017; (d) Ferreira, Q.; Bragança, A. M.; Alcácer, L.; Morgado, J., Conductance of Well-Defined Porphyrin Self-Assembled Molecular Wires up to 14 nm in Length. *The Journal of Physical Chemistry C* **2014**, *118* (13), 7229-7234.
104. Sprafke, J. K.; Kondratuk, D. V.; Wykes, M.; Thompson, A. L.; Hoffmann, M.; Drevinskas, R.; Chen, W.-H.; Yong, C. K.; Kärnbratt, J.; Bullock, J. E.; Malfois, M.; Wasielewski, M. R.; Albinsson, B.; Herz, L. M.; Zigmantas, D.; Beljonne, D.; Anderson, H. L., Belt-Shaped π -Systems: Relating Geometry to Electronic Structure in a Six-Porphyrin Nanoring. *Journal of the American Chemical Society* **2011**, *133* (43), 17262-17273.
105. Aradhya, S. V.; Meisner, J. S.; Krikorian, M.; Ahn, S.; Parameswaran, R.; Steigerwald, M. L.; Nuckolls, C.; Venkataraman, L., Dissecting Contact Mechanics from Quantum Interference in Single-Molecule Junctions of Stilbene Derivatives. *Nano Letters* **2012**, *12* (3), 1643-1647.
106. Guedon, C. M.; Valkenier, H.; Markussen, T.; Thygesen, K. S.; Hummelen, J. C.; van der Molen, S. J., Observation of quantum interference in molecular charge transport. *Nat Nano* **2012**, *7* (5), 305-309.
107. Arroyo, C. R.; Tarkuc, S.; Frisenda, R.; Seldenthuis, J. S.; Woerde, C. H. M.; Eelkema, R.; Grozema, F. C.; van der Zant, H. S. J., Signatures of Quantum Interference Effects on Charge Transport Through a Single Benzene Ring. *Angewandte Chemie International Edition* **2013**, *52* (11), 3152-3155.
108. Arroyo, C.; Frisenda, R.; Moth-Poulsen, K.; Seldenthuis, J.; Bjornholm, T.; van der Zant, H., Quantum interference effects at room temperature in OPV-based single-molecule junctions. *Nanoscale Research Letters* **2013**, *8* (1), 234.
109. Ballesteros, L. M.; Martín, S.; Momblona, C.; Marqués-González, S.; López, M. C.; Nichols, R. J.; Low, P. J.; Cea, P., Acetylene Used as a New Linker for Molecular Junctions in Phenylene–Ethyne Oligomer Langmuir–Blodgett Films. *The Journal of Physical Chemistry C* **2012**, *116* (16), 9142-9150.
110. Buschbeck, R.; Low, P. J.; Lang, H., Homoleptic transition metal acetylides. *Coordination Chemistry Reviews* **2011**, *255* (1–2), 241-272.
111. Tao, F.; Xu, G. Q., Attachment Chemistry of Organic Molecules on Si(111)-7 × 7. *Accounts of Chemical Research* **2004**, *37* (11), 882-893.
112. Solomun, T.; Christmann, K.; Baumgaertel, H., Interaction of acetonitrile and benzonitrile with the gold (100) surface. *The Journal of Physical Chemistry* **1989**, *93* (20), 7199-7208.
113. Armarego, W. L. F.; Perrin, D. D., *Purification of Laboratory Chemicals*. Butterworth Heinemann: 1997.
114. Su, Y. Z.; Fu, Y. C.; Wei, Y. M.; Yan, J. W.; Mao, B. W., The electrode/ionic liquid interface: electric double layer and metal electrodeposition. *ChemPhysChem* **2010**, *11* (13), 2764-2778.
115. Vaidyanathan, Vaidyanathan G.; Nair, Balachandran U., Nucleobase Oxidation of DNA by (Terpyridyl)chromium(III) Derivatives. *European Journal of Inorganic Chemistry* **2004**, *2004* (9), 1840-1846.